

DISS. ETH NO. 21415

**GEOMECHANICAL ANALYSIS OF EXCAVATION-INDUCED ROCK MASS BEHAVIOR
OF FAULTED OPALINUS CLAY
AT THE MONT TERRI UNDERGROUND ROCK LABORATORY
(SWITZERLAND)**

A thesis submitted to attain the degree of
DOCTOR OF SCIENCES of ETH ZURICH
(Dr. sc. ETH Zurich)

presented by

RETO THÖNY

MSc of Science in Earth Sciences, ETH Zurich

born on 22. December 1981
citizen of Zillis-Reischen, Graubünden

accepted on the recommendation of

Prof. Dr. Simon Löw

Dr. Florian Amann

Dr. Edward A. Button

Prof. Dr. Mark S. Diederichs

2014

Copyright © 2014 Reto Thöny
All Rights Reserved

Engineering Geology
Geological Institute
ETH Zurich
Sonneggstrasse 5
CH-8092 Zurich
Switzerland

www.engineeringgeology.ethz.ch

**GEOMECHANICAL ANALYSIS OF EXCAVATION-INDUCED ROCK MASS BEHAVIOR
OF FAULTED OPALINUS CLAY
AT THE MONT TERRI UNDERGROUND ROCK LABORATORY
(SWITZERLAND)**

RETO THÖNY

CONTENTS

EXTENDED ABSTRACT	V
ZUSAMMENFASSUNG.....	IX
ACKNOWLEDGEMENTS	XI
LIST OF FIGURES	XIII
LIST OF TABLES	XVIII
1 INTRODUCTION	1
1.1 Motivation and objectives	1
1.1.1 Previous experimental field studies.....	2
1.1.2 Previous numerical studies	3
1.2 Thesis structure	4
1.3 References	4
2 MINE-BY EXPERIMENT.....	7
2.1 Introduction.....	7
2.2 Experiment layout	7
2.3 Excavation procedure and support measures	8
2.4 Field investigations	9
2.5 Rock mass characterization.....	10
2.5.1 Borehole-based investigations.....	10
2.5.1.1 <i>Drillcore logging</i>	10
2.5.1.2 <i>Optical televiewer logging</i>	11
2.5.1.3 <i>Ultrasonic interval velocity measurements</i>	11
2.5.2 Excavation surface investigations	12
2.5.2.1 <i>Geological mapping</i>	12
2.5.2.2 <i>Seismic refraction tomography</i>	13
2.6 Monitoring surveys	13
2.6.1 Excavation surface monitoring.....	13
2.6.1.1 <i>Geodetic measurements</i>	13
2.6.1.2 <i>Laser scanning measurements</i>	14
2.6.2 Borehole monitoring.....	15
2.6.2.1 <i>TRIVEC measurements</i>	15
2.6.2.2 <i>Extensometer measurements</i>	17
2.6.2.3 <i>Deflectometer measurements</i>	18

2.6.2.4	Rock temperature measurements.....	19
2.7	References.....	20
3	STRUCTURAL AND KINEMATIC RELATIONSHIP BETWEEN NATURAL AND EXCAVATION-INDUCED FRACTURES AROUND A TUNNEL IN TECTONICALLY DISTURBED OPALINUS CLAY.....	41
	Abstract.....	41
3.1	Introduction.....	42
3.2	Background.....	43
3.3	Field investigation methods.....	44
3.3.1	Drillcore logging.....	44
3.3.2	Optical televiewer logging.....	44
3.3.3	Ultrasonic interval velocity measurements.....	45
3.3.4	Tunnel mapping.....	45
3.3.5	Seismic refraction tomography.....	46
3.4	Structural analysis of the natural fracture network.....	46
3.5	Geophysical characterization of rock mass heterogeneities.....	48
3.5.1	Spatial variations in rock mass deformability.....	48
3.5.2	Spatial variations in borehole damage.....	49
3.6	Induced fracturing and associated failure mechanisms.....	49
3.6.1	EDZ fracture types and their spatial distribution.....	50
3.6.1.1	Induced fracturing at the sidewalls.....	50
3.6.1.2	Induced fracturing at the tunnel invert.....	50
3.6.1.3	Induced fracturing at the tunnel face.....	51
3.6.2	EDZ failure mechanisms.....	52
3.6.3	Inferred induced stresses around the advancing tunnel.....	53
3.7	Geometrical aspects of EDZ extent.....	53
3.7.1	Spatial variations in EDZ depth.....	53
3.7.1.1	EDZ depth at the tunnel sidewalls.....	53
3.7.1.2	EDZ depth below the tunnel invert.....	55
3.7.2	Conceptual EDZ model.....	55
3.7.2.1	Comparison between EDZ and BdZ.....	56
3.8	Conclusions.....	57
3.9	References.....	58
4	EFFECTS OF TECTONIC FAULTS ON THE SPATIAL AND TEMPORAL EVOLUTION OF THE DISPLACEMENT FIELD AROUND A TUNNEL IN FAULTED OPALINUS CLAY.....	73
	Abstract.....	73
4.1	Introduction.....	74

4.2	Mont Terri Underground Rock Laboratory	74
4.3	Mine-by experiment	75
4.4	Borehole deformation monitoring	76
4.4.1	TRIVEC measurements	76
4.4.2	Extensometer measurements	77
4.4.3	Deflectometer measurements	78
4.5	Excavation surface monitoring	78
4.5.1	Geodetic monitoring	78
4.5.2	Laser scanning monitoring	79
4.6	Results and interpretation	79
4.6.1	Rock mass response on the tunnel-scale	80
4.6.1.1	<i>General displacement pattern</i>	80
4.6.1.2	<i>Integration of geodetic and laser scanner measurements</i>	81
4.6.1.3	<i>Rock mass response at the tunnel crown</i>	81
4.6.1.4	<i>Rock mass response at the tunnel sidewalls</i>	82
4.6.2	Rock mass response on the fracture-scale	83
4.6.2.1	<i>Rock mass response below the tunnel invert</i>	83
4.6.2.2	<i>Rock mass response along the tunnel sidewall</i>	84
4.6.2.3	<i>Rock mass response around the advancing tunnel face</i>	85
4.7	Comparison between short- and long-term rock mass response around the mine-by experiment	86
4.8	Summary and conclusions	88
4.9	References	89
5	EFFECTS OF DEFORMABILITY AND STRENGTH HETEROGENEITIES IN FAULTED OPALINUS CLAY ON THE EXCAVATION-INDUCED STRESS REDISTRIBUTION AND ASSOCIATED ROCK MASS BEHAVIOR	107
	Abstract	107
5.1	Introduction	108
5.2	Mont Terri Underground Rock Laboratory	109
5.3	Mine-by experiment	109
5.4	Numerical modeling of the mine-by experiment	110
5.4.1	Model geometry	110
5.4.2	Excavation process and support measures	111
5.4.3	In-situ stress state and boundary conditions	112
5.4.4	Geodetic and stress path monitoring	112
5.5	Rock mechanical properties of Opalinus Clay	112
5.5.1	Elastic material properties of Opalinus Clay	113

5.5.2	Plastic material properties of Opalinus Clay	113
5.6	Elastic analysis of the short-term rock mass response	114
5.6.1	Longitudinal stress variations in heterogeneous rock	115
5.6.2	Stress path analyses	116
5.6.3	Displacement pattern in anisotropic rock.....	117
5.7	Elasto-plastic analysis of the short-term rock mass response.....	118
5.7.1	Three-dimensional EDZ extent along the mine-by section	119
5.7.2	Three-dimensional displacement pattern along the mine-by section	120
5.8	Discussion of numerical modeling approach	122
5.9	Summary and conclusions.....	122
5.10	References	124
6	SUMMARY AND RECOMMENDATIONS	149
6.1	Summary.....	149
6.1.1	Structural and kinematic relationship between natural and excavation-induced fractures	149
6.1.2	Spatial and temporal evolution of the excavation-induced displacement field.....	150
6.1.3	Stress redistribution around an excavation in anisotropic and heterogeneous clay rock.....	151
6.2	Recommendations	152
6.3	Outlook.....	153
	APPENDIX A	155
A1	Borehole data: Drillcore maps.....	155
	APPENDIX B	173
B1	Tunnel data: Geological maps	173

EXTENDED ABSTRACT

Clay rock formations are widely accepted as potential host rocks for deep geological disposal of nuclear waste as they inherently exhibit favorable isolation characteristics in their natural state. However, due to unfavorable rock mechanical characteristics such as a relatively low strength and a brittle failure behavior the rock mass around an excavation may exhibit substantial perturbations. Thus, construction of underground openings in clay rocks may lead to the formation of a distinct excavation damage zone (EDZ) when redistributed stresses exceed the rock mass strength in the near-field of the tunnel. Exploring the contributing factors that influence the redistributed stress field and the EDZ damage around an advancing tunnel are particularly relevant in the context of risk assessment of deep geological disposal facilities for nuclear waste in clay rock formations.

To investigate the geomechanical processes associated with the rock mass response of faulted Opalinus Clay during conventional tunneling, a full-scale mine-by experiment was carried out in the Gallery 08 at the Mont Terri Underground Rock Laboratory (URL) in Switzerland. Excavation of the mine-by section was carried out concurrently with the construction of the Gallery 08. The mine-by section has a 5 m high horseshoe-shaped profile with a length of 32.5 m and was excavated full-face in 23 steps using a roadheader. The tunnel advanced approximately perpendicular to the bedding strike and in the direction of bedding dip (approximately 45°). The displacements and deformations in the surrounding rock mass were measured by geotechnical instrumentation including borehole inclinometer, extensometer and deflectometer, together with high resolution geodetic displacement measurements and laser scanning measurements of the excavation surfaces. Complimentary data was gathered from structural and geophysical characterization of the surrounding rock mass, comprising detailed geological mapping of the excavation surfaces, borehole logging data and seismic velocity tomography.

Analysis and interpretation of the gained field data was carried out in three parts:

In the first part complementary geological and geophysical characterization techniques on the tunnel and borehole-scale were used for a qualitative and quantitative analysis of the structural and kinematic relationship between the natural and excavation-induced fracture network surrounding the mine-by experiment. Integrating the results from seismic refraction tomography, borehole logging, and tunnel surface mapping revealed that spatial variations in fault frequency along the tunnel axis alter the rock mass deformability and strength which has a substantial effect on the location and radial extent of induced damage on both, the borehole and the tunnel-scale. It could be demonstrated that failure mechanisms, orientations and frequencies of excavation-induced fractures are significantly influenced by the occurrence and characteristics of tectonic faults. At the sidewalls where fault plane reactivation or bedding shear was kinematically constrained, extensional fracturing tangential to the tunnel circumference was the dominating failure mode. At the tunnel face and the tunnel invert, where fault and bedding planes were kinematically free, extensional brittle failure and shearing along bedding planes was dominant in sparsely faulted (0 - 1 fault/m²) tunnel sections, while a combination of shearing along fault planes associated with extensile failure

prevailed in tunnel sections that are intersected by 1 - 3 faults/m². With increasing fault density (> 4 faults/m²), reactivation of densely spaced fault planes became more evident indicating a transition from extensional macroscopic failure to shearing. Based on geological and geophysical data a new conceptual model of the EDZ geometry around the mine-by section was established. The model suggests a strongly damaged inner zone with a consistent radial extent of 0.5 - 1.5 m and less damaged outer zones with a radial extent of 4 m within fault zones and 2 - 3 m in between the fault zones. The depth of the inner zone seems to be unaffected by variations in fault plane density, while the radial extent of the outer zone is substantially influenced by pre-existing tectonic structures.

In the second part excavation-induced displacements and deformations around the mine-by experiment were analyzed on the fracture and the tunnel-scale to assess the influence of pre-existing faults and fault zones on the short- and long-term rock mass response. Displacements and deformations were continuously monitored throughout the excavation of the mine-by experiment and after its construction using borehole inclinometer, extensometers and deflectometer as well as high resolution geodetic and laser scanning measurements. Displacement monitoring data from the mine-by experiment revealed that the rock mass response of faulted Opalinus Clay is substantially governed by both the rock anisotropy and the kinematic failure behavior of individual fault planes, while the overall rock mass behavior correlates more with variations in larger-scale deformability and strength heterogeneities. Integration of the deformation measurements considering both the fracture and the tunnel-scale revealed that individual fault planes were most influential on the rock mass response at the tunnel face, crown and the invert, but were less influential at the sidewalls and at larger depths in the rock mass. At the sidewalls, where fault plane reactivation was of minor relevance due to their unfavorable orientation, the rock mass response was dominated by extensional fracturing through the intact rock matrix resulting in large displacements (up to 40 mm) adjacent to minor and major fault zones. Such excavation-induced fractures showed the potential to evolve into large spalls at the sidewalls, which decisively influenced the local stability of the tunnel. These findings suggest that in faulted Opalinus Clay both, deformations at the fracture and the tunnel-scale must be considered to understand the excavation-induced rock mass response and thus the associated spatial and temporal evolution of the displacement field associated with the development of the EDZ.

In the third part site-specific three-dimensional numerical modeling was used to examine the spatial and temporal evolution of the redistributed stress field around the mine-by section during its step-wise excavation. Elastic analyses demonstrated that deformability and strength heterogeneities in Opalinus Clay, primary caused by multi-scale fault zones, resulted in substantial stress concentrations in the adjacent rock mass leading to an enhanced potential for induced fracturing. Thus, numerical modeling requires considerations of both the rock anisotropy due to the bedding as well as the rock mass heterogeneity and anisotropy due to faults and fault zones to adequately reproduce the failure mechanisms and the associated displacement field observed during the mine-by experiment. Numerical model results showed that the observed spatial variations in failure depth and in the displacement pattern are reasonably reproduced with the utilized linear elasto-plastic model by using constitutive material properties derived from conventional laboratory testing. Although not explicitly implemented in the elasto-

plastic model, information regarding the kinematic failure modes of bedding and fault planes was gained from elastic stress path analysis and determined to be highly informative for identifying potential failure modes associated with variably orientated structural weaknesses.

ZUSAMMENFASSUNG

Für die geologische Tiefenlagerung von radioaktiven Abfällen erlangen Tongesteine aufgrund ihres hohen Einschlussvermögens zunehmend Akzeptanz als Wirtsgesteine. Die geringe Gesteinsfestigkeit und das spröde Bruchverhalten wirken sich beim Bau eines Untertagebauwerkes jedoch negativ auf das umgebende Gestein aus und können unter genügend hohen Gebirgsspannungen zu einer hohlraumnahen Auflockerungszone führen. Das Verständnis über die durch den Tunnelbau induzierten Spannungsumlagerungen um den Hohlraum, sowie deren Einflussfaktoren sind daher für den Bau und die Risikoabschätzung von zukünftigen, geologischen Tiefenlager in Tongesteinen von grosser Bedeutung.

Um die geomechanischen Prozesse und das damit verbundene Gebirgsverhalten in tektonisch überprägtem Opalinuston während des Tunnelvortriebs zu untersuchen, wurde in der Gallery 08 des Felslabors Mont Terri ein massstabgetreues Experiment auf der Tunnelskala durchgeführt. Der untersuchte Tunnelabschnitt hat einen hufeisenförmigen Querschnitt mit einem Durchmesser von rund 5 Metern und wurde während des Auffahrens der Gallery 08 ausgebrochen. Der Vollausschuss des 32.5 m langen Tunnelabschnittes erfolgte in 23 Abschlüssen mit Hilfe eines Roadheaders. Das Gebirgsverhalten und die damit verbundenen Deformationen um den Tunnelhohlraum wurden zum einen mit Hilfe von Deformationsmessgeräten in Bohrlöchern (Inklinometer, Deflektometer, Extensometer) und zum anderen mit geodätischen und Laserscanner Messungen an der Tunneloberfläche erfasst. Zusätzliche Daten umfassen geologische Kartierungen der Tunneloberflächen, Bohrkernanalysen, optische und geophysikalische Bohrlochmessungen, sowie seismische Refraktionsmessungen an der Tunneloberfläche.

Die Analyse und die Interpretation der gewonnenen Messdaten wurden in drei Schritten durchgeführt:

Im ersten Schritt wurde das natürliche und das durch den Tunnelbau induzierte Trennflächengefüge mit Hilfe von geologischen und geophysikalischen Messmethoden qualitativ und quantitativ erfasst. Seismische Geschwindigkeitsmessungen, Bohrkernaufnahmen und Tunnelkartierungen haben ergeben, dass räumliche Variationen der tektonischen Trennflächen entlang der Tunnelachse zu Festigkeits- und Steifigkeitsheterogenitäten im Gebirgsverband führen. Diese Gebirgsheterogenitäten haben sowohl auf der Bohrlochskala, sowie auf der Tunnelskala einen wesentlichen Einfluss auf die Lokalität und die radiale Ausdehnung von induzierten Brüchen um den Hohlraum. Es konnte gezeigt werden, dass sowohl der Bruchmechanismus, die Orientierung, als auch die Häufigkeit von induzierten Brüchen entscheidend von den prä-existenten Klüften und deren Eigenschaften abhängen. An den Tunnelwänden, an denen die Klüfte kinematisch nicht frei sind, dominiert sprödes Bruchverhalten tangential zum Hohlraumrand. An der Tunnelbrust und an der Sohle sind die tektonischen Scher- und Schichtungsflächen durch den Tunnelausbruch kinematisch frei. In Tunnelabschnitten mit einer tektonischen Trennflächenhäufigkeit von 0 - 1 Trennfläche pro Quadratmeter dominieren vor allem Spröd- und Scherbrüche entlang von Schichtungsflächen. In Tunnelabschnitten mit einer tektonischen Trennflächenhäufigkeit zwischen 1 - 3 Trennflächen pro Quadratmeter treten vorwiegend reaktivierte Scherflächen und dadurch induzierte Extensionsbrüche

auf. Mit zunehmender Trennflächenhäufigkeit ändert sich das Bruchverhalten von vorwiegend sprödem Bruchverhalten zu hauptsächlichem Scherversagen entlang von prä-existenten Trennflächen. Basierend auf geologischen und geophysikalischen Messdaten wurde ein konzeptuelles Modell der Auflockerungszone für den untersuchten Tunnelabschnitt erstellt. Die Auflockerungszone besteht aus einer inneren, stark gestörten Zone mit einer radialen Ausdehnung zwischen 0.5 - 1.5 m und einer äusseren, weniger stark gestörten Zone mit einer radialen Ausdehnung von bis zu 4 m innerhalb von Störzonen und 2 - 3 m zwischen den Störzonen. Die innere Zone weist eine relative konstante Ausdehnung über den gesamten Tunnelabschnitt auf, während die radiale Ausdehnung der äusseren Zone, aufgrund der sich ändernden Trennflächenhäufigkeit, entlang der Tunnelachse stark variiert.

Um den Einfluss von prä-existenten, tektonischen Trennflächen und Störzonen auf das kurz- und langfristige Gebirgsverhalten zu untersuchen, wurden die durch den Vortrieb induzierten Verschiebungen und Deformationen auf zwei verschiedenen Grössenskalen analysiert (Trennflächen- und Tunnelskala). Das Gebirgsverhalten und die damit verbundenen Deformationen und Verschiebungen während und nach dem Ausbruch des untersuchten Tunnelabschnittes wurden zum einen mit Hilfe von Deformationsmessgeräten in Bohrlöchern und zum andern mit geodätischen und Laserscanner Messungen an der Tunneloberfläche erfasst. Die Messresultate haben gezeigt, dass das Gebirgsverhalten in stark tektonisiertem Opalinuston, sowohl von individuellen Trennflächen und deren Versagensmechanismen, als auch von den grossskaligen Gebirgsfestigkeits- und Steifigkeitsheterogenitäten bestimmt wird. Die Untersuchungen haben zusätzlich ergeben, dass Verschiebungen an individuellen Trennflächen vorwiegend an der Tunnelfirste, der Sohle und der Tunnelbrust auftreten. Das Bruchverhalten an den Tunnelwänden wird vor allem von spröden Bruchprozessen dominiert, welche im Nahbereich von Störzonen zu stark erhöhten Verformungen führen. Feldbeobachtungen haben ergeben, dass diese Verformungen im Zusammenhang mit grossskaligen Abschalungen an den Seitenwänden stehen, welche die Tunnelstabilität wesentlich beeinflussen. Diese Resultate zeigen, dass sowohl kleinskalige als auch grossskalige Deformationsprozesse berücksichtigt werden müssen, um das vortriebsinduzierte Gebirgsverhalten in tektonisch überprägtem Opalinuston und die damit verbundenen Deformationen zu verstehen.

Im dritten Schritt wurde mit Hilfe von dreidimensionalen, numerischen Modellierungen die zeitliche und räumliche Entwicklung der durch den Vortrieb induzierten Spannungen um den Hohlraum untersucht. Elastische Modellierungen haben gezeigt, dass Festigkeits- und Steifigkeitsheterogenitäten im Opalinuston zu erheblichen Spannungskonzentrationen im angrenzenden Gestein führen, was eine potentielle Erhöhung von spannungsinduzierten Brüchen zur Folge hat. Numerische Modellresultate haben ergeben, dass im Feld beobachtete Bruchtiefen und Verschiebungsmagnituden adäquat reproduziert werden können. Die dafür verwendeten Materialeigenschaften stammen ausschliesslich aus Laboruntersuchungen. Obwohl individuelle, tektonische Scher- und Schichtflächen nicht explizit im numerischen Modell implementiert wurden, haben elastische Spannungspfadanalysen wertvolle Informationen hinsichtlich deren kinematischen Versagensmechanismen ergeben.

ACKNOWLEDGEMENTS

First of all, I would like to thank Florian Amann, the main supervisor of my dissertation. He started his research in the field of radioactive waste disposal about the same time as I started my PhD thesis. So we could share all the highs and lows of the challenging learning process inherently accompanying a dissertation. Thanks Flo, for the great collaboration, your supportive and extremely motivating way, all illuminating and mostly fruitful discussions during and in between lunch and coffee breaks, and the good times we had in the field and on all our business trips. Similarly, I thank Teddy Button for his tireless field and lab support and help with various rock mechanical related problems, and for sharing lots of ideas as well as helpful discussions. All this largely contributes to the success of the present work. I also express special gratitude to Prof. Simon Löw for giving me the opportunity to broaden my engineering geological knowledge by doing this PhD at the Chair of Engineering Geology at ETH Zurich. Gratitude further goes to Prof. Dr. Mark S. Diederichs for acting as the external co-referee, and for reviewing and commenting on the entire thesis manuscript.

I would like to acknowledge the Swiss Federal Nuclear Safety Inspectorate (ENSI) for providing major funding for this research project. I'm also grateful to the cost-sharing project partners Swisstopo (Federal Office of Topography, Switzerland), BGR (Federal Institute for Geosciences and Natural Resources, Germany) and Chevron (USA) for their cooperation.

This thesis also benefited from the collaboration with various people within and outside of ETH. Without their support and engagement, realization of such an intensely collaborative research project would not have been possible. Geological data was provided by Christophe Nussbaum, David Jäggi, Claude Giarardin, Nicolas Badertscher and Lukas Glur. Seismic borehole data was provided by Kristof Schuster with field support from Torsten Tietz. OPTV logging was performed by Marcos Gracia from Terratec Geophysical Services. Seismic tomography data was provided by Valentin Gischig with field support from Freddy Xavier Yugsi Molina and Jürgen Hansemann. Travel time inversion of the seismic data was performed by Manukyan and Marelli from the Geophysical Institute of ETH Zurich. Geodetic measurements and preliminary data processing were conducted by Stephan Schütz from the Geodetic Metrology and Engineering Geodesy Group of ETH Zurich. Laser scanner surveys were performed by Florence Vaudan (Geodetic Metrology and Engineering Geodesy Group, ETH Zurich) and processed by Stephan Schütz. Matthias Kistler provided valuable information about the invert heaving in Gallery o8.

Thanks also to Manfred Blümel, Toni Kauffman, Christian Haug, Katrin Wild, Sebastian Zimmer and Linda Wymann for the time we spent together in the laboratory and for the outcomes of your laboratory investigations. Observations and results of your laboratory investigations formed the basis of the newly established strength criteria for the shaley facies of the Opalinus Clay.

I would also like to thank the entire Engineering Geology group for their camaraderie and providing a pleasant working environment. Especially to Valentin Gischig, Katrin Wild,

Freddy Xavier Yugsi Molina, Martin Ziegler, Santos Jiménez Parras, Ömer Ündül, Keith Frederick Evans, Ralf Brauchler and Peter Bayer who provided support in the office.

Special gratitude goes to my parents Maria and Florian, and to Sarah, for all their unconditional and tireless support, encouragement and motivation throughout the highs and lows of my PhD.

LIST OF FIGURES

Figure 2-1: Geological map of the Mont Terri Underground Rock Laboratory	22
Figure 2-2: Excavation progress and support installation throughout the construction of the mine-by section between GM 94.5 and GM 127.	22
Figure 2-3: Longitudinal plan and cross-section view of the mine-by section showing the tunnel geometry and the final support measures.	23
Figure 2-4: Cross-sectional profiles through the lateral niche and through the mine-by section showing the tunnel geometry and the final support measures.	23
Figure 2-5: Borehole instrumentation around the mine-by section	24
Figure 2-6: Geological structures indentified by optical televiewer and drill core logging of BRC-1, BRC-2, BRC-3, and BRC-4.	25
Figure 2-7: Derived seismic parameters from single-hole interval velocity measurements along the SW-sidewall of the pre-excavation borehole BRC-2	26
Figure 2-8: Locations of the four horizontal geophone arrays along the NE-sidewall and the SW-sidewall presented together with the geological sidewall mapping.	27
Figure 2-9: Horizontal slices through the initial velocity models.....	28
Figure 2-10: Inverted velocities for the receiver Line 1.....	28
Figure 2-11: Inverted velocities for the receiver Line 3	29
Figure 2-12: Inverted velocities for the receiver Line 5.....	29
Figure 2-13: Longitudinal displacement vector plots of the geodetic prisms located on the NE-sidewall and on the SW-sidewall.....	30
Figure 2-14: Cross-sectional displacement vector plots of two geodetic profiles located at GM 100.1 and GM 107.4.	31
Figure 2-15: Unwrapped laser scans of the mine-by section.....	31
Figure 2-16: Incremental and cumulative displacements derived from the TRIVEC measurements in borehole BRC-1 throughout the excavation of the mine-by section.....	32
Figure 2-17: Incremental and cumulative displacements derived from TRIVEC measurements in borehole BRC-1 after the completion of the mine-by experiment.....	33
Figure 2-18: Time series of the measuring intervals of the Magnet-Extensometer (Mag-X 1) throughout the excavation of the mine-by section.....	34
Figure 2-19: Time series of the measuring intervals of the Magnet-Extensometer (Mag-X 2) throughout the excavation of the mine-by section.....	34
Figure 2-20: Time series of the measuring intervals of the Magnet-Extensometer (Mag-X 1) from April 2008 to June 2011	35

Figure 2-21: Time series of the measuring intervals of the Magnet-Extensometer (Mag-X 2) from April 2008 to June 2011	35
Figure 2-22: Time series for measuring points of the Chain-Deflectometer during the excavation phase	36
Figure 2-23: Time series for measuring points of the Chain-Deflectometer of the entire measuring period from June 2008 to May 2011.....	36
Figure 2-24: Evolution of the rock temperature in borehole BRC-2 during the excavation phase	37
Figure 2-25: Annual variations of the rock temperature in borehole BRC-2	37
Figure 3-1: Structural map of the Mont Terri underground rock laboratory.....	61
Figure 3-2: Longitudinal plan and cross-section view of the mine-by section showing the tunnel geometry and the final support measures.	62
Figure 3-3: Mean orientations of tectonic fault sets between GM 40 and GM 127 of Gallery 08 represented in stereographic projection.....	63
Figure 3-4: Fault frequency and spacing distributions along the Gallery 08.....	64
Figure 3-5: Derived seismic parameters from single-hole interval velocity measurements along the SW borehole wall of the pre-excitation borehole BRC-2	65
Figure 3-6: Conceptual model which illustrates the generalized structural and kinematic relationship between pre-existing tectonic faults and excavation-induced EDZ fractures around the mine-by section.....	66
Figure 3-7: Induced fracturing mapped on the walls of the side niche entrances intersecting the Gallery 08 at GM 42 and GM 122 (after C. Girardin et al. 2008).	67
Figure 3-8: Spatial correlation between fault and EDZ fractures derived from systematic window-mapping of the tunnel invert between GM 40 and GM 127.	67
Figure 3-9: Inverted p-wave velocities parallel to the bedding planes for receiver Line 1, receiver Line 3, and receiver Line 5, before and after applying a Kernel filtering.	68
Figure 3-10: EDZ fracture frequencies below the tunnel invert derived from OPTV and core logging of the boreholes BRC-1, BRC-3 and BRC-4.....	69
Figure 3-11: Concept for EDZ geometry around the mine-by section.....	69
Figure 4-1: Geological cross-section along the Mont Terri motorway tunnel	91
Figure 4-2: Structural map of the Mont Terri underground rock laboratory	91
Figure 4-3: Layout and borehole instrumentation of the mine-by experiment	92
Figure 4-4: Displacement vector plots derived from the geodetic measurements showing the short-term displacement pattern throughout the excavation of the mine-by section.....	93

Figure 4-5: Comparison between differential displacements derived from laser scanning measurements and relative displacements derived from geodetic measurements	94
Figure 4-6: Observed failure mechanisms of the rock mass throughout the excavation of the mine-by section leading to minor and major tunnel instabilities.	95
Figure 4-7: Geodetic displacement map showing the cumulative vertical displacement magnitudes along the mine-by section	96
Figure 4-8: Geodetic displacement map showing the cumulative horizontal displacement magnitudes along the mine-by section	96
Figure 4-9: Fault plane reactivation associated with the formation of major sidewall spalls.	97
Figure 4-10: Cumulative horizontal displacement components derived from geodetic measurements showing the evolution of sidewall spalls on both sidewalls	98
Figure 4-11: Incremental and cumulative displacements derived from the TRIVEC measurements in borehole BRC-1 throughout the excavation of the mine-by section.....	99
Figure 4-12: Temporal and spatial evolution of the invert heaving during the excavation of the mine-by experiment.....	100
Figure 4-13: Temporal evolution of the invert heaving after the excavation of the mine-by experiment.....	101
Figure 4-14: Measured invert heaving (i.e. vertical displacement component) along the Gallery o8 in comparison with the integrated vertical displacement derived from the TRIVEC measurement.	102
Figure 4-15: Longitudinal deformations along the borehole BRC-2 presented as incremental and cumulative axial strains derived from extensometer measurements.	103
Figure 4-16: Horizontal deformations derived from deflectometer measurement in borehole BRC-2.....	104
Figure 4-17: Vertical deformations derived from deflectometer measurement in borehole BRC-2.	105
Figure 4-18: Rock mass deformations of the NE-sidewall with distance from tunnel face.....	106
Figure 5-1: Geological cross-section along the Mont Terri motorway tunnel.....	128
Figure 5-2: Horizontal cross-section through the Mont Terri URL	128
Figure 5-3: FLAC 3D model showing the model dimensions and the excavated tunnel geometry.....	129
Figure 5-4: Excavation sequence for the different tunnel sections indicated by their lengths and utilized round lengths.	129
Figure 5-5: Support measures utilized in Section 1 and 2 after its completion.	130
Figure 5-6: Adapted excavation scheme utilized in the mine-by section.....	130

Figure 5-26: Observed failure mechanisms of the rock mass throughout the excavation of the mine-by section leading to minor and major tunnel instabilities.	142
Figure 5-27: Distribution of accumulated plastic shear strain magnitudes of the rock matrix and the fault zones	143
Figure 5-28: Distribution of accumulated plastic shear strain magnitudes of the ubiquitous joints.....	143
Figure 5-29: Horizontal displacement magnitudes derived from geodetic measurements at the end of the mine-by experiment presented as unwrapped contour map.....	143
Figure A 1: Layout of the four boreholes drilled throughout the mine-by experiment.....	156
Figures A 2 - A 4: Drillcore maps of BRC-1 (Girardin et al. 2008).....	157
Figures A 5 - A 14: Drillcore maps of BRC-2 (Girardin et al. 2008).	158
Figures A 15 - A 23: Drillcore maps of BRC-3 (Girardin et al. 2009).	163
Figures A 24 - A 30: Drillcore maps of BRC-4 (Pfister et al. 2011).....	168
Figure B 1: Geological map of the tunnel invert and the tunnel sidewalls between GM 40 and GM 67 (after Nussbaum et al. 2008).	174
Figure B 2: Geological map of the tunnel invert and the tunnel sidewalls between GM 67 and GM 94 (after Nussbaum et al. 2008).....	175
Figure B 3: Geological map of the tunnel invert and the tunnel sidewalls between GM 94 and GM 127 (after Nussbaum et al. 2008).	176
Figure B 4: Geological map of the tunnel invert and the tunnel sidewalls between GM 94 and GM 127 (after Nussbaum et al. 2013).....	177
Figure B 5: Geological maps of the tunnel faces from GM 40.3 to GM 55.0 (after Nussbaum et al. 2008).	178
Figure B 6: Geological maps of the tunnel faces from GM 56.5 to GM 75.2 (after Nussbaum et al. 2008).	179
Figure B 7: Geological maps of the tunnel faces from GM 76.3 to GM 91.8 (after Nussbaum et al. 2008).....	180
Figure B 8: Geological maps of the tunnel faces from GM 92.3 to GM 109.7 (after Nussbaum et al. 2008).	181
Figure B 9: Geological maps of the tunnel faces from GM 111.2 to GM 126.7 (after Nussbaum et al. 2008).	182

LIST OF TABLES

Table 2-1: Detailed list of excavation stops throughout the excavation of the mine-by experiment.....	38
Table 2-2: Detailed list of construction activities and excavation support measures applied throughout the construction of the mine-by experiment	38
Table 2-3: Summary of rock mass characterization methods applied at different stages of the mine-by experiment.....	39
Table 2-4: Summary of monitoring methods applied at different stages of the mine-by experiment.....	39
Table 2-5: Description of the borehole characteristics.....	40
Table 3-1: Mean orientations of fault and bedding planes derived from geological mapping of excavation surfaces of Gallery o8.....	70
Table 3-2: Mean orientations of tectonic faults and bedding planes derived from structural data obtained from the boreholes BRC-1, BRC-2, BRC-3 and BRC-4.....	70
Table 3-3: Classification of identified EDZ fracture types in terms of orientation, location and fractographic markings on fracture surfaces	71
Table 5-1: Magnitudes and orientations of the in-situ principle stresses.....	144
Table 5-2: Elastic material properties	144
Table 5-3: Linear strength properties for peak and residual strength of P-, S- and Z-specimen	144
Table 5-4: Bi-linear strength properties for peak and residual strength of P-, S- and Z-specimen.....	145
Table 5-5: Linear strength properties for peak and residual strength of bedding and fault planes	145
Table 5-6: Bi-linear strength properties for peak and residual strength of bedding and fault planes	146
Table 5-7: Material properties used for the isotropic and anisotropic elastic model.....	146
Table 5-8: Material properties used for the elasto-plastic ubiquitous joint model	147

1 INTRODUCTION

1.1 Motivation and objectives

Clay rock formations are widely accepted as potential host rocks for deep geological disposal of nuclear waste as they inherently exhibit favorable isolation characteristics in their natural state. However, due to unfavorable rock mechanical characteristics such as a relatively low strength and a brittle failure behavior the rock mass around an underground excavation may exhibit substantial perturbations during construction. Thus, construction of underground openings in clay rocks may lead to the formation of a distinct excavation damage zone (EDZ) when redistributed stresses exceed the rock mass strength in the near-field of the excavation. Exploring the contributing factors that influence the redistributed stress field and the associated formation and temporal evolution of the EDZ around an advancing tunnel are particularly relevant in the context of risk assessment of deep geological disposal facilities for nuclear waste in clay rock formations.

In Switzerland, the Opalinus Clay was recently selected as host rock for high and intermediate level nuclear waste. To assess its suitability in the context of radioactive waste disposal and demonstrate the constructability of disposal facilities, the international geoscientific platform, called Mont Terri Project, started operation in 1996 in the Mont Terri Underground Rock Laboratory (URL) in northwestern Switzerland (Bossart & Thury 2008). The underground laboratory is located in the southeastern limb of the Mont Terri anticline in the Opalinus Clay formation at a depth between 250 to 320 m and serves as a generic research facility not located at a potential future repository site.

The Mont Terri URL is intersected by a variety of multi-scale natural faults (Nussbaum & Bossart 2008) and thus is well suited for analyzing the mechanical relevance of pre-existing faults on the excavation-induced rock mass behavior in the tunnel near-field in variably faulted Opalinus Clay. This is particularly relevant for the geotechnical assessment of potential future repository sites located in slightly tectonic overprinted regions, where an enhanced occurrence of multi-scale faults must be anticipated. However, to date little is known about the rock mechanical characteristics of such pre-existing tectonic faults and their mechanical influence on rock mass properties and excavation-induced rock mass behavior in over-consolidated clay rocks during conventional tunneling. Spatial variations in fault characteristics may significantly alter the homogeneity of the rock mass in strength, stress and deformability, and thus may have a significant effect on induced fracturing and associated short and long-term deformations (Grossauer et al. 2003). Understanding the relationship between the excavation-induced rock mass behavior and pre-existing tectonic structures requires a qualitative and quantitative characterization of both, the spatial and temporal evolution of the displacement field as well as the tectonic and induced fracture network of the surrounding rock mass. Integration of these data sets on the fracture and the tunnel-scale allows analyzing the mechanical and kinematic behavior of individual faults as well as the overall rock mass behavior in four dimensions. Combined with three-dimensional site-specific numerical modeling, deformation monitoring data are utilized to gain insights into the role of spatial variations in rock mass properties on the formation and temporal evolution of the EDZ in an anisotropic and heterogeneous medium. The numerical analyses aim to explore effects of deformability and strength heterogeneities

on the excavation-induced stress redistribution and associated induced fracturing in the near-field of the excavation.

1.1.1 Previous experimental field studies

Knowledge of the in-situ rock mass properties and the in-situ stress field is crucial for understanding geomechanical processes and associated failure mechanisms around underground excavations. However, an accurate quantification of both parameters is challenging in a strongly anisotropic material such as the Opalinus Clay which is highly susceptible to environmental changes (e.g. humidity) and thus inevitably subjected to uncertainties. Rock mechanical properties of the intact Opalinus Clay from the Mont Terri URL were investigated in numerous laboratory programs using standard laboratory tests (Rummel & Weber 2004, 2007; Schnier & Stuehrenberg 2007; Zhang et al. 2007; Lux et al. 2007; Popp & Salzer 2006, 2007; Graesle & Plischke 2007) and were summarized by Bock (2001, 2009). Both, the number of laboratory tests as well as the knowledge about factors influencing their short and long-term strength have significantly increased in the last years and thus must be considered for future investigations and predictions. The in-situ stress state at the level of the Mont Terri URL was estimated by Martin and Lanyon (2003) using three-dimensional numerical modeling and field data from stress-induced borehole breakouts and different stress measurement methods in the shaley facies, including undercoring, borehole slotter and hydrofracture tests. Their analyses suggest a sub-vertical maximum principle stress direction which is steeply (70°) inclined towards SSW with a magnitude of 6.5 MPa, a sub-horizontal intermediate principle stress direction trending with 10° towards NW with a magnitude of 4 MPa, and a sub-horizontal minimum principle stress direction trending towards NE with a magnitude of 0.6 MPa. However, Martin and Lanyon (2003) showed that in-situ stress measurements in the Opalinus Clay at the Mont Terri URL are challenging and thus their proposed stress tensor is uncertain. In particular, there is some uncertainty about the magnitude of the minimum principle stress, since this magnitude is less than the undisturbed pore pressure of about 2 MPa measured outside the excavation-disturbed zone at the level of the laboratory (Martin & Lanyon 2004). Thus, Corkum et al. (2006) proposed to adjust the magnitude of the minimum principle stress to 2.2 MPa. Based on the results from the hydrofracture measurements conducted in the inclined borehole at the IS niche, Evans (1999) proposed a value of 2.9 MPa for the minimum principle stress magnitude.

At the Mont Terri URL, several in-situ experiments were conducted or are currently underway to investigate rock mechanical processes in the tunnel near-field that lead to the formation and the temporal evolution of the EDZ in the Opalinus Clay around galleries, niches and boreholes using various geological and geophysical investigation methods (Yong et al. 2004; Bossart & Thury 2008). Established conceptual models for the EDZ geometry (Schuster et al. 2001; Bossart et al. 2002, 2004; Martin et al. 2004; Yong 2008) significantly differ in their extent and geometry depending on the investigation method, the excavation diameter and technique, and especially the orientation of the excavation in respect to the bedding and the in-situ stress tensor. Bossart et al. (2004) proposed a conceptual EDZ model valid for a tunnel excavated in slightly faulted Opalinus Clay with a diameter of 4 m and an excavation axis oriented perpendicular to bedding strike (bedding dip of approximately 45°). Based on structural and hydrogeological investigations, Bossart et al. (2004) divided the EDZ around the tunnel into an inner and an outer shell. In the inner shell, with a maximum radial extent of 1 m,

the induced fractures are interconnected and consist of sub-vertical extensional fractures linked by small-scale shear fractures. In the outer shell, with a maximum radial extent of 2 m, the induced fractures are only partly interconnected and wider spaced. Additional results from ultrasonic velocity measurements (Schuster et al. 2001), electric resistivity tomography (Yaramanci et al. 2002) and hydraulic testing are in general agreement with the model proposed by Bossart et al. (2004), but suggest an asymmetric geometry of the EDZ with a larger extent at the tunnel roof and tunnel invert, and a smaller extent at the sidewalls. Martin et al. (2004) suggest a maximum EDZ depth of one tunnel diameter in the direction of the maximum principle stress orientation and half a tunnel diameter in the direction of the minor principal stress. This is in contrast to findings found by Yong (2008) which propose a maximum EDZ depth of 0.2 - 0.3 m around a 2.5 m diameter niche with a similar excavation direction. Based on local observations of the fracture network around tunnels and boreholes, several processes were proposed for the formation of the EDZ at the Mont Terri URL (Martin et al. 2004; Bossart et al. 2004; Marshall et al. 2006; Bluemling et al. 2007; Yong 2008; Yong et al. 2010, 2013). Martin et al. (2004) suggested that extensional fracturing at the sidewalls, and bedding-parallel slip in the tunnel roof and below the tunnel invert are the main processes promoting the formation of the EDZ for a tunnel and borehole orientation perpendicular to bedding strike. Latest findings on induced macroscopic fracturing around tunnels in slightly faulted Opalinus Clay provide evidence that reactivation of tectonic faults as consequence of excavation-induced stress redistributions play an essential role in the development of the EDZ fracture network (Marshall et al. 2006; Bluemling et al. 2007; Yong 2008; Yong et al. 2010, 2013; Nussbaum et al. 2011). However, relationships between rock mass heterogeneities and spatial variations in induced fracturing in terms of intensity (i.e. EDZ fracture density), changes in failure mechanisms and EDZ extent along the tunnel axis has not been previously investigated.

1.1.2 Previous numerical studies

Complementary to the in-situ experiments, numerous modeling studies have addressed the formation, the geometry, and the extent of the EDZ in the Opalinus Clay around galleries, niches and boreholes using different numerical codes, constitutive models and material properties (e.g. Bluemling & Konietzky 2003; Martin et al. 2004; Corkum & Martin 2007; Te Kamp & Camusso 2009; Yong et al. 2010, 2013). These studies mainly focused on the characterization of deformations and induced failure processes around individual tunnel cross-sections and utilized numerical models typically assumed homogeneous and anisotropic conditions to account for the strength anisotropy due to the pronounced bedding. At the Mont Terri, however, the rock anisotropy due to its pronounced bedding is superimposed by a larger rock mass anisotropy as consequence of frequently occurring natural faults which must be accounted for (Yong 2008). Yong et al. 2010 and 2013 studied the role of individual tectonic faults on the redistributed stress field in the tunnel near-field by back-calculating their mechanical properties from excavation surface displacement measurements. Their numerical analysis proposed a cohesion of 0.8 - 1.1 MPa and a friction angle of 22 - 24° for the tectonic faults. Laboratory results, however, revealed that these values rather represent the strength properties of bedding planes than the strength properties of tectonic fault planes (Haug 2009). As a consequence, a new numerical study using material properties that are solely derived from conventional laboratory testing explores the excavation-induced stress

redistribution and the associated short-term geomechanical processes in an anisotropic and heterogeneous medium. Particular emphasis was placed on the influence of large-scale deformability and strength heterogeneities (i.e. fault zones) on the stress redistribution and associated displacements.

1.2 Thesis structure

The introductory chapter consists of the research motivation and scientific aims of this PhD study including a summary of previous experimental and numerical studies that are related to the main topics discussed in this thesis.

Chapter 2 summarizes the excavation history, the tunneling works and the staged field investigations conducted in 2008. A detailed description of the experiment layout and the used monitoring system is presented together with the resulting data sets.

The following three chapters are written in paper format, so that each chapter can stand alone:

Chapter 3 explores the rock mechanical processes associated with spatial variations in fault frequency, and their effect on the formation of an excavation-induced fracture network around the mine-by experiment.

Chapter 4 examines the spatial and temporal evolution of the displacement field around the mine-by experiment during and after its construction by analyzing excavation-induced deformations and displacements at both the fracture and the tunnel-scale. Special consideration is given to the influence of pre-existing discontinuities and fault zones on the excavation-induced deformation pattern.

Chapter 5 explores the excavation-induced stress redistribution and the associated short-term rock mass response in anisotropic and heterogeneous rock by using 3-dimensional numerical modeling. Particular emphasis was placed on the influence of large-scale deformability and strength heterogeneities (i.e. fault zones) on the stress redistribution and associated displacements.

Chapter 6 summarizes the major findings and scientific results of this research project and provides recommendations for further investigations related to the mechanical behavior of Opalinus Clay under changing environmental conditions.

1.3 References

- Bluemling P, Konietzky H (2003) Development of an excavation disturbed zone in Clay stone (Opalinus Clay). Geotechnical measurements and modelling, Natau, Fecker & Pimentel (eds), Swets & Zeitlinger, Lisse, ISBN 90-5809-603-3
- Bluemling P, Bernier F, Lebon P, Martin CD (2007) The excavation damaged zone in clay formations: Time-dependent behaviour and influence on performance assessment. *Physics and Chemistry of the Earth* 32: 588-599
- Bock H (2001) RA experiment: Rock mechanics analyses and synthesis: Data report on rock mechanics. Unpublished Mont Terri Technical Report 2000-02, Mont Terri Project, Switzerland

- Bock H (2009) RA experiment: Updated review of the rock mechanics properties of the Opalinus Clay of the Mont Terri URL based on laboratory and field testing. Unpublished Mont Terri Technical Report 2008-04, Mont Terri Project, Switzerland
- Bossart P, Meier PM, Moeri A, Trick T, Mayor J-C (2002) Geological and hydraulic characterisation of the excavation disturbed zone in the Opalinus Clay of the Mont Terri Rock Laboratory. *Eng Geol* 66: 19-38
- Bossart P, Trick T, Meier PM, Mayor JC (2004) Structural and hydrogeological characterisation of the excavation-disturbed zone in the Opalinus Clay (Mont Terri Project, Switzerland). *Applied Clay Science* 26: 429-448
- Bossart P, Thury M (2008) Mont Terri Rock Laboratory, project, programme 1996 to 2007 and results. Geological report No. 3, Swiss Geological Survey, Switzerland
- Corkum AG (2006) Non-linear behaviour of Opalinus Clay around underground excavations, PhD thesis, Department of Civil and Environmental Engineering, University of Alberta, Canada
- Corkum AG, Martin CD (2007) Modelling a mine-by test at the Mont Terri rock laboratory, Switzerland. *International Journal of Rock Mechanics & Mining Sciences* 44: 846-859
- Evans KF (1999) Comment to 'Measurement of in-situ stress in weak rocks at Mont Terri Rock Laboratory, Switzerland' by C.D. Martin and G.W. Lanyon. Unpublished report. Geological Institute, ETH Zurich, Switzerland
- Graesle W, Plischke I (2007) LT experiment: Strength and deformation of Opalinus Clay. Unpublished Mont Terri Technical Report 2007-05, Mont Terri Project, Switzerland
- Grossauer K, Schubert W, Kim CY (2003) Tunnelling in heterogeneous ground - stresses and displacements. ISRM 2003, Technology roadmap for rock mechanics, South African Institute of Mining and Metallurgy
- Haug C (2009) Mechanische Charakterisierung präexistenter tektonischer Trennflächen im Opalinuston. MSc thesis, Department of Earth Sciences, ETH Zurich, Switzerland
- Lux KH, Duesterloh U, Czaikowski O (2007) Laboratory tests on indurated clay. Clausthal University of Technology. Final Report for EDZ long term evolution (WP 4.4). European Commission NF-PRO (Contract Number: FI6W-CT-2003-02389) (D 4.4.13)
- Marschall P, Distinguin M, Shao H, Bossart P, Enachescu C, Trick T (2006) Creation and evolution of damage zones around a microtunnel in a claystone formation of the Swiss Jura Mountains. Proceedings of the 2006 SPE International Symposium and Exhibition on Formation Damage Control, Lafayette, Society of Petroleum Engineers, USA
- Martin CD, Lanyon GW (2003) Measurement of in-situ stress in weak rocks at Mont Terri Rock Laboratory, Switzerland. *Int J Rock Mech Min Sci* 40: 1077-1088
- Martin CD, Lanyon GW (2004) Excavation disturbed zone (EDZ) in Clay Shale: Mont Terri. Unpublished Mont Terri Technical Report 2001-01, Mont Terri Project, Switzerland
- Nussbaum C, Bossart P (2008) Geology. In P. Bossart & M. Thury (Eds.), Mont Terri Rock Laboratory. Project, programme 1996 to 2007 and results. Geological report No. 3, Swiss Geological Survey, Switzerland

- Nussbaum C, Bossart P, Amann F, Aubourg C (2011) Analysis of tectonic structures and excavation induced fractures in the Opalinus Clay, Mont Terri underground rock laboratory (Switzerland). *Swiss J Geosci* 104: 187-210
- Popp T, Salzer K (2006) HE-D experiment: Influence of bedding planes. Unpublished Mont Terri Technical Report 2005-34, Mont Terri Project, Switzerland
- Popp T, Salzer K (2007) HE-D experiment: Influence of bedding planes. Unpublished Mont Terri Technical Report 2007-04, Mont Terri Project, Switzerland
- Rummel F, Weber U (2004) RA experiment: Rock mechanical testing and characterization on drillcores of boreholes BRA-1 and BRA-2. Unpublished Mont Terri Technical Note 2004-38, Mont Terri Project, Switzerland
- Rummel F, Weber U (2007) Rock mechanics analyses (RA) experiment: Results of uniaxial and triaxial tests on Opalinus Clay samples. Unpublished Mont Terri Technical Note 2005-57, Mont Terri Project, Switzerland
- Schnier H, Stuehrenberg D (2007) LT experiment: Strength tests on cylindrical specimens, documentation and evaluation. Unpublished Mont Terri Technical Report 2003-04, Mont Terri Project, Switzerland
- Schuster K, Alheid H-J, Boeddener D (2001) Seismic investigation of the excavation damaged zone in Opalinus Clay. *Eng Geol* 61: 189-197
- Te Kamp L, Camusso M (2009) MB (mine-by test) experiment: Numerical modeling of the MB experiment. Unpublished Mont Terri Technical Note 2009-24, Mont Terri Project, Switzerland
- Yaramanci U, Kruschwitz S, Maultzsch S (2002) Geophysical characterisation of the excavation disturbed zone (ED-C) experiment: Geoelectrical characterization of the Opalinus Clay formation in the underground rock laboratory of Mont Terri, Unpublished Mont Terri Technical Report 2000-04, Mont Terri Project, Switzerland
- Yong S, Evans KF, Fidelibus C, Loew S (2004) Fracture generation experiment: a review of the Mont Terri project literature. Unpublished Mont Terri Technical Note 2004-40, Mont Terri Project, Switzerland
- Yong S (2008) A three-dimensional analysis of excavation-induced perturbations in the Opalinus Clay at the Mont Terri Rock Laboratory. PhD thesis, Department of Earth Sciences, ETH Zurich, Switzerland
- Yong S, Kaiser PK, Loew S (2010) Influence of tectonic shears on tunnel-induced fracturing. *International Journal of Rock Mechanics & Mining Sciences* 47: 894-907
- Yong S, Kaiser PK, Loew S (2013) Rock mass response ahead of an advancing face in faulted shale. *International Journal of Rock Mechanics & Mining Sciences* 60: 301-311
- Zhang C-L, Rothfuchs T, Jockwer N, Wiczorek K, Dittrich J, Müller J, Hartwig L, Komischke M (2007) HE-D experiment: Thermal effects on the Opalinus Clay. Unpublished Mont Terri Technical Report 2007-02, Mont Terri Project, Switzerland

2 MINE-BY EXPERIMENT

2.1 Introduction

To investigate the geomechanical processes associated with the rock mass response of faulted Opalinus Clay during conventional tunneling, a full-scale experiment was carried out in the Gallery 08 at the Mont Terri Underground Rock Laboratory (URL) in Switzerland. The fracture network characteristics within the experimental section were characterized prior to and after excavation by integrating structural data from geological mapping of the excavation surfaces and from four pre- and post-excavation boreholes, comprising geological drillcore logging and optical televiewer imaging. Complementary geophysical investigations including single-hole interval velocity measurements and seismic refraction tomography were conducted to quantify spatial variations in the seismic velocities and thus in the rock mass properties and the extent of the excavation-induced damage zone. The displacements and deformations in the surrounding rock mass were measured by geotechnical instrumentation including borehole inclinometer, extensometers and deflectometer, together with high resolution geodetic displacement measurements and laser scanning measurements of the excavation surfaces.

The primary objective of this mine-by experiment is to improve the understanding of the short-term (i.e. excavation phase) and long-term (i.e. open drift phase) rock mass behavior in the near-field of a future repository drift in moderately to strongly faulted Opalinus Clay. Of particular interest are the mechanical properties of the rock mass and the factors that control the deformations in the surrounding rock. Complementing the mine-by experiment, a laboratory investigation program was conducted to improve the understanding of the failure process and strength of intact Opalinus Clay under different loading conditions (Haug 2009; Wild 2010; Amann et al. 2010, 2011a,b,c; Zimmer 2012; Wymann 2013). The synthesis of the acquired geological, laboratory and monitoring data contributes to a better understanding of the short- and long-term excavation-induced rock mechanical processes in the tunnel near-field in a transversal isotropic and heterogeneous clay rock. The conclusions of this work guide the requirements for properly characterizing this material for future project tasks and the associated design specifications.

This chapter provides a summary of the experiment layout and the conducted field investigations. The excavation sequence and the multi-component monitoring system of the mine-by experiment are described in detail, and the main data sets are presented as instrument response plots.

2.2 Experiment layout

In 2008, the Mont Terri URL was expanded through the construction of Gallery 08 southwest of the existing underground laboratory (Figure 2-1). The new gallery has a total length of 167 m and links the existing Galleries 98 and 04. Based on the geological context and the location of the proposed side niches, the mine-by experiment was proposed in a well-defined straight tunnel section between GM 94.5 and GM 127 where the Gallery 08 is intersected by a major fault zone (Figure 2-1). The experiment was carried out concurrently with the construction of the Gallery 08, and lasted from March

27th to July 17th 2008. The mine-by section has a 5 m high horseshoe-shaped profile with a length of 32.5 m. The advance design consisted of 1.5 m excavation steps per day carried out in a repetitive spatial and temporal sequence. The tunnel advanced towards azimuth 152° at a down grade of approximately 2.14%, which is approximately perpendicular to the bedding strike and in the direction of bedding dip. Bedding and bedding-parallel fault planes dip approximately with 45° towards SSE. Only minor rock mass support (i.e. rock bolts and wire mesh) was required, thus allowing initial observations and monitoring of the rock mass response to the excavation. After the excavation of the mine-by section additional data was gathered from new boreholes drilled from the completed gallery and from pre-installed instruments located in boreholes along the gallery boundaries.

2.3 Excavation procedure and support measures

For the construction of the mine-by section between GM 94.5 and GM 127, the excavation procedure and support measures of Gallery 08 were adapted in accordance with the experiment requirements (Burrus & Hagmann 2009). Figure 2-2 shows the excavation progress and support installation throughout the construction of the mine-by experiment, while Table 2-1 summarizes the date and duration of prolonged excavation breaks.

Prior to the excavation of the mine-by section, a lateral niche (Figure 2-3) was constructed in the NE-sidewall of the Gallery 08 between GM 89.5 and GM 94.5. Excavation and lining of the niche was carried out from March 27th to March 28th 2008. The cross-sectional profile through the niche showing the geometry and the support measures is presented in Figure 2-4. The niche was reinforced by rock bolts with a length of 3 m and with a 150 mm thick shotcrete lining. From April 15th to April 18th 2008 concreting of the tunnel invert between GM 37 and GM 88 took place. Excavation of the mine-by section from GM 94.5 - 127 started on April 22nd and ended on June 6th 2008. The 32.5 m long gallery section was mechanically excavated using a roadheader (hydraulic drum cutter Erkat ER 600) in 22 steps over a period of 44 days. The use of the roadheader minimized extraneous damage to the surrounding rock mass and allowed a repetitive excavation process. The same excavation pattern was utilized by the roadheader for each excavation step to create a similar stress path in the rock mass around the tunnel face. With a consistent stress path, variations in the rock mass response can be attributed to changes in the rock mass conditions with higher confidence. As shown in Figure 2-2 the planned 1.5 m excavation steps could not be maintained and the actual excavation rate ranged from 0.5 to 1.9 m/day but did average 1.5 meter per day throughout the construction of the mine-by experiment. As shown in Table 2-1 the down time was approximately 50% of the total excavation period.

Support measures throughout the experiment were installed immediately after each excavation round and consisted of wire mesh reinforcement (K 196) affixed on the tunnel ceiling and eight rock bolts installed approximately 0.7 m behind the advancing tunnel face (Burrus & Hagmann 2009). The geometry and the final support measures for the mine-by section are shown in the schematic cross-section and longitudinal profile in Figure 2-3 and Figure 2-4, respectively. Typically, rock bolts were 22 mm in diameter and 3 m in length, and were installed in 30 mm diameter boreholes. The positions and angles of the rock bolts are shown in Figure 2-4. The gallery section between GM 109 and GM 118 is intersected by a major fault zone and thus was reinforced with five steel arches (UNP

160) and an increased rock bolt length of 4.5 m (Figure 2-3). Shotcrete was not continuously applied throughout the excavation of the mine-by section. A 150 mm thick shotcrete lining was required between GM 94.5 and GM 98 (April 30th - May 5th 2008) and between GM 98 and GM 111.5 (May 15th - May 19th 2008) due to increased radial deformations of the corresponding tunnel profiles which reached action levels defined for the safety management plan (Burrus et al. 2010). From GM 111.5 - 113.5, only the crown was lined with shotcrete. The remaining part of the mine-by section was shotcreted after concluding the main excavation and mapping between June 4th and June 6th 2008. The thickness of the final shotcrete lining varies between 16 and 23 cm. The tunnel invert consisting of a 30 cm thick concrete slab was installed from GM 88 - 130 from July 16th to July 17th 2008. Construction activities and excavation support measures applied throughout the construction of the mine-by experiment are summarized in detail in Table 2-2.

2.4 Field investigations

Field investigations can be subdivided into two categories: (1) investigation methods that were applied for the characterization of the in-situ geological conditions prior to and after excavation, and (2) monitoring surveys that captured the rock mass deformation response throughout the experiment and after its completion. The utilized investigation methods for both categories are summarized in Table 2-3 and Table 2-4, respectively. Data obtained from the field investigations can be further subdivided into those involving information gathering either in or around boreholes, or from the excavation surfaces. Surface measurements include geodetic and laser scanning surveying, seismic refraction tomography as well as geological mapping of excavation surfaces. Borehole based measurements consisted of optical televiewer (OPTV) imaging, single-hole ultrasonic interval velocity measurements (USIVM), continuous deflectometer and extensometer measurements, periodic TRIVEC measurements and rock temperature monitoring. Figure 2-5 shows an overview of the borehole monitoring devices located around the mine-by experiment.

For the comprehensive characterization of the in-situ geological conditions and monitoring of the mechanical rock mass response to the step-wise excavation of the mine-by experiment, field investigations were carried out in three stages: pre-, syn- and post-excavation stage. The pre-excavation stage involved reference measurements for borehole-based monitoring devices and the geological and geophysical characterization of the undisturbed rock mass surrounding the future mine-by section. The syn-excavation stage focused on deformation and displacement monitoring of the surrounding rock mass and the systematic documentation of pre-existing and excavation-induced structures on the excavation surfaces. In the post-excavation stage, the temporal evolution of borehole deformations were continuously monitored extending up to 2.5 years. Additionally, the initial EDZ created during the excavation phase was explored with geophysical methods and by two additional boreholes.

In the following sections, all methods and monitoring systems used throughout the mine-by experiment are described in detail and presented together with relevant details of installation, specifications and recorded data.

2.5 Rock mass characterization

2.5.1 Borehole-based investigations

Four boreholes with different orientations and lengths (Figure 2-3) were used to characterize the natural and excavation-induced fracture network around the mine-by experiment in terms of fracture frequency, orientation and location. Boreholes BRC-1 and BRC-2 were drilled prior to the excavation of the mine-by section and BRC-3 and BRC-4 were drilled after its completion. All boreholes were drilled with double (BRC-1 and 2) or triple (BRC-3 and 4) tube core barrels to minimize drilling-induced fracturing and to acquire high quality core samples for rock mechanical laboratory testing. Borehole BRC-1 is located at GM 93.5 and was drilled from the tunnel invert vertically down to a depth of 8.1 m, crossing the bedding at approximately 45 degrees. Borehole BRC-2 is located within the NE-sidewall of the mine-by section and was drilled from the start niche sub-parallel to the proposed tunnel alignment at the level of the springline to a length of 29.2 m. The borehole axis dips with 2 degrees towards azimuth 144°, thus crossing the bedding at an angle of approximately 45 degrees. Boreholes BRC-3 and BRC-4 were both drilled from the tunnel invert with an inclination of 60 degrees towards azimuth 335° and 331°, respectively. Thus both cross the bedding sub-perpendicularly. Borehole BRC-3 was drilled at GM 110 with a length of 24.5 m, and borehole BRC-4 was drilled at GM 107 with a length of 19.6 m. Borehole-based data include geological drillcore logging, digital imaging of borehole walls with an optical televiewer, and single-hole seismic interval velocity measurements (Table 2-5).

2.5.1.1 Drillcore logging

Drillcores from all four boreholes were obtained either before (BRC-1 and 2) or after (BRC-3 and 4) the tunnel excavation. Drillcores were mapped and photographed immediately after drilling focusing on the identification of natural and excavation-induced discontinuities. Discontinuities with a tectonic origin are consistently characterized by multiple striated surfaces forming discrete mm-thin shear bands which allow tectonic and excavation or drilling-induced fractures to be distinguished. Excavation and drilling-induced fractures were distinguished based on their surface characteristics. In contrast to excavation-induced fractures, drilling-induced fractures have stepped core edges or show signs of drill scoring that can be attributed to core handling or to the drilling process. If discontinuities were healed with a mm-thick calcite infilling they were termed veins. Based on detailed core analyses and the above mentioned surface characteristics, identified discontinuities were classified as: (1) bedding planes, (2) tectonic fractures, (3) excavation-induced fractures, (4) veins, and (5) drilling-induced fractures (i.e. artificial fractures). Drilling-induced fractures were not used for further analyses, except those associated with bedding planes. These were mapped as bedding planes and their angles were measured in respect to the borehole axis and later reoriented according to the known dip direction of the bedding. In addition to above mentioned discontinuity types, lithological heterogeneities such as sandy layers were systematically mapped and have been used to match the drillcore logs with the OPTV logs. The mismatch between drill core and OPTV depth was more pronounced in the downward directed boreholes and was up to 0.7 m for borehole BRC-3. Identified discontinuities and lithological heterogeneities from all four boreholes are presented in Figure 2-6 together with the

results from OPTV logging. Drillcore maps from all four boreholes are compiled in Appendix A.

2.5.1.2 *Optical televiewer logging*

Optical borehole inspections of all four boreholes were performed with a Slimhole Optical Televiewer OPTV52 immediately after drilling and subsequent cleaning of the borehole walls with compressed air (Gracia 2008, 2009, 2010). The true-color image of the borehole wall was instantly oriented to magnetic north in case of a vertical borehole (BRC-1) or to the high side for horizontal and inclined boreholes (BRC-2, BRC-3, and BRC-4). For the given borehole diameters (Table 2-5) and a logging speed of 1.5 - 2.0 m/min, the maximum image resolution is in the range of 0.5 - 1.0 mm in the vertical direction and between 0.2 - 0.5 mm in the horizontal direction. Visualization and evaluation of the high resolution OPTV images was performed using the Software WellCAD 4.3 (Advanced Logic Technology ALT). On the unwrapped OPTV images, geological structures intersecting the borehole are displayed as sinusoids. Based on their geometrical characteristics identified geological features can be characterized in terms of their location (i.e. depth along borehole) and their orientation (i.e. dip and dip direction). Beside this general classification, a more detailed description of their size (i.e. thickness of fault zones and sandy layers), their internal structure (i.e. type of fault zone) and their in-situ hydrogeological condition (i.e. dampness along fault plane intersections) was made. Based on this optical characterization identified geological structures were classified as: (1) bedding planes, (2) tectonic fractures, (3) excavation-induced fractures, (4) veins, and (5) sandy layers. Since tectonic faults are closed within the rock mass, their identification as well as their differentiation from well developed bedding planes is challenging. However, to minimize the subjective nature of the optical classification, identified geological structures were cross-checked with drillcore logging data and found to be in general agreement. OPTV images of all four boreholes superimposed with the identified structures are shown in Figure 2-6 together with the drillcore logging data.

2.5.1.3 *Ultrasonic interval velocity measurements*

Complementary to OPTV logging and geological drillcore mapping, continuous single-hole ultrasonic interval velocity measurements (USIVM) were performed in borehole BRC-2 (Schuster 2008). A BGR mini-sonic probe with a maximum sampling frequency of 10 MHz was utilized. The probe consists of four linearly distributed piezo-electric transducers. One transducer is used as seismic source and the remaining three receivers are located at a distance of 10, 20 and 30 cm from the source. Coupling of the transducers with the borehole wall was accomplished with pneumatic cylinders. For the survey the mini-sonic probe was progressively moved into the borehole at predefined steps. Within the first 6.5 m measurements were carried out in 5 cm steps and for the remaining part of the borehole 10 cm steps were used. The first 6.5 m of the borehole were measured two hours after drilling to a depth of 7.3 m. The remaining part of the 29.2 m long borehole was measured eight hours after drilling was completed.

Seismic velocities and amplitudes derived from first p- and s-wave arrivals were calculated according to travel time and distance, assuming straight ray propagation. However, seismic penetration depth will be different for each of the three measuring intervals (10, 20 and 30 cm), whereby the largest interval length results in the deepest

seismic penetration of approximately 1 to 2 cm (K. Schuster, pers. comm.). According to former USIVM surveys in the Mont Terri URL, a p-wave velocity of 2700 m/s can be regarded as an average velocity of undisturbed Opalinus clay for a wave propagation direction which is 45 degrees inclined in respect to the bedding orientation (K. Schuster, pers. comm.). Deviations from this average p-wave velocity reflect changes in the elastic properties of the surrounding rock mass, and hence can be used for the identification of rock mass heterogeneities and stress-induced rock mass perturbations. Distinct lateral variations of elastic rock mass properties are reflected in a similar increase or decrease of all three velocities (i.e. v_{p1} , v_{p2} and v_{p3}). However, a normal velocity gradient ($v_{p1} < v_{p2} < v_{p3}$) indicates intensified damage towards the borehole and thus allow for the identification of an induced borehole disturbed zone (BdZ) around the borehole. Based on travel time differences of the three different channel configurations, a corrected p-wave velocity which accounts for the BdZ was calculated (K. Schuster, pers. comm.). Normalization of the seismic wave amplitudes was necessary to enable comparison between the three channels as attenuation increased rapidly with increasing distance between the source and the receiver. Based on derived p- and s-wave velocities, elastic parameters such as dynamic Young's and shear modulus, and the dynamic Poisson's ratio were determined (Schuster 2008). Seismic parameters derived from the USIVM survey are presented in Figure 2-7 overlain on the unwrapped OPTV image of the borehole walls of BRC-2 to correlate distinct variations in seismic parameters with identified geological structures.

2.5.2 Excavation surface investigations

2.5.2.1 Geological mapping

Systematic geological tunnel face and sidewall mapping took place immediately after each excavation round between GM 94.5 and GM 127 (Nussbaum et al. 2010). Emphasis was placed on the identification and characterization of pre-existing tectonic and excavation-induced discontinuities and their spatial relationships to identify possible interactions. Sidewalls were mapped repeatedly to characterize the progressive development of macroscopic EDZ fractures as a function of distance to the advancing tunnel face. Since the tunnel invert cannot be mapped during excavation (due to muck), systematic mapping was performed after careful cleaning of the invert when the tunnel face reached GM 94.5 and GM 159, respectively. Geological maps from GM 40 - 127 were used to determine fault frequency and spacing along three scanlines positioned along both sidewalls and the tunnel invert. To analyze potential correlations between the frequency of excavation-induced and tectonic fractures, window-mapping with a window size of 1 x 1 m was performed for the tunnel invert between GM 40 and GM 127. Sidewall mapping of subsequently excavated side niches normal to the direction of Gallery o8 was used to characterize induced fracturing parallel to the sidewalls of Gallery o8, and to obtain estimates for their radial extent into the rock mass (i.e. EDZ depth). Geological maps of the tunnel invert, the tunnel sidewalls and the tunnel faces of Gallery o8 and the adjacent niches that were utilized for the analysis in this study are enclosed in Appendix B.

2.5.2.2 *Seismic refraction tomography*

Seismic refraction tomography was performed on both sidewalls between GM 94 and GM 116. The survey consisted of four horizontal receiver lines (i.e. two lines on each sidewall) located approximately 1.0 and 2.8 m above the invert (Figure 2-8). Each line was equipped with 48 single-component geophones using a geophone and shot spacing of approximately 0.5 m. Geophones were glued 50 mm into the rock or the shotcrete lining to ensure tight contact with the ground. A demolition hammer was used as seismic source. Travel time inversion of the seismic data was performed with the tomography code from Zhou and Greenhalgh (2008) which is valid for tilted transversely isotropic media like the Opalinus Clay. Since the anisotropy axis is not in the plane of the receiver lines, inversion of the four receiver lines was carried out with a 3-dimensional model and inversion algorithm to correctly account for anisotropy effects (Manukyan & Marelli 2009). The dimensions of the inversion model measure 25 m along the tunnel axis (Y-axis), 6 m in height (Z-axis), and 4 m deep into the rock (X-axis). The inversion model cells are sized 0.5 m in X-direction, and 1 m in both Y- and Z-direction. For the initial velocity model a surface velocity of 600 m/s with a depth gradient of 550 m/s per meter has been chosen for the velocity component perpendicular to the anisotropy axis (i.e. parallel to bedding). For the velocity component parallel to the anisotropy axis (i.e. perpendicular to bedding) a surface velocity of 400 m/s with a depth gradient of 370 m/s per meter was assumed (Figure 2-9). For each receiver line only the velocity component parallel and perpendicular to the anisotropy axis was inverted. Out of the four lines, Line 1 (Figure 2-10), Line 3 (Figure 2-11) and Line 5 (Figure 2-12) achieved convergence. The final results from the inversion are presented for a horizontal plane, further referred to as an inversion slice that contains the receiver lines. Note that the outer sections of the inversion slices (i.e. the deepest regions, and the lateral regions) were not updated by the inversion itself, and hence reflect the initial velocity of the inversion model. This is due to the utilized source-receiver positioning and the ray path coverage.

A detailed description of the inversion results together with an interpretation of the relationship between the measured variations in seismic velocities and the natural and excavation-induced fracture network is presented in Chapter 3.

2.6 Monitoring surveys

2.6.1 Excavation surface monitoring

2.6.1.1 *Geodetic measurements*

Geodetic measurements were conducted during the step-wise excavation of the mine-by section between April 22nd and June 2nd 2008. The geodetic monitoring system consisted of a Leica TCRP 1201 total station (accuracy 2 mm + 2 ppm in distance, and 0.3 mgon in angle), 10 reference prisms, and 20 geodetic profiles evenly distributed over the entire length of the mine-by section (Figure 2-13). Subsequent to each excavation round, a geodetic profile consisting of 5 prisms was installed 0.6 to 0.8 m behind the advancing tunnel face as shown in Figure 2-14. Different prisms (Solexperts mini prisms, Geodata prisms, and Leica prisms GPR1) were mounted on steel bolts and glued (HILTI HIT-HY injection glue) 200 - 250 mm into the rock (Schuetz 2009a). Measurements of newly installed prism were conducted 3 to 4 hours after installation to allow curing of the glue.

After installation and curing of the glue displacements were automatically measured every hour by the total station. Due to the large number of geodetic prisms and the length of the experimental section, it was necessary to adjust the position of the total station three times during the excavation to maintain full view of all monitoring profiles. For all three setups the total station was installed on the NE-sidewall approximately 2.5 - 3 m above the tunnel invert level. Since it was not assumed that the total stations remained static over the entire monitoring period, coordinates of the total stations were recalculated hourly.

The direction of displacements are referred to a local coordinate system where the X-axis corresponds to the horizontal alignment of the mine-by section, the Z-axis corresponds to the vertical direction and the Y-axis is directed perpendicular to the tunnel axis. The positive X-axis runs in the direction of the tunnel advance, the positive Z-axis points upwards and the positive Y-axis follows the rule of a left hand coordinate system (Schuetz 2009a).

Geodetic data were analyzed in terms of longitudinal and cross-sectional displacement vector plots, lines of influence, and in terms of contour line plots. For the longitudinal and cross-sectional displacement vector plots the scaled (1:10) cumulative in-plane vector path is plotted for each of the geodetic prisms located in the same plane, thus providing the local cross-section displacement at each location. To observe the longitudinal distribution of the displacement development at a given position on the cross-section, lines of influence are produced by connecting the values of the same displacement component of several measuring points along the tunnel axis recorded at the same time. Plotting several lines of influence in the same plot allows the temporal displacement development along the tunnel axis to be evaluated. For the developed plots the displacements occurring ahead of the tunnel face and between the tunnel face and the prism location are not taken into account by assuming that the displacement at the monitoring section is zero. Due to the systematic installation of the geodetic prisms at a nearly consistent time and distance from the tunnel face the error in ignoring the pre-displacements is considered to be consistent and has minimal influence on the interpretation of the development of the displacement with distance from the tunnel face. Contour line plots are established by interpolating (i.e. krigging) the displacement field between the individual measuring points recorded at the same time.

2.6.1.2 Laser scanning measurements

To complement the geodetic measurements (point measurements), the tunnel surface displacements were evaluated from repeated laser scanning data. An Imager 5006 laser scanner from Zoller+Froehlich was utilized throughout the excavation of the mine-by experiment to record the excavation surface deformations. Scanning was carried out after each excavation round whereby the laser scanner was progressively moved with the advancing tunnel face. For all measurements the laser scanner was placed on a tripod at the centre of tunnel, so that the height of the tipping axis was approximately 1.3 m above the tunnel invert. All scans were performed with a resolution of 10'000 pixel/360° which corresponds to a pixel size of approximately 2 mm at the tunnel walls. The point clouds acquired by the laser scanner consist of x-, y-, and z-coordinates. For a direct comparison between the different laser scans, each point cloud was transformed according to the local established coordinate system using the 3D point cloud processing software Leica Cyclone 6.0 (Schuetz 2009b). The georeferenced scans were subsequently analyzed with

the software TMS Tunnelscan from Amberg Engineering Ltd. to create differential displacement maps by comparing two spatially overlapping scans taken at different excavation stages. The absolute coordinates of each resolution cell are projected on an idealized tunnel profile (normal projection on the tunnel contour) and were then extracted from the coordinates of a reference scan resulting in relative displacements of the excavation surfaces towards the tipping axis of the laser scanner. Reference scans of the excavation surfaces taken at April 29th, May 15th and June 2nd 2008 were obtained prior to the emplacement of shotcrete. Thus, the measuring period of the corresponding tunnel sections was limited to the duration until shotcrete was applied. Differential maps of lined tunnel sections with a nominal shotcrete thickness of 150 mm showed no further increase in relative displacements, indicating that the measuring period prior to the application of the final support is capturing the major part of the measurable displacements. The displacement pattern derived from laser scanning can be compared with the radial displacement pattern obtained by geodetic measurement of the unlined rock mass. A compilation of the obtained differential displacement maps covering the entire mine-by section is presented in Figure 2-15.

Complementary to the laser scanning of the tunnel walls, scanning of the tunnel invert after completion of the mine-by experiment was used to provide geometrical information of the rock surface morphology. Scanning of the tunnel invert between GM 88 and GM 133 required seven individual scans (Schuetz 2009b). From the compiled invert scan three longitudinal profile lines with a resolution of 1 cm were extracted and used to analyze the relationship between the fracture pattern and the invert morphology.

2.6.2 Borehole monitoring

2.6.2.1 TRIVEC measurements

The spatial and temporal evolution of the displacements below the tunnel invert was monitored using a TRIVEC TDR (Solexperts AG). This high precision monitoring system consists of a specially machined HPFC casing that accommodates the measuring probe and allows the three orthogonal components of the displacement vectors along a vertical measuring line to be measured. The TRIVEC was installed into borehole BRC-1 that was drilled vertically from the tunnel invert down to a depth of 8.1 m, crossing the bedding at approximately 45 degrees. The casing was cemented into the borehole on April 7th 2008. The casing consists of 7 measuring intervals with a base length of 1 m, starting at a depth of 0.15 m and ending at a depth of 7.15 m (Keller 2008). A schematic view of the TRIVEC configuration and its location in borehole BRC-1 is shown in Figure 2-5. All measurements were conducted manually with the same TRIVEC probe manufactured by Solexperts AG, following standard procedures (Solexperts AG). The initial TRIVEC measurement was performed 14 days after cementing the casing and right before the excavation of the mine-by section on April 21st 2008. Repeat measurements were conducted immediately after each excavation round and periodically after the completion of the mine-by experiment. The difference between a repeat and the initial measurements gives the profile of inclination and interval length change along the borehole. Multiplying the inclination change by the base-length of the probe (1 m), displacement of the upper end of the instrument with respect to the lower end can be obtained. The horizontal components are measured along two perpendicular axes, further referred as the positive X'-axis and Y'-axis. These measuring directions are predefined within the measuring

heads of the casing that accommodate the TRIVEC probe and are oriented during the installation of the TRIVEC. The positive X'-axis is oriented towards N123°E and the positive Y'-axis towards N033°E. For the evaluation of the horizontal displacements, the measured values were transformed into a direction parallel (X-axis) and perpendicular (Y-axis) to the gallery axis (see Figure 2-16). Inclinometer sensors for the X'- and Y'-directions allow for angle changes up to 14.5° from the vertical (Keller 2008). The accuracy was 0.05 mm/m for the incremental horizontal displacements. The vertical displacement sensor measures changes in distance between the lower and the upper end of the probe (base-length of 1 m), with negative values denoting extension. Vertical displacement measurements have an accuracy of 0.003 mm, and an extension or shortening of the probe of up to 10 mm can be accommodated (Keller 2008).

Data are presented as incremental or cumulative displacements along the borehole axis. Differential displacements derived from the lowest measuring interval show that the TRIVEC does not reach stable ground. Additionally, accurate measurements of the borehole top are not available due to the construction process. To develop the relative displacement profile and the changes during the excavation the displacements were integrated from the farthest measuring point located at a depth of 7.15 m. Thus, measured accumulated displacements indicate a lower limit of the measurable deformations.

Both incremental and cumulative displacements measured in borehole BRC-1 throughout the excavation of the mine-by section between April 22nd and June 2nd 2008 are presented in Figure 2-16. Further shown in Figure 2-16 are the orientations of the horizontal measuring axis within the TRIVEC casing and the orientations of the evaluated displacement directions parallel and perpendicular to the gallery axis. Patterns of both horizontal displacement components show distinct displacements concentrated across pre-existing tectonic faults and excavation-induced unloading fractures. Horizontal displacements parallel to the tunnel axis are generally larger and consistently trend in the direction of the excavation advance. Elongation was consistently measured for all measuring intervals, whereby axial displacements were largest across natural and induced discontinuities. This behavior is interpreted as mechanical unloading of the rock mass as consequence of tunnel advance. In between these discontinuities, small horizontal and vertical displacements indicate block movements. The same behavior can also be deduced from the cumulative displacement patterns. Figure 2-17 shows displacement patterns derived from two repeated surveys conducted 241 and 312 days after the reference measurement. Both of the repeat measurements show a similar deformation pattern as measured at the end of the mine-by construction, but magnitudes are strongly increased, particularly in the uppermost 4 meters. It is suggested that the reason for this behavior is most likely caused by time-dependent processes such as mechanical or clay mineral swelling. A complete kinematic interpretation of borehole deformations is presented in Chapter 4.

Due to large deformations at the borehole top, the borehole BRC-1 became inaccessible for further TRIVEC measurements after the measuring campaign in February 2009. Thus, the monitoring period for the TRIVEC is limited to a total duration of 11 months.

2.6.2.2 Extensometer measurements

Two arrays of magnetic extensometers (Mag-X 1 and 2) were installed in borehole BRC-2 to continuously measure the relative longitudinal displacement of the surrounding rock mass throughout and after the construction of the mine-by section. Borehole BRC-2 is located within the NE-sidewall and was drilled from the start niche sub-parallel to the proposed tunnel alignment at the level of the springline. The borehole axis dips with 2 degrees towards azimuth 144° , thus crossing the bedding at an angle of approximately 45 degrees. Both arrays were installed prior to the excavation, thus capturing the entire longitudinal rock mass response to the step-wise excavation of the mine-by section. The extensometer arrays consists of two individual 15 m long high precision multi-point extensometers (Mag-X 1 and 2) overlapping over an interval of 3 m between 11.9 and 14.9 m so that they can be treated as one single extensometer. Each extensometer array consists of a total of 20 measuring points (i.e. magnets) with a separation of 0.7 to 0.8 m (Keller 2008). The first measuring point is located 0.5 m from the start of the borehole and the last one at a distance of 26.3 m, resulting in a total monitoring length of 25.8 m. The borehole axis is oriented sub-parallel to the tunnel axis (i.e. deviation of 8°), thus the radial distance of the extensometers to the tunnel alignment linearly increases from 1.3 m at the head of the instrument up to 4.6 m at the end of it. A schematic of the used extensometer configuration is shown in Figure 2-5. To achieve the maximum measurement accuracy of 0.002 mm the assembly was grouted into the borehole on April 7th 2008 (Keller 2008), thus anchoring the magnets (measurement points) to the surrounding rock. A connection from the extensometers to the data acquisition system allows simultaneous measuring and recording of all measurement positions relative to the location of the extensometer heads. Changes in distance between the individual measuring points were calculated with respect to the first measurements, further referred as reference measurement. Reference measurements of both extensometer arrays were conducted 14 days after their installation to allow curing of the grout. Throughout the excavation of the mine-by section measurements were taken every 2 minutes, and after construction was completed every 10 minutes. Seven months after the installation of the two extensometer arrays the acquisition system for the extensometer Mag-X 1 was interrupted from the end of November 2008 until the beginning of June 2009 for unknown reasons.

Cumulative changes in interval lengths are presented for both extensometers individually in Figure 2-18 and Figure 2-19 for the excavation phase, and in Figure 2-20 and Figure 2-21 for the open drift phase, respectively. Time series for both extensometers were filtered with a 4-hours median algorithm, and resampled every 24 hours at 3 am. Measuring intervals were numbered 1 through 34 starting from the borehole mouth and are color-coded with the corresponding time series. Negative values denote a shortening of the interval length and thus indicate a contractive deformation behavior, while positive values denote an elongation of the initial interval length, and hence indicate a dilative deformation behavior. Also shown is the unwrapped OPTV image of the borehole wall including the location of the measuring intervals and the identified tectonic faults and fault zones along the borehole.

In Chapter 4 measured interval changes are evaluated in terms of cumulative longitudinal strains to allow for a better correlation with the geological structures.

2.6.2.3 Deflectometer measurements

Complementary to the two extensometer arrays installed in borehole BRC-2, the borehole was additionally equipped with a Chain-Deflectometer (Solexperts AG). This multiple deflectometer provides continuous biaxial deflection measurements along the borehole axis with respect to the initial measurement. The measuring instrument consists of a continuous aluminum rod that is equipped with 14 individual measuring heads. The instrument is emplaced in a specially machined HPVC casing that was bonded to the rock with cementitious grout prior to the excavation of the mine-by experiment on April 7th 2008 (Keller 2008). Each of the measuring heads, except of the first and the last one, are equipped with strain gauge sensors to measure deflections in two perpendicular directions. They were oriented in the vertical and radial (i.e. horizontal) direction during the emplacement of the measuring probe into the casing on April 15th 2008 (Keller 2008). The first four and the last two measuring heads are separated by a distance of 3 m, while the measuring heads in between are located at an interval of 1.5 m. The total length of the deflectometer is 25.5 m with the first measuring head being located 0.4 m from the borehole mouth. The borehole axis is oriented sub-parallel to the tunnel axis (i.e. deviation of 8°), thus the radial distance from the deflectometer to the tunnel alignment is linearly increasing from 1.3 m at the head of the instrument up to 4.6 m at the end. A schematic of the utilized deflectometer configuration is shown in Figure 2-5. After its installation the deflectometer was connected to a dedicated data acquisition system to record deformations every 2 min throughout the excavation of the mine-by section and every 10 min after completion of it. In December 2010 the acquisition system failed for unknown reasons, thus the entire monitoring period covers a time span of approximately 32 months.

The Chain-Deflectometer can be regarded as a continuous beam (Keller 2008). Hence, local deformations along the deflectometer affect deflections of several measuring points. This relation was taken into account for transforming the measured deflections into effective angle changes (mm/m) by using a specific calibration matrix which was provided from the manufacturer (Solexperts AG) for the utilized configuration. The calibration matrix was determined in the laboratory by deflecting each measuring head by a constant distance in both directions and by simultaneously capturing the deformation behavior of the other measuring heads (M. Keller, pers. comm.).

Time series of cumulative radial and vertical deflections are presented in Figure 2-22 for the excavation phase, and in Figure 2-23 for the entire measuring period of 32 months. Time series for both directions were filtered with a 4-hours median algorithm, and resampled every 24 hours at 3 am. Measuring heads equipped with strain gauges are numbered 1 through 12 starting from the borehole mouth and are color-coded with the corresponding time series. Negative deflections denote bending of the deflectometer probe towards the tunnel in case of radial deflections and downward bending in case of vertical deflections, as indicated with a sketch in both figures. Also shown is the unwrapped OPTV image of the borehole wall including the location of the measuring heads and the identified tectonic faults and fault zones.

Distinct changes in radial and vertical deflections during the excavation phase (Figure 2-22) indicate localized deformation of the rock mass in both directions. These signals were consistently measured for measuring points that are located within or adjacent to strongly tectonized zones. Measuring points located in borehole sections that were only intersected by individual fault planes show no or only marginal signs of relative

deformations, indicated by unchanged deflections. As expected for the position of the instrument in the sidewall, the radial deformations are larger than the vertical ones. The most pronounced radial deflections occurred for measuring point 1 located in a minor shear zone close to the start niche and for the measuring points 8, 10 and 11, located ahead and within the major fault zone. Their distinct onset of deflection increase can be correlated with the advancing tunnel face and the resulting kinematic freedom in the radial direction. While increased deflections of measuring point 1 stagnates after lining of the tunnel walls until GM 98, the measuring points located in the major fault zone are steadily displaced towards the tunnel at an increased rate during excavation advances and with a decreased rate during excavation breaks. Vertical deflection changes are most pronounced for the measuring points 3, 4 and 5 located between GM 104 and GM 107, and for the measuring points 9 to 12 located within and behind the major fault zone. In comparison with the radial component, vertical deflections are generally smaller and show a more complex deformation pattern. It is suggested that this pattern is related to complex stress redistributions around the advancing tunnel face, in particular in the near-field of the major fault zone where multiple discontinuities can result in various relative displacements on individual structures.

Cumulative radial and vertical deflections of the entire measuring period ranging from April 2008 to December 2010 are presented in Figure 2-23. The largest variations in the radial and vertical deflections were measured during the excavation phase between the April 21st and June 2nd 2008. This is explained by the advancing tunnel face and the resulting kinematic freedom, especially for the radial direction. During the open drift phase between June 2008 and May 2011, small variations in deflection were limited to weaker fault zones and some of them last until the end of the measuring period in December 2010. For measuring points located in less fractured rock mass, cumulative radial and vertical deflections revealed constant values after completion of Gallery 08 at the end of December 2008. Note, that 6 months after installation of the deflectometer both strain gauges of measuring point 5 failed for unknown reasons. Simultaneously, the time series of the measuring point 7 (purple line in Figure 2-23) shows a pattern that deviates strongly from the others. The reason for this anomalous behavior is unknown, but most likely caused by a measuring error, since this strong deflection is not compensated by the adjacent measuring points.

A more detailed interpretation of the deflectometer data in terms of cumulative angle changes ahead and behind of the advancing tunnel face will be presented in Chapter 4.

2.6.2.4 *Rock temperature measurements*

Three PT1000 temperature sensors were installed in borehole BRC-2 to continuously monitor the evolution of the borehole temperature during and after the construction of the mine-by section. Prior to excavation, temperature sensors were grouted outside of the deflectometer casing at a borehole depth of 0.4 m, 13.90 m and 25.90 m (Keller 2008), thus resulting in a radial distance to the final tunnel alignment of 1.3 m, 3.0 m and 4.6 m, respectively. Temperature measurements were recorded from April 15th 2008 to May 31st 2011 at a sampling rate of 10 min.

Figure 2-24 shows the borehole temperatures derived from the three temperature sensors as a function of time and depth throughout the excavation phase of the mine-by experiment. Temperatures at 0.4 m depth are the highest with a general increase from

18°C at the beginning of the excavation towards 21°C at the end of it. Superimposed are smaller temperature fluctuations that can be attributed to the extensive heat production during the excavation procedure. During excavation advance, measured temperatures are increasing and during excavation breaks temperatures are decreasing. This behavior, however, is only reflected in the temperature measurements of Sensor 1. Rock temperatures at a radial distance of 3.0 m (i.e. 13.9 m borehole depth) and 4.6 m (i.e. 25.9 m borehole depth) to the tunnel alignment show undisturbed rock temperatures of approximately 16°C ahead of the advancing tunnel face. Their onset of temperature increases occur 7 and 21 days after the tunnel has passed their location along the tunnel axis. This is due to the larger horizontal distances to the tunnel alignment. After inference with the tunnel temperature, however, both sensors show similar temperature profiles with only slight fluctuations due to the excavation sequence. This indicates a much stronger attenuation of the temperature signal for the Sensors 2 and 3 compared with Sensor 1 and suggests that the both sensors (i.e. Sensor 2 and 3) are not connected with the tunnel through EDZ fractures as it is the most likely case for Sensor 1.

Figure 2-25 presents the recorded annual temperature changes of the three sensors for the entire measuring period between April 2008 and May 2011. The overall pattern is similar to that one described for the excavation phase. Sensor 1 shows the largest annual temperature variations superimposed by smaller temperature fluctuations most probably reflecting the temperature changes in Gallery 08. Temperatures deeper in the rock (Sensor 2 and 3) generally have similar temperature profiles showing substantially smaller annual temperature changes. Their onset of temperature changes, however, is delayed by some days with respect to Sensor 1.

2.7 References

- Amann F, Button EA, Bluemel M, Thoeny R (2010) Insight into the mechanical behaviour of Opalinus Clay. Paper presented at European Rock Mechanics Symposium 2010, Lausanne, Switzerland, Rock Mechanics and Environmental Engineering, edited by Zhao, Labious, Dudt and Mathier, Taylor & Francis Group, London, ISBN 978-0-415-58654-2
- Amann F, Button EA, Evans KF, Gischig VS, Bluemel M (2011a) Experimental study of the brittle behavior of clay shale in rapid unconfined compression. *Rock Mech Rock Eng* 44: 415-430
- Amann F, Kaiser PK, Button EA (2011b) Experimental study of brittle behavior of clay shale in rapid triaxial compression. *Rock Mech Rock Eng* 45: 21-33
- Amann F, Thoeny R, Kaiser PK, Button EA (2011c) Insight into the brittle failure behavior of clay shales in unconfined and confined compression. Proceedings of the 45th US Rock Mechanics/Geomechanics Symposium 2011, San Francisco, CA, American Rock Mechanics Association, ARMA 11-536
- Burrus F, Hagmann S (2009) RC experiment: Project and experimental requirements during the excavation of RC section of Gallery 08. Unpublished Mont Terri Technical Note 2008-44, Mont Terri Project, Switzerland

- Burrus F, Bossart P, Nussbaum C (2010) Gallery 08 - Documentation of the excavation and the convergence measurements. Unpublished Mont Terri Technical Note 2008-10, Mont Terri Project, Switzerland
- Gracia M (2008) Bohrlochmessungen Mont Terri Bohrung BRC-1 und BRC-2. Unpublished report, Terratec Geophysical Services, Germany
- Gracia M (2009) Borehole logging in the Mont Terri test site in the hole BRC-3. Unpublished report, Terratec Geophysical Services, Germany
- Gracia M (2010) Borehole logging in the Mont Terri test site in the hole BRC-4. Unpublished report, Terratec Geophysical Services, Germany
- Haug C (2009) Mechanische Charakterisierung prä-existenter tektonischer Trennflächen im Opalinuston. MSc thesis, Department of Earth Sciences, ETH Zurich, Switzerland
- Keller M (2008) Mont Terri - RC experiment: Instrumentation report. Unpublished Mont Terri Technical Note 2008-34, Mont Terri Project, Switzerland
- Manukyan E, Marelli S (2009) Anisotropic travel time inversion seismic data along an EDZ at Mont Terri. Internal technical note, Department of Earth Sciences, ETH Zurich, Switzerland
- Nussbaum C, Girardin C, Badertscher N, Risse V, Veuve C, Mayoraz J, Bossart P (2010) Extension of the rock laboratory: Geological documentation of the Gallery 08 and adjacent niches. Unpublished Mont Terri Technical Note 2008-12, Mont Terri Project, Switzerland
- Nussbaum C, Bossart P, Amann F, Aubourg C (2011) Analysis of tectonic structures and excavation induced fractures in the Opalinus Clay, Mont Terri underground rock laboratory (Switzerland). *Swiss J Geosci* 104: 187-210
- Schuetz S (2009a) RC experiment: Convergence measurements in Gallery 98 and 08 during excavation of RC section. Unpublished Mont Terri Technical Note 2008-50, Mont Terri Project, Switzerland
- Schuetz S (2009b) RC experiment: Laser scanning in Gallery 08 during excavation of RC section. Unpublished Mont Terri Technical Note 2008-64, Mont Terri Project, Switzerland
- Schuster K (2008) Ultrasonic interval velocity measurements. RC experiment - Mont Terri RL. Unpublished report. Federal Institute for Geosciences and Natural Resources (BRG), Germany
- Wild K (2010) Charakterisierung des Verhaltens von Opalinuston unter Zugbeanspruchung. BSc thesis, Department of Earth Sciences, ETH Zurich, Switzerland
- Wymann L (2013) The influence of saturation on the uniaxial compressive strength of Opalinus Clay. MSc thesis, Department of Earth Sciences, ETH Zurich, Switzerland
- Zhou B, Greenhalgh S (2008) Non-linear travelttime inversion for 3-d seismic tomography in strongly anisotropic media. *Geophysical Journal International* 172(1): 383-394
- Zimmer S (2012) Untersuchungen zur einaxialen Zugfestigkeit von Opalinuston in Abhängigkeit der Saugspannung. BSc thesis, Department of Earth Sciences, ETH Zurich, Switzerland

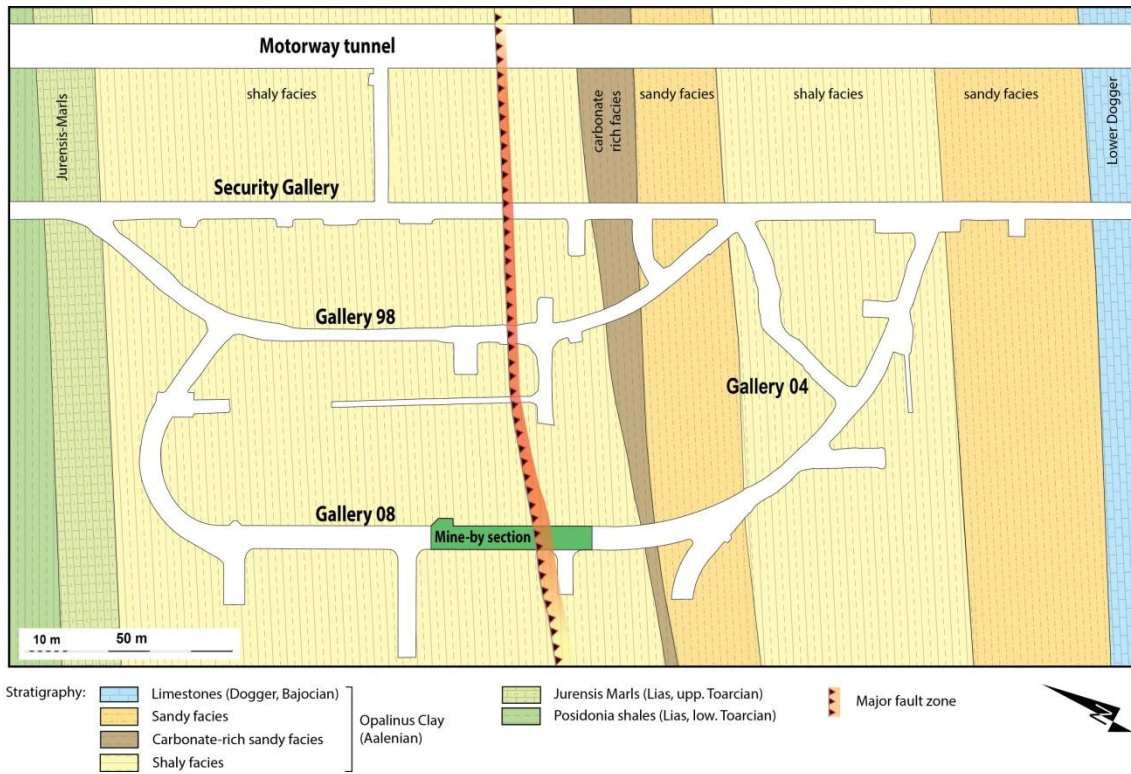


Figure 2-1: Geological map of the Mont Terri Underground Rock Laboratory (from Nussbaum et al. 2011), showing the various galleries and niches. The mine-by section, highlighted in green, was carried out in the straight tunnel section between GM 94.5 and GM 127 where the Gallery o8 is intersected by a major fault zone.

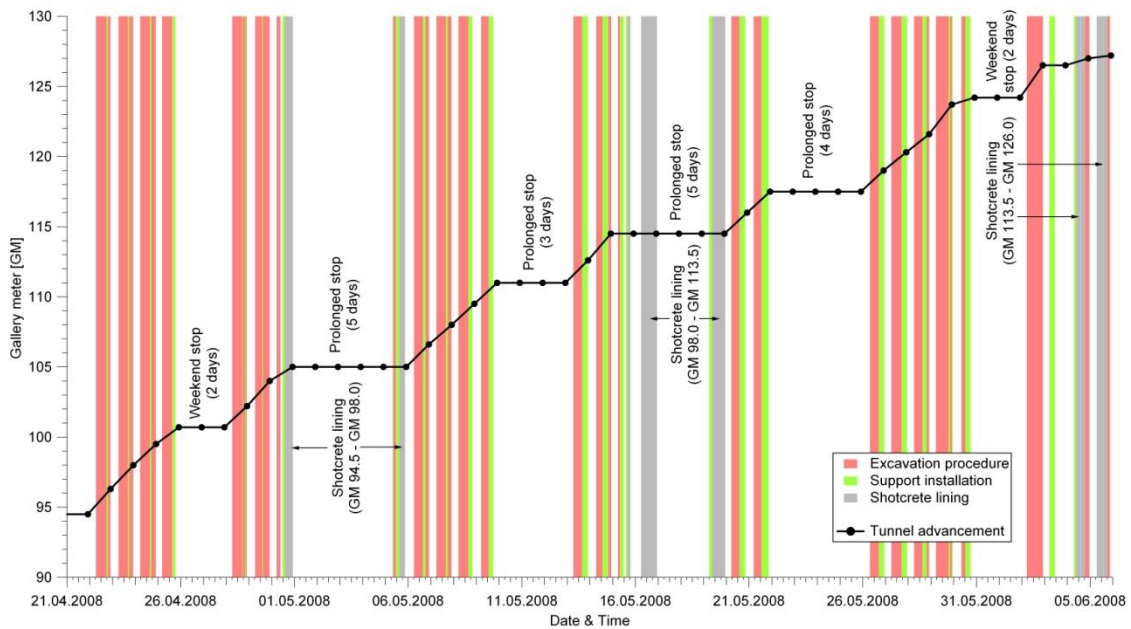


Figure 2-2: Excavation progress and support installation throughout the construction of the mine-by section between GM 94.5 and GM 127.

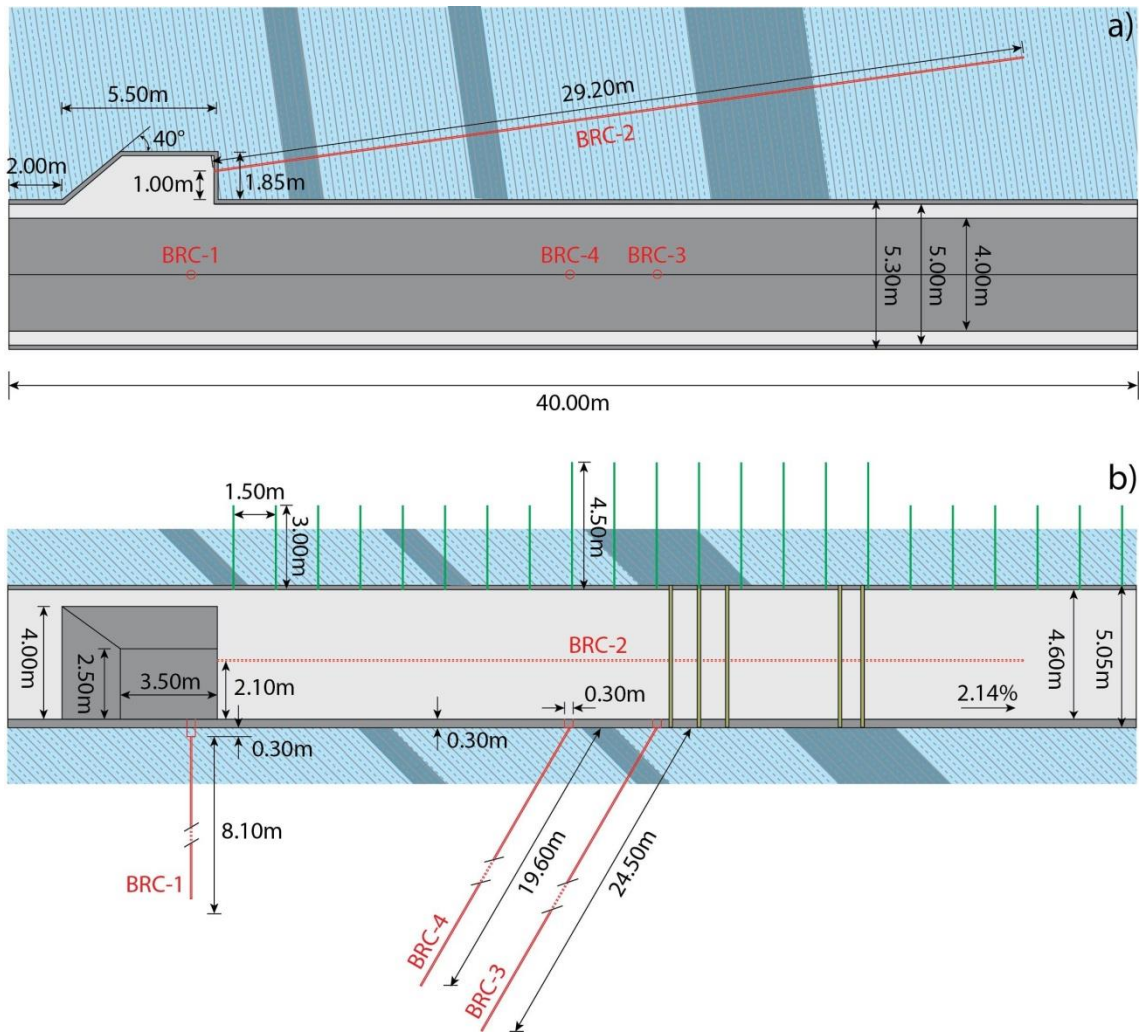


Figure 2-3: Longitudinal a) plan and b) cross-section view of the mine-by section showing the tunnel geometry and the final support measures.

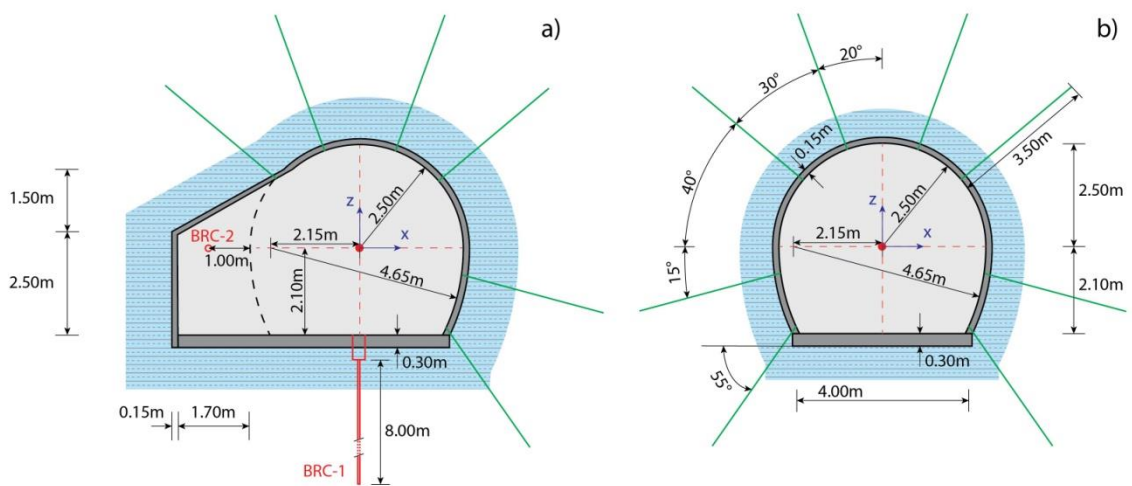


Figure 2-4: Cross-sectional profiles a) through the lateral niche and b) through the mine-by section showing the tunnel geometry and the final support measures.

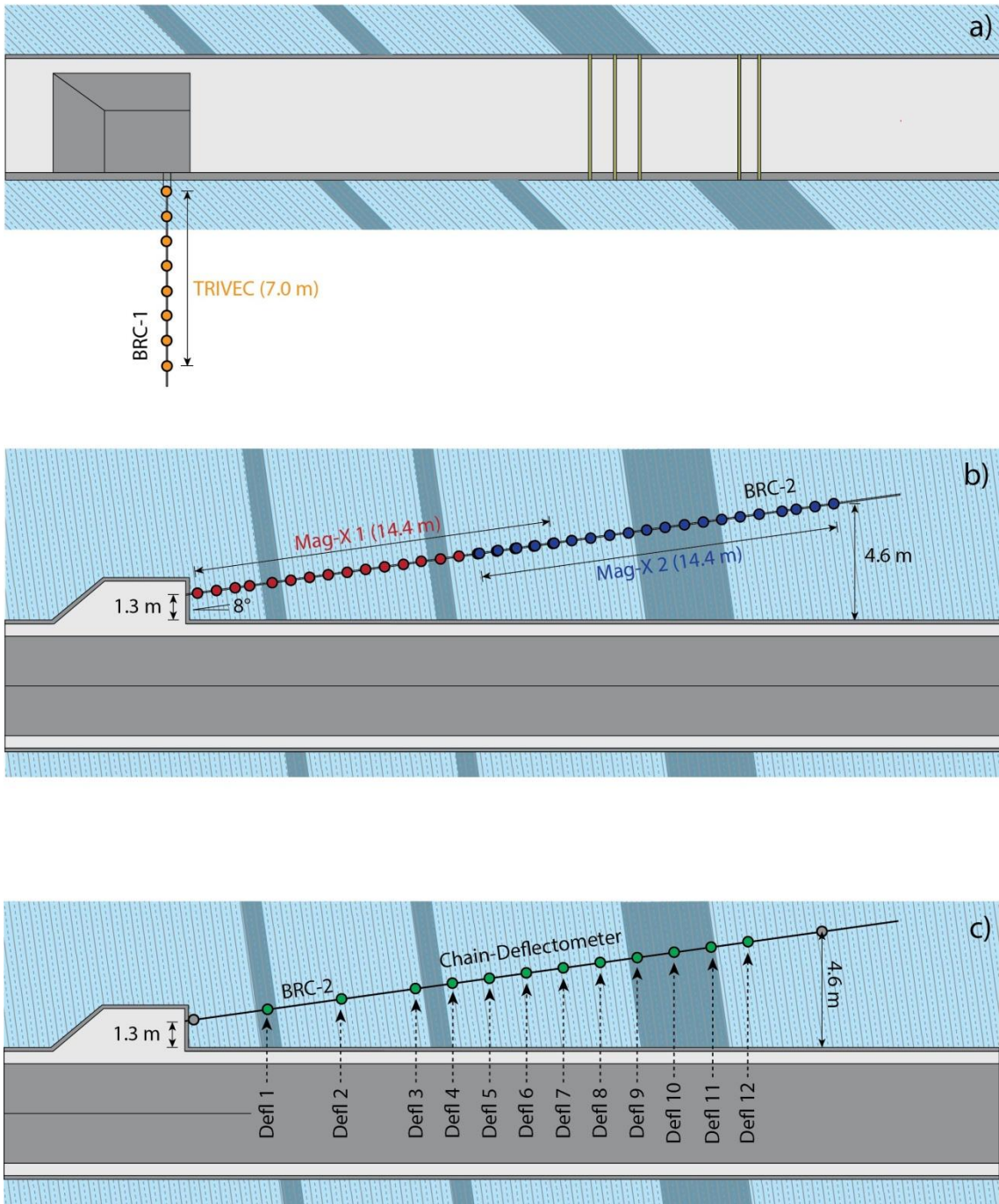


Figure 2-5: Borehole instrumentation around the mine-by experiment, including a) a borehole inclinometer, b) two Magnet-Extensometers, and c) a Chain-Deflectometer.

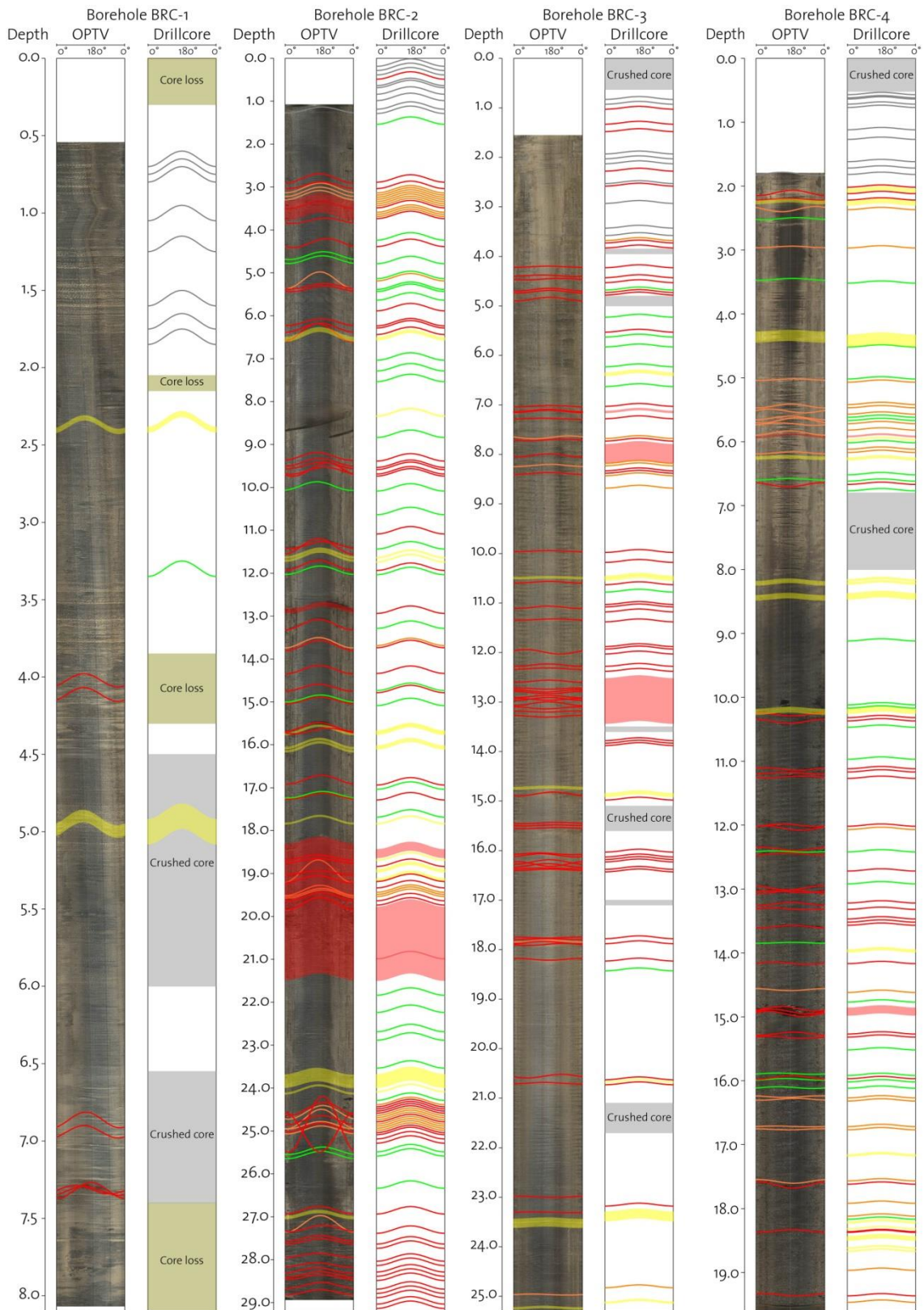


Figure 2-6: Geological structures identified by optical televiwer and drillcore logging of BRC-1, BRC-2, BRC-3, and BRC-4. Tectonic faults and fault zones are shown in red, EDZ fractures in grey, calcite veins in orange, bedding planes in green, and sandy layers in yellow.

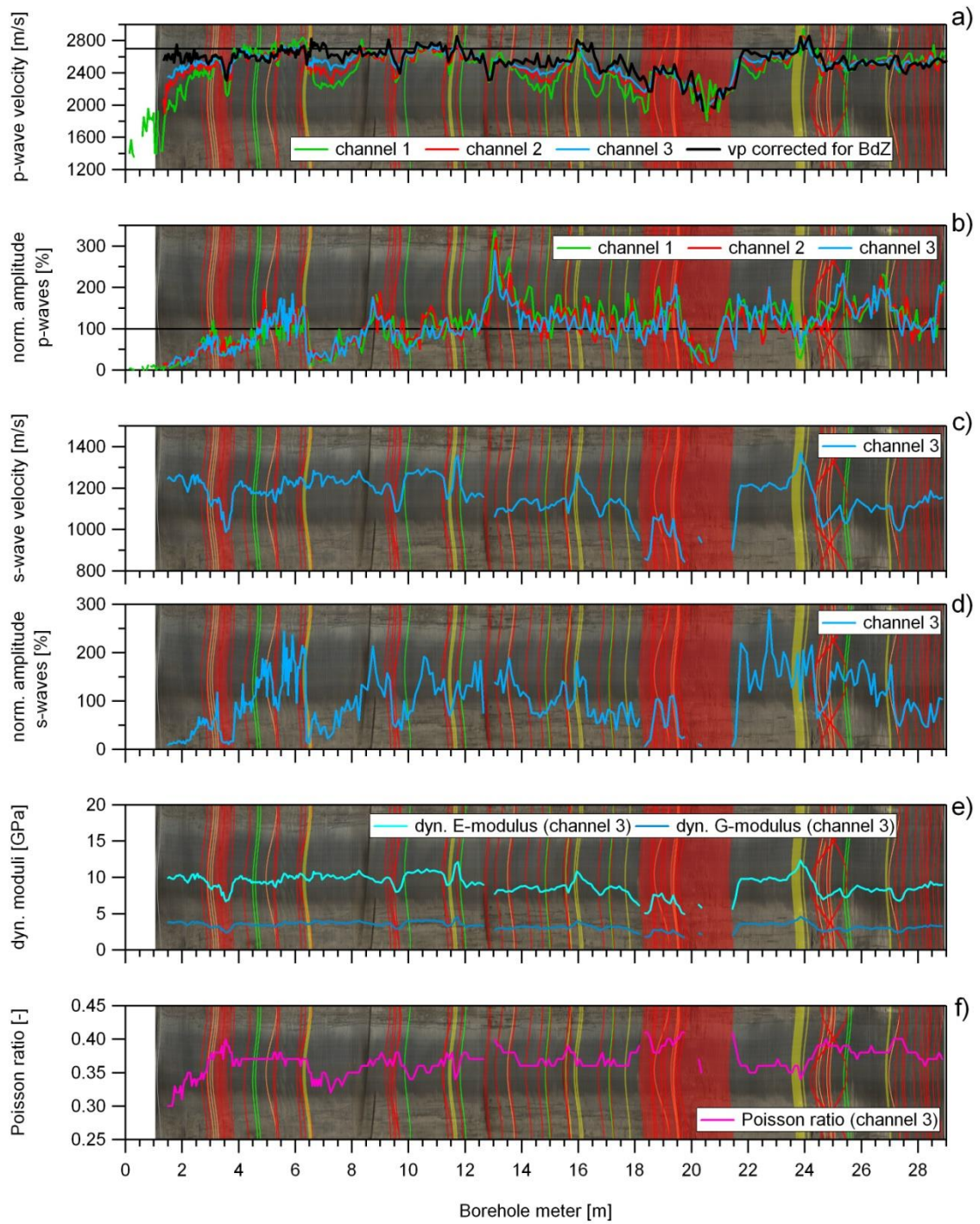


Figure 2-7: Derived seismic parameters from single-hole interval velocity measurements along the SW-sidewall of the pre-excavation borehole BRC-2 including: a) p-wave velocities and b) normalized amplitudes for all three channels, c) s-wave velocity and d) normalized amplitudes for channel 3, e) dynamic Young's and shear modulus, and f) Poisson ratio derived from p- and s-wave velocities from channel 3.

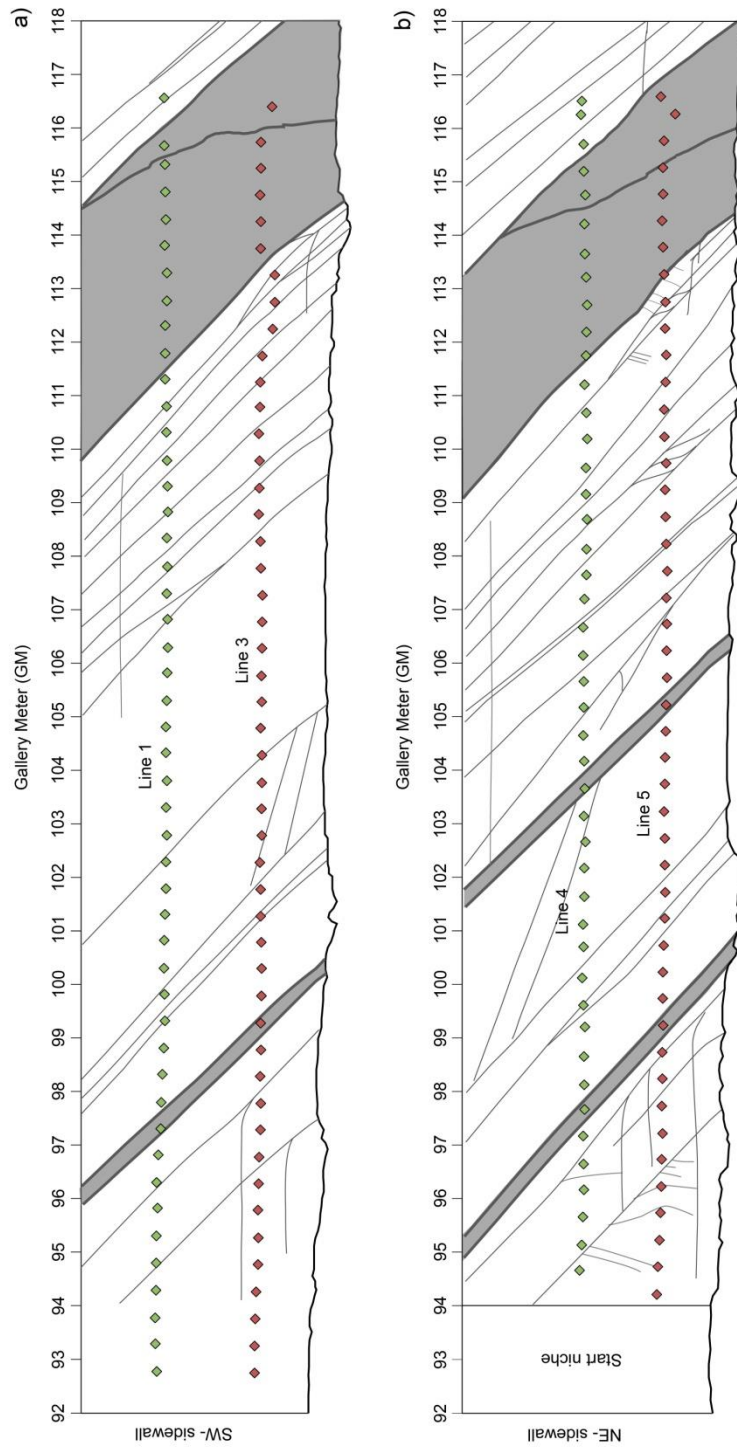


Figure 2-8: Locations of the four horizontal geophone arrays along a) the SW-sidewall and b) the NE-sidewall presented together with the geological sidewall mapping. Note, that only Line 1, Line 3 and Line 5 achieved convergence during inversion. Thus, Line 4 could not be used for further analyses.

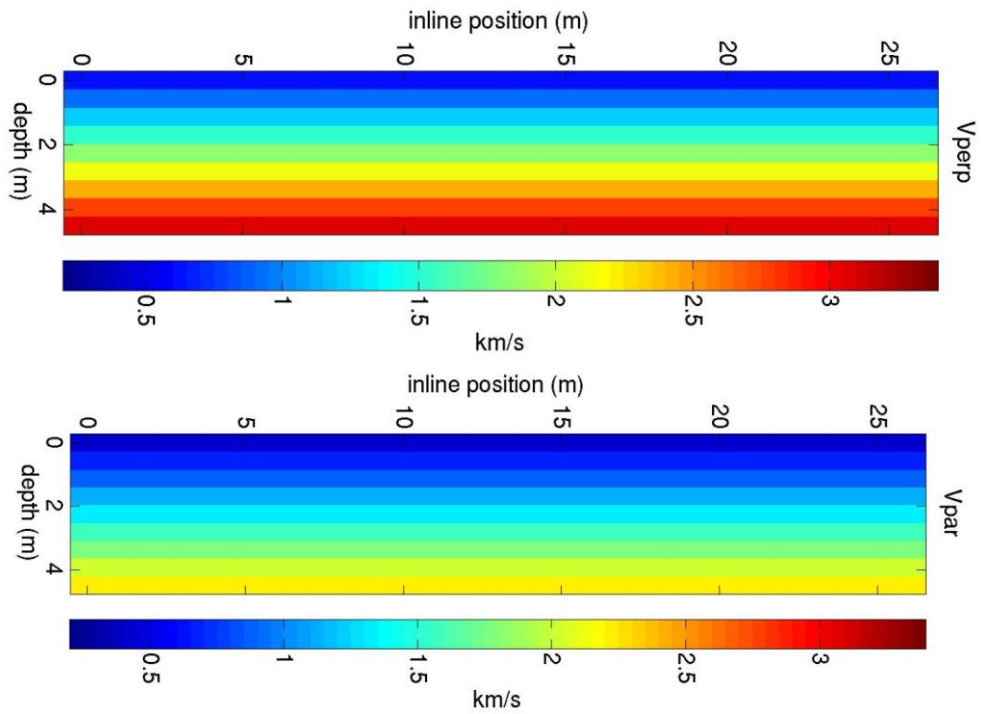


Figure 2-9: Horizontal slices through the initial velocity model for the velocity component perpendicular (at the top) and parallel (at the bottom) to the anisotropy axis (Manukyan & Marelli 2009).

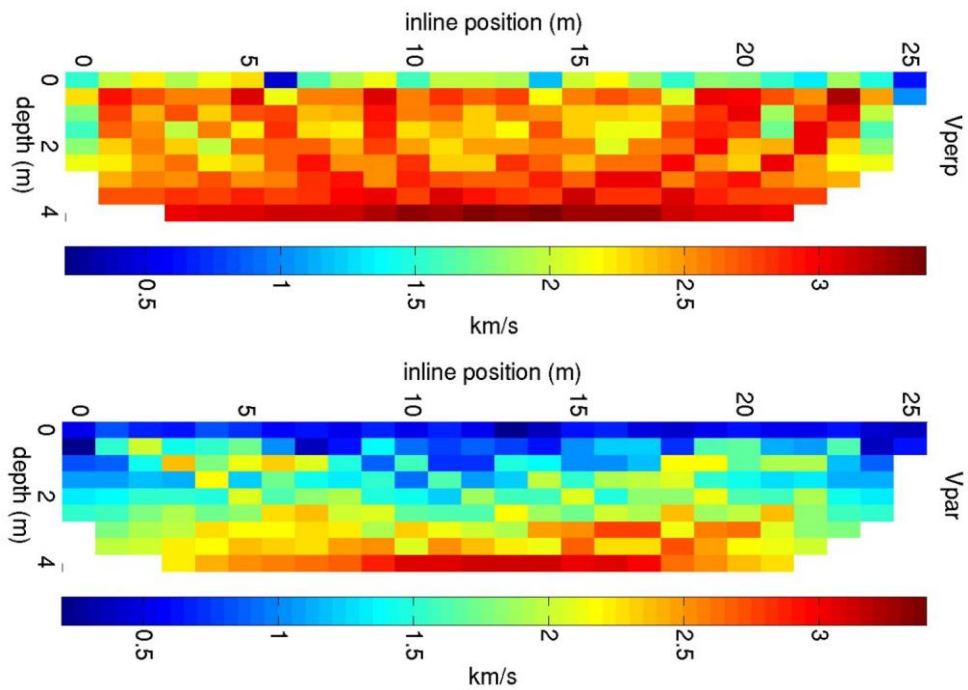


Figure 2-10: Inverted velocities for the receiver Line 1 perpendicular (at the top) and parallel (at the bottom) to the anisotropy axis (Manukyan & Marelli 2009).

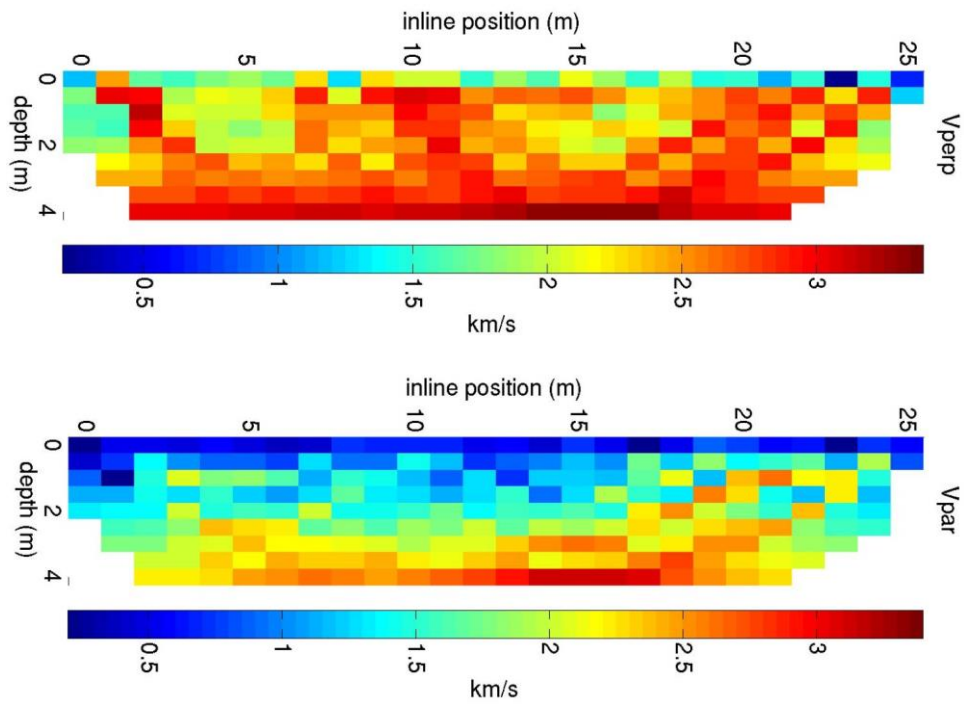


Figure 2-11: Inverted velocities for the receiver Line 3 perpendicular (at the top) and parallel (at the bottom) to the anisotropy axis (Manukyan & Marelli 2009).

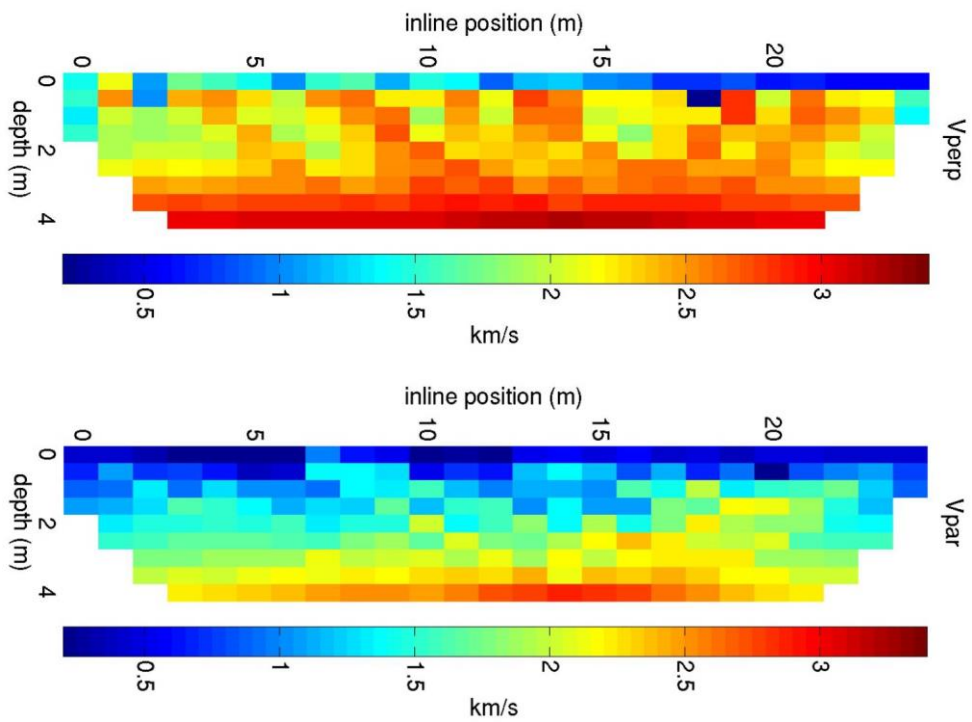


Figure 2-12: Inverted velocities for the receiver Line 5 perpendicular (at the top) and parallel (at the bottom) to the anisotropy axis (Manukyan & Marelli 2009).

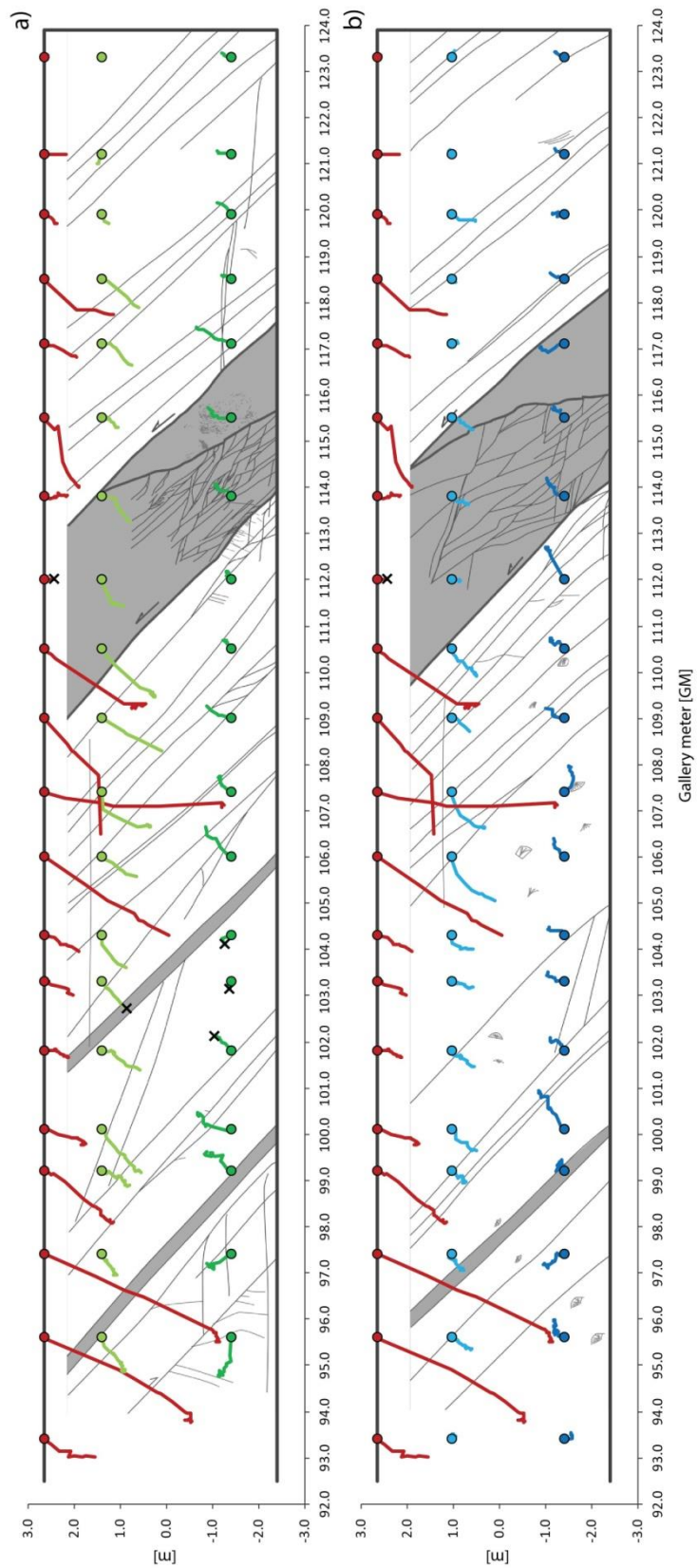


Figure 2-13: Longitudinal displacement vector plots of the geodetic prisms located a) on the NE-sidewall and b) on the SW-sidewall. Displacement magnitudes are scaled by a factor of 10 relative to the size of the tunnel.

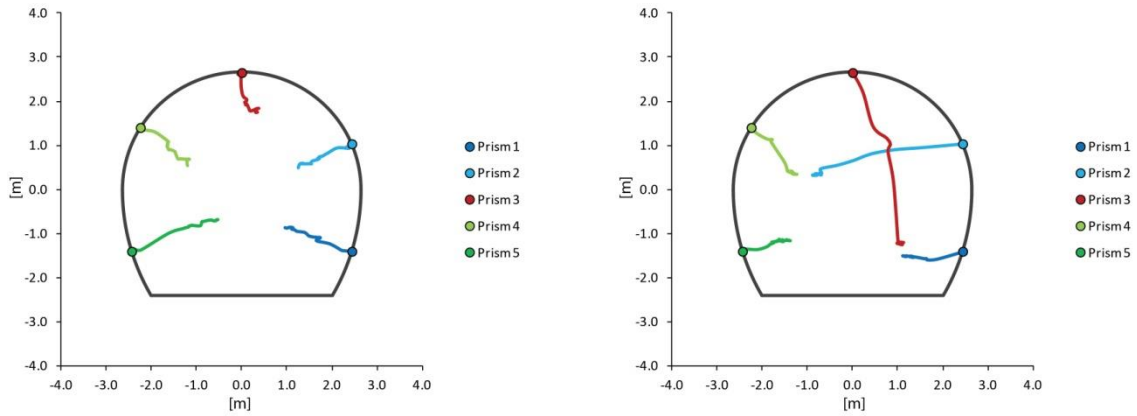


Figure 2-14: Cross-sectional displacement vector plots of two geodetic profiles located at GM 100.1 and GM 107.4, respectively. Displacement magnitudes are scaled by a factor of 10 relative to the size of the tunnel.

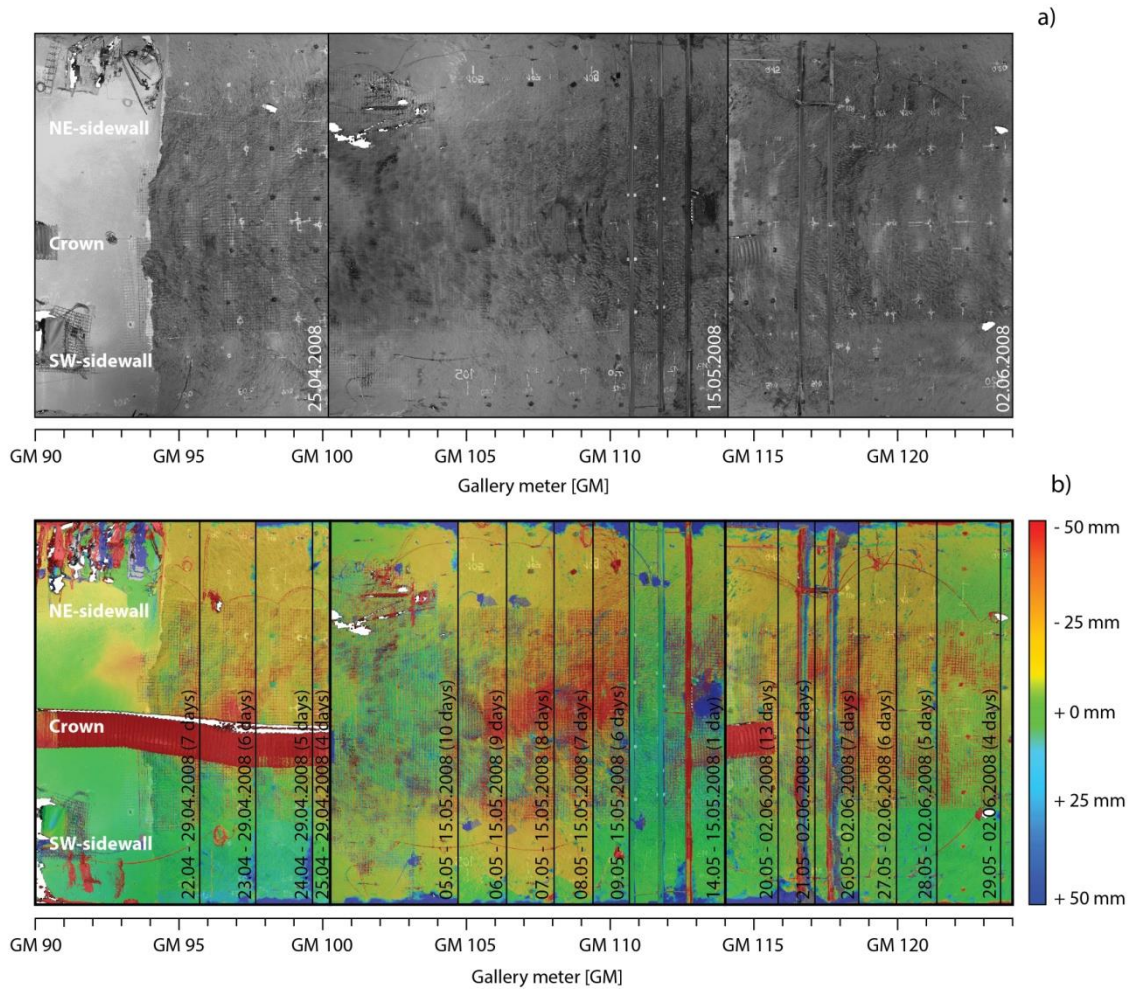


Figure 2-15: Unwrapped laser scans of the mine-by section. a) Reference scans taken prior to the emplacement of shotcrete. b) Compilation of differential displacement maps covering the entire mine-by section. Negative values (red to yellow) show displacements towards the tipping axis of the scanner, positive values (light blue to blue) away from it, and turquoise values represent zero displacement.

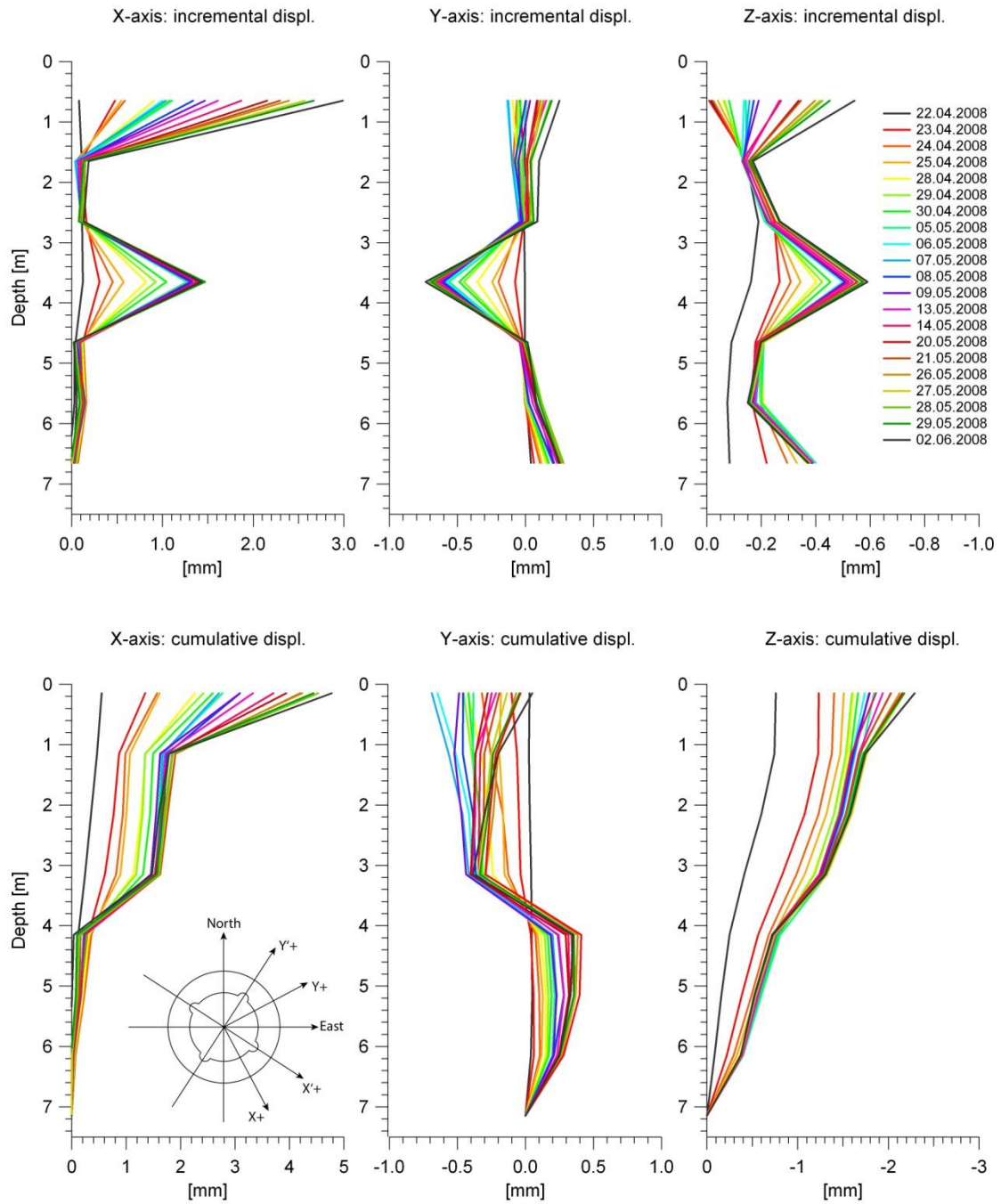


Figure 2-16: Incremental and cumulative displacements derived from the TRIVEC measurements in borehole BRC-1 throughout the excavation of the mine-by section.

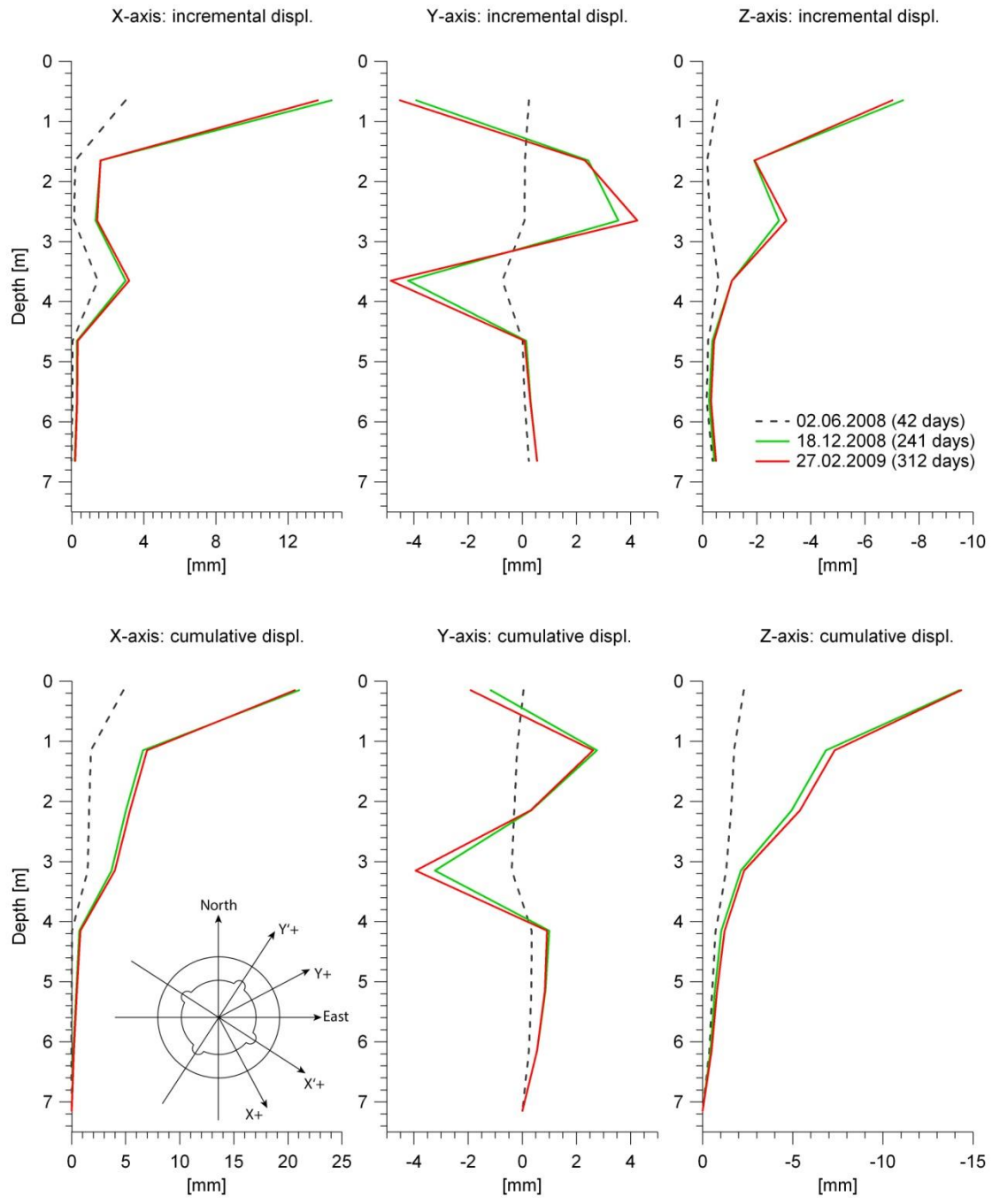


Figure 2-17: Incremental and cumulative displacements derived from TRIVEC measurements in borehole BRC-1 after the completion of the mine-by experiment.

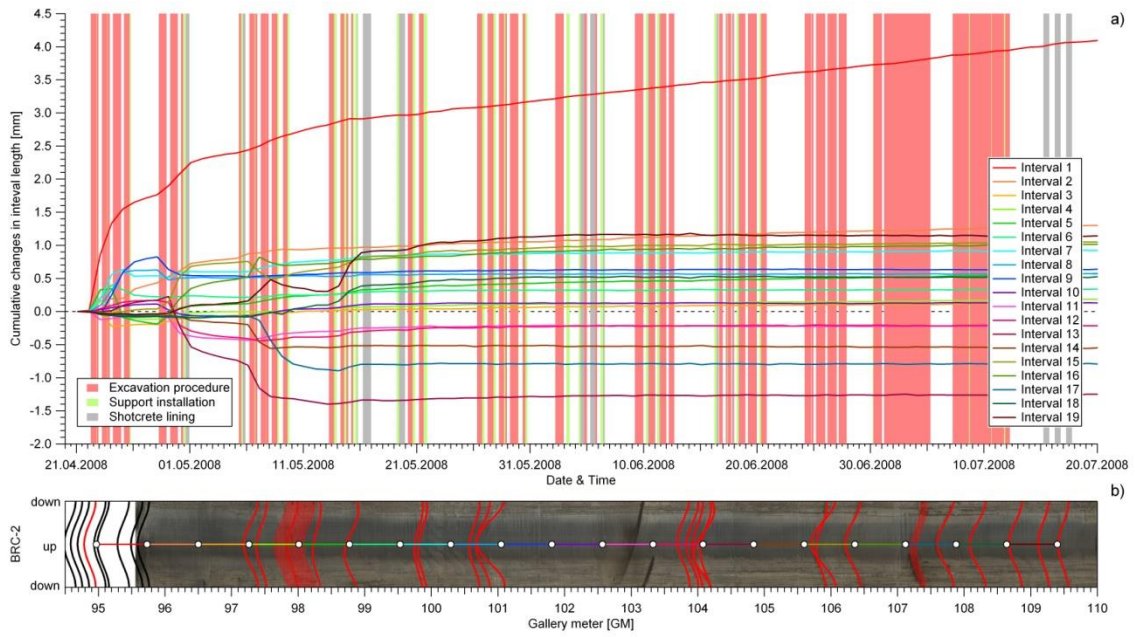


Figure 2-18: Time series of the measuring intervals of the Magnet-Extensometer (Mag-X 1) throughout the excavation of the mine-by section presented as cumulative changes in interval length. Negative values denote a shortening of the interval length, while positive values denote an elongation of the initial interval length. b) Optical televiewer image of the borehole BRC-2 with the identified geological structures and the positions of the measuring intervals. Faults and fault zones are shown in red and EDZ fractures in black.

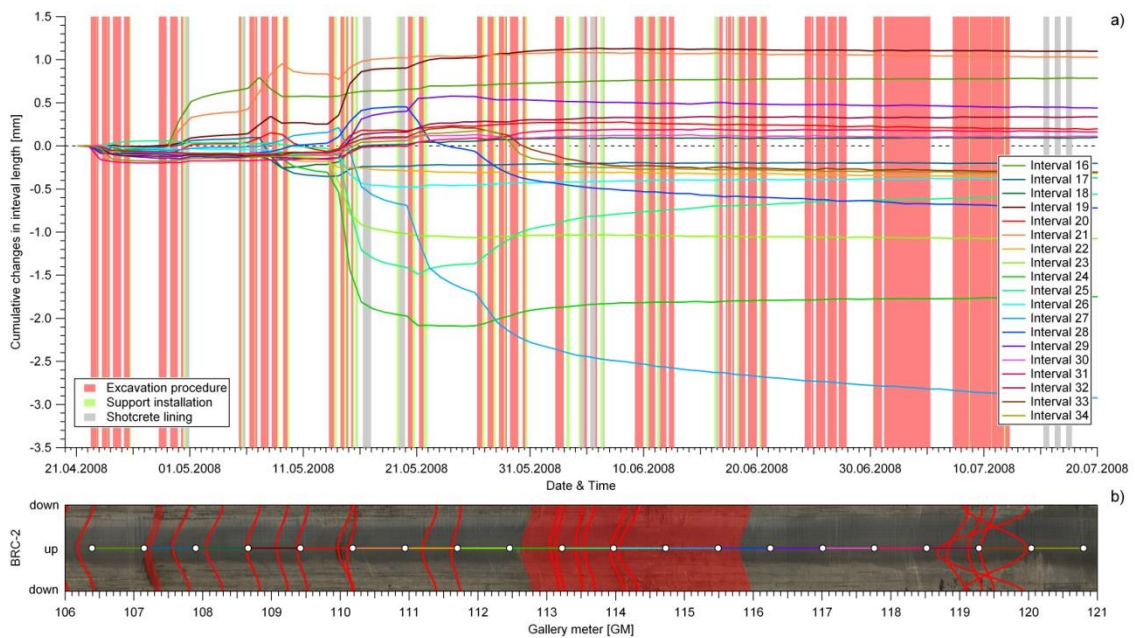


Figure 2-19: Time series of the measuring intervals of the Magnet-Extensometer (Mag-X 2) throughout the excavation of the mine-by section presented as cumulative changes in interval length. Negative values denote a shortening of the interval length, while positive values denote an elongation of the initial interval length. b) Optical televiewer image of the borehole BRC-2 with the identified tectonic structures and the positions of the measuring intervals.

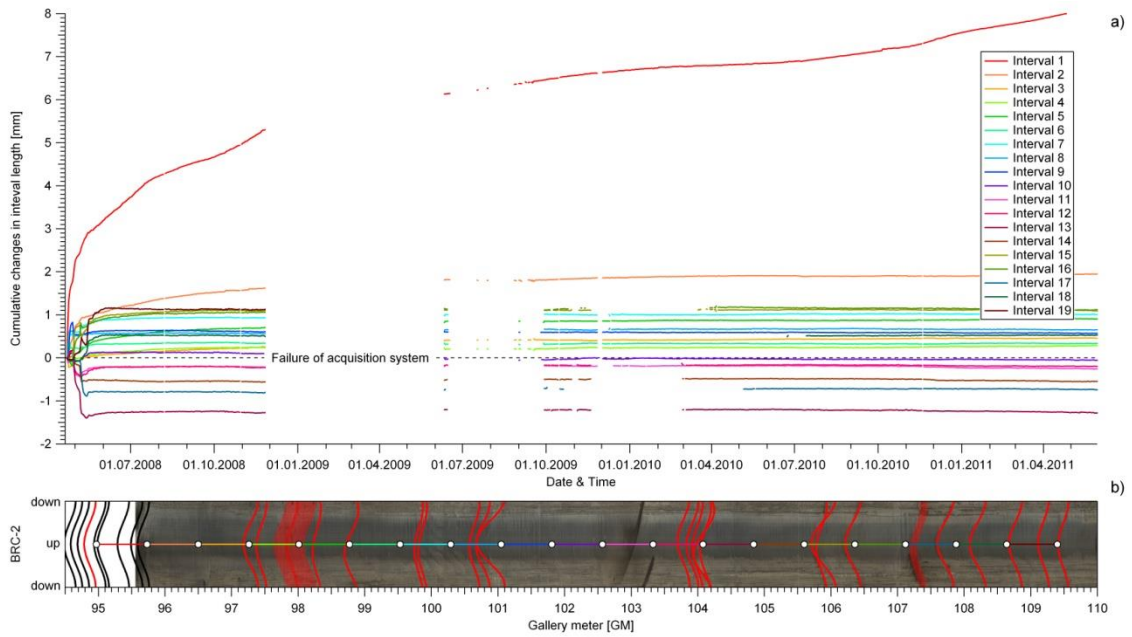


Figure 2-20: Time series of the measuring intervals of the Magnet-Extensometer (Mag-X 1) from April 2008 to June 2011 presented as cumulative changes in interval length. Negative values denote a shortening of the interval length, while positive values denote an elongation of the initial interval length. b) Optical televiewer image of the borehole BRC-2 with the identified geological structures and the positions of the measuring intervals. Faults and fault zones are shown in red and EDZ fractures in black.

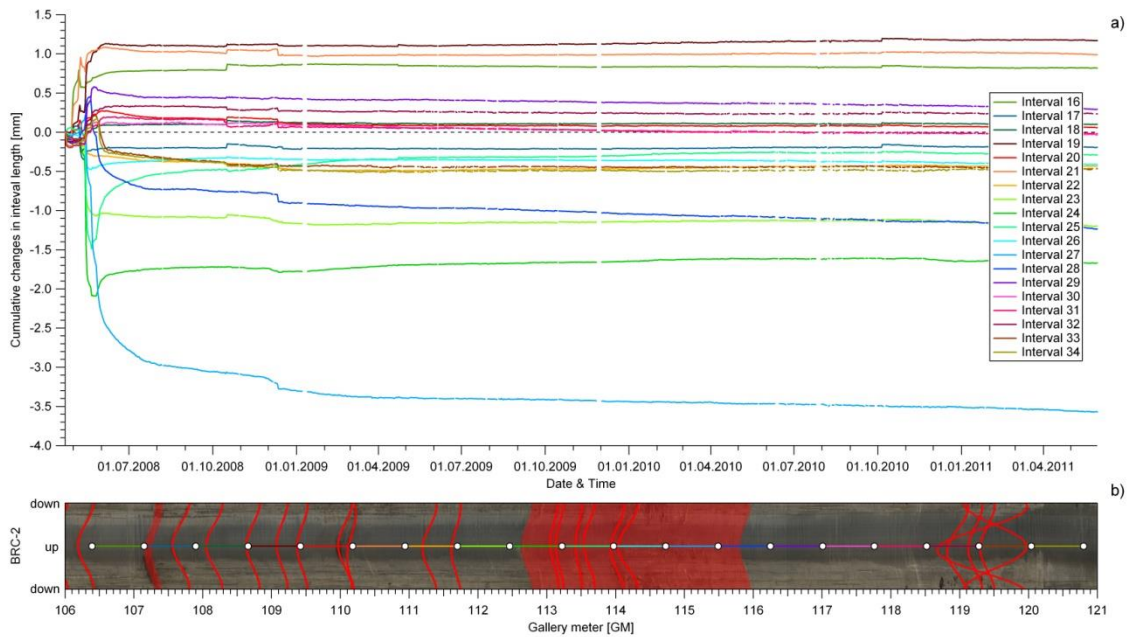


Figure 2-21: Time series of the measuring intervals of the Magnet-Extensometer (Mag-X 2) from April 2008 to June 2011 presented as cumulative changes in interval length. Negative values denote a shortening of the interval length, while positive values denote an elongation of the initial interval length. b) Optical televiewer image of the borehole BRC-2 with the identified tectonic structures and the positions of the measuring intervals.

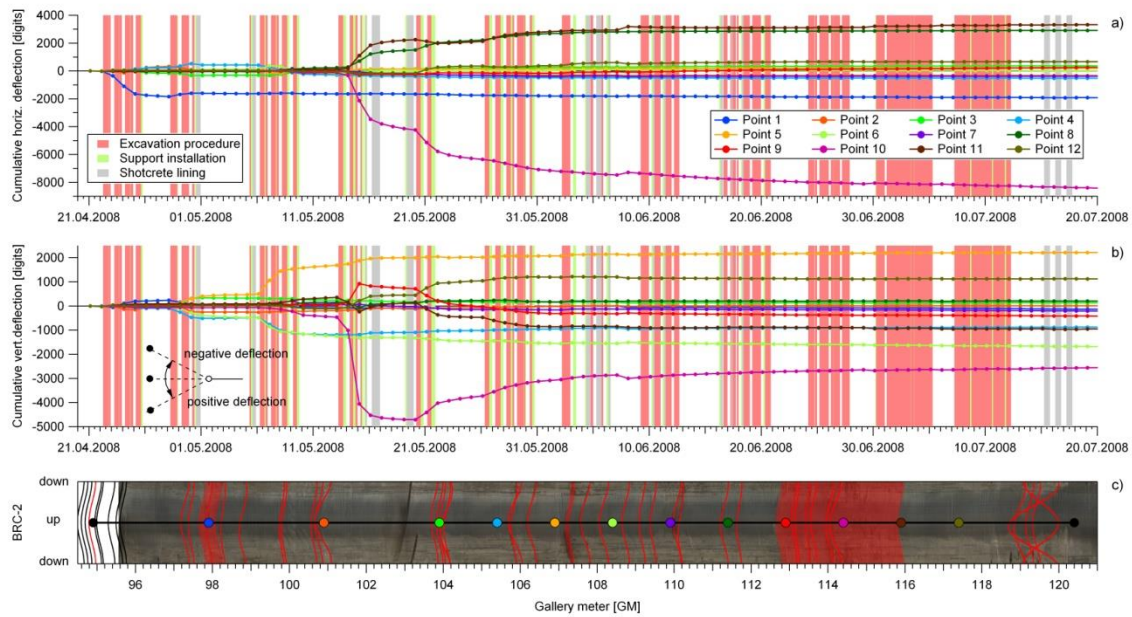


Figure 2-22: Time series for measuring points of the Chain-Deflectometer during the excavation phase presented as cumulative a) horizontal (i.e. radial) deflections and b) vertical deflections. Negative deflections denote bending of the deflectometer probe towards the tunnel in case of horizontal deflections and downward bending in case of vertical deflections. c) Optical televiwer image of the borehole wall of BRC-2 with identified geological structures and positions of the measuring points along the borehole. Faults and fault zones are shown in red and EDZ fractures in black.

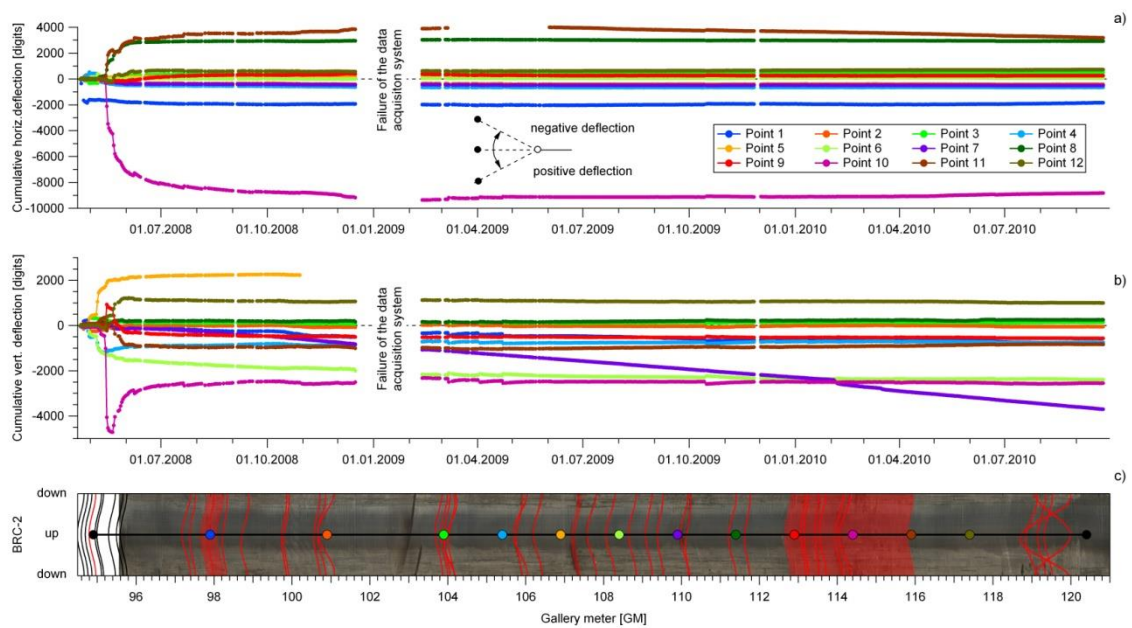


Figure 2-23: Time series for measuring points of the Chain-Deflectometer of the entire measuring period from June 2008 to December 2010 presented as cumulative a) horizontal (i.e. radial) deflections and b) vertical deflections. Negative deflections denote bending of the deflectometer probe towards the tunnel in case of horizontal deflections and downward bending in case of vertical deflections c) Optical televiwer image of the borehole wall of BRC-2 with identified geological structures and positions of the measuring points along the borehole. Faults and fault zones are shown in red and EDZ fractures in black.

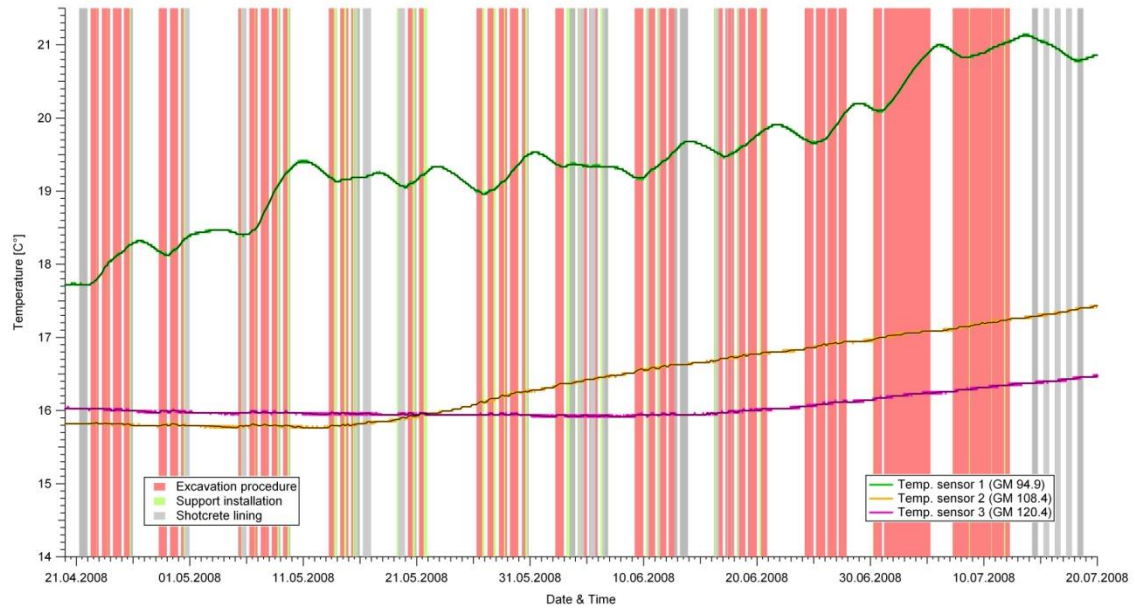


Figure 2-24: Evolution of the rock temperature in borehole BRC-2 during the excavation phase derived from three temperature sensors. The sensors are located in a radial distance to the final tunnel alignment of 1.3 m (Sensor 1), 3.0 m (Sensor 2) and 4.6 m (Sensor 3).

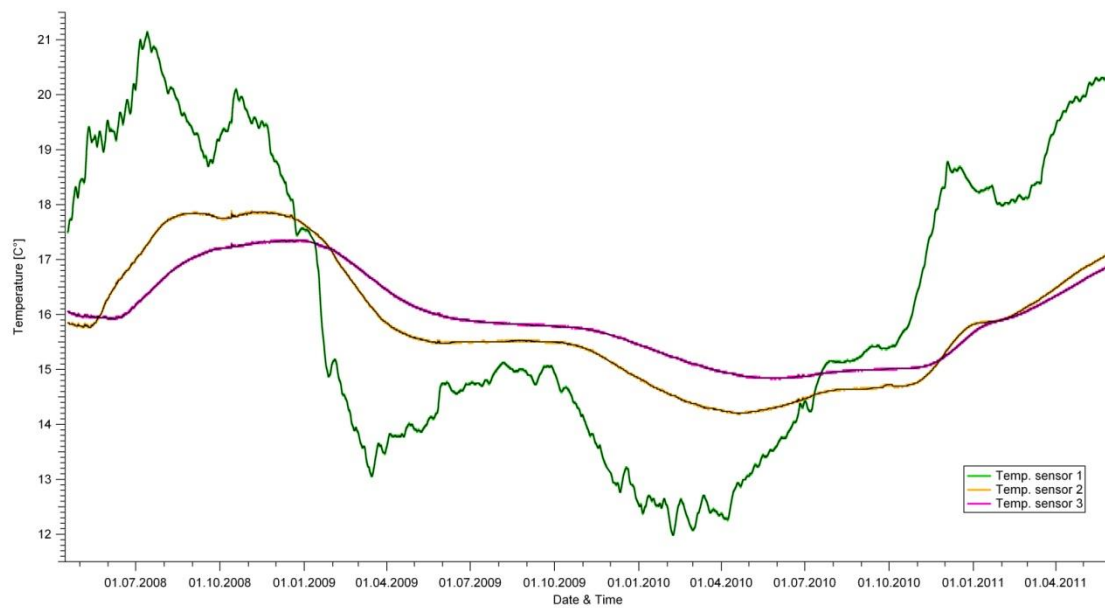


Figure 2-25: Annual variations of the rock temperature in borehole BRC-2 recorded between April 2008 and May 2011. The three temperature sensors are located in a radial distance to the final tunnel alignment of 1.3 m (Sensor 1), 3.0 m (Sensor 2) and 4.6 m (Sensor 3).

Table 2-1: Detailed list of excavation stops throughout the excavation of the mine-by experiment

Excavation activity	Date	Tunnel face	Duration
Excavation start	April 22 nd , 2008	GM 94.5	
Weekend stop	April 26 th , 2008	GM 100.7	2 days
Prolonged stop	May 1 st , 2008	GM 105.0	5 days
Prolonged stop	May 10 th , 2008	GM 111.0	3 days
Prolonged stop	May 15 th , 2008	GM 114.5	5 days
Prolonged stop	May 22 nd , 2008	GM 117.5	4 days
Weekend stop	May 31 st , 2008	GM 124.2	2 day
Excavation completed	June 6 th , 2008	GM 127.0	

Table 2-2: Detailed list of construction activities and excavation support measures applied throughout the construction of the mine-by experiment

Excavation stage	Date	Construction activity	Gallery meter
Pre-excavation	27.03. - 28.03. 08	Excavation and lining of start niche	GM 89.5 - GM 94.5
	15.04. - 18.04. 08	Concreting of tunnel invert	GM 37.0 - GM 88.0
Syn-excavation	22.04. - 30.04. 08	Excavation	GM 94.5 - GM 105.0
	30.04. / 05.05. 08	Shotcreting	GM 94.5 - GM 98.0
	06.05. - 14.05. 08	Excavation	GM 105.0 - GM 114.5
	13.05.2008	Installation of first steel arch	GM 110.5
	14.05.2008	Installation of second steel arch	GM 111.5
	15.05.2008	Installation of third steel arch	GM 112.5
	15.05. / 19.05. 08	Shotcreting	GM 98.0 - GM 113.5
	20.05. - 02.06. 08	Excavation	GM 114.5 - GM 126.5
	21.05.2008	Installation of fourth steel arch	GM 116.5
	26.05.2008	Installation of fifth steel arch	GM 117.5
Post-excavation	04.06. - 06.06. 08	Shotcreting	GM 113.5 - GM 127.0
	15.07. - 17.07. 08	Concreting of tunnel invert	GM 88.0 - GM 130.0

Table 2-3: Summary of rock mass characterization methods applied at different stages of the mine-by experiment

Characterization methods		Pre-excitation stage (27.03. - 21.04.08)	Syn-excitation stage (22.04. - 06.06.08)	Post-excitation stage (07.06.08 - 31.05.11)
excavation surface	Geological mapping	start niche / face	side walls / face (after each round)	floor / niches (before shotcrete)
	Seismic refraction tomography	-	side walls / floor (22.05. / 23.05.08)	floor (16.07.08)
borehole	Drill core logging	BRC-1 (03.04.08) BRC-2 (02.04.08)	-	BRC-3 (26.05.09) BRC-4 (09.02.10)
	OPTV logging	BRC-1 (03.04.08) BRC-2 (02.04.08)	-	BRC-3 (27.05.09) BRC-4 (14.06.10)
	USIV measurements	BRC-2 (04.04.08)	-	-

Table 2-4: Summary of monitoring methods applied at different stages of the mine-by experiment

Monitoring methods		Pre-excitation stage (27.03. - 21.04.08)	Syn-excitation stage (22.04. - 06.06.08)	Post-excitation stage (07.06.08 - 31.05.11)
excavation surface	Geodetic survey	-	hourly	-
	Laser scanning	-	after each round length	-
borehole	TRIVEC measurement (BRC-1)	Reference measurement	after each round length	irregularly
	Chain-Defelctometer (BRC-2)	Reference measurement	2 min measuring interval	10 min measuring interval
	Magnet-Extensometer (BRC-2)	Reference measurement	2 min measuring interval	10 min measuring interval
	Temp. monitoring (BRC-2)	Reference measurement	10 min measuring interval	10 min measuring interval

Table 2-5: Description of the borehole characteristics. The orientation of the boreholes was measured after drilling using both a borehole geometry probe (Flexit GyroSmart) and an optical televiewer

Borehole	Location	Orientation	Length	Diameter	Drilling	Investigations
BRC-1	GM 93.5	90/000	8.1 m	101 mm	03.04.08	DCL, OPTV
BRC-2	GM 94.5	02/144	29.2 m	131 mm	02.04.08	DCL, OPTV, USIVM
BRC-3	GM 110.0	60/335	24.5 m	116 mm	26.05.09	DCL, OPTV
BRC-4	GM 107.0	60/331	19.6 m	116 mm	09.02.10	DCL, OPTV

DCL = drillcore logging, OPTV = optical televiewer logging, USIVM = ultrasonic interval velocity measurements

3 STRUCTURAL AND KINEMATIC RELATIONSHIP BETWEEN NATURAL AND EXCAVATION-INDUCED FRACTURES AROUND A TUNNEL IN TECTONICALLY DISTURBED OPALINUS CLAY

Abstract

Excavation-induced fractures are inevitably created in the near-field of an underground opening during its construction when redistributed stresses exceed the strength of the rock mass. This fracture development results in the formation of an excavation disturbed zone (EdZ) and/or an excavation damaged zone (EDZ). Understanding the failure mechanisms and the contributing factors leading to the formation of such a damage zone around repository tunnels for nuclear waste in clay rocks is a major issue in the context of site selection, repository architecture and repository design. Recently the Opalinus Clay was chosen as the host rock for high-level nuclear waste in Switzerland. Due to its pronounced bedding the Opalinus Clay is characterized by an anisotropic rock strength and deformability. Additionally, tectonically disturbed Opalinus Clay may exhibit large-scale heterogeneities in both the rock mass strength and deformability as a consequence of frequently occurring natural faults and fault zones. The influence of the rock mass heterogeneity associated with such pre-existing tectonic faults on the rock mass behavior and their effects on induced fracturing associated with the excavation is not well understood.

A full-scale experiment conducted in the Gallery o8 at the Mont Terri Underground Rock Laboratory in Switzerland was used to investigate rock mechanical processes associated with spatial variations in fault frequency, and their effect on the formation of an excavation-induced fracture network. The fracture network prior to and after excavation was characterized by integrating structural data from geological mapping of excavation surfaces and from four pre- and post-excavation boreholes, comprising geological drillcore logging and optical televiewer imaging. Geophysical investigations including single-hole interval velocity measurements and seismic refraction tomography were used to quantify spatial variations in the seismic velocities and thus in rock mass properties and the extent of the excavation-induced damage zone. Analyses of the documentation obtained during and following the excavation of the mine-by experiment revealed a heterogeneous network of excavation-induced macroscopic fractures that can be associated with extensile brittle failure and shearing of tectonic fault and bedding planes. Observed failure mechanisms and associated changes in the radial EDZ extent are related to changes in the rock mass deformability due to spatial variations in fault frequency.

Key words: Opalinus Clay, fault characteristics, EDZ fracture types, failure mechanisms

3.1 Introduction

Due to their favorable isolation characteristics, clay rock formations are widely accepted as potential host rocks for deep geological disposal of nuclear waste. However, clay rocks often exhibit numerous unfavorable rock mechanical properties regarding their strength and deformation behavior in the near-field of an underground opening. At depth, their low strength and brittle failure behavior may lead to the formation of an excavation disturbed zone (EdZ) and/or an excavation damage zone (EDZ) around the tunnel, thereby affecting the isolation characteristics of the surrounding rock mass. Understanding the failure mechanisms and the contributing factors leading to the formation of a damage zone around a repository drift is a major issue in the context of site selection, design and architecture of deep geological disposal facilities for nuclear waste in clay rock formations.

At the Mont Terri Underground Rock Laboratory (URL) in Switzerland, several in-situ experiments were conducted or are currently underway to investigate the EDZ in the Opalinus Clay around galleries, niches and boreholes using various geological and geophysical investigation methods (Yong et al. 2004; Bossart & Thury 2008). Established conceptual models for the EDZ geometry (Schuster et al. 2001; Bossart et al. 2002, 2004; Martin et al. 2004; Yong 2008) significantly differ in their extent and geometry depending on the investigation method, the excavation diameter and technique, and especially the orientation of the excavation in respect to the bedding and the in-situ stress tensor. Bossart et al. (2004) proposed a conceptual EDZ model valid for a tunnel excavated in slightly faulted Opalinus Clay with a diameter of 4 m and an excavation axis oriented perpendicular to bedding strike (i.e. in case of the Mont Terri URL towards NNE-SSW). Based on structural and hydrogeological investigations, Bossart et al. (2004) divided the EDZ around the tunnel into an inner and an outer shell. In the inner shell, with a maximum radial extent of 1 m, the fractures are interconnected and consist of sub-vertical extensional fractures linked by small-scale shear fractures. In the outer shell, with a maximum radial extent of 2 m, the induced fractures are only partly interconnected and wider spaced. Additional results from ultrasonic velocity measurements (Schuster et al. 2001), electric resistivity tomography (Yaramanci et al. 2002) and hydraulic testing are in general agreement with the model proposed by Bossart et al. (2004), but suggest an asymmetric geometry of the EDZ with a larger extent at the tunnel roof and tunnel invert, and a smaller extent at the sidewalls. Martin et al. (2004) suggest a maximum EDZ depth of one tunnel diameter in the direction of the maximum principle stress orientation and half a tunnel diameter in the direction of the minor principal stress. Previous studies, however, mainly focused on the characterization of the EDZ around individual tunnel cross-sections. Relationships between spatial variations in induced fracturing in terms of intensity (i.e. EDZ fracture density), and changes in failure mechanisms and EDZ extent as consequence of rock mass heterogeneities along the tunnel axis have not been investigated yet.

Based on local observations of the fracture network around tunnels and boreholes, several processes were proposed by Martin et al. (2004) for the formation of the EDZ at the Mont Terri URL. They suggested that extensional fracturing at the sidewalls and bedding-parallel slip in the tunnel roof and below the tunnel invert are the main processes promoting the formation of the EDZ for a tunnel and borehole orientation perpendicular to bedding strike. Latest findings on induced macroscopic fracturing

around tunnels in slightly faulted Opalinus Clay provide evidence that reactivation of tectonic faults as consequence of excavation-induced stress redistributions play an essential role in the development of the EDZ fracture network (Marshall et al. 2006; Bluemling et al. 2007; Yong 2008; Yong et al. 2010, 2013; Nussbaum et al. 2011). This is particularly relevant in situations where tectonic fractures parallel to bedding exist and the rock anisotropy is superimposed by a rock mass heterogeneity and anisotropy due to spatial variations in fault plane density. However, little is known about the rock mechanical characteristics of such pre-existing tectonic faults and their influence on rock mass properties and behavior in clay rocks. Spatial variations in fault characteristics may significantly alter the homogeneity of the rock mass in strength, stress and deformability, and thus may have a significant effect on induced fracturing. Understanding the relationship between induced fracturing and pre-existing tectonic structures requires a qualitative and quantitative description of both, tectonic and induced fracture characteristics such as surface conditions, geometry, frequency and mechanical properties.

In this study, the natural and induced fracture network around a 30 m long gallery section excavated in faulted Opalinus Clay was investigated. Characterization of the in-situ rock mass structure was based on geological and geophysical methods at the borehole and the tunnel-scale. On the borehole-scale, data were obtained from geological drillcore logging, single-hole seismic interval velocity measurements, and digital imaging of borehole walls with an optical televiewer. On the tunnel-scale, geological mapping of excavation surfaces and seismic refraction tomography along the tunnel sidewalls was utilized. Both the field data and observations were integrated to identify the rock mechanical processes associated with spatial variations in fault characteristics and their effect on excavation-induced fracturing.

3.2 Background

Field data analyzed in this study were obtained from a 32.5 m long tunnel section between GM 94.5 and GM 127 in the recently excavated Gallery 08 of the Mont Terri URL in northwestern Switzerland (Figure 3-1). The underground laboratory is located in the southeastern limb of the Mont Terri anticline in the Opalinus Clay formation at a depth between 250 to 320 m. Environmental changes during sedimentation of the clay rock lead to three different facies at the Mont Terri URL: 1) the shaley facies, 2) the sandy facies, and 3) the carbonate-rich facies (Thury & Bossart 1999). The mine-by experiment conducted in this study is located entirely in the shaley facies, consisting of argillaceous and marly shales with intercalated cm-thick sandy layers and lenses (Nussbaum et al. 2011). The shaley facies is characterized by a porosity ranging between 12 to 18% and a natural water content between 7 and 8% (Amann et al. 2011a,b; Zimmer 2012; Wymann 2013). Sedimentation and physical compaction during the burial history resulted in a pronounced bedding which dips moderately towards SSE due to the regional folding. The axis of Gallery 08 is sub-perpendicular to bedding strike and was excavated from NW to SE with an azimuth of 152 degrees (Figure 3-1). Beside the pervasive bedding planes, the URL is intersected by various tectonic faults and fault zones at different scales and orientations (Nussbaum & Bossart 2008).

Stress measurements performed by Martin and Lanyon (2003) at the Mont Terri URL suggest that the maximum principle stress orientation is sub-vertical, dipping towards

SSW. Both, the intermediate and minimum principal stress axes are sub-horizontal. The minimum principal stress is slightly inclined towards NE, while the intermediate principle stress axis dips slightly towards NW, thus running sub-parallel to the gallery axis (inset in Figure 3-1).

Excavation of the mine-by section was carried out concurrently with the construction of the Gallery o8, and lasted from April 22nd to June 6th 2008. The mine-by experiment is located in the straight tunnel section of Gallery o8 between GM 94.5 and GM 127 where the gallery is intersected by a major fault zone (Figure 3-1). The mine-by section has a 5 m high horseshoe-shaped profile with a length of 32.5 m and was excavated full-face in 23 steps using a roadheader. The round length was 1.5 m on average and was carried out in a repetitive spatial and temporal sequence to ensure a consistent stress redistribution around the tunnel face. The tunnel advanced towards azimuth 152° at a down grade of approximately 2.14%, which is approximately perpendicular to the bedding strike and in the direction of bedding dip. Support measures throughout the experiment were installed immediately after each excavation round and consisted of wire mesh reinforcement (K 196) affixed on the tunnel ceiling and eight rock bolts installed approximately 0.7 m behind the advancing tunnel face. Shotcrete was not applied continuously to allow for direct observations on the formation of EDZ fractures as a function of distance to the advancing tunnel face.

3.3 Field investigation methods

3.3.1 Drillcore logging

Drillcores from four boreholes with different orientations (Figure 3-2) were obtained either before (BRC-1 and 2) or after (BRC-3 and 4) the tunnel excavation. All boreholes were drilled with double (BRC-1 and 2) or triple (BRC-3 and 4) tube core barrels to minimize drilling-induced fracturing and to provide optimal core recovery and quality. Drillcores were logged immediately after drilling focusing on the identification of natural and excavation-induced discontinuities. Discontinuities with a tectonic origin are consistently characterized by multiple striated surfaces forming discrete mm-thin shear bands which allow tectonic and excavation or drilling-induced fractures to be distinguished. Excavation and drilling-induced fractures were distinguished based on their surface characteristics. In contrast to excavation-induced fractures, drilling-induced fractures have stepped core edges or show signs of drill scoring that can be attributed to core handling or to the drilling process. Discontinuities healed with a mm-thick calcite infilling were termed veins. Based on detailed core analyses and the above mentioned surface characteristics, identified discontinuities were classified as: (1) bedding planes, (2) tectonic fractures, (3) excavation-induced fractures, (4) veins, and (5) drilling-induced fractures (i.e. artificial fractures).

3.3.2 Optical televiewer logging

Optical borehole inspections of all four boreholes were performed with a Slimhole Optical Televiewer OPTV52 immediately after drilling and cleaning of the borehole walls with compressed air. OPTV images of the borehole walls were used to identify and characterize geological structures in terms of their location (i.e. depth along borehole),

their geometry (i.e. dip and dip direction) and their thickness (shear zones and sandy layers) using the Software WellCAD 4.3 (Advanced Logic Technology ALT). Based on the optical characterization identified geological structures were classified as described previously. Since tectonic fractures are closed and often sealed with clay minerals, their identification as well as their differentiation from well developed bedding planes is challenging. Identified geological structures were therefore cross-checked with drillcore logging data to increase the reliability of the data set.

3.3.3 Ultrasonic interval velocity measurements

Complementary to OPTV logging and geological drillcore mapping, continuous single-hole ultrasonic interval velocity measurements (USIVM) were performed in borehole BRC-2 (Figure 3-2). A BGR mini-sonic probe with a maximum sampling frequency of 10 MHz was utilized. The probe consists of four linearly distributed piezo-electric transducers. One transducer is used as seismic source and the remaining three receivers are located at a distance of 10, 20 and 30 cm from the source. Coupling of the transducers with the borehole wall was done with pneumatic cylinders. For the measurements the mini-sonic probe was progressively moved into the borehole at predefined steps. Within the first 6.5 m measurements were carried in 5 cm steps and for the remaining part of the borehole 10 cm steps were used. The first 6.5 m of the borehole were measured two hours after drilling to a depth of 7.3 m. The remaining part of the 29.2 m long borehole was measured eight hours after drilling.

Seismic velocities and amplitudes derived from first p- and s-wave arrivals were calculated according to travel time and distance, assuming straight ray propagation. However, seismic penetration depth will be different for each of the three measuring interval (10, 20 and 30 cm), whereby the largest interval length results in the deepest seismic penetration of approximately 1 to 2 cm (K. Schuster, pers. comm.). Deviations from a seismic velocity of 2700 m/s, which can be regarded as an average velocity for intact Opalinus Clay for the given borehole orientation, reflect variations in elastic rock properties and hence provide indications of micro- and macroscopic damage near the borehole wall (Schuster et al. 2001). Distinct lateral variations of elastic rock mass properties are reflected in a similar increase or decrease of all three velocities (i.e. v_{p1} , v_{p2} and v_{p3}). However, a normal velocity gradient ($v_{p1} < v_{p2} < v_{p3}$) indicates intensified damage towards the borehole and thus allow for the identification of induced micro-damage around the borehole. Based on derived p- and s-wave velocities, elastic parameters such as dynamic Young's and shear modulus, and the dynamic Poisson's ratio were determined.

3.3.4 Tunnel mapping

Systematic geological tunnel face and sidewall mapping took place immediately after each excavation round between GM 94.5 and GM 127. Sidewalls were mapped repeatedly to characterize the progressive development of macroscopic EDZ fractures as a function of distance to the advancing tunnel face. Since the tunnel invert cannot be mapped during excavation (i.e. covered by muck), systematic mapping was performed after careful cleaning of the floor when the tunnel face reached GM 94.5 and GM 159, respectively. Geological maps from GM 40 to GM 127 were used to determine fault frequency and spacing along three scanlines at both sidewalls and the tunnel invert. To

analyze potential correlations between the frequency of excavation-induced and tectonic fractures, window-mapping with a window size of 1 x 1 m was performed for the tunnel invert between GM 40 and GM 127. Sidewall mapping of subsequently excavated side niches normal to the direction of Gallery 08 was used to characterize induced fracturing parallel to the sidewalls of Gallery 08, and to obtain estimates for their radial extent into the rock mass (i.e. EDZ depth). The geological map of the mine-by section between GM 94 and GM 127 is presented in Figure B 4. The geological maps of the Gallery 08 (i.e. GM 40 - 94) and of the adjacent side niches are presented in Appendix B.

3.3.5 Seismic refraction tomography

Seismic refraction tomography was used to characterize and quantify the radial extent of the initial EDZ between GM 94 and GM 116. Four horizontal receiver lines consisting of 48 single-component geophones with a spacing of approximately 0.5 m were tightly mounted on both sidewalls using gypsum plaster. A demolition hammer was used as seismic source. Source locations were defined by the separation of geophones. Travel time inversion of the seismic data was performed with the tomography code from Zhou and Greenhalgh (2008) which is valid for tilted transversely isotropic media like the Opalinus Clay. For the initial velocity model, a surface velocity of 600 m/s with a depth gradient of 550 m/s per meter has been chosen for the velocity component perpendicular to the anisotropy axis (i.e. parallel to bedding). For the velocity component parallel to the anisotropy axis (i.e. perpendicular to bedding) a surface velocity of 400 m/s with a depth gradient of 370 m/s per meter was assumed. Note, that for each receiver line only the velocity component parallel and perpendicular to the anisotropy axis was inverted. After inversion a Kernel smoothing was applied to the original data to allow for a better interpretation of the overall velocity patterns.

3.4 Structural analysis of the natural fracture network

Characterization of the natural discontinuities around Gallery 08, and particularly around the mine-by section, was done by integrating structural data from geological mapping of excavation surfaces between GM 40 and GM 127 with structural data obtained from four pre- and post-excavation boreholes located between GM 94 and GM 125 (Figure 3-2). Stereographic projections of both data sets are presented in Figure 3-3. Orientation clustering revealed four different discontinuity sets, which are consistent in both data sets. Mean orientations derived from surface mapping are presented in Table 3-1, and in Table 3-2 for the borehole-based data. The derived discontinuity set orientations are in general agreement with the previously identified discontinuity sets in the Mont Terri URL by Nussbaum and Bossart (2008), although some slight differences in orientation are evident. For the present study, the three fault sets that intersect the mine-by experiment were labeled F₁ - 3 according to their frequency. The mapped discontinuity sets within the mine-by section can be summarized as follows:

- Bedding consists of thinly spaced, well-developed bedding planes with a mean orientation of 44°/146° (mean dip / dip direction), thus moderately dipping towards SSE. Bedding orientation within the mine-by section is approximately 10° steeper than between GM 40 and GM 94 where the bedding orientation was on average 35°/150° (see Table 3-1).

- Fault set F1 consists of gently to moderately SSE-dipping reverse faults with a mean orientation of 50°/148°. Dip angles range between 25° and 80° with most measurements between 40° and 50°. Thus, the majority of the fault planes are bedding-parallel. Both, geological mapping and borehole data revealed that 70 - 80% of the identified faults belong to this frequently occurring fault set. F1 fault planes are typically characterized by dark polished surfaces with slickensides indicating a NW thrusting direction. Most of these faults can be traced over the entire tunnel circumference indicating a high persistence (Figure B 4). Fault zones with thicknesses ranging from the decimeter to meter-scale (i.e. 0.1 - 2.5 m) are consistently associated with this fault set. The most pronounced fault zone with a thickness of 2.5 - 3 m intersects the mine-by section between GM 109 and GM 118. As shown in Figure B 4 this major fault zone is composed of a strongly deformed and folded upper part (i.e. hanging wall), and less disturbed lower part (i.e. foot wall).
- Fault set F2 is composed of sub-horizontal fault planes which branch from the SSE-dipping faults (Figure B 4). They have a mean orientation of 12°/134° with dip angles ranging from 0° to 25°. In the borehole data, dip directions revealed a large scatter. Approximately 10 - 20% of the mapped faults belong to this fault set. In the mine-by section, sub-horizontal faults were only found in isolated regions, in particular at the lower sidewalls between GM 94 - 99 and between GM 116 - 123 on the NE-sidewall (Figure B 4). At these locations the fault traces often show a slight curvature and the trace lengths typically range from 2 to 5 meters. Sub-horizontal fault planes were also observed in the lower footwall of the major fault zone, but with significantly shorter trace lengths (i.e. 0.5 - 1 m).
- Fault set F3 is composed of gently SW-dipping fault planes with dip angles ranging from 10° to 35°. The fault set has a mean orientation of 19°/214° and was only encountered locally within the mine-by section, in particular between GM 98 and GM 105. This is consistent with the borehole data which suggests that only 5% of the identified faults belong to this fault set. Measured trace lengths range from 3 to 6 m and are consistently limited by SSE-dipping fault planes as indicated in the geological map (Figure B 4).

Although fault plane orientations derived from geological mapping of excavation surfaces and from borehole logging are consistent, correlating individual tectonic fault planes is challenging. Even for borehole BRC-3 and BRC-4, which are separated by only 2 meters, a consistent correlation between individual geological features could not be established. This finding suggests considerable lateral variations in fault plane orientations and/or persistence. This is in contrast to minor (fault zone thickness < 1 m) and major (fault zone thickness > 1 m) fault zones which revealed a much larger persistence. The two minor fault zones encountered in the foot wall of the major fault zone could be identified in three boreholes suggesting a persistence > 10 m. The major fault zone was mapped in several galleries of the Mont Terri URL (Figure 3-1) thus indicating a persistence of > 100 m. The thickness and internal architecture of this major fault zone, however, varies laterally over relatively short distances (i.e. 20 - 30 m) as documented by Nussbaum et al. (2011).

Fault spacing and frequency derived from scanline mapping and borehole logging is presented in Figure 3-4. Figure 3-4a shows the fault frequency distribution along Gallery 08 between GM 40 and GM 127. Within strongly tectonized zones (i.e. fault zones) fault

planes are densely spaced and cannot be distinguished individually. For these zones a frequency of > 20 faults per meter (f/m) was utilized for the analysis. Fault frequencies vary considerably along the gallery, in particular within the mine-by section between GM 94 - 127. Two distinct zones with different fault frequency patterns were distinguished: (A) in the tunnel section between GM 40 - 94 fault frequencies vary between 0 - 2 f/m, and (B) in the tunnel section between GM 94 - 127 with fault frequencies up to 20 f/m. Spacing distributions were determined for each tunnel section individually. Resulting spacing distributions were normalized according to the corresponding borehole or tunnel length and are presented in Figure 3-4b and c. The natural fracture spacing around both tunnel sections can be characterized by a log-normal distribution. However, between GM 40 - 94 the data show a strong bias towards spacing > 2 m, while within the mine-by section a bias towards 0.6 - 2.0 m spacing was observed. Small spacing originating from minor and major fault zones are significantly more pronounced in the mine-by section which can be attributed to the complexity of the natural fracture network in the vicinity of the major fault zone.

3.5 Geophysical characterization of rock mass heterogeneities

Single-hole seismic interval velocity measurements were performed in borehole BRC-2 to characterize the influence of spatial variations in fault frequency on the elastic properties of the rock mass prior to excavation. Derived seismic parameters are compiled in Figure 3-5 and are presented together with the fault frequency distribution along the borehole BRC-2. The fault frequency shown in Figure 3-5 was established by interval logging with an interval length of 0.5 m. Note that the orientation was not considered. The horizontal line in Figure 3-5a reflects the average seismic p-wave velocity (i.e. 2700 m/s) for undisturbed Opalinus Clay (K. Schuster, pers. comm.). Further, the black line in the velocity profiles represents a corrected p-wave velocity which accounts for the borehole disturbed zone (BdZ). The corrected p-wave velocity was determined from differences in travel time of three different channel configurations (K. Schuster, pers. comm.). Normalization of the seismic wave amplitudes was necessary to enable comparison between the channels as attenuation increased rapidly with increasing distance between the source and the receiver.

3.5.1 Spatial variations in rock mass deformability

Strong variations in the seismic parameters indicate significant changes in the elastic rock mass properties along the borehole axis (Figure 3-5). Closer examination of the seismic wave data shows that these variations are associated with discrete geological features such as sandy layers, calcite veins, single fault planes or minor and major fault zones. Low velocities and amplitudes are associated with damaged and faulted rock, high velocities and amplitudes are associated with sandy layers or calcite veins (Figure 3-5a and b). A similar behavior is reflected in the dynamic Young's modulus with values varying between 5 and 12 GPa (Figure 3-5c). Some borehole sections, in particular between 0 - 1.5 m, 12.7 - 13.0 m, 18.2 - 18.3 m, 19.8 - 21.4 m) are not covered due to difficulties in the recognition of the first arrival of the shear waves (i.e. s-waves). It is assumed that the dynamic Young's modulus at these locations might be < 5 GPa. Based on the dynamic Young's moduli, the rock mass along the borehole BRC-2 (and thus along the mine-by section) can be divided into three domains (Figure 3-5c): Domain I between 0

- 12 m and 21.5 - 24.5 m with an average Young's modulus of 10 GPa and an average fault frequency smaller than 1 fault per meter (f/m), Domain II between 12 - 17.5 m and 24.5 - 29 m with an average Young's modulus of 8 GPa and an average fault frequency of 2 f/m, and Domain III with a Young's modulus < 5 GPa and a fault frequency of up to 20 f/m across the major fault zone. Local variations in the dynamic Young's modulus superimpose this large-scale heterogeneity in rock mass deformability. These local variations can be related to lithological (i.e. sandy layers or calcite filled veins) and material changes (i.e. fault gouge). As shown in Figure 3-5c, pronounced stiffness drops consistently coincide with strongly tectonized borehole sections. Depending on the thicknesses of these tectonized zones, resulting dynamic Young's moduli vary between 6 GPa for minor fault zones (e.g. at 3.5 m) and smaller than 5 GPa for the major fault zone between 18.3 and 21.5 m. For a dynamic Young's modulus of 10 GPa for intact rock, the corresponding stiffness ratios of 3/5 and 2/5 for minor and major fault zones are consistent with static stiffness ratios derived from laboratory testing on tectonically disturbed Opalinus Clay specimens (Amann et al. 2011a).

3.5.2 Spatial variations in borehole damage

OPTV and borehole camera inspection prior to and immediately after USIV measurements revealed no indications of borehole instabilities. However, perturbations along the borehole are evident in the USIVM data. Significant differences in seismic velocities of the three channels (i.e. $v_{p1} < v_{p2} < v_{p3}$), as observed between 0.0 - 3.0 m, 6.5 - 8.5 m, 13.5 - 15.5 m, 16.5 - 18.5 m and 21.5 - 24.0 m, are interpreted to be indicative for induced damage around the borehole, further referred to as borehole disturbed zone (BdZ). As shown in Figure 3-5 these intervals consistently coincide with Domain I and II, but not with Domain III. However, they appear to be closely related to Domain III, since they are well pronounced adjacent to the major fault zone (i.e. Domain III). Closer examination of seismic velocity variations indicate that velocity gradients are highest in borehole intervals that were not intersected by any tectonic faults (i.e. 1.5 - 3.0 m, 6.5 - 8.5 m, 16 - 17 m, 17.5 - 18.5 m and 21.5 - 24.0 m) and vanish at locations with sandy layers (i.e. 6.5 m, 8.5 m, 16 m and 24 m). This observations suggest that stresses around the borehole cause damage in the clayey Opalinus Clay, but not in sandy layers. However, spatial analysis of the BdZ reveals that both, small- and large-scale variations in rock mass deformability have a significant influence on induced damage along the borehole. While the spatial distribution of induced borehole damage along the borehole is primarily associated with large-scale variations in rock mass deformability, small-scale stiffness and strength contrasts (i.e. sandy layers) cause local variations in the BdZ extent.

3.6 Induced fracturing and associated failure mechanisms

The EDZ is typically defined as a zone around an underground excavation characterized by inelastic deformations (i.e. extensional failure, shear failure, or tensile failure) as a consequence of excavation-induced stress redistributions. However, in this study it is distinguished between fractures which form as a consequence of intact rock failure, and excavation-induced shearing along pre-existing faults, further referred to as fault plane reactivation.

3.6.1 EDZ fracture types and their spatial distribution

Systematic geological mapping of excavation surfaces between GM 40 and GM 127 revealed a large number of EDZ fractures, in particular at the tunnel faces and along the tunnel invert where shotcrete was not applied continuously throughout the excavation. Detailed geometrical and fractographic analyses of fractures surfaces revealed that EDZ fractures often form within sets which occur at specific locations around the tunnel circumference (Table 3-3). Figure 3-6 presents a conceptual model showing the spatial distribution and geometrical relationship of the different EDZ fracture types along the mine-by section.

3.6.1.1 *Induced fracturing at the sidewalls*

Sidewall mapping of Gallery 08 and three adjacent niches located in the SW-sidewall revealed an EDZ fracture network that formed at the sidewalls of Gallery 08 (Figure 3-7). Two different types of steeply inclined induced fractures (IF) were identified. They are oriented parallel (IF1) and oblique (IF2) to the tunnel axis and are locally associated with reactivated sub-horizontal and moderately dipping fault planes (RF). Fracture surfaces of both fracture types are typically characterized by plumose structures, indicating extensional fracturing. Tunnel-parallel fractures (IF1) do not intersect with the Gallery 08 and were therefore only mapped in niches normal to Gallery 08. In the three investigated niches the zones containing IF1 fractures have a maximum radial extent between 2 and 2.5 m. In the first 0.4 - 0.6 m induced fractures are densely spaced (i.e. 5 - 10 cm) with a trace lengths up to 2 m (Figure 3-7). With increasing distance both, fracture frequency and trace lengths decrease. The fracture type IF2 was only mapped in the footwall of the major fault zone (Figure 3-6). These often closely spaced extensional fractures do not penetrate reactivated faults and their orientation is sub-perpendicular to the reactivated fault planes.

3.6.1.2 *Induced fracturing at the tunnel invert*

Invert mapping of the Gallery 08 between GM 40 and GM 127 revealed a heterogeneous EDZ fracture network that is composed of macroscopic extensional fractures that are partly associated with sheared bedding and reactivated fault planes (Figure 3-6). In the absence of tectonic faults or in sparsely faulted tunnel sections, two different types of EDZ fractures were pre-dominantly observed at the tunnel invert: sub-horizontal (IF3) and bedding parallel (IF4) EDZ fractures. Sub-horizontal IF3 fractures surfaces are limited to the metric-scale and can be characterized by well developed plumose structures indicating the fracture origin (i.e. nucleation point) and propagation direction. Their lateral extent is limited by tectonic or bedding-parallel EDZ fractures and the tunnel surface. This fracture type is best documented between GM 65 and GM 70 of Gallery 08 (Appendix B). Bedding-parallel IF4 fractures have a mean orientation of $42^{\circ}/151^{\circ}$ (dip / dip direction) and mapped trace lengths ranges from 1 to 4 meters. Some of these fractures revealed poorly developed down-dip shear fibers on their surfaces, but the majority of them show no fractographic markings. The occurrence of IF3 and IF4 fractures is generally expressed in morphological ridges along the tunnel invert, indicating reduced disintegration of the rock mass (see Figure 3-6 between GM 103 and GM 107). In contrast, morphological depressions in the tunnel invert can be related to a different EDZ fracture pattern that is associated with the occurrence of reactivated fault planes (see Figure 3-6

between GM 107 and GM 113). At these locations, macroscopic EDZ fractures (IF5) have a mean orientation of $43^{\circ}/332^{\circ}$ and thus are pre-dominantly oriented perpendicular to the pre-existing fault planes. The extent of IF5 fractures is consistently limited by reactivated bedding or fault planes. The fracture surfaces are characterized by plumose structures, indicating an extensional failure mode. Fault planes at the tunnel invert are consistently reactivated in reverse faulting mode.

Systematic window-mapping of the tunnel invert between GM 40 and GM 127 revealed a spatial correlation between fault plane and EDZ fracture densities (fracture/m²). For 171 of 1000 mapped EDZ fractures both the dip and dip direction could be determined accurately. Out of these, 90 EDZ fractures belong to the induced fracture type IF4 which is oriented parallel to the bedding and 81 of them belong to the induced fracture type IF5 which is oriented sub-perpendicular to the bedding planes. Figure 3-8 presents the distribution of the unclassified EDZ fractures as well as the distribution of the different EDZ types IF4 and IF5 in relation to the fault density (faults/m²). It is shown that independent of their orientation approximately 2/3 (62%) of the mapped EDZ fractures occur in tunnel sections that were not intersected by tectonic faults. With increasing fault plane density the EDZ fracture density is decreasing rapidly. Beyond a fault density of 4 faults per square meter, induced macroscopic EDZ fractures disappear. However, the distribution of IF4 and IF5 fractures does not show the same trend. For the bedding-parallel IF4 fractures, fracture density decreases with increasing fault plane density in a similar manner as for the unclassified EDZ fractures. This is in contrast to the IF5 fractures which show their highest density when the fault plane density ranging between 1 and 2 faults/m². Therefore, in tectonically undisturbed tunnel sections (0 faults/m²) the general EDZ fracture density is highest and predominantly consists of bedding-parallel IF4 fractures. In tunnel sections with a fault plane density ranging from 1 to 3 faults/m², the macroscopic EDZ fracture network is generally less pronounced and mainly composed of IF5 fractures and reactivated fault planes. In tectonically disturbed tunnel sections where the fault plane density exceeds 4 faults/m², macroscopic EDZ fractures are not visible. This observation suggests that fault plane reactivation may dominate in these tunnel sections.

3.6.1.3 *Induced fracturing at the tunnel face*

Geological mapping of 58 tunnel faces between GM 40 and GM 127 revealed a macroscopic EDZ fracture network composed of extensional fractures associated with either shear fractures through intact rock or reactivated fault planes. Shear dislocation of a few millimeters observed in the field suggests that the latter were reactivated as normal faults. On tunnel faces, where tectonic faults are rare or even absent, induced shear fractures (IF6) with trace lengths ranging from 0.5 to more than 5 m were observed. In contrast to tectonic faults which are typically characterized by dark polished surfaces with slicken-sides, shear fractures show poorly developed down-dip striations, indicating normal faulting along these fracture planes. They have a mean orientation of $49^{\circ}/149^{\circ}$, thus dipping in the same direction but slightly steeper than bedding planes (Table 3-3). In general, induced shear fractures with large trace lengths are preferentially found in the lower half of the tunnel face, while shorter traces were typically found in the upper right and the lower left corner. EDZ fractures (IF7) with a mean orientation of $68^{\circ}/318^{\circ}$ are always associated with either shear fractures (IF6) or reactivated fault planes. These fractures are sub-perpendicular to the shear fractures or reactivated fault planes which

consistently limit their extent (see tunnel face mapping at GM 109.7). IF7 fracture surfaces are typically characterized by plumose structures, indicating extensional failure.

3.6.2 EDZ failure mechanisms

As shown in the previous section, failure mechanisms, orientations and frequencies of induced fractures are significantly influenced by the pronounced bedding and the frequency of pre-existing faults. If kinematically free, shearing along both, bedding and fault planes may occur when the shear stress exceeds their shear strength. However, shearing of bedding planes was less dominant and restricted to tunnel sections with a fault plane spacing larger than 2 meters, or at locations where pre-existing faults have an unfavorable orientation in respect to the excavation (i.e. SW-dipping faults). This observation indicates a higher bedding plane shear strength compared to tectonic faults. Direct observations of dislocations along pre-existing faults suggest that reactivation at the tunnel face occurred in normal faulting mode and was initiated already ahead of the tunnel face. This is supported by the analysis of poorly developed down-dip striations on mobilized bedding planes at the tunnel face which indicate a discrete dislocation along their fracture surfaces eventually under high normal stresses. At the tunnel invert, however, reactivation of fault planes was consistently observed in reverse faulting mode. Newly formed fractures parallel to bedding typically showed rough and undulated surfaces. Striations along these fractures were rarely observed and were typically poorly developed. Undulated rough surfaces without any sign of shearing suggest tensile failure as a consequence of unloading of the tunnel invert. Poorly developed striations indicate reverse shearing and suggest that these striations developed eventually under low normal stresses and small shear displacements. Based on these observations it is assumed that at the invert newly formed fractures parallel to bedding are formed behind the advancing tunnel face.

Independent of their shear modes, reactivated faults or bedding planes are often associated with brittle extensional fractures oriented normal or sub-perpendicular to them. Their fracture surfaces are exposed at the tunnel invert (IF5 fractures), and at the tunnel face (IF7 fractures). Fracture origins and propagation directions derived from plumose structures indicate that these fractures emanated as mode I fractures (Kim et al. 2004) from mobilized bedding-parallel shear fractures or reactivated fault planes and thus can be attributed to secondary fracturing associated with the primary bedding or fault plane slip.

Extensional brittle failure sub-parallel to the tunnel circumference was observed to occur approximately one tunnel diameter behind the advancing tunnel face. No evidence could be found that the formation of these sidewall spalls is associated with the rock or rock mass anisotropy. This might be related to kinematic constraints associated with the orientation of fault and bedding planes in respect to the tunnel. As a consequence of these kinematic constraints failure through intact Opalinus Clay occurred parallel to the maximum tangential stress direction, and ultimately led to the formation of extensional fractures parallel to the tunnel circumference. In sparsely faulted tunnel sections, in particular adjacent to more compliant fault zones, such extensional fractures showed the potential to evolve into sidewall spalls at the meter-scale. Extensional brittle failure oblique to the tunnel axis was solely observed in the foot wall of the major fault zone,

and is most probably related to excavation-induced stress concentrations as a consequence of stiffness contrasts between the fault zone and the adjacent rock mass.

Sub-horizontal fractures at the tunnel invert were typically observed in sparsely faulted tunnel sections where induced stresses cannot be transferred into shear displacements due to reactivation of pre-existing faults. Fracture origins and propagation directions derived from plumose structures indicate that these fractures emanated as mode I fractures from bedding-parallel EDZ fractures or fault planes, and propagated normal to the tunnel axis towards the center of the tunnel invert.

In strongly faulted tunnel sections with a fault density higher than 5 faults/m² (i.e. minor and major shear zones) none of the above described macroscopic EDZ fractures were observed indicating a distinct change in failure mode from dominantly extensional (mode I) fracturing to shear dominated failure mode. The change in failure mode is also supported by the results of the seismic refraction tomography along the tunnel walls. Seismic p-wave velocities are consistently higher across strongly faulted regions (i.e. major fault zone) indicating no evidence of extensional failure processes.

3.6.3 Inferred induced stresses around the advancing tunnel

Reactivation in normal faulting mode ahead of the tunnel face suggests a sub-vertical oriented maximum induced stress component. Steeply inclined IF1 fractures that promote spalling at the tunnel sidewalls are typically associated with a sub-vertical orientated induced stress orientation. Since these spalls only occur at the sidewalls it is reasonable to assume that the maximum in-situ stress component is also sub-vertical. This is consistent with the analyses of various stress measurement data analyzed by Martin & Lanyon (2003).

At the tunnel invert, propagation directions derived from plumose structures suggest two different maximum induced stress components: 1) close to the sidewalls fractures tend to propagate perpendicular to the tunnel axis (i.e. maximum induced stress orientations perpendicular to tunnel axis), 2) at the center of the tunnel invert fractures propagate parallel to the tunnel axis (i.e. maximum induced stress orientations parallel to tunnel axis). The latter is consistent with observations on reactivated bedding and fault planes. These planes were reactivated in reverse faulting mode which supports a sub-horizontal oriented maximum induced stress orientation which is directed along the tunnel axis.

3.7 Geometrical aspects of EDZ extent

3.7.1 Spatial variations in EDZ depth

3.7.1.1 EDZ depth at the tunnel sidewalls

Seismic refraction tomography was used to quantify spatial variations in the seismic velocities and thus the elastic rock mass properties between GM 94 and GM 116. Figure 3-9a,b and c represent the final results of the anisotropic travel time inversions for the receiver Lines 1, 3 and 5 before and after applying Kernel filtering. For each inversion slice only the velocity component parallel to the bedding orientation is shown with p-wave velocities ranging between 0.5 and 3.5 km/s. In this study it is assumed that decreasing

seismic velocity are related to the intensity of damage as consequence of inelastic strain due to extensional or shear fracturing. The degree of p-wave velocity reduction is thereby more pronounced for extensional fracturing than for shear fracturing. Thus, lower seismic velocities are interpreted as a higher degree of extensional fracturing. Schuster (pers. comm.) found from in-situ seismic investigations that the p-wave velocity for intact Opalinus Clay parallel to bedding ranges between 3.0 and 3.5 km/s. Thus, it was assumed in this study that regions with p-wave velocities exceeding 3.0 km/s can be considered undisturbed, and hence were used to establish the maximum EDZ extent. Note that the outer part of the inversion slices (i.e. the deepest region, and the lateral regions) were not updated by the inversion itself, and therefore reflect the initial velocity of the inversion model. This is essentially due to the source-receiver positioning and the resulting ray path coverage.

Figure 3-9a and b represent receiver Lines 1 and 3, which were both located at the SW-sidewall approximately 2.8 and 1 m above the floor. At the tunnel surface, both inversion slices show a distinct 0.5 m thick low-velocity layer. Seismic velocities are in the order of 1.8 km/s and thus are on average 1.5 to 2 times lower than the velocities derived for the adjacent rock mass. Additionally, Line 1 shows an elongated low-velocity region (i.e. Region I) between GM 103 and GM 109 with the lowest velocities (2.3 km/s) at about 2 meters depth. A slightly shifted but more pronounced velocity anomaly (2.0 km/s) can be observed for Line 3 between GM 105 and GM 110, extending from the tunnel surface to a depth of 2.5 - 3 m. A second low-velocity region (i.e. Region II) can be detected in Line 1 between GM 94 and GM 97 at 2 meters depth and in Line 3 between GM 96 and GM 100. The low-velocity anomaly (i.e. Region II) in Line 3 is more pronounced with generally lower velocities (2.0 km/s) and extends from 2.5 m depth to the excavation surface. The similar shift of around 2 meters for the two anomalies identified in both lines can be explained by the general inclination of the geological structures by approximately 45 degrees into the direction of the tunnel advance. In between the identified low-velocity regions seismic data indicate velocities between 2.5 - 3.0 km/s. In Line 1 similar velocities appear as elongated features parallel to the tunnel surface at a depth of 0.5 to 1 m, while in Line 3 they show more individual branches bounded by the low-velocity regions.

Figure 3-9c represent the inversion results for Line 5 located approximately 1 m above the tunnel floor at the NE-sidewall. Overall, the velocity distribution on the NE-sidewall is less heterogeneous compared to SW-sidewall with average velocities of 2.3 km/s. The low-velocity layer within the first 0.5 m depth showed considerably lower seismic velocities. The average velocity was 1.2 km/s with decreasing velocities from 1.5 to 0.6 km/s in the direction of the advancing face and thus in the direction of the major fault zone. The two low-velocity regions previously discussed for the SW-sidewall can be observed also on Line 5, at locations similar to those of Line 3. However, the low velocity zone (i.e. Region I) located between GM 94 - 100 is much more extended in Line 5 which may reflect the influence of the start niche. Slightly decreased velocities (2.0 - 2.5 km/s) were found at similar locations and with a similar distribution as those in Line 3, but with less pronounced changes.

Similarities in location and tendencies of seismic velocity changes in all three receiver lines suggest that geological structures such as faults and fault zones have a strong influence on the failure type (i.e. extensional or shear failure) and the radial extent of the excavation-induced rock mass perturbations. In between and beyond the low velocity zones, p-wave velocities are significantly higher. Increased velocities close to the tunnel

surface, as observed in Line 1, can be explained by the formation of major sidewall slabs that detached along discrete fractures parallel to the tunnel circumference. At the location of these discrete fractures seismic velocities are substantially lower. Lines 1 and 3 present an overall comparable velocity distribution pattern, while Line 5 has, on average, lower velocities which reach deeper into the rock mass. This difference might be explained by the different locations of the receiver lines around the tunnel circumference in respect to the orientations of the in-situ stress tensor. At the Mont Terri URL the maximum principle stress is steeply inclined towards SSW and thus the maximum tangential stresses are to be expected at the lower NE-sidewall (i.e. location of Line 5) and the upper SW-sidewall. It is reasonable to assume that at the lower NE-sidewall stresses are additionally enhanced due to the unfavorable tunnel geometry caused by the flat tunnel invert (i.e. stress raiser). Higher induced stresses at the location of Line 5 may cause more intense damage associated with extensional type failure and thus overly lower velocities which affect a larger volume of the rock mass. P-wave velocities measured across fault zones or strongly faulted tunnel sections, in particular in the vicinity and across the major fault zone, located between GM 111 - 116 for Line 1 and between GM 113 - 117 for Lines 3 and 5, are in the order of 2.5 - 3.0 km/s. This suggests that extensional fracturing is not the dominant failure mode. The measurements obtained after excavation are in contrast to ultrasonic interval velocity measurements obtained before the excavation of the mine-by section which indicated substantially lower seismic velocities across fault zones. This discrepancy is interpreted to be either related to desaturation of the fault zones after its exposure to the tunnel environment, or to a different failure mechanism which involves shearing and eventually compaction. Note that the seismic tomography was performed 8 - 9 days after the excavation encountered the major fault zone, while USIVM were conducted 2 - 8 hours after drilling of the borehole.

3.7.1.2 EDZ depth below the tunnel invert

Complementary to seismic refraction tomography, drillcore logging of BRC-1, BRC-3 and BRC-4 allows for a direct determination of EDZ fracture distribution and extent below the tunnel invert. The maximum true vertical depth (TVD) to which macroscopic EDZ fractures were traced was 1.8 m for BRC-1, 2.47 m for BRC-3, and 2.65 m for BRC-4, respectively. In all boreholes, EDZ fractures were primarily oriented parallel to bedding planes without any fractographic markings on their surfaces. Derived fracture frequencies are presented in Figure 3-10. The highest frequency was found within the first 0.5 m TVD with an average of 14 EDZ fractures per meter. Between 0.5 and 2.0 m TVD fracturing is significantly reduced indicated by an average frequency of 4 to 5 fractures per meter. Beyond a TVD of 2 meters, the fracture frequency was consistently < 1 fracture per meter. Low fracture frequencies in the uppermost meters are typically associated with tectonic fault planes which intersect BRC-3 at 0.5 m TVD and BRC-4 at 0.75 and 1.75 m TVD, respectively. These findings supports that shearing along fault planes renders intact rock fracturing less likely.

3.7.2 Conceptual EDZ model

Geological and geophysical characterization of the EDZ extent around the mine-by section suggest a heterogeneous EDZ depth along both sidewalls with a maximum

extent of 2 - 3 m in between strongly faulted tunnel sections. However, geophysical characterization did not allow for a quantification of the EDZ extent within the fault zones. Thus, borehole deformation measurements in BRC-2 reported by Thoeny 2014 were utilized to better constrain the EDZ depth within the fault zones. Borehole deformations during and after construction of the mine-by section revealed significant radial displacements across the major fault zones at a radial distance of 3.5 - 4 m from the tunnel contour, while in the adjacent rock no borehole deformations were measured. These observations implies that the EDZ within the major fault zone extends to a minimum radial distance of 4 meters, while the adjacent rock mass at this depth is not affected.

A conceptual EDZ model was derived by integrating previously described geological and geophysical data (Figure 3-11). The model is valid for a 5 m diameter horseshoe-shaped tunnel excavated perpendicular to bedding strike and into the direction of bedding dip. Depth ranges derived from different methodologies and on different scales (i.e. borehole and tunnel-scale) suggest that the EDZ around the mine-by section is subdivided into an inner and outer zone as proposed by Bossart et al. (2004):

- The inner zone has a radial extent of 0.4 - 0.6 m at the sidewalls and consists of densely spaced IF1 and IF2 fractures. This is consistent with substantially decreased p-wave velocities (ranging between 0.6 and 1.2 km/s) identified in the seismic tomography in the first 0.5 m of the sidewalls. At the tunnel invert the inner zone is composed of reactivated fault planes and IF3, IF4 and IF5 fractures with a frequency of > 14 fractures per meter in the uppermost 0.5 m.
- The outer zone at the sidewalls reaches to a depth of 2 - 2.5 m and is composed of IF1 fractures. This is consistent with a maximum EDZ extent of 2.0 to 3.0 m derived from the seismic tomography survey. At the NE-sidewall, where only data from one seismic array were available, borehole deformation monitoring data were used to better constrain the EDZ depth. Deformation measurements in borehole BRC-2 indicate that significant radial deformations of the NE-sidewall are measurable to a depth of 2.5 - 3.0 m adjacent to fault zones and to a depth of 4 m within the major fault zone.

The data obtained in this study suggest, that the depth of the inner zone does not markedly vary along the tunnel axis even though fault frequencies change substantially. This is in contrast to the depth of the outer zone which shows a considerable dependency on large-scale strength and stiffness heterogeneities. The cross-sectional shape and the fracture pattern of the damage zone is consistent with observations from previous studies (Bossart et al. 2004; Martin et al. 2004) performed around tunnels and galleries with the same orientation as the mine-by experiment. However, longitudinal variations in the outer EDZ zone depth are remarkable and strongly influenced by changes in fault frequencies and resulting strength or stiffness heterogeneities.

3.7.2.1 *Comparison between EDZ and BdZ*

Geophysical characterization of the EDZ around the tunnel and borehole BRC-2 revealed a similar spatial distribution of induced damage independent of the scale. In both scales, induced damage is controlled by the density of pre-existing fault planes which alter the homogeneity of the rock mass in strength and deformability. The EDZ around the tunnel is composed of a network of macroscopic fractures which locally evolve into major

sidewall spalls, while, the BdZ around the borehole showed no evidence of borehole instabilities neither in the OPTV images nor with the camera inspection. However, borehole inspection was done immediately after drilling and damage associated with time-dependent effects were not captured. This might explain why borehole breakouts were not observed.

3.8 Conclusions

Complementary geological and geophysical characterization techniques on the tunnel and borehole-scale were used for a qualitative and quantitative analysis of the structural and kinematic relationship between natural and excavation-induced fractures in faulted Opalinus Clay at the Mont Terri URL in Switzerland. Integrating the results from seismic refraction tomography, borehole logging, and tunnel surface mapping allowed the evaluation of spatial variations in induced fracturing along the tunnel axis, and to identify key rock mass properties which influence both the characteristics and depth of excavation-induced damage. It was demonstrated that the spatial variations in fault frequency along the tunnel axis alter the homogeneity of the rock mass in strength and deformability which has a substantial effect on the location and the radial extent of induced damage on both, the borehole and the tunnel-scale. Based on geological and geophysical data a new conceptual model of the EDZ geometry around the mine-by section was established. The model suggests a strongly damaged inner zone with a consistent radial extent of 0.5 - 1.5 m and less damaged outer zones with a radial extent of 4 m within fault zones and 2 - 3 m in between the fault zones. The depth of the inner zone seems to be unaffected by variations in fault plane density, while the radial extent of the outer zone is substantially influenced.

Integration of geological mapping and borehole logging data revealed that the excavation-induced damage zone around the mine-by experiment is composed of reactivated fault planes and seven different types of induced fractures (IF):

- (IF1) extensional fractures parallel to the sidewalls,
- (IF2) extensional fractures oblique to the tunnel axis at the sidewalls,
- (IF3) sub-horizontal extensional fractures parallel to the tunnel invert,
- (IF4) extensional and/or shear fractures along bedding planes at the tunnel invert,
- (IF5) extensional fractures perpendicular to sheared bedding or reactivated fault planes at the tunnel invert,
- (IF6) shear fractures along bedding planes at the tunnel face,
- (IF7) extensional fractures sub-perpendicular to sheared bedding planes or reactivated tectonic faults at the tunnel face.

It could be demonstrated that failure mechanisms, orientations and frequencies of excavation-induced fractures are significantly influenced by the occurrence and characteristics of tectonic faults. At the sidewalls where fault plane reactivation or bedding shear was kinematically constrained, extensional fracturing tangential to the tunnel circumference was the dominating failure mode. At the tunnel face and the tunnel invert, where fault and bedding planes were kinematically free, extensional brittle failure and shearing along bedding planes was dominant in sparsely faulted (0 - 1 fault/m²) tunnel sections, while a combination of shearing along fault planes associated with extensile failure prevailed in tunnel sections that are intersected by 1 - 3 faults/m².

With increasing fault density (> 4 faults/m²), reactivation of densely spaced fault planes became more evident indicating a transition from extensional macroscopic failure to shearing. Furthermore it was observed that bedding shear and reactivation of tectonic fault planes occurred in normal faulting mode at the tunnel face, and in thrust faulting mode at the tunnel invert.

3.9 References

- Amann F, Button EA, Evans KF, Gischig VS, Bluemel M (2011a) Experimental study of the brittle behavior of clay shale in rapid unconfined compression. *Rock Mech Rock Eng* 44: 415-30
- Amann F, Kaiser PK, Button EA (2011b) Experimental study of brittle behavior of clay shale in rapid triaxial compression. *Rock Mech Rock Eng* 45: 21-33
- Bluemling P, Bernier F, Lebon P, Martin CD (2007) The excavation damaged zone in clay formations: Time-dependent behaviour and influence on performance assessment. *Physics and Chemistry of the Earth* 32: 588-599
- Bossart P, Meier PM, Moeri A, Trick T, Mayor J-C (2002) Geological and hydraulic characterisation of the excavation disturbed zone in the Opalinus Clay of the Mont Terri Rock Laboratory. *Eng Geol* 66: 19-38
- Bossart P, Trick T, Meier PM, Mayor JC (2004) Structural and hydrogeological characterisation of the excavation-disturbed zone in the Opalinus Clay (Mont Terri Project, Switzerland). *Applied Clay Science* 26: 429-448
- Bossart P, Thury M (2008) Mont Terri Rock Laboratory, project, programme 1996 to 2007 and results. Geological report No. 3, Swiss Geological Survey, Switzerland
- Burrus F, Hagmann S (2009) RC experiment: Project and experimental requirements during the excavation of RC section of Gallery o8. Unpublished Mont Terri Technical Note 2008-44, Mont Terri Project, Switzerland
- Burrus F, Bossart P, Nussbaum C (2010) Gallery o8: Documentation of the excavation and the convergence measurements. Unpublished Mont Terri Technical Note 2008-10, Mont Terri Project, Switzerland
- Freivogel M (2001) Modellierung bilanzierter Profile und Geologische Kartierung im Gebiet Mont Terri - La Croix (Kanton Jura). Diplomarbeit am Geologisch-Paläontologischen Institut der Universität Basel, Switzerland
- Girardin C, Theurillat T, Badertscher N, Nussbaum C (2008) Drilling campaign of Phase 13: drilling data, photo documentation and drillcore documentation. Unpublished Mont Terri Technical Note 2008-05, Mont Terri Project, Switzerland
- Girardin C, Theurillat T, Badertscher N, Nussbaum C (2009) Drilling campaign of Phase 14: drilling data, photo documentation and drillcore documentation. Unpublished Mont Terri Technical Note 2009-06, Mont Terri Project, Switzerland
- Kim Y-S, Peacock DCP, Sanderson DJ (2004) Fault damage zones. *Journal of Structural Geology* 26: 503-517
- Manukyan E, Marelli S (2009) Anisotropic travel time inversion seismic data along an EDZ at Mont Terri. Unpublished report, ETH Zurich, Switzerland

- Marschall P, Distinguin M, Shao H, Bossart P, Enachescu C, Trick T (2006) Creation and evolution of damage zones around a microtunnel in a claystone formation of the Swiss Jura Mountains. Proceedings of the 2006 SPE International Symposium and Exhibition on Formation Damage Control, Lafayette, Society of Petroleum Engineers, USA
- Martin CD, Lanyon GW (2003) Measurement of in-situ stress in weak rocks at Mont Terri Rock Laboratory, Switzerland. *Int J Rock Mech Min Sci* 40: 1077-1088
- Martin CD, Lanyon GW (2004) Excavation disturbed zone (EDZ) in Clay Shale: Mont Terri. Unpublished Mont Terri Technical Report 2001-01, Mont Terri Project, Switzerland
- Nussbaum C, Wileveau Y, Bossart P, Moeri A, Armand G (2007) Why are the geometries of the EDZ fracture networks different in the Mont Terri and Meuse/Haute-Marne Rock Laboratories? Structural Approach, Clays In Natural & Engineered Barriers For Radiactive Waste Confinement, Lille, France.
- Nussbaum C, Bossart P (2008) Geology. In P. Bossart & M. Thury (Eds.), Mont Terri Rock Laboratory. Project, programme 1996 to 2007 and results. Geological report No. 3, Swiss Geological Survey, Switzerland
- Nussbaum C, Girardin C, Badertscher N, Risse V, Veuve C, Mayoraz J, Bossart P (2010) Extension of the rock laboratory: Geological documentation of the Gallery 08 and adjacent niches. Unpublished Mont Terri Technical Note 2008-12, Mont Terri Project, Switzerland
- Nussbaum C, Bossart P, Amann F, Aubourg C (2011) Analysis of tectonic structures and excavation induced fractures in the Opalinus Clay, Mont Terri underground rock laboratory (Switzerland). *Swiss J Geosci* 104: 187-210
- Pfister A, Jaeggi D, Nussbaum C (2011) Drilling campaign of Phase 15: drilling data, photo documentation and drillcore documentation. Unpublished Mont Terri Technical Note 2010-38, Mont Terri Project, Switzerland
- Schuster K, Alheid H-J, Boeddener D (2001) Seismic investigation of the excavation damaged zone in Opalinus Clay. *Eng Geol* 61: 189-197
- Thoeny R, Amann F, Button EA (2010) Ground conditions and the relationship to ground behavior - a new mine-by project in Opalinus Clay at Mont Terri Rock Laboratory. In: Zhao J, Labiouse V, Dudt J-P, Mathier J-F (eds) Rock mechanics and environmental engineering. Paper presented at European Rock Mechanics Symposium 2010, Lausanne, Switzerland. Taylor & Francis Group, London, pp 775-778. ISBN 978-0-415-58654-2
- Thoeny R (2014) Geomechanical analysis of excavation-induced rock mass behavior of faulted Opalinus Clay at the Mont Terri Underground Rock Laboratory (Switzerland). PhD thesis, Department of Earth Sciences, ETH Zurich, Switzerland
- Thury M, Bossart P (1999) Results of the hydrogeological, geochemical and geotechnical experiments performed in the Opalinus Clay (1996-1997). Geological report No. 2, Swiss Geological Survey, Switzerland
- Wymann L (2013) The influence of saturation on the uniaxial compressive strength of Opalinus Clay. MSc thesis, Department of Earth Sciences, ETH Zurich, Switzerland

- Yaramanci U, Kruschwitz S, Maultzsch S (2002) Geophysical characterisation of the excavation disturbed zone (ED-C) experiment: Geoelectrical characterization of the Opalinus Clay formation in the underground rock laboratory of Mont Terri, Unpublished Mont Terri Technical Report 2000-04, Mont Terri Project, Switzerland
- Yong S, Evans KF, Fidelibus C, Loew S (2004) Fracture generation experiment: a review of the Mont Terri project literature. Unpublished Mont Terri Technical Note 2004-40, Mont Terri Project, Switzerland
- Yong S (2008) A three-dimensional analysis of excavation-induced perturbations in the Opalinus Clay at the Mont Terri Rock Laboratory. PhD thesis, Department of Earth Sciences, ETH Zurich, Switzerland
- Yong S, Kaiser PK, Loew S (2010) Influence of tectonic shears on tunnel-induced fracturing. *International Journal of Rock Mechanics & Mining Sciences* 47: 894-907
- Yong S, Kaiser PK, Loew S (2013) Rock mass response ahead of an advancing face in faulted shale. *International Journal of Rock Mechanics & Mining Sciences* 60: 301-311
- Zhou B, Greenhalgh S (2008) Non-linear travelttime inversion for 3-d seismic tomography in strongly anisotropic media. *Geophysical Journal International* 172(1): 383-394

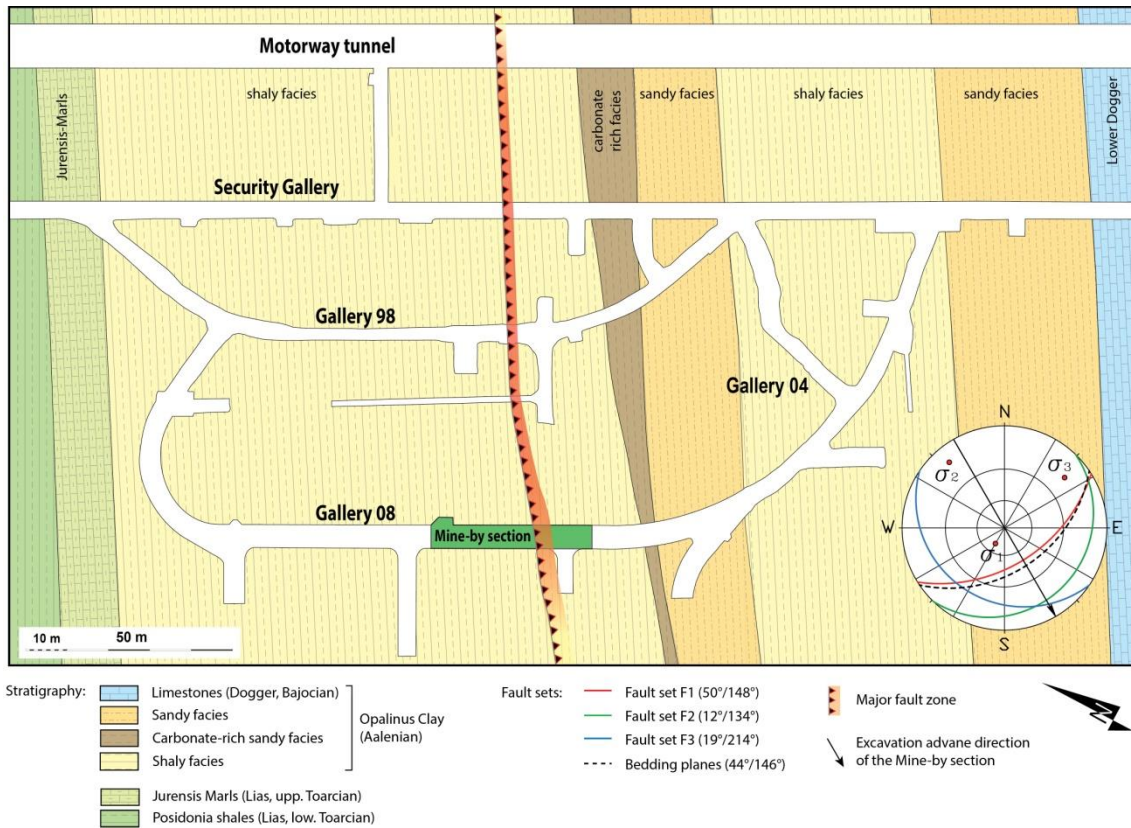


Figure 3-1: Structural map of the Mont Terri Underground Rock Laboratory (modified from Nussbaum et al. 2011), showing the various galleries and niches. The rock laboratory is intersected by three fault sets and a major fault zone. The mean orientation of the pronounced bedding and the three fault sets encountered within the mine-by section are shown in a lower hemisphere projection. The mine-by section is highlighted in green and entirely located within the shaly facies of the Opalinus Clay.

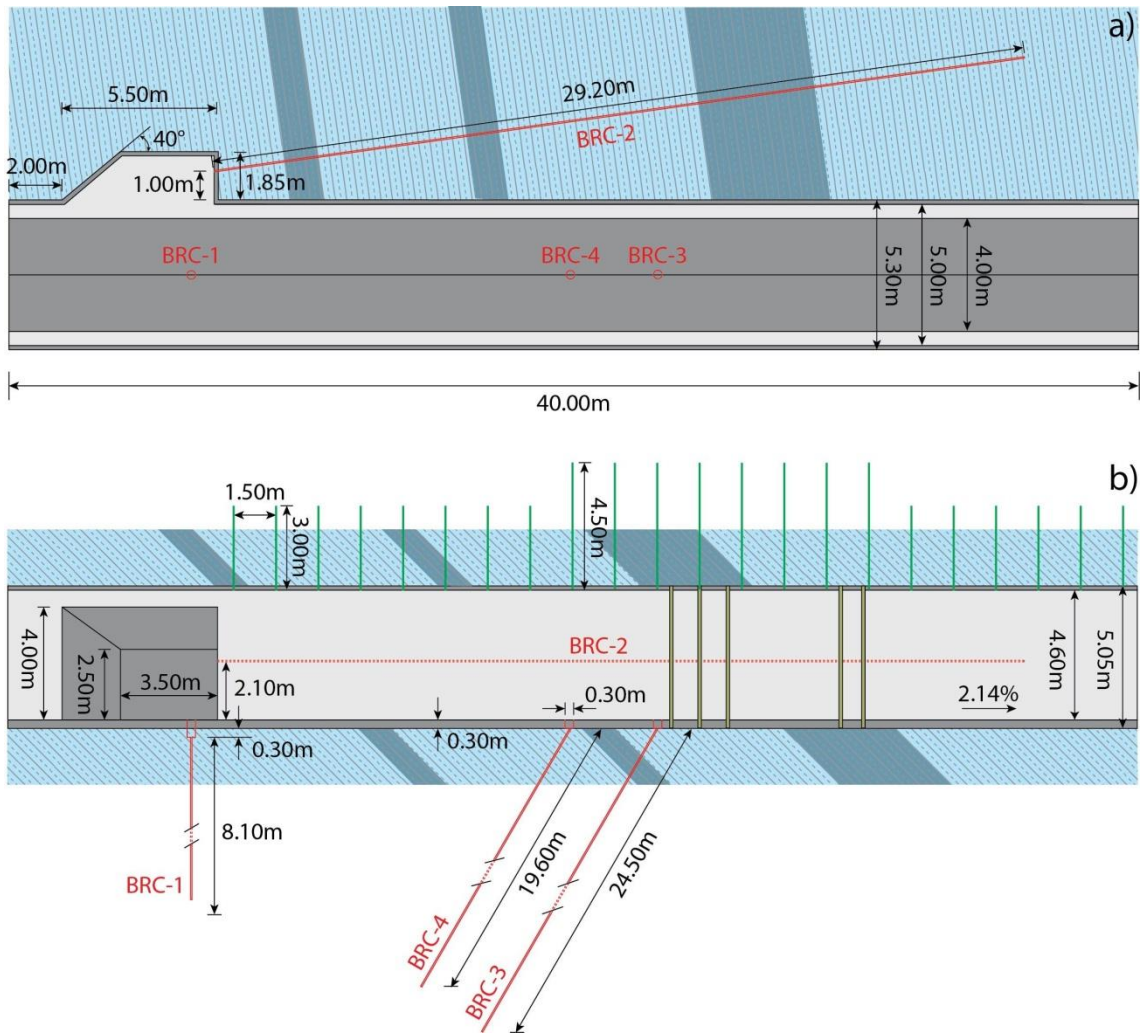


Figure 3-2: Longitudinal a) plan and b) cross-section view of the mine-by section showing the tunnel geometry and the final support measures. Further shown are the borehole orientations and lengths used for the characterization of the surrounding rock mass.

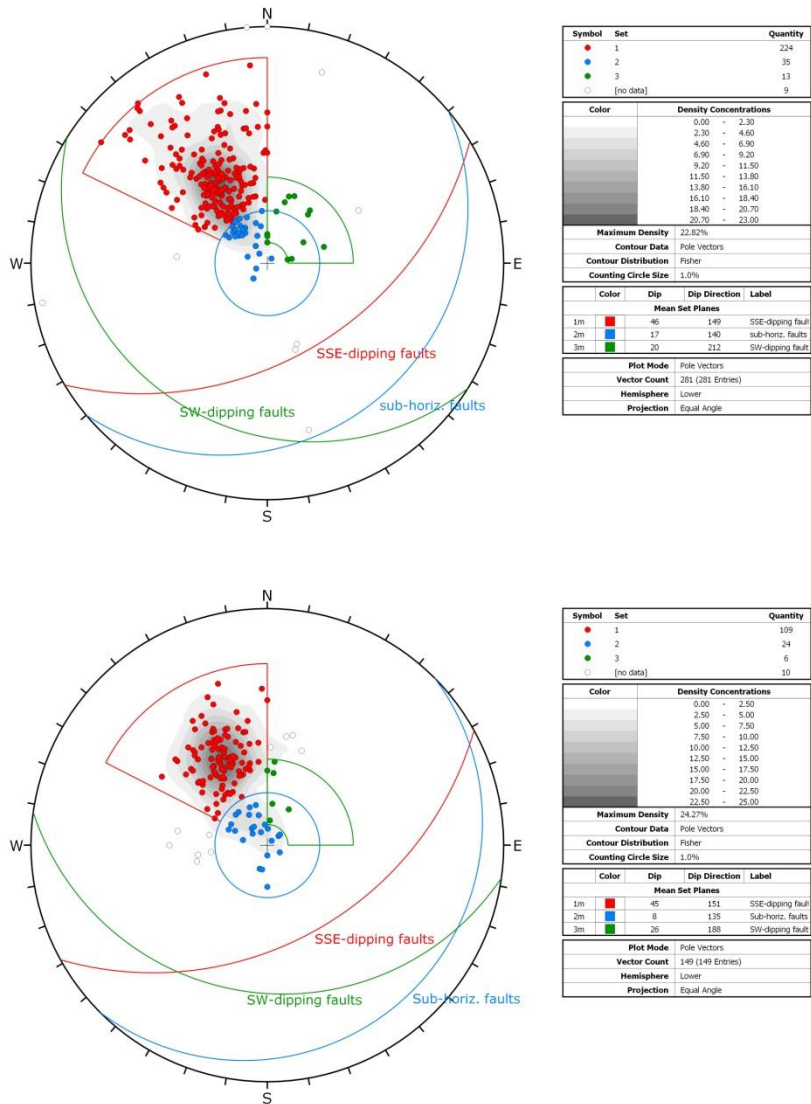


Figure 3-3: Mean orientations of tectonic fault sets between GM 40 and GM 127 of Gallery o8 represented in stereographic projections (lower hemisphere). Faults were classified in three different sets following the conventional nomenclature of the Mont Terri URL proposed by Nussbaum & Bossart 2008: (1) SSE-dipping faults, (2) sub-horizontal faults, and (3) SW-dipping faults. a) Tectonic faults derived from geological mapping of excavation surfaces between GM 40 and GM 127. b) Tectonic faults identified by core and optical televiewer logging of the boreholes BRC-1, BRC-2, BRC-3 and BRC-4 located between GM 93 and GM 125.

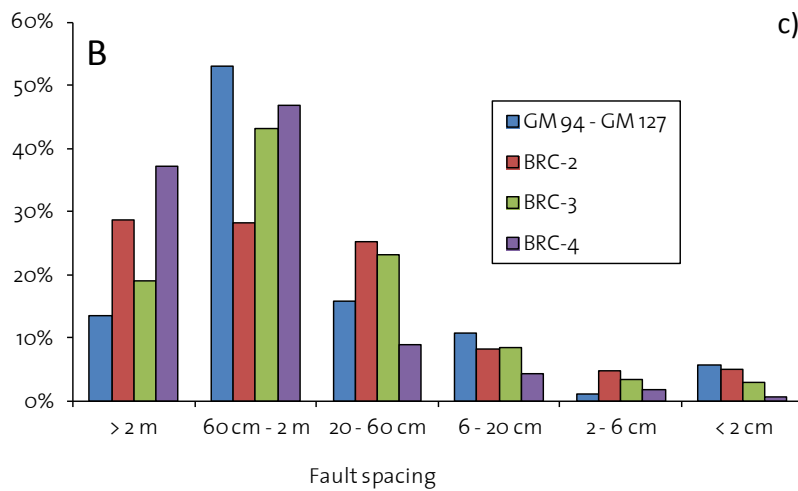
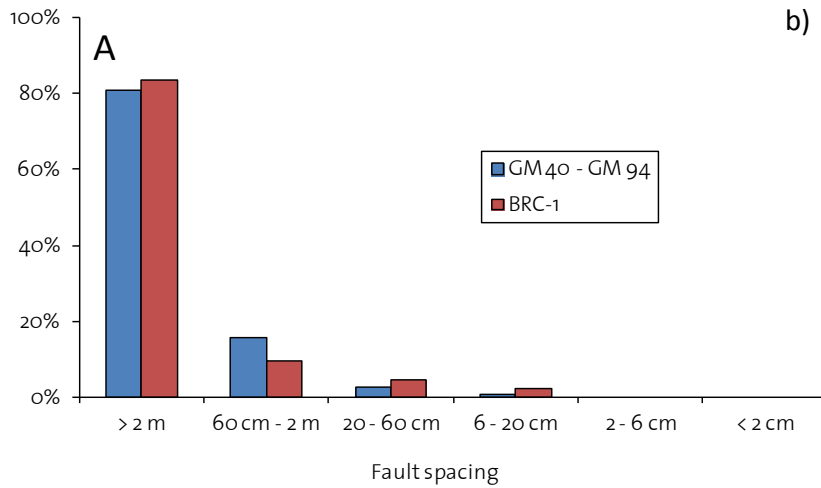
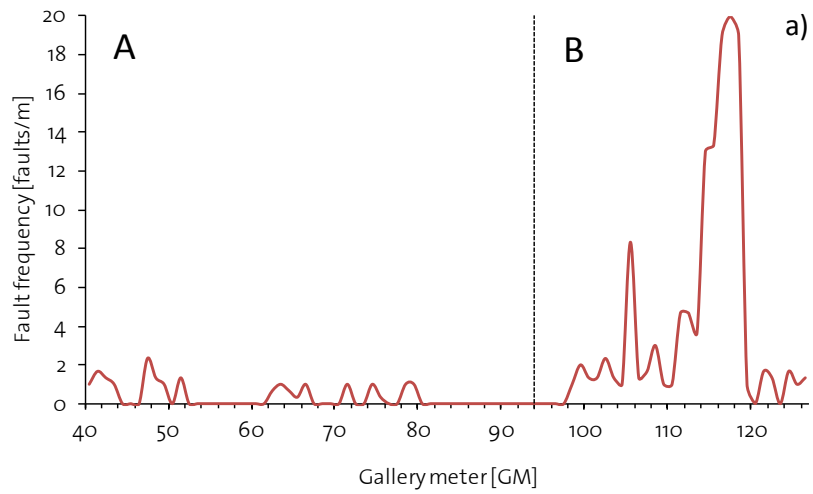


Figure 3-4: Fault frequency and spacing distributions along the Gallery o8 derived from scanline mapping of excavation surfaces and borehole logging of four boreholes between GM 40 and GM 127. a) Fault frequency distribution derived from scanline mapping on the tunnel invert. Spacing distributions for b) the tunnel section between GM 40 and GM 94 and c) the tunnel section between GM 94 and GM 127 (i.e. mine-by section).

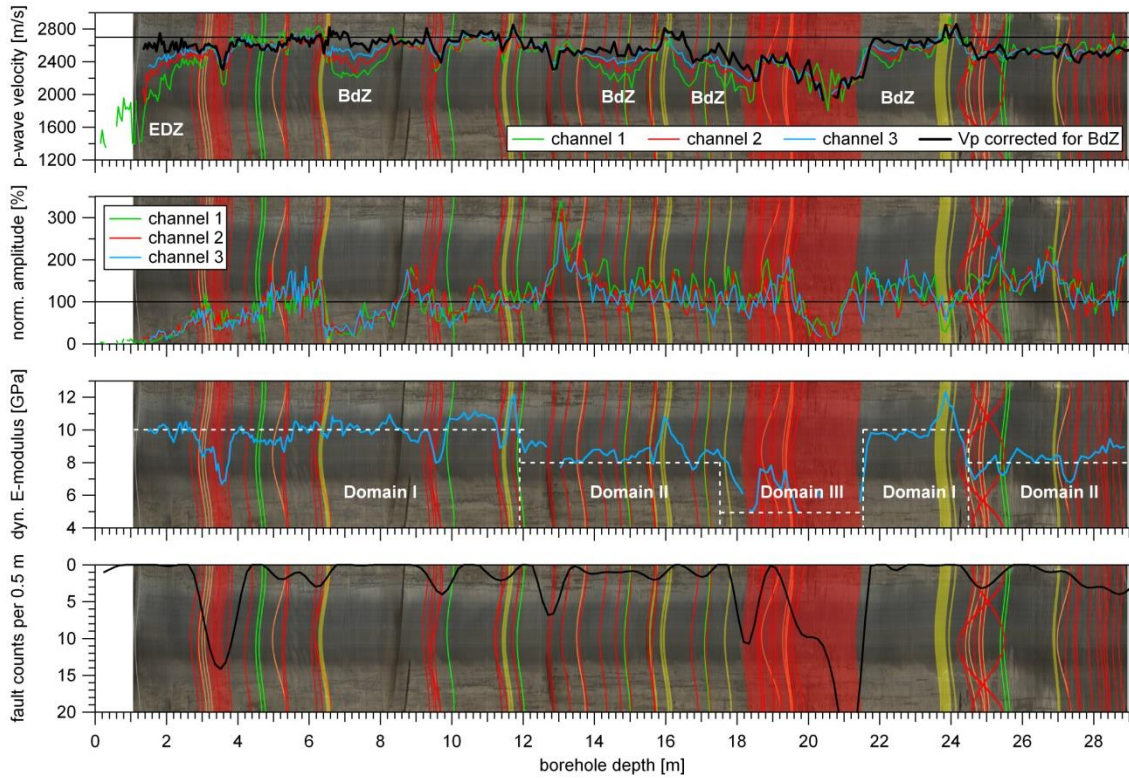


Figure 3-5: Derived seismic parameters from single-hole interval velocity measurements along the SW borehole wall of the pre-excitation borehole BRC-2: a) p-wave velocities and b) normalized amplitudes for all three channels. c) dynamic young's modulus derived from p- and s-wave velocities from channel 3. d) fault frequency (i.e. 0.5 m interval) derived from OPTV and core logging data. Significant differences in seismic velocities of the three channels indicate borehole sections with induced fracturing (i.e. BdZ).

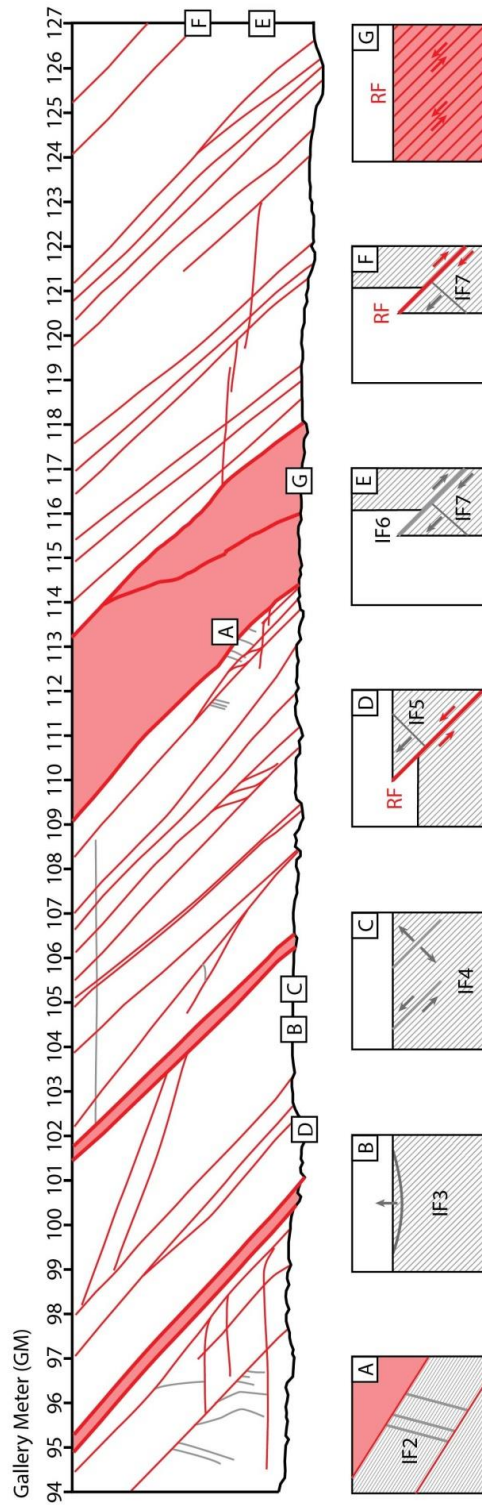


Figure 3-6: Conceptual model which illustrates the generalized structural and kinematic relationship between pre-existing tectonic faults and excavation-induced EDZ fractures around the mine-by section. The pronounced bedding of the Opalinus Clay is indicated by the grey dotted lines parallel to the SSE-dipping faults (red lines). Orientations of the EDZ fractures are shown by grey lines.

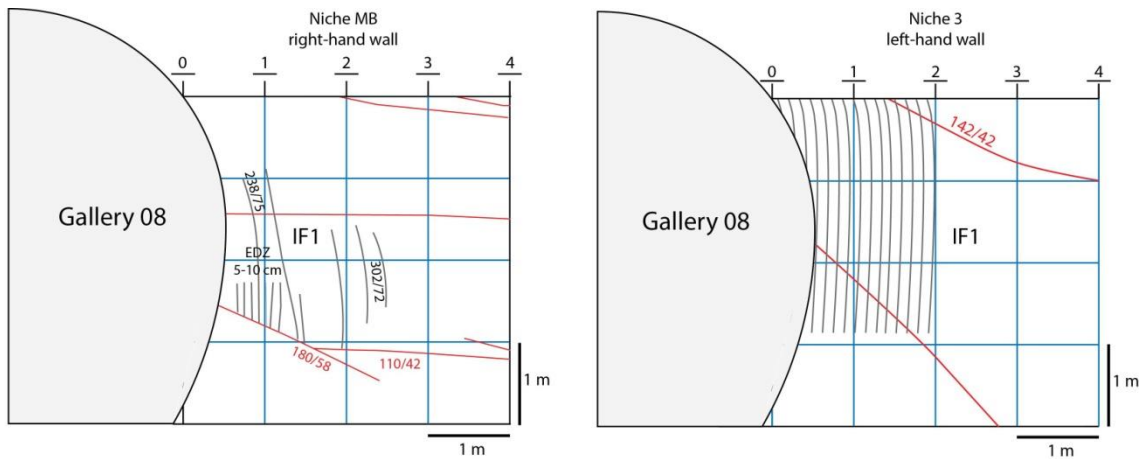


Figure 3-7: Induced fracturing mapped on the walls of the side niche entrances intersecting the Gallery 08 a) at GM 42 and b) at GM 122 (after C. Girardin et al. 2008).

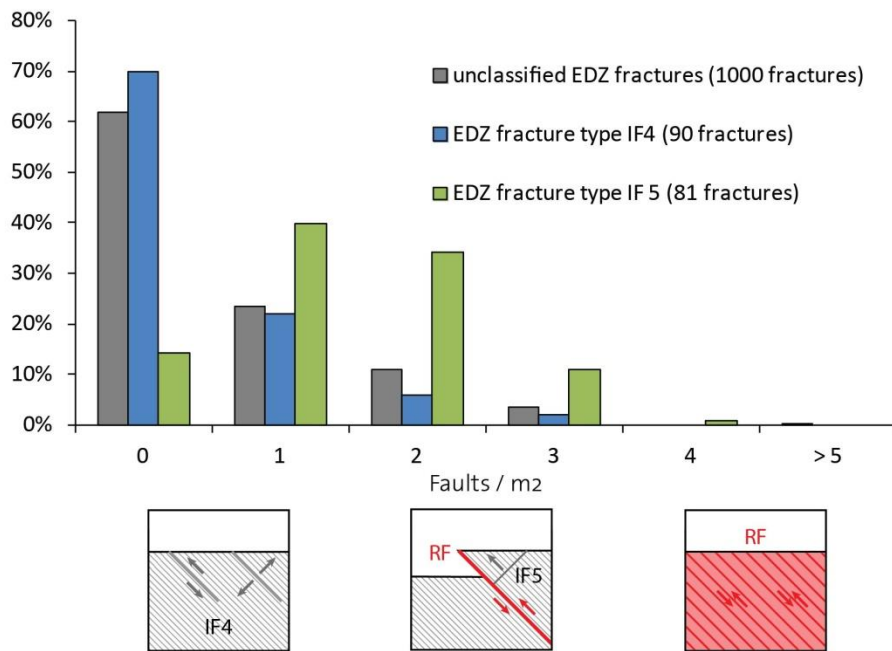


Figure 3-8: Spatial correlation between fault and EDZ fractures derived from systematic window-mapping of the tunnel invert between GM 40 and GM 127. EDZ distributions were normalized according to the total amount of measurements of the corresponding EDZ type. For each EDZ type an illustrative sketch of the prevailing fracture pattern is given.

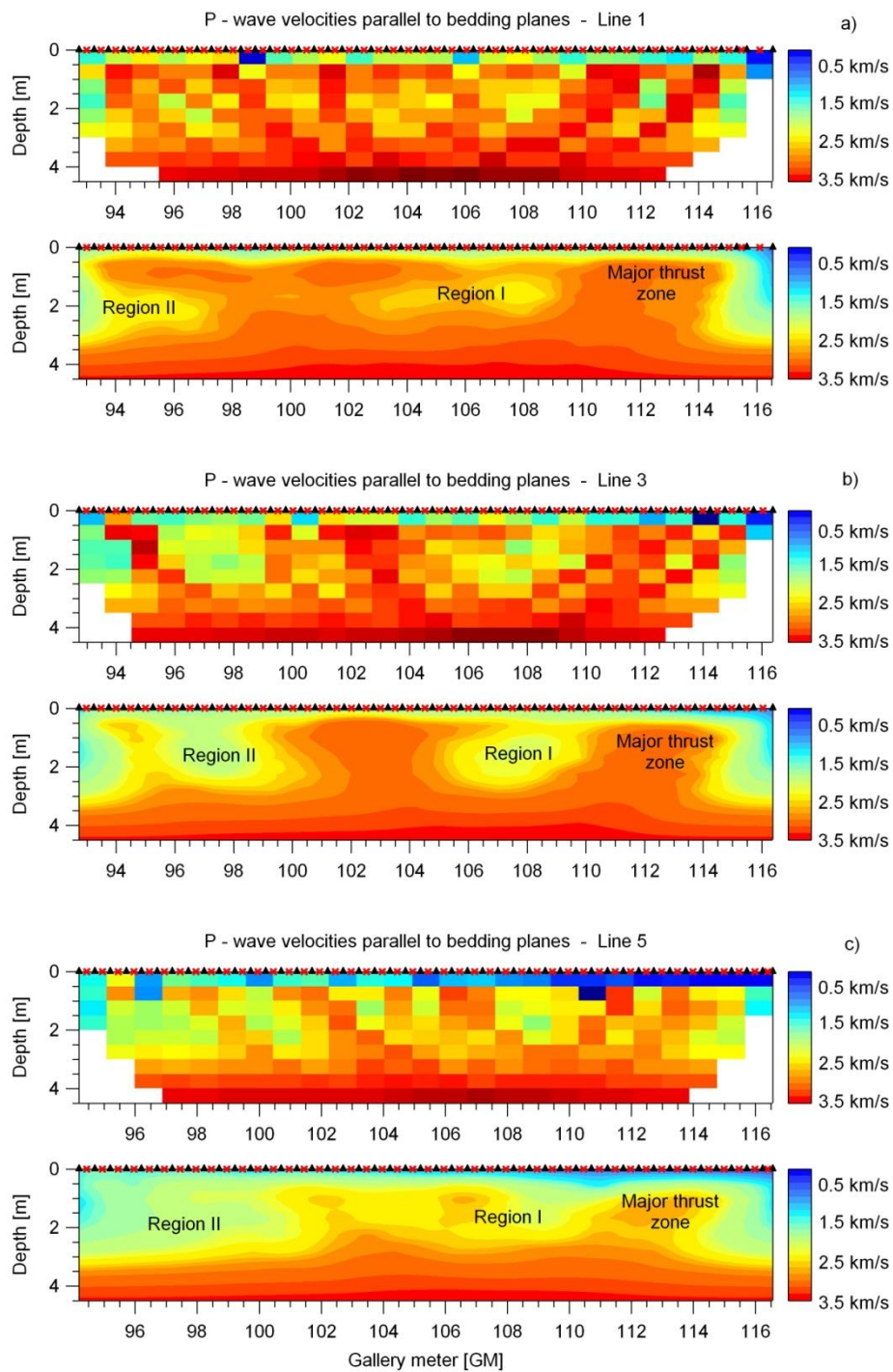


Figure 3-9: Inverted p-wave velocities parallel to the bedding planes for a) receiver Line 1, b) receiver Line 3, and c) receiver Line 5, before and after applying a Kernel filtering.

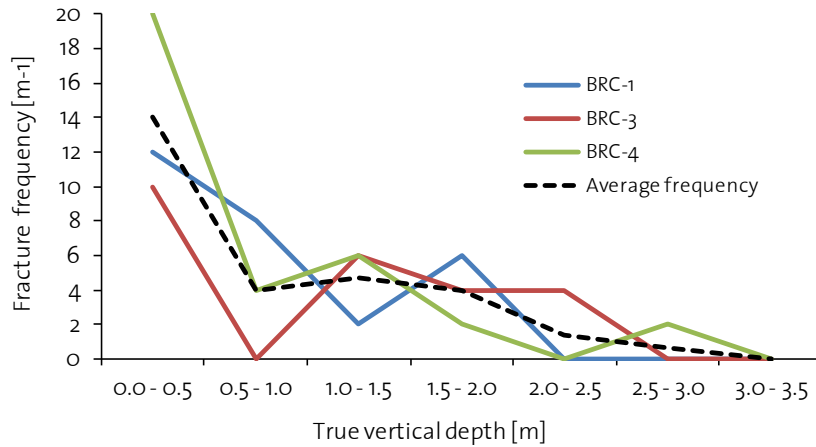


Figure 3-10: EDZ fracture frequencies below the tunnel invert derived from OPTV and core logging of the boreholes BRC-1, BRC-3 and BRC-4.

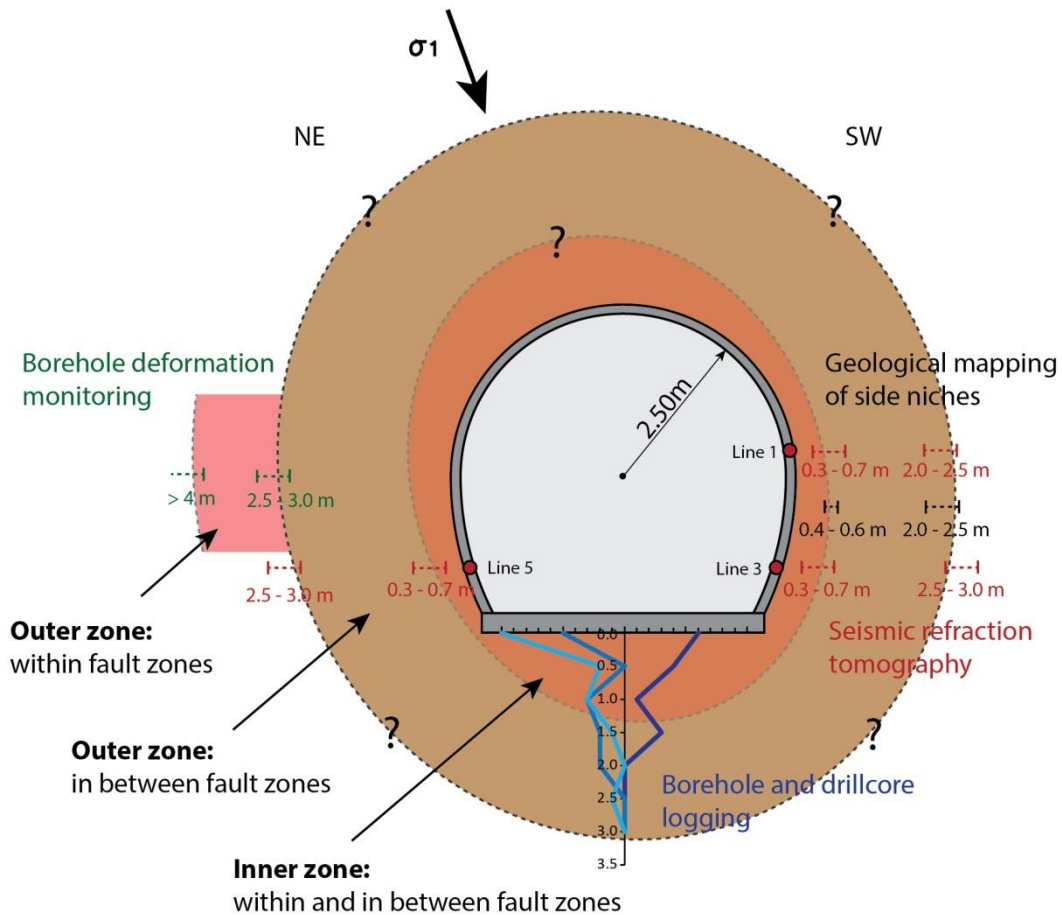


Figure 3-11: Concept for EDZ geometry around the mine-by section derived by integrating data from seismic refraction tomography, drill core logging, geological mapping of adjacent niches, and from deformation measurements in borehole BRC-2. The strongly damaged inner zone has a consistent radial extent of approximately 0.5 m at the sidewalls and of 1.0 - 1.5 m below the tunnel invert. The outer zone has a minimum radial extent of 4 m within fault zones and a maximum radial extent of 2 - 3 m in between the fault zones.

Table 3-1: Mean orientations of fault and bedding planes derived from geological mapping of excavation surfaces of Gallery 08

Gallery meter [GM]	Fault set F1 [dip/dip dir.]	Fault set F2 [dip/dip dir.]	Fault set F3 [dip/dip dir.]	Bedding [dip/dip dir.]
GM 40 - GM 94	41°/149° (99)	18°/142° (26)	24°/209° (4)	35°/150° (21)
GM 94 - GM 127	50°/148° (125)	12°/134° (9)	19°/214° (9)	44°/146° (5)
GM 40 - GM 127	46°/149° (224)	17°/140° (35)	20°/212° (13)	36°/149° (26)

Table 3-2: Mean orientations (dip / dip direction) of tectonic fault and bedding planes derived from structural data obtained from the boreholes BRC-1, BRC-2, BRC-3 and BRC-4

Borehole	Borehole length	Pre-existing tectonic faults			Bedding
		Fault set F1	Fault set F2	Fault set F3	
BRC-1	8.10 m	39°/147° (5)	-	-	43°/144° (2)
BRC-2	29.20 m	43°/151° (45)	11°/129° (3)	26°/195° (2)	37°/150° (18)
BRC-3	24.50 m	49°/154° (42)	12°/151° (11)	29°/183° (3)	37°/146° (11)
BRC-4	19.60 m	44°/146° (17)	04°/087° (10)	20°/187° (1)	42°/146° (15)
All boreholes	81.40 m	45°/151° (109)	08°/135° (24)	26°/188° (6)	39°/148° (46)

Table 3-3: Classification of identified EDZ fracture types in terms of orientation, location and fractographic markings on fracture surfaces

Type	Orientation	Location around tunnel contour	Fractographic markings on fracture surfaces
IF1	Steeply inclined (>75°) extensional fractures striking parallel to tunnel axis	Sidewalls	Plumose structures
IF2	Steeply inclined (>75°) extensional fractures striking oblique to tunnel axis	NE-sidewall below major fault zone	Plumose structures
IF3	Sub-horizontal extensional fractures	Tunnel invert	Plumose structures with ripple marks
IF4	Parallel to bedding planes (42°/151°)	Tunnel invert	No fractographic markers (rarely striations)
IF5	Perpendicular to fault planes (43°/332°)	Tunnel invert	Plumose structures
IF6	Sub-parallel to bedding planes (49°/149°)	Tunnel face	Poorly developed striations
IF7	Sub-perpendicular to fault planes (68°/318°)	Tunnel face	Plumose structures
RF	Predominately bedding-parallel (50°/148°)	Tunnel face and invert	Dark polished fracture surfaces with slickensides

IF = induced fractures, RF = reactivated fault planes

4 EFFECTS OF TECTONIC FAULTS ON THE SPATIAL AND TEMPORAL EVOLUTION OF THE DISPLACEMENT FIELD AROUND A TUNNEL IN FAULTED OPALINUS CLAY

Abstract

A full-scale mine-by experiment was conducted at the Mont Terri Underground Rock Laboratory in Switzerland to examine the influence of multi-scale tectonic faults on the rock mass response of Opalinus Clay during conventional tunneling. To capture the rock mass response to tunneling a multi-component monitoring system was implemented. To measure rock mass deformations geotechnical instrumentation including a borehole inclinometer, extensometer and deflectometer were utilized and to quantify the tunnel surface displacements high resolution geodetic surveying and laser scanning measurements were performed. Displacement monitoring data from this mine-by experiment revealed that the rock mass response of faulted Opalinus Clay is substantially governed by both the failure behavior of individual fault planes and their kinematics, while the overall rock mass behavior correlates more with variations in larger-scale deformability and strength heterogeneities. In the investigated tunnel section these heterogeneities are primarily associated with fault zones and spatial variations in fault plane densities. Integration of the deformation measurements considering both the fracture and the tunnel-scale revealed that individual fault planes were most influential on the rock mass response at the tunnel face, crown and the invert, but were less influential in the sidewalls and at larger depths in the rock mass. At the sidewalls, where fault plane reactivation was of minor relevance due to their unfavorable orientation, the rock mass response was dominated by extensional fracturing through the intact rock matrix resulting in large displacements adjacent to large-scale rock mass heterogeneities. These findings suggest that in faulted Opalinus Clay both, deformations at the fracture and the tunnel-scale must be considered to understand the excavation-induced rock mass response and thus the associated spatial and temporal evolution of the displacement field.

Key words: Rock mass behavior, excavation-induced displacements, Opalinus Clay

4.1 Introduction

Pre-existing discontinuities can decisively influence excavation-induced rock mass behavior and therefore play a crucial role for design and safety-related issues of nuclear waste disposal in clay rock formations. The Mont Terri Underground Rock Laboratory (URL) enables access to the so-called Opalinus Clay, which was recently selected as the host rock formation for deep geological disposal of nuclear waste in Switzerland. Beside the anisotropy due to its pronounced bedding, Opalinus Clay at the Mont Terri additionally exhibits a large-scale rock mass anisotropy due to the frequent occurrence of natural faults. Observations obtained during several in-situ experiments at the Mont Terri URL (Marshall et al. 2006; Bluemling et al. 2007; Nussbaum et al. 2007, 2011; Yong 2008; Thoeny 2014) consistently showed that reactivation of tectonic fault planes as consequence of excavation-induced stress redistributions play an essential role in the development of the excavation-induced fracture network in the tunnel near-field. However, previous studies were primarily focused on the influence of tectonic faults on local fracture processes and behavior. Thoeny 2014 showed that in addition to these locally observed fracture processes spatial variations in fault plane density along the tunnel axis alters the homogeneity of the rock mass in deformability and strength, and impact fracture processes on a considerably larger scale. While addressed in local situations, a detailed study focusing on the influence of pre-existing discontinuities such as fault planes or fault zones on the rock mass deformation behavior at both the fracture and the tunnel-scale was not investigated so far.

In this paper the spatial and temporal evolution of the displacement field around a tunnel in faulted Opalinus Clay during and after its construction was examined by analyzing excavation-induced deformations and displacements at both the fracture and the tunnel-scale. Capturing the rock mass response to the excavation with only minor influence of the support measures allows the mechanisms responsible for and the factors that influence the induced deformations to be identified. High resolution displacement and deformation monitoring data provides a sound basis for characterizing and quantifying the measured displacement field and deriving the kinematic behavior of the surrounding rock mass based on detailed characterization of the existing and induced fracture networks (Chapter 3). Special consideration is given to the mechanical influence of pre-existing discontinuities and fault zones on the excavation-induced deformation pattern and resulting rock mass damage.

4.2 Mont Terri Underground Rock Laboratory

The mine-by experiment discussed in this study was conducted in Gallery 08 of the Mont Terri Underground Rock Laboratory in northwestern Switzerland. The rock laboratory is located in the southeastern limb of the Mont Terri anticline in the Opalinus Clay formation at a depth of 250 - 320 m (Figure 4-1). Variations in the sedimentary environments during the time of deposition resulted in three main facies at the Mont Terri URL: 1) the shaley facies, 2) the sandy facies, and 3) the carbonate-rich facies (Thury & Bossart 1999). The mine-by experiment is located entirely in the shaley facies of the Opalinus Clay (Figure 4-2), consisting of argillaceous and marly shales with intercalated cm-thick sandy layers and lenses (Nussbaum et al. 2011). The shaley facies is characterized by a porosity ranging between 12 to 18% with a natural water content measured on core

samples taken from the level of the URL ranging between 7 and 8% (Wild 2010; Amann et al. 2011; Wymann 2013). The rock laboratory is intersected by a variety of tectonic fault planes and fault zones at different scales and orientations (Figure 4-2). Within the mine-by section pronounced bedding is dipping towards SSE and dip angles are ranging between 35 and 50° (Thoeny 2014). Between GM 109 and GM 117 the mine-by section is intersected by a 2 - 3 m thick fault zone which can be traced through the entire rock laboratory (Figure 4-2). In addition to this major tectonic structure three fault sets were mapped in the mine-by section. The most frequently occurring fault set F₁ is bedding-parallel dipping with 48° towards azimuth 150°. The second fault set F₂ (mean dip / dip direction: 12°/134°) is minor and composed of sub-horizontal faults branching from SSE-dipping fault planes. Fault set F₃ consists of slightly SW-dipping faults (19°/214°) and was only found in isolated regions of the mine-by section (Thoeny 2014).

The in-situ stress state at the level of the Mont Terri URL is difficult to characterize, but assumed to be as suggested by Martin and Lanyon (2003). They propose a sub-vertical maximum principle stress direction which is steeply inclined towards SSW with the intermediate and minor stresses being sub-horizontal. While the maximum principal stress magnitude lies in the order of 6.5 MPa reflecting the present overburden, the magnitude of the minimum principle stress is less defined and ranges between 2 and 3 MPa. The minimum principle stress direction is slightly inclined towards NE. The intermediate principle stress direction is roughly aligned with the axis of the Gallery o8, trending with 10° towards NW and its magnitude ranges between 4 - 5 MPa.

4.3 Mine-by experiment

The mine-by experiment is located in the straight section of Gallery o8 between GM 94 and GM 127 (Figure 4-2). Excavation of the mine-by section was carried out concurrently with the construction of the Gallery o8, and lasted from April 22nd to June 6th 2008. The mine-by section has a 5 m high horseshoe-shaped profile with a length of 32.5 m (Figure 4-3). A full-face excavation using a roadheader with an average round length of 1.5 m/day was utilized. The use of the roadheader minimized extraneous damage to the surrounding rock mass and allowed a repetitive excavation process. The same excavation pattern was utilized by the roadheader for each excavation step to create a similar stress path in the rock mass around the tunnel face. With a consistent stress path, the influence of rock mass heterogeneity and anisotropy can be studied quantitatively. The tunnel advanced towards azimuth 152° at a down grade of approximately 2.14%, which is approximately perpendicular to the bedding strike and in the direction of bedding dip. Support measures throughout the experiment were installed immediately after each excavation round and consisted of wire mesh reinforcement (K 196) affixed on the tunnel ceiling and eight rock bolts installed approximately 0.7 m behind the advancing tunnel face. Shotcrete was not applied continuously allowing initial observations and monitoring of the short-term rock mass response to the excavation by geodetic and laser scanning surveys. A 150 mm thick shotcrete lining was required between GM 94.5 and GM 98 (April 30th - May 5th 2008) and between GM 98 and GM 111.5 (May 15th - May 19th 2008) due to significantly increased radial deformations of the corresponding tunnel profiles. From GM 111.5 - 113.5, only the crown was lined with shotcrete. The remaining part of the mine-by section was shotcreted between June 4th and June 6th 2008. The thickness of the final shotcrete lining varies between 16 and 23 cm. The tunnel invert, consisting of a 30 cm thick concrete slab, was installed from GM 88 - 130 from July 16th to July 17th 2008.

A detailed description of the excavation procedure and the support measures can be found in Chapter 2.

Prior to the excavation, the rock mass surrounding the mine-by experiment was instrumented with geotechnical borehole instrumentation to continuously monitor the mechanical rock mass response during the construction of the mine-by experiment and after its completion. Complementing the borehole measurements, geodetic and laser scanning surveying of the excavation surfaces were conducted throughout the step-wise excavation of the mine-by section. Complimentary data was gathered from structural and geophysical characterization of the surrounding rock mass, comprising detailed geological mapping of the excavation surfaces, borehole logging data and seismic refraction tomography.

4.4 Borehole deformation monitoring

To examine the mechanical influence of discrete faults on the local deformation behavior on the fracture-scale deformation data from two differently oriented boreholes (Figure 4-3) around the proposed alignment of Gallery o8 were utilized. Borehole BRC-1 is located at GM 93.5 and was drilled from the tunnel invert vertically down to a depth of 8.1 meters, crossing the bedding at approximately 45 degrees. Borehole BRC-2 is located within the NE-sidewall of the mine-by section and was drilled from the start niche sub-parallel to the proposed tunnel alignment at the level of the springline. The borehole axis dips with 2 degrees towards azimuth 144° , thus crossing the bedding at an angle of approximately 45 degrees (Figure 4-3). Both boreholes were drilled prior to the excavation of the mine-by experiment and were initially investigated with geological and geophysical methods to properly identify and characterize intersecting tectonic faults in terms of their orientation and location along the borehole axis. Prior to the excavation of the mine-by section borehole BRC-1 was instrumented with an inclinometer (TRIVEC) and borehole BRC-2 was instrumented with a deflectometer and two extensometers. The instruments were designed to measure the vertical, radial and longitudinal displacement fields in the surrounding rock mass throughout the excavation phase as well as following the completion of the mine-by experiment. Various measurements extend for a period of 2.5 years after their installation. The instrumentation layout is shown in plan and section view in Figure 4-3.

4.4.1 TRIVEC measurements

The spatial and temporal evolution of the displacement field below the tunnel invert was monitored using a TRIVEC TDR. This high precision monitoring system consists of a specially machined HPFC casing that accommodates the measuring probe and allows the three orthogonal components of the displacement vectors along a vertical measuring line to be measured. The TRIVEC casing was cemented into the borehole BRC-1 on April 7th 2008. The casing consists of 7 measuring intervals with a base length of 1 m, starting at a depth of 0.15 m and ending at a depth of 7.15 m (Keller 2008). All measurements were conducted manually with the same TRIVEC probe manufactured by Solexperts AG, following standard procedures (Solexperts AG). The initial TRIVEC measurement was performed 14 days after cementing the casing and right before the excavation of the mine-by section on April 21st 2008. Repeat measurements were conducted immediately

after each excavation round and periodically after the completion of the mine-by experiment. The difference between a repeat and the initial measurement gives the profile of inclination and interval length change along the borehole. Multiplying the inclination change by the base-length of the probe (1 m), displacement of the upper end of the instrument with respect to the lower one can be obtained. The horizontal components are measured along two perpendicular axes, further referred to as the positive X'-axis and Y'-axis. These measuring directions are predefined within the measuring heads of the casing that accommodate the TRIVEC probe and are oriented during the installation of the TRIVEC. The positive X'-axis is oriented towards N123°E and the positive Y'-axis towards N033°E. For the evaluation of the horizontal displacements, the measured values were transformed into a direction parallel (X-axis) and perpendicular (Y-axis) to the gallery axis. The TRIVEC probe captures incremental horizontal displacements with an accuracy of 0.05 mm/m (Keller 2008). The vertical displacement sensor measures changes in distance between the lower and the upper end of the probe (base-length of 1 m), with negative values denoting extension. Vertical displacement measurements have an accuracy of 0.003 mm (Keller 2008).

4.4.2 Extensometer measurements

Two arrays of magnetic extensometers (Mag-X 1 and 2) were installed in borehole BRC-2 to continuously measure the relative longitudinal displacements of the surrounding rock mass throughout and after the construction of the mine-by section. Both arrays were installed prior to the excavation to capture the entire longitudinal rock mass response to the step-wise excavation of the mine-by section. The extensometer arrays consist of two individual 15 m long high precision multi-point extensometers (Mag-X 1 and 2) overlapping over an interval of 3 m between 11.9 and 14.9 m (Figure 4-3). The overlap allows the two instruments to be treated as a single extensometer. Each extensometer array consists of 20 measuring points (i.e. magnets) with a base-length between 0.7 to 0.8 m (Keller 2008). The first measuring point is located 0.5 m from the borehole mouth and the last at a depth of 26.3 m, resulting in a total monitoring length of 25.8 m. The borehole axis is oriented sub-parallel to the tunnel axis (i.e. deviation of 8°), thus the radial distance of the extensometers to the tunnel alignment linearly increases from 1.3 m at the head of the instrument up to 4.6 m at the end of it (Figure 4-3). The assembly was grouted into the borehole on April 7th 2008 to anchor the magnets (i.e. measurement points) to the surrounding rock. For a high quality installation the maximum measurement accuracy is 0.002 mm (Keller 2008). A connection from the extensometers to the data acquisition system allows simultaneous measuring and recording of all measurement positions relative to the location of the extensometer heads. Changes in distance between the individual measuring points were calculated with respect to the first measurement, further referred to as the reference measurement. Reference measurements of both extensometer arrays were conducted 14 days after their installation to allow curing of the grout and related displacements. Throughout the excavation of the mine-by section, measurements were taken every 2 minutes and after its construction every 10 minutes. Seven months after the installation of the two extensometer arrays the acquisition system for the extensometer Mag-X 1 was interrupted from the end of November 2008 until the beginning of June 2009 for unknown reasons.

4.4.3 Deflectometer measurements

Complementary to the two extensometer arrays, the borehole BRC-2 was additionally equipped with a Chain-Deflectometer. This is a series of multiple deflectometers that provide continuous biaxial deflection measurements along the borehole with respect to the initial measurement. The measuring instrument consists of a continuous aluminum rod that is equipped with 14 individual measuring heads. The instrument is emplaced in a specially machined HPVC casing bonded to the rock with cementitious grout prior to the excavation of the mine-by experiment on April 7th 2008 (Keller 2008). Each of the measuring heads, except of the first and the last one, are equipped with strain gauge sensors to measure deflections in two perpendicular directions. They were oriented in the vertical and horizontal direction during the emplacement of the measuring probe into the casing on April 15th 2008. The first four and the last two measuring heads are separated by a distance of 3 m, while the measuring heads in between are located at an interval of 1.5 m. Thus, the total length of the deflectometer measures 25.5 m with the first measuring head being located 0.4 m from the borehole mouth. The borehole axis is oriented sub-parallel to the tunnel axis (i.e. deviation of 8°), thus the radial distance from the deflectometer to the tunnel alignment is linearly increasing from 1.3 m at the head of the instrument up to 4.6 m at the end of it. After its installation the chain deflectometer was connected to a dedicated data acquisition system to record deformations every 2 min throughout the excavation of the mine-by section and every 10 min after its completion. In December 2010 the acquisition system for the deflectometer failed for unknown reasons, thus the entire monitoring period covers a time span of approximately 32 months. The chain deflectometer can be regarded as a continuous beam. Hence, a local deformation along the deflectometer does not only result in a deflection of one measuring point, but also have an effect on the neighboring measuring points. This relation was taken into account for transforming the measured deflections into effective angle changes by using a calibration matrix which is specific for each deflectometer configuration and was provided from the manufacturer (Solexperts AG). The calibration matrix was determined in the laboratory by deflecting each measuring head by a constant distance in both directions by simultaneously capturing the deformation behavior of the other measuring heads.

4.5 Excavation surface monitoring

4.5.1 Geodetic monitoring

Geodetic measurements were conducted to measure both point-wise and surface displacement during the step-wise excavation of the mine-by section between April 22nd and June 2nd 2008. The geodetic monitoring system consisted of a Leica TCRP 1201 total station (accuracy 2 mm + 2 ppm in distance, and 0.3 mgon in angle), 10 reference prisms, and 20 geodetic profiles evenly distributed over the entire length of the mine-by section (Figure 4-4). Subsequent to each excavation round, a geodetic profile consisting of 5 prisms was installed 0.6 to 0.8 m behind the advancing tunnel face as shown in Figure 4-4. Different prisms (Solexperts mini prisms, Geodata prisms, and Leica prisms GPR1) were mounted on steel bolts and glued (HILTI HIT-HY injection glue) 200 - 250 mm into the rock (Schuetz 2009a). Measurements of newly installed prism were conducted 3 to 4 hours after installation to allow initial curing of the glue. After installation and curing of

the glue displacements were measured automatically every hour by the total station. The direction of displacements are referred to a local coordinate system where the X-axis corresponds to the horizontal alignment of the mine-by section, the Z-axis corresponds to the vertical direction and the Y-axis is directed perpendicular to the tunnel axis. The positive X-axis runs in the direction of the tunnel advance, the positive Z-axis points upwards and the positive Y-axis follows the rule of a left hand coordinate system.

Geodetic data were analyzed in terms of longitudinal and cross-sectional displacement vector plots, and in terms of contour line plots. For the longitudinal and cross-sectional displacement vector plots the scaled (1:10) cumulative in-plane vector path is plotted for each of the geodetic prisms. Contour line plots are established by interpolating (i.e. krigging) the displacement field between the individual measuring points recorded at the same time.

4.5.2 Laser scanning monitoring

Complementary to the geodetic measurements, the tunnel surfaces were scanned with a laser scanner (Imager 5006 from Zoller+Froehlich) during the excavation of the mine-by experiment. Scanning was carried out after each excavation round whereby the laser scanner was progressively moved with the advancing tunnel face. For all measurements the laser scanner was placed on a tripod at the centre of tunnel with the height of the tipping axis approximately 1.3 m above the tunnel invert. All scans were performed with a resolution of 10'000 pixel/360° which corresponds to a pixel size of approximately 2 mm at the tunnel walls. The point clouds acquired by the laser scanner consist of x-, y-, and z-coordinates. For a direct comparison between the different laser scans, each point cloud was transformed according to the local established coordinate system using the 3D point cloud processing software Leica Cyclone 6.0 (Schuetz 2009b). The georeferenced scans were subsequently analyzed with the software TMS Tunnelscan from Amberg Engineering Ltd. to create differential displacement maps by comparing two spatially overlapping scans taken at different excavation stages. The absolute coordinates of each resolution cell are projected on an idealized tunnel profile (normal projection on the tunnel contour) and were then extracted from the coordinates of a reference scan resulting in relative displacements of the excavation surfaces towards the tipping axis of the laser scanner. Reference scans of the excavation surfaces taken on April 29th, May 15th and June 2nd 2008 were obtained prior to the emplacement of shotcrete. Thus, the measuring period of the corresponding tunnel sections was limited to the duration until an initial shotcrete layer was applied. Differential maps of lined tunnel sections with a nominal shotcrete thickness of 150 mm show no further increase in relative displacements, indicating that the measuring period prior to the application of the final support is capturing the major part of the measurable displacements and the support suppressed any further deformations. Thus, the displacement pattern derived from laser scanning can be compared with the radial displacement pattern obtained by geodetic measurement of the unlined rock mass.

4.6 Results and interpretation

In this study, the response of the rock mass throughout the excavation of the mine-by section (i.e. excavation phase) is termed short-term behavior. Long-term behavior is used

for slow rock mechanical processes that become relevant during the open drift phase. While the monitoring setup for excavation surface displacement monitoring was designed to capture the short-term rock mass behavior to the step-wise tunnel excavation, borehole-based deformation monitoring was designed to capture both, the short and long-term rock mass response. Furthermore, monitoring of excavation surfaces allows only a part of the entire rock mass response to be captured, while deformation monitoring in pre-excavation boreholes offers the capability to capture the entire response ahead of the advancing tunnel. To investigate the influence of individual fault planes and large-scale rock mass heterogeneities such as fault zones on the rock mass response, the monitoring data were analyzed on two different scales: (1) on the fracture-scale, and (2) on the tunnel-scale.

4.6.1 Rock mass response on the tunnel-scale

4.6.1.1 General displacement pattern

Monitoring data derived from the geodetic and the laser scanning surveys were utilized to examine the short-term rock mass response on the tunnel-scale. The general displacement pattern along the mine-by section is best represented by displacement vector plots derived from geodetic measurements (Figure 4-4). Longitudinal displacements along the NE and SW-sidewall show that displacement vector orientations are significantly influenced by the pronounced bedding planes and the frequently occurring bedding-parallel faults, which both dip moderately into the direction of tunnel advance. Displacement vectors are generally oriented sub-perpendicular to bedding which corresponds with the direction of the higher deformability of the Opalinus Clay. Measurements from the lower sidewall prisms generally indicate heaving normal to bedding pointing into the direction of tunnel advance, while the upper sidewall and crown prisms show the opposite behavior with settlements normal to bedding pointing against the direction of tunnel advance (Figure 4-4). This general displacement pattern is altered by the occurrence of minor and major fault zones along the mine-by section. Displacement magnitudes adjacent to fault zones are larger and across fault zones generally smaller. The displacement vector orientation, however, is not significantly affected by smaller fault zones that are oriented parallel to bedding.

Even though the general displacement vector orientation in the longitudinal direction is only marginally influenced by bedding-parallel faults zones, minor and major fault zones have a distinct influence on the radial displacement pattern, in particular in the regions preceding and following these structures. This is illustrated by selected cross-sectional vector plots along the experimental section shown in Figure 4-4. Radial displacements measured at GM 119.9 (Figure 4-4c) represent the general cross-sectional displacement pattern relatively unaffected by rock mass heterogeneities. As expected for the given in-situ stress state, displacements at both sidewalls are slightly larger than at the crown (i.e. zones with highest tangential stresses). Upper sidewall and crown prisms indicate a settlement of the rock mass, while the lower sidewall prisms indicate heaving. In the vicinity of the major fault zone at GM 107.4 (Figure 4-4d) displacements at the sidewalls and at the crown are substantially larger. Furthermore, displacement vectors at the sidewall indicate a tendency towards a horizontal vector orientation. The influence of isolated tectonic fault planes oblique to bedding on the displacement field is illustrated in Figure 4-4e. Sub-horizontal fault planes encountered in the lower NE-sidewall led to

comparatively larger radial displacement at this location. Similar observations were made for sub-horizontal faults at the lower sidewalls between GM 95 and GM 98, as well as for moderately SW-dipping faults at the upper NE-sidewall between GM 99 and GM 102. These measurements indicate that non bedding-parallel fault planes alter the displacement field in terms of displacement vector magnitude and orientation.

4.6.1.2 *Integration of geodetic and laser scanner measurements*

Integration of geodetic and laser scanning measurements allows the quantification of the excavation-induced displacement pattern with a high temporal (geodetic survey) and spatial (laser scanning survey) resolution. It is important to note, that the geodetic measurements capture all three components of the displacement vector and allow for tracking the entire three-dimensional vector path of each monitoring point, while laser scanning measurements only capture the relative displacement in the direction normal to the tipping axis of the laser scanner (height of the tipping axis is 1.3 m above the tunnel invert). For a direct comparison of the two data sets, geodetic displacements were evaluated with respect to the tipping axis of the laser scanner. Derived displacement magnitudes are presented in Figure 4-5 together with the differential maps derived from laser scanning measurements. Displacement maps are consistent in both, the displacement magnitudes and the overall displacement pattern. For the laser scanning survey measured displacements throughout the excavation of the mine-by section ranged from -50 mm to 50 mm. Negative values (red to yellow) show displacements towards the tipping axis of the scanner, positive values (light blue to blue) away from it, and turquoise values represent zero displacement. Note that the apparent positive values result from breakouts (Figure 4-6) and excavated material (i.e. reshaped tunnel profile). Both, geodetic and laser scanner measurements show that the most pronounced displacements occur at the sidewalls and at the crown (Figure 4-5). In the following, the vertical and horizontal components of the displacement vectors were individually analyzed to distinguish between the rock mass response at the sidewalls where tectonic structures are oriented perpendicular to the tunnel axis (i.e. in the plane of isotropy) and at the crown, where the same structures are oriented oblique to the tunnel axis (i.e. oblique to the plane of isotropy).

4.6.1.3 *Rock mass response at the tunnel crown*

Figure 4-7 shows the spatial distribution of cumulative vertical displacement magnitudes along the mine-by section with an unwrapped contour line plot. Positive values (green to blue) indicate heaving, negative values (green to red) settlement of the rock mass. The traces of the single fault planes and the fault zones in the overlaid geological map are extrapolated from the sidewall maps, and thus their location is somewhat uncertain at the tunnel crown (indicated by dashed lines). The largest vertical displacements were measured at the crown adjacent to minor and major fault zones, in particular between GM 95 - 99 and between GM 105 - 110 (Figure 4-7). These two zones were both associated with structural-driven slab formation which resulted in displacement magnitudes up to 45 mm. Figure 4-6b shows that the slab between GM 105 - 110 was detached along locally occurring pre-existing SW-dipping fault planes and buckled due to gravity. Minor crown instabilities related to pre-existing structures and spalling phenomena were also observed at GM 110.5 (Figure 4-6c) and GM 118.5 (Figure 4-6d), respectively. Displacement

magnitudes and locations of these crown instabilities are consistent with the laser scanning measurements (Figure 4-5). In contrast to these structurally-controlled instabilities, stress-driven breakouts at the crown predominantly form close to the tunnel face where induced stresses are significantly increased due to the sharp tunnel geometry. The most pronounced stress-induced breakout occurred at the tunnel crown between GM 113 - 114.5 and formed between the geodetic prisms (Figure 4-6a). Thus, the breakout was only captured by the laser scanner measurements (Figure 4-5). In tunnel sections which were not affected by crown instabilities both, geodetic and the laser scanner measurements indicate crown settlements between 5 and 10 mm.

4.6.1.4 *Rock mass response at the tunnel sidewalls*

In Figure 4-8 the distribution of the cumulative horizontal (i.e. normal to the tunnel axis) displacement magnitudes are presented. Positive and negative values denote both horizontal displacements towards the tunnel, however, due to the utilized sign convention displacement vectors point in the opposite direction for the NE and SW-sidewall (see Section 4.5.1 for sign convention used in this study). The geodetic displacement map is overlain by the structural map of the mine-by section to allow for a spatial correlation of the measured displacement pattern with the geological structures (i.e. faults, fault zones, EDZ fractures). Displacements in Figure 4-8 show a consistent pattern on both sidewalls between GM 95 - 115 with relatively uniform displacement magnitudes ranging between 10 - 20 mm (yellowish to orange regions). The uniform pattern suggests that the displacements are not significantly affected by the intersecting geological structures. However, increased displacements ranging between 20 - 40 mm (reddish regions) mainly occur in the vicinity of minor and major fault zones. Field observations during the excavation of the mine-by section revealed that these displacements are associated with the development of major sidewall spalls which were most pronounced adjacent to the encountered fault zones. It was further observed that these sidewall spalls were sharply bounded and internally intersected by pre-existing faults and/or newly formed EDZ fractures. High resolution (resolution cell size of 2 mm) differential displacement maps were able to identify shear displacements along discrete fractures that can be correlated with mapped EDZ fractures and tectonic fault planes (Figure 4-9). However, in the sidewalls shearing along fault planes was only observed at the major spalls, suggesting that this failure behavior can be associated with secondary fracturing which contributes to the formation of the major sidewall spalls.

Figure 4-10 presents a series of cumulative horizontal displacement maps showing the spatial and temporal evolution of the major spalls on both sidewalls as a function of distance to the advancing tunnel face. The data suggest that the vertical extent of the spalls developed rapidly approximately half a tunnel diameter (i.e. 2.5 m) behind the tunnel face. The vertical extent on the SW-sidewall is slightly higher and consistent with the inclined in-situ stress field. The propagation of the spalls in the longitudinal direction, however, is related to the step-wise advance of the tunnel face. As shown in the displacement plot in Figure 4-8 the longitudinal spall propagation was finally arrested at the major fault zone and thus at the transition to the more deformable rock mass.

4.6.2 Rock mass response on the fracture-scale

4.6.2.1 Rock mass response below the tunnel invert

The deformation behavior of the tunnel invert throughout and after the excavation of the mine-by experiment was derived from repeated TRIVEC measurements in borehole BRC-1 (Figure 4-3). These data were combined with the results from OPTV and core logging to identify the influence of individual pre-existing tectonic faults and excavation-induced fractures on the resulting rock mass deformations below the tunnel invert. Throughout the excavation of the mine-by experiment between April 22nd and June 2nd 2008 a total of 21 repeat measurements were conducted with the TRIVEC. The resulting incremental and cumulative displacement profiles are shown in Figure 4-11 and are presented for the directions parallel and perpendicular to the gallery axis, and for the vertical direction (i.e. along the borehole axis).

Distinct peaks in the incremental displacement profiles which progressively increase with time, indicate localized differential displacements across pre-existing and excavation-induced fractures. In these intervals horizontal displacements parallel to the tunnel axis are generally larger than displacements perpendicular to it and consistently trend into the direction of the excavation advance. Vertical displacements consistently indicate extension for all measuring intervals, whereby largest displacement magnitudes were measured across discrete tectonic and induced fractures. The uppermost 1.8 m which are intersected by several EDZ fractures with multiple orientations, is too complex to associate dislocations to specific fractures. However, the differential displacements at 3.5 m depth are associated with two distinct SSE-dipping fault planes (Figure 4-12). For this interval incremental horizontal displacements of 1.5 mm and 0.7 mm were measured parallel and perpendicular to the tunnel axis, and a vertical extension of 0.6 mm (Figure 4-11). The three components were combined to obtain the magnitude and orientation of the relative displacement across the SSE-dipping faults. The normal and shear components of the dislocation resolved across these planes revealed a predominant opening-mode component with a minor shear component with the hanging wall moving down-dip with respect to the footwall. Measuring intervals that were not intersected by discontinuities revealed no evidence of differential displacements. The same deformation behavior can also be deduced from the cumulative displacement patterns shown in Figure 4-11.

Figure 4-12 shows the temporal evolution of the cumulative vertical displacements for each individual measuring interval throughout the excavation of the mine-by experiment. Cumulative vertical displacements indicate a total invert heave of 2.4 mm. However, it must be noted that the bottom of the borehole cannot be considered as stable, and accurate measurements of the borehole top are not available. Thus, measured displacements can only be interpreted in relation to each other and integrated displacements indicate a lower limit of the measurable deformations. Excavation of the first two round lengths (i.e. from GM 94.5 - 98) revealed similar heaving rates of 0.1 - 0.2 mm/day for all measuring intervals, except of the uppermost which revealed a constant heaving rate of approximately 0.03 mm/day throughout the entire excavation phase. During the excavation of the remaining part of the mine-by section ongoing vertical deformations were limited to measuring intervals across natural and induced fractures, indicating a discrete block displacement related to localized deformations. Figure 4-13 shows the vertical displacement patterns derived from two repeated surveys conducted

241 and 312 days after the reference measurement in comparison with the measurements taken at the end of the excavation phase (i.e. 42 days after the reference measurement). Cumulative vertical displacements indicate a total invert heave of 6.8 and 7.3 mm, respectively, with considerable heaving magnitudes within the uppermost 4 m. The magnitude of the cumulative vertical displacement for this borehole section was 4.9 and 5.3 mm, respectively, and thus contribute substantially (up to 72%) to the total invert heaving. In contrast to the excavation phase, measuring intervals 2 and 3, which are both not intersected by natural faults show a considerable cumulative interval heaving between 2 - 3 mm (Figure 4-13).

In the context of a long-term heaving project (MH experiment), the Swiss Federal Office of Topography (Swisstopo) performed high resolution invert leveling measurements along the entire Gallery 08 during and after its construction. Figure 4-14 shows the measured invert heaves derived from Swisstopo in comparison with the cumulative vertical displacements derived from the TRIVEC measurements. Note that the measuring time-intervals are slightly different for the TRIVEC and geodetic measurements (indicated in Figure 4-14) since the measuring campaigns were not consistently performed on the same dates. The integrated vertical displacements along the TRIVEC (i.e. a total length of 7 m) was 7.3 mm, which is consistent with geodetic measured heaving magnitudes of 7.2 mm and 6.3 mm at GM 79.5 and GM 111.1, respectively. However, there is a large discrepancy between the measuring points located ahead of GM 41.2 and behind GM 111.1. At GM 9.6 and GM 25.9 the axis of the Gallery 08 runs sub-parallel to bedding strike and invert heave magnitudes are considerably smaller than for the measuring points located along the straight section of Gallery 08 which runs perpendicular to bedding strike. This suggests a substantial influence of the orientation of the bedding (and subsequently the development of the EDZ) on the long-term heave of the tunnel invert. The substantially increased invert heave magnitudes at GM 116.3 and GM 119.6 are most probably associated with their location in respect to the major fault zone which intersects the tunnel invert between GM 114 and GM 118. Since the entire Gallery 08 was excavated with a consistent excavation procedure by using a roadheader, local discrepancies in heaving magnitudes are solely related to the variations in tectonic fault plane densities and the tunnel direction in respect to the bedding plane orientation.

4.6.2.2 Rock mass response along the tunnel sidewall

The deformation behavior of the rock mass along the NE-sidewall throughout and after the excavation of the mine-by experiment was derived from continuous extensometer and deflectometer measurements in borehole BRC-2 (Figure 4-3). Extensometer data presented in Figure 4-15 are shown in terms of incremental and cumulative longitudinal strains of the individual measuring intervals recorded at the end of the excavation phase (06.06.2008) and 31 month later at the end of the measuring period (31.05.2011). Contractive strain is denoted as positive and extensional strain as negative. Deflectometer data are presented as cumulative changes in inclination (i.e. mm/m) along each measuring interval (interval lengths of 1.5 and 3 m) during and after the excavation phase. Figure 4-16 shows the horizontal changes in inclination and Figure 4-17 the vertical changes in inclination along the borehole axis. For both figures a schematic of the deflectometer configuration prior to and after the excavation of the mine-by section illustrates the general horizontal and vertical deformation pattern. Negative changes in

inclination denote a deformation of the deflectometer casing towards the tunnel in the horizontal plane, and downward directed deformations in the vertical plane.

Both, incremental and cumulative longitudinal strains show significant variations in strain magnitudes and strain distribution along the borehole BRC-2, which correlate with variations in the fault plane density (Figure 4-15). In borehole sections with a fault plane density < 2 faults per meter longitudinal strains tend to be extensional, while in borehole sections with a higher fault plane density longitudinal strains are contractive. To illustrate this trend, longitudinal strains in Figure 4-15 are colored red if the measured strains are extensional, and green if they are contractive. Complementary, deflectometer data revealed that the largest changes in inclinations and thus the largest horizontal and vertical differential deformations along the borehole BRC-2 occurred across minor and major fault zones (Figure 4-16 and Figure 4-17). In between the fault zones, deflectometer measurements indicate no or only marginal differential deformations thus indicating that individual fault planes are only of minor relevance for the deformation behavior at greater depths. In the first 8 m of the borehole, which corresponds to a radial distance of 1.3 - 2.5 m to the tunnel contour, cumulative strains consistently show an extensional behavior, even though the borehole is intersected by a minor fault zone at 3.5 m depth (Figure 4-15). Similar to the extensometer data, the deflectometer response indicated increased horizontal deformations to the same borehole depth. Assuming that this deformation behavior is related to the formation of the EDZ, these findings suggest a minimum radial EDZ extent of approximately 2 - 3 m at the NE-sidewall.

Both, extensometer and deflectometer data indicate that the largest deformations occurred during the excavation phase. Long-term time series of inclination changes for the horizontal (Figure 4-16) and the vertical (Figure 4-17) direction revealed only marginal differential deformations during the open drift phase. These were consistently associated with minor or major fault zones or can be related to the ongoing formation of the EDZ within the first 8 m of the borehole. The same tendency can be observed in the longitudinal strain measurements (Figure 4-15b) where the magnitudes recorded at the end of the measuring period (i.e. 31 month after the excavation phase) are only marginal larger than at the end of the excavation phase. Except for the first 2 m of the borehole where the extensometer reflects the radial deformations towards the start niche (Figure 4-15).

4.6.2.3 *Rock mass response around the advancing tunnel face*

Longitudinal strain, and cumulative vertical and horizontal inclination changes measured in borehole BRC-2 are shown in Figure 4-18 relative to the position of the actual tunnel face. A negative face position denotes the distance ahead of the tunnel face, a positive face position denotes the distance behind the tunnel face. As shown in Figure 4-18a axial strains were consistently initiated 1 - 2 tunnel diameters ahead of the tunnel face and stabilized at approximately $\frac{1}{2}$ - 1 tunnel diameter behind the tunnel face, except for interval 27. This interval is located within the major fault zone and shows an ongoing shortening but with a decreased rate over the measurement time. Measuring intervals located within or across strongly faulted zones generally show a slight extension ahead of the face and considerable contraction when the tunnel faces passes their location (Figure 4-18a). Measuring intervals in less faulted borehole sections (< 2 faults/m) consistently show extensional behavior ahead of the face and slightly contractive behavior approximately half a tunnel diameter behind the tunnel face (Figure 4-18a).

Vertical and horizontal inclination changes were consistently initiated 1 and $\frac{1}{2}$ tunnel diameter, respectively, ahead of the face. In the horizontal direction, inclination changes are most pronounced within one tunnel diameter behind the tunnel face (Figure 4-18b). This is in contrast to vertical inclination changes which primarily occurred ahead of the tunnel face. This discrepancy in the deformation behavior around the tunnel face can be explained by the transversal isotropic behavior of the Opalinus Clay. In longitudinal and vertical measuring direction (both approximately 45° inclined to the mean orientation of the bedding and the bedding-parallel faults and fault zones) the rock mass is more deformable than in the radial direction parallel to the bedding. Thus significant deformations towards the tunnel are substantially controlled by the advancing tunnel face and the resulting kinematic freedom of minor and major fault zones.

4.7 Comparison between short and long-term rock mass response around the mine-by experiment

Continuous borehole monitoring provided a unique opportunity to analyze the deformation behavior associated with the excavation advance and the time-dependent deformations that occurred after the excavation of the mine-by experiment. Depending on the borehole location around the tunnel circumference and depending on the borehole direction in respect to the orientation of the rock mass anisotropy, borehole instrumentations showed a substantially different deformation behavior during the excavation and the open drift phase.

Interpreting the short and long-term rock mass response of the tunnel sidewall measured by the deflectometer and the extensometer is challenging because the borehole axis is oriented sub-parallel to the tunnel axis (i.e. deviation of 8°), thus the radial distance of both borehole monitoring devices to the tunnel alignment linearly increases from 1.3 m at the heads of the instruments up to 4.6 m at the ends of them. Due to the increase in radial distance to the tunnel contour, rock mechanical processes might be different along the borehole axis and thus cannot be directly compared. Within the first 8 meters of the borehole, both deflectometer and extensometer data measured an extensional rock mass behavior that indicates enhanced deformations towards the start niche and the tunnel. Assuming that this deformation behavior is related to the formation of the initial EDZ, these findings suggest a minimum radial EDZ extent of approximately 2 - 3 m at the NE-sidewall. The borehole data indicate that beyond this depth individual fault planes have a limited impact on the short-term rock mass response and thus are of minor relevance at depth. The overall radial displacement characteristics, instead, is mainly controlled by minor or major fault zones associated with weaker and more deformable mechanical properties, and particularly by their boundary zones which accommodate the largest differential deformations during the excavation phase. This is in contrast to the rock mass response captured at the excavation surfaces where measured displacement magnitudes are largest adjacent to fault zones and generally smaller across fault zones. It is suggested that heterogeneities in rock mass deformability, caused by the fault zones, substantially alter the homogeneity of induced stresses with considerable stress concentrations in the stiffer rock mass adjacent to the fault zones. These stress concentrations appear to trigger extensional fracture processes leading to large radial deformations, when the strength of the rock mass is exceeded approximately half a tunnel diameter behind the advancing tunnel face. These findings

suggest that large-scale deformability heterogeneities have a substantially different effect on the short-term deformation behavior at depth and at the excavation surfaces. In contrast to the short-term deformation behavior, long-term monitoring data from both the extensometer and deflectometer indicated that differential longitudinal, horizontal and vertical deformations are nearly negligible in the long-term, except of the borehole section that is located within the EDZ of the niche and the tunnel (i.e. the first 8 borehole meters). For this section ongoing deformations were measured, whereby radial deformations towards the niche (i.e. in the direction oblique to the rock anisotropy) are significantly larger than deformations towards the tunnel (i.e. in the direction parallel to the rock anisotropy). These findings suggest that the long-term differential deformations radial to the tunnel (i.e. in the plane of isotropy) are limited to the EDZ, but are of minor relevance deeper in the rock mass, even though the rock mass is considerably heterogeneous along the tunnel axis.

TRIVEC measurements in borehole BRC-1 revealed that tectonic faults which are oriented parallel to the intact rock anisotropy have a substantial influence on the short-term deformation behavior below the tunnel invert. Monitoring results showed that measuring intervals which were intersected by tectonic faults indicated substantial larger heaving rates, thus resulting in larger vertical displacements during the excavation phase. This observation implies that short-term deformations below the tunnel invert are primarily accommodated by individual tectonic fault planes thus resulting in a characteristic block movement. However, in the long-term, significant deformations (i.e. up to 70% of the total vertical displacement) are limited to the uppermost 4 meters where the borehole was not intersected by tectonic faults and thus are most probably related to hydro-mechanically-coupled processes associated with newly formed EDZ fractures. These findings suggest that the depth range where long-term deformations occur is to a certain extent influenced by the initial deformation characteristics associated with the rock mass perturbations that were induced by the excavation process, while pre-existing fault planes appear to become less relevant. It is suggested that the contrasting long-term behavior of the uppermost 4 meters is associated with different geomechanical processes. While the short-term deformation behavior is mainly associated with the stress redistribution as a consequence of tunneling, it is assumed that in the long-term the tunnel invert is primarily affected by clay mineral swelling. The latter process is supported by swelling laboratory tests conducted by Voegtli and Bossart (1999). Their results showed significant anisotropic swelling behavior with higher swelling pressures (i.e. up to 2 MPa) and swelling heaves normal to bedding which is in agreement with a displacement vector orientation perpendicular to bedding in the uppermost 4 meters. The anticipated swelling behavior in the open drift phase is also supported by the observed time-dependent cracking of the invert slab along galleries at the Mont Terri URL. Long-term heaving magnitudes derived from the TRIVEC are in general agreement with high resolution invert leveling measurements in tunnel sections with a similar structural setting (i.e. similar fault plane density) and a similar orientation of the geological structures (i.e. bedding and fault planes) with respect to the tunnel axis. Thus, it is suggested that the locally observed long and short-term deformation behavior below the tunnel invert can be well quantified by the TRIVEC measurements, and the results valid for extrapolating to the tunnel-scale.

Due to a tunnel direction which is perpendicular to bedding strike and 45 degrees inclined in respect to the bedding orientation, the overall short-term behavior observed

at the tunnel invert might be very similar to the short-term behavior at the tunnel crown. Differences in the behavior are to be anticipated, primarily due to gravitational effects at the tunnel crown and the influence of the flat tunnel invert on the redistributed stress field. However, field observations during the excavation of the mine-by section revealed that minor and major crown instabilities are often associated with structural-driven slab formation along pre-existing tectonic fault planes which slowly detached from the surrounding rock mass with the advance of the tunnel face. These observations suggest that individual fault planes at the crown decisively influence the short-term rock mass response on the tunnel-scale.

Although not specifically captured with geodetic and laser scanning measurements, short-term deformations at the tunnel face were nonetheless evident in terms of fault and bedding plane reactivation and associated structural related face instabilities. At the tunnel face small to medium sized blocks detached along steeply inclined EDZ fractures that formed as consequence of excavation-induced shearing along bedding and fault planes.

4.8 Summary and conclusions

Excavation-induced displacements and deformations around a tunnel in faulted Opalinus Clay at the Mont Terri URL in Switzerland were analyzed on the fracture and the tunnel-scale to assess the influence of pre-existing faults and fault zones on the short and long-term rock mass response. Displacements and deformations were continuously monitored throughout the excavation of the mine-by experiment and after its construction using borehole inclinometer, extensometers and deflectometer as well as high resolution geodetic and laser scanning measurements. Displacement monitoring data revealed that the overall rock mass response of faulted Opalinus Clay is mainly controlled by the intact rock anisotropy due to the pronounced bedding. Displacement vectors consistently showed a preferred orientation sub-perpendicular to bedding planes thereby indicating heaving at the lower sidewalls and below the tunnel invert and settlements at the crown and the upper sidewalls. Pre-existing tectonic faults and their spatial variations along the tunnel axis significantly modify the general surface displacement field in magnitude, but also in direction depending on their orientation relative to the tunnel direction. The spatial and temporal evolution of the displacement pattern around the mine-by section is thereby substantially governed by both the kinematic behavior of single fault planes and the overall rock mass behavior as consequence of large-scale deformability and strength heterogeneities along the tunnel axis. Along the experimental section these heterogeneities were primary caused by minor and major bedding-parallel fault zones. Integration of the deformation measurements considering both the fracture and the tunnel-scale revealed that individual fault planes were most influential on the rock mass response at the tunnel face, crown and the invert, but were less influential in the sidewalls and at larger depths in the rock mass. At the sidewalls, where fault plane reactivation was of minor relevance due to their unfavorable orientation, the rock mass response in the tunnel near-field was dominated by extensional fracturing through the intact rock matrix resulting in large displacements adjacent to large-scale rock mass heterogeneities. This failure behavior was associated with the formation of slab-like structures approximately half a tunnel diameter behind the advancing tunnel face which decisively affected the tunnel stability.

Continuous borehole monitoring provided a unique opportunity to analyze the deformation behavior associated with the excavation advance and the time-dependent deformations that occurred after the excavation of the mine-by experiment. Depending on the borehole location around the tunnel circumference and depending on the borehole direction in respect to the orientation of the rock mass anisotropy, borehole instrumentations showed a substantially different deformation behavior during the excavation and the open drift phase. Deflectometer and the extensometer measurements at the sidewall revealed that the long-term rock mass deformations were extremely small compared to the deformations during the excavation advance. The monitoring data further showed that the short-term rock mass response parallel to the rock mass anisotropy is significantly governed by differential deformations along minor and major fault zones, while for the long-term response these large-scale heterogeneities are only of minor importance. TRIVEC measurements, however, revealed that long-term deformations below the tunnel exceeded the deformations that were measured during the excavation phase by far, in particular in the vertical direction oblique to the rock mass anisotropy. Furthermore, the long-term response of the tunnel invert appears to be strongly affected by the extent of the initial EDZ that formed during the excavation phase and thus by the orientation of the primary structures relative to the tunnel excavation.

4.9 References

- Amann F, Button EA, Evans KF, Gischig VS, Bluemel M (2011) Experimental study of the brittle behavior of clay shale in rapid unconfined compression. *Rock Mech Rock Eng* 44: 415-430
- Bluemling P, Bernier F, Lebon P, Martin CD (2007) The excavation damaged zone in clay formations: Time-dependent behaviour and influence on performance assessment. *Physics and Chemistry of the Earth* 32: 588-599
- Freivogel M, Huggenberger P (2003) Modellierung bilanzierter Profile im Gebiet Mont Terri - La Croix (Kanton Jura). In: Heitzmann P, Tripet J-P, editors. Reports of the Federal Office for Water and Geology, Switzerland
- Keller M (2008) Mont Terri - RC experiment. Instrumentation report. Unpublished Mont Terri Technical Note 2008-34, Mont Terri Project, Switzerland
- Kistler M (2008) RC Experiment: 1. - 3. Messkampagne. Unpublished report, Swisstopo, Switzerland
- Kistler M (2009) RC/MH Experiment: 4. Messkampagne. Unpublished report, Swisstopo, Switzerland
- Marschall P, Distinguin M, Shao H, Bossart P, Enachescu C, Trick T (2006) Creation and evolution of damage zones around a microtunnel in a claystone formation of the Swiss Jura Mountains. Proceedings of the 2006 SPE International Symposium and Exhibition on Formation Damage Control, Lafayette, Society of Petroleum Engineers, USA
- Martin CD, Lanyon GW (2003) Measurement of in-situ stress in weak rocks at Mont Terri Rock Laboratory, Switzerland. *Int J Rock Mech Min Sci* 40: 1077-1088

- Nussbaum C, Wileveau Y, Bossart P, Moeri A, Armand G (2007) Why are the geometries of the EDZ fracture networks different in the Mont Terri and Meuse/Haute-Marne Rock Laboratories? Structural Approach, Clays In Natural & Engineered Barriers For Radiactive Waste Confinement, Lille, France
- Nussbaum C, Bossart P (2008) Geology. In P. Bossart & M. Thury (Eds.), Mont Terri Rock Laboratory. Project, programme 1996 to 2007 and results. Geological report No. 3, Swiss Geological Survey, Switzerland
- Nussbaum C, Bossart P, Amann F, Aubourg C (2011) Analysis of tectonic structures and excavation induced fractures in the Opalinus Clay, Mont Terri underground rock laboratory (Switzerland). *Swiss J Geosci* 104: 187-210
- Schuetz S (2009a) RC experiment: Convergence measurements in Gallery 98 and 08 during excavation of RC section. Unpublished Mont Terri Technical Note 2008-50, Mont Terri Project, Switzerland
- Schuetz S (2009b) RC experiment: Laser scanning in Gallery 08 during excavation of RC section. Unpublished Mont Terri Technical Note 2008-64, Mont Terri Project, Switzerland
- Thoeny R (2014) Geomechanical analysis of excavation-induced rock mass behavior of faulted Opalinus Clay at the Mont Terri Underground Rock Laboratory (Switzerland). PhD thesis, Department of Earth Sciences, ETH Zurich, Switzerland
- Thury M, Bossart P (1999) Results of the hydrogeological, geochemical and geotechnical experiments performed in the Opalinus Clay (1996-1997). Geological report No. 23, Swiss Geological Survey, Switzerland
- Voegtli B, Bossart P (1999) Swelling experiments (DS). Mont Terri Rock Laboratory, Results of the hydrogeological, geochemical and geotechnical experiments performed in 1996 and 1997, *Geol. Rep. Swiss natl. hydrol. Geol. Surv.* 23, Switzerland
- Wild K (2010) Charakterisierung des Verhaltens von Opalinuston unter Zugbeanspruchung. BSc thesis, Department of Earth Sciences, ETH Zurich, Switzerland
- Wymann L (2013) The influence of saturation on the uniaxial compressive strength of Opalinus Clay. MSc thesis, Department of Earth Sciences, ETH Zurich, Switzerland
- Yong S (2008) A three-dimensional analysis of excavation-induced perturbations in the Opalinus Clay at the Mont Terri Rock Laboratory. PhD thesis, Department of Earth Sciences, ETH Zurich, Switzerland

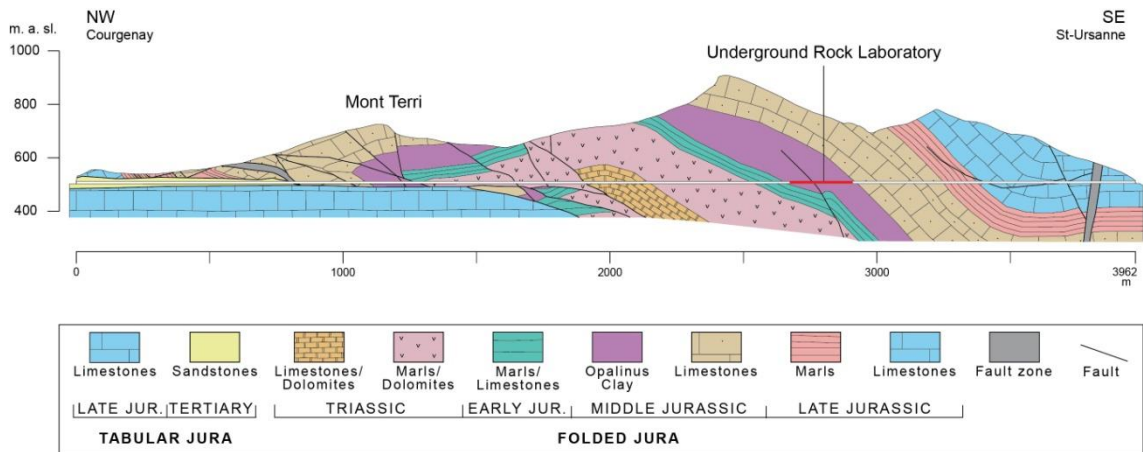


Figure 4-1: Geological cross-section along the Mont Terri motorway tunnel (from Freivogel & Huggenberger 2003). The rock laboratory is located in the southeastern limb of the Mont Terri anticline in the Opalinus Clay formation at a depth of 250 - 320 m.

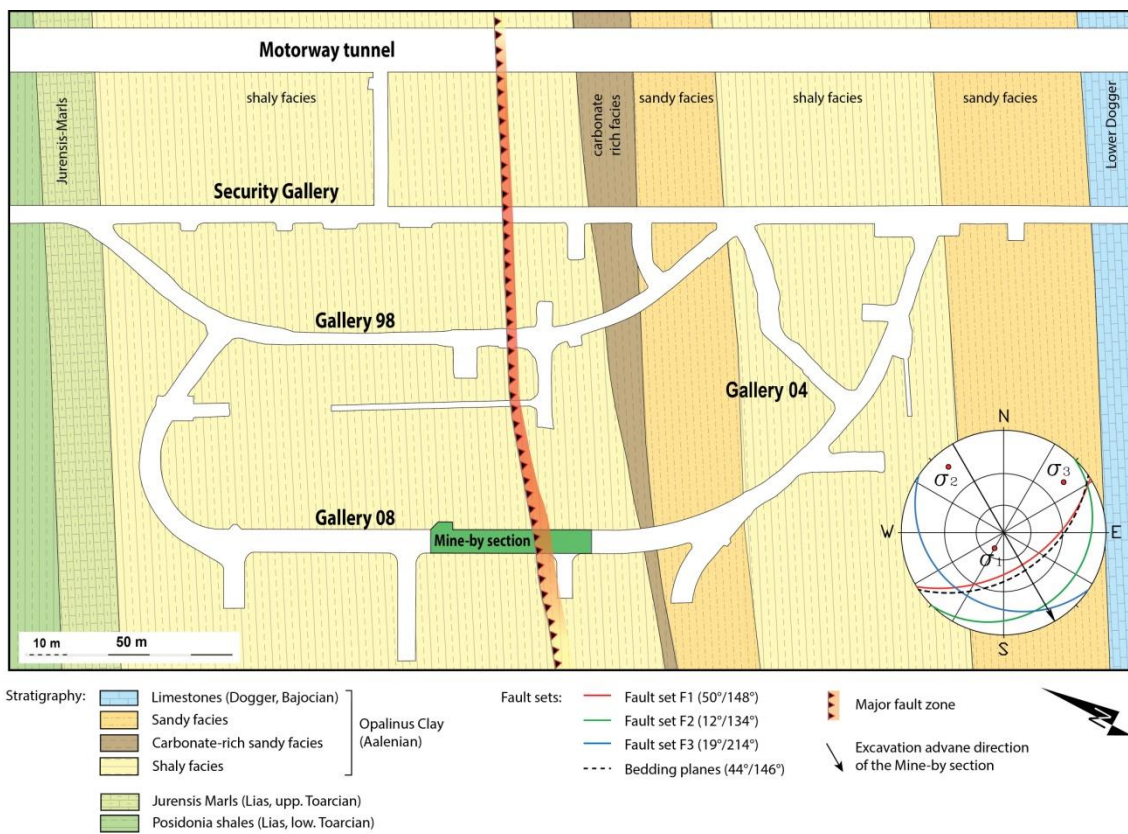


Figure 4-2: Structural map of the Mont Terri Underground Rock Laboratory (modified from Nussbaum et al. 2011), showing the various galleries and niches. The rock laboratory is intersected by three fault sets and a major fault zone. The mean orientation of the pronounced bedding and the three fault sets encountered within the mine-by section are shown in a lower hemisphere projection. The mine-by section, which was used to examine the influence of multi-scale tectonic faults on the rock mass response, is highlighted in green and entirely located within the shaly facies of the Opalinus Clay.

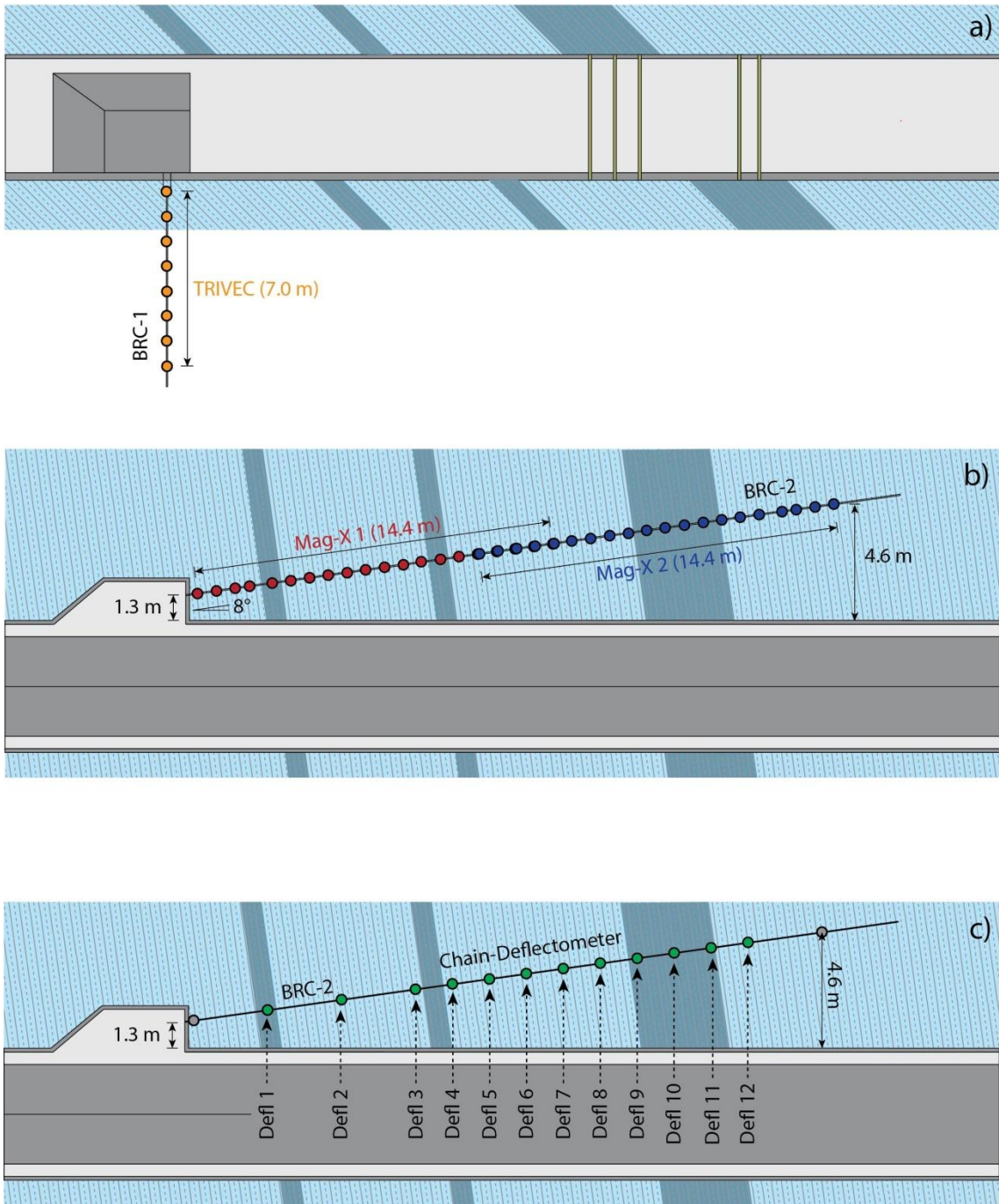


Figure 4-3: Layout and borehole instrumentation of the mine-by experiment including a) a borehole inclinometer, b) two Magnet-Extensometers, and c) a Chain-Deflectometer.

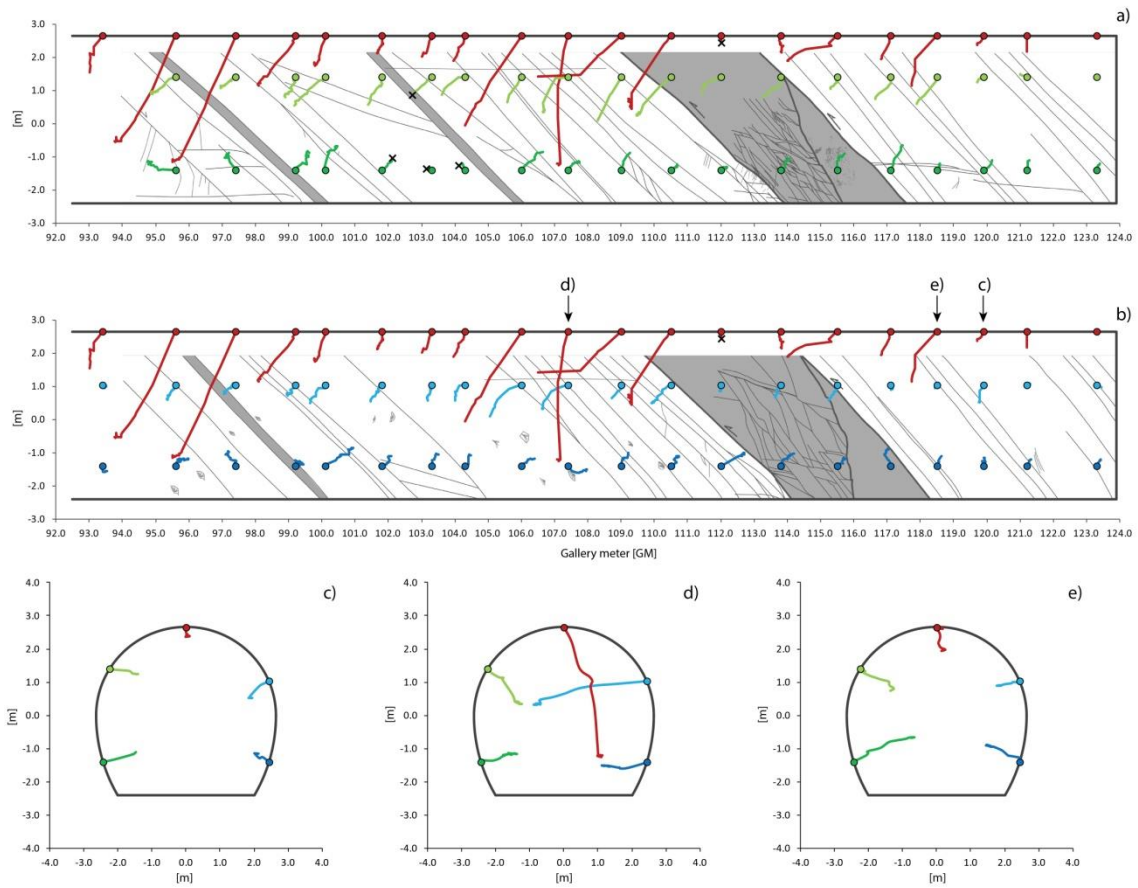


Figure 4-4: Displacement vector plots derived from the geodetic measurements showing the short-term displacement pattern throughout the excavation of the mine-by section. Longitudinal displacements along a) the NE-sidewall and b) the SW-sidewall showing the general displacement pattern altered by the occurrence of minor and major fault zones along the mine-by section. Radial displacements representative for c) the general displacement pattern, d) the displacement pattern in the vicinity of a major fault zone, and e) the influence of sub-horizontal faults. Displacement magnitudes for all plots are scaled 1:10 relative to the size of the tunnel.

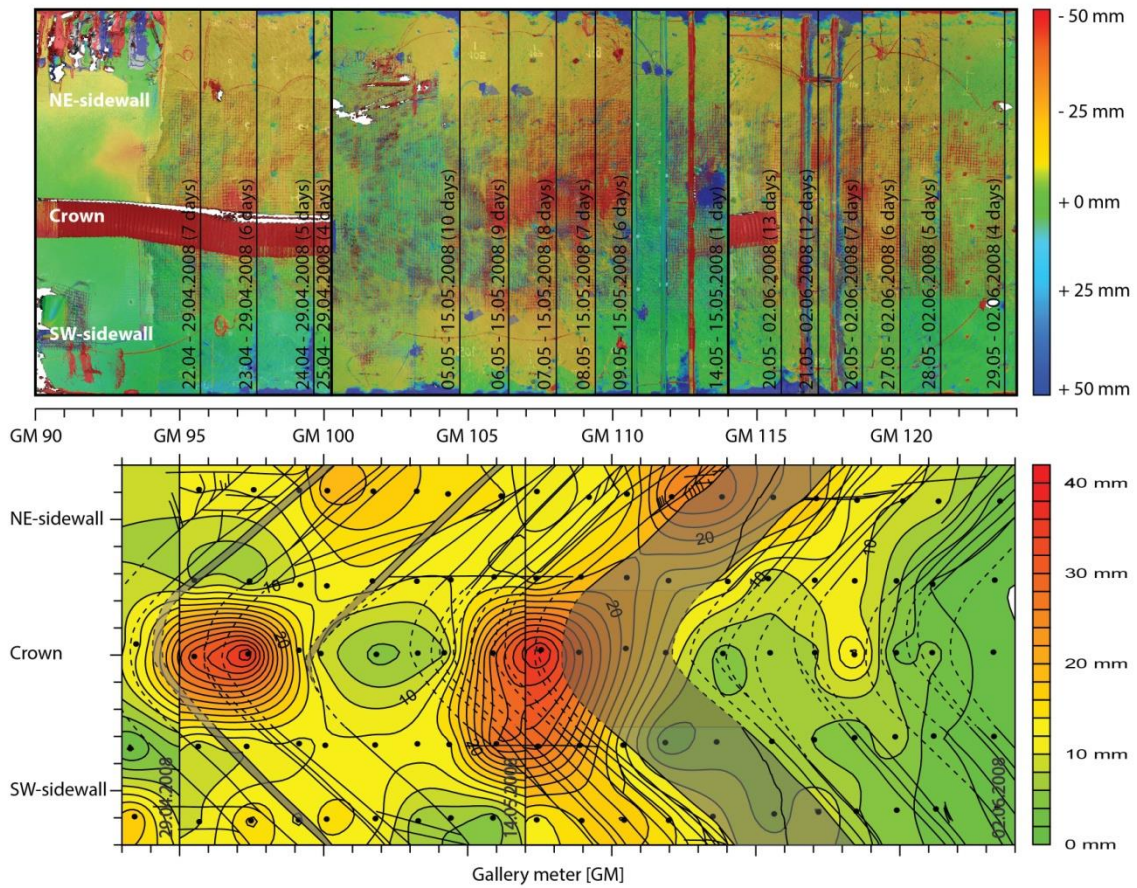


Figure 4-5: Comparison between differential displacements derived from laser scanning measurements (at the top) and relative displacements derived from geodetic measurements (at the bottom) throughout the excavation of the mine-by experiment. Note, that the displacements in both maps are measured in the direction normal to the tipping axis of the laser scanner (1.3 m above the tunnel invert). Overlaid geological structures were derived from geological sidewall mapping throughout the excavation and consists of pre-existing faults and fault zones (shown in black) and EDZ fractures (shown in grey).

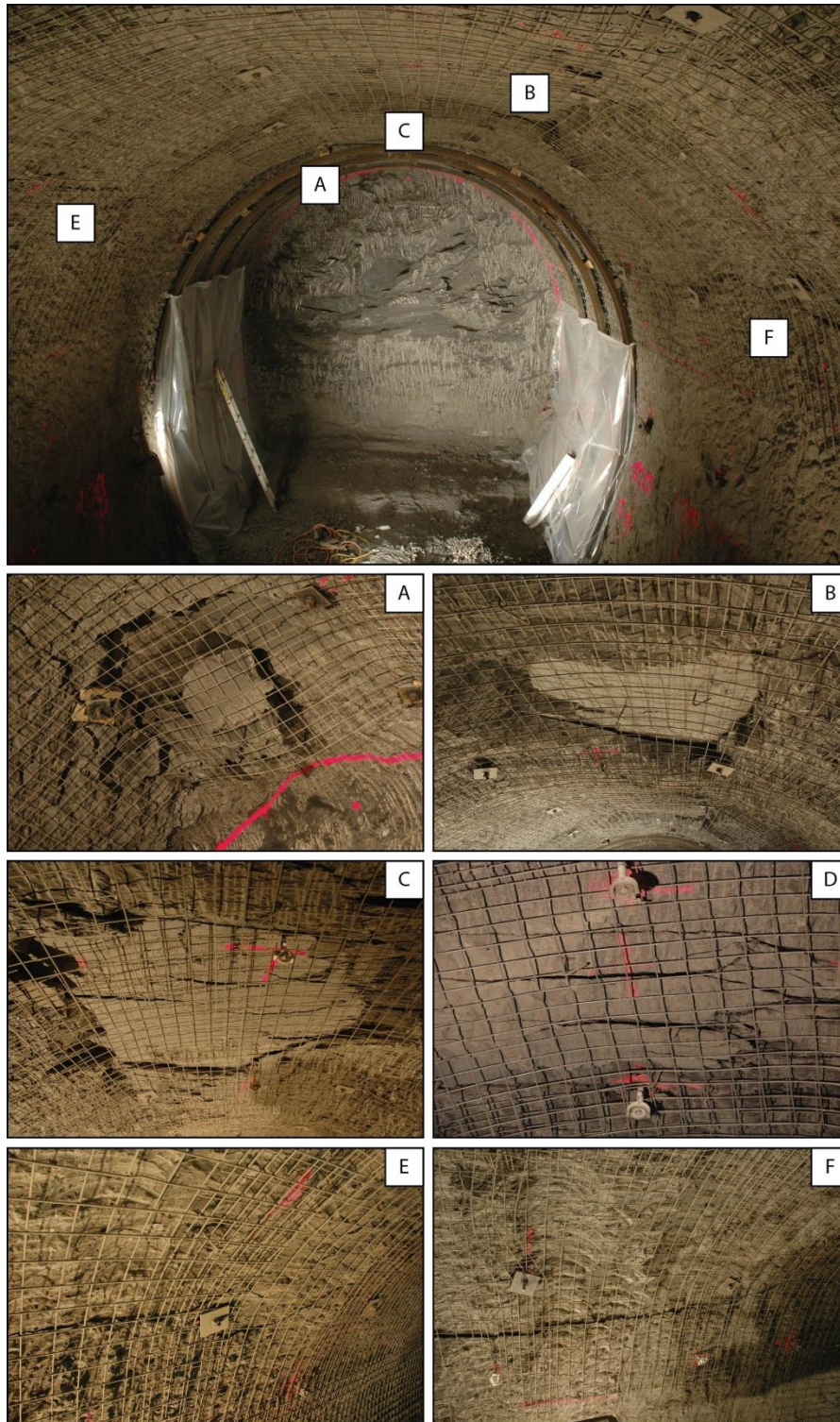


Figure 4-6: Observed failure mechanisms of the rock mass throughout the excavation of the mine-by section leading to minor and major tunnel instabilities. (A) Stress-induced breakout at the tunnel crown. (B) Slab at the crown (GM 106 - 108) that progressively detached along a SW-dipping fault plane leading to settlements up to 45 mm. (C) Structural-controlled crown instability between GM 109 - 112. (D) Locally disintegrated rock mass at GM 118.5. Upper discrete boundary of the sidewall spalls on the (E) NE-sidewall and (F) on the SW-sidewall between GM 102 - 109. The upper sidewall prisms located on the spalls indicating horizontal displacements up to 40 mm.

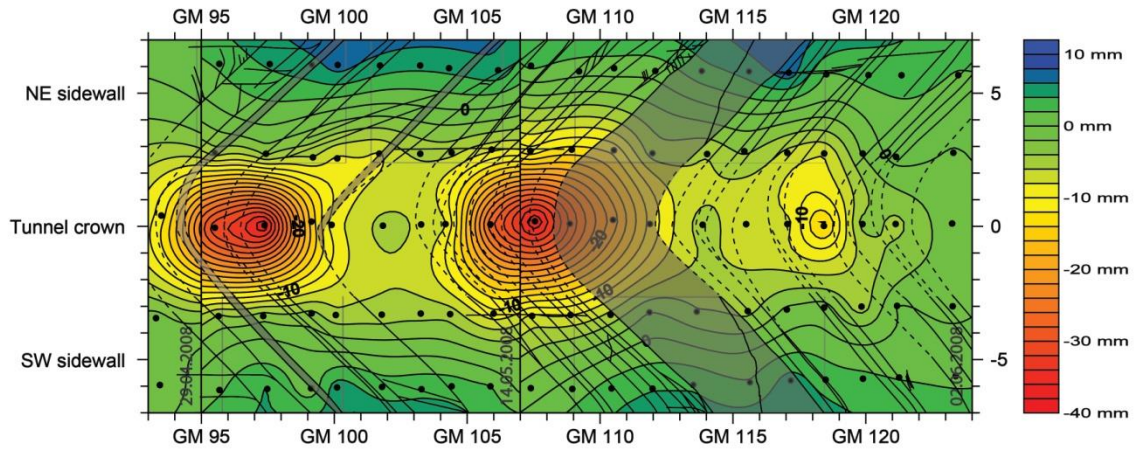


Figure 4-7: Geodetic displacement map showing the cumulative vertical displacement magnitudes along the mine-by section when the tunnel face was located at GM 124. Positive values (green to blue) indicate heaving, negative values (green to red) settlement of the rock mass. Overlaid geological structures were derived from geological sidewall mapping throughout the excavation and consists of pre-existing faults and fault zones (shown in black) and EDZ fractures (shown in grey).

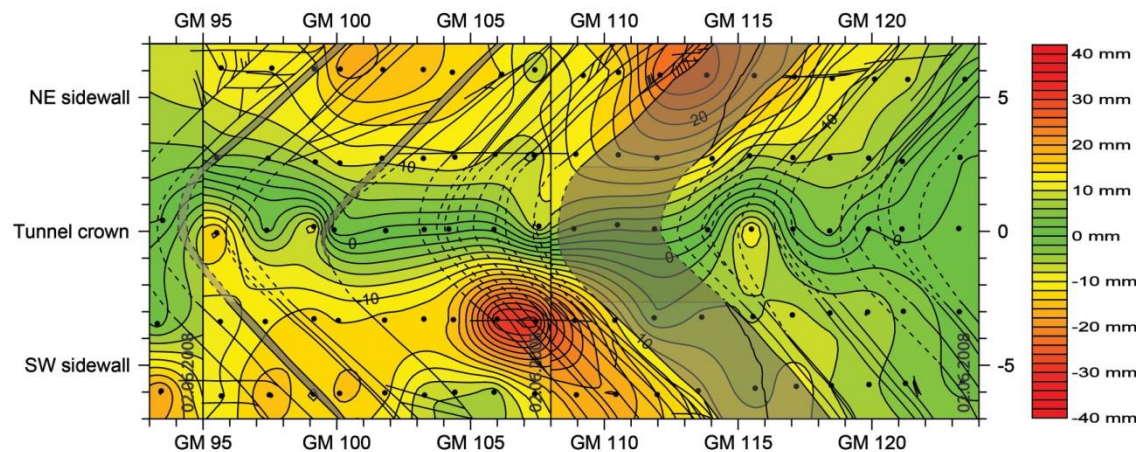


Figure 4-8: Geodetic displacement map showing the cumulative horizontal displacement magnitudes along the mine-by section when the tunnel face was located at GM 124. Overlaid geological structures were derived from geological sidewall mapping throughout the excavation and consists of pre-existing faults and fault zones (shown in black) and EDZ fractures (shown in grey). Zones with horizontal displacements ranging between 10 - 40 mm can be attributed to the formation of major sidewall spalls during the excavation of the mine-by section.

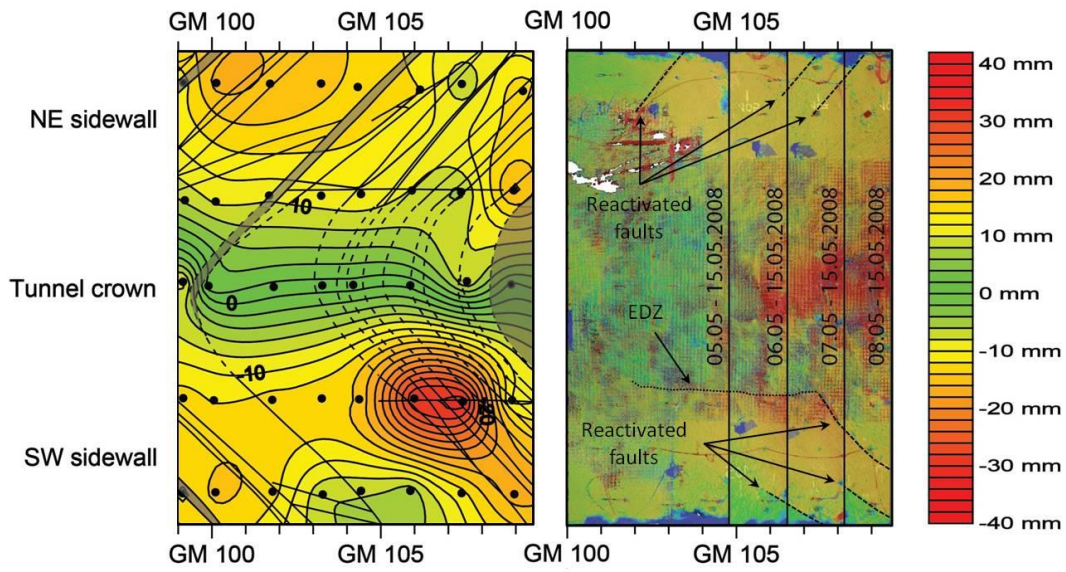


Figure 4-9: Fault plane reactivation associated with the formation of major sidewall spalls. Magnitude distribution of horizontal displacement vector magnitudes are shown on the left, and differential displacements derived from the laser scanner measurements are shown on the right.

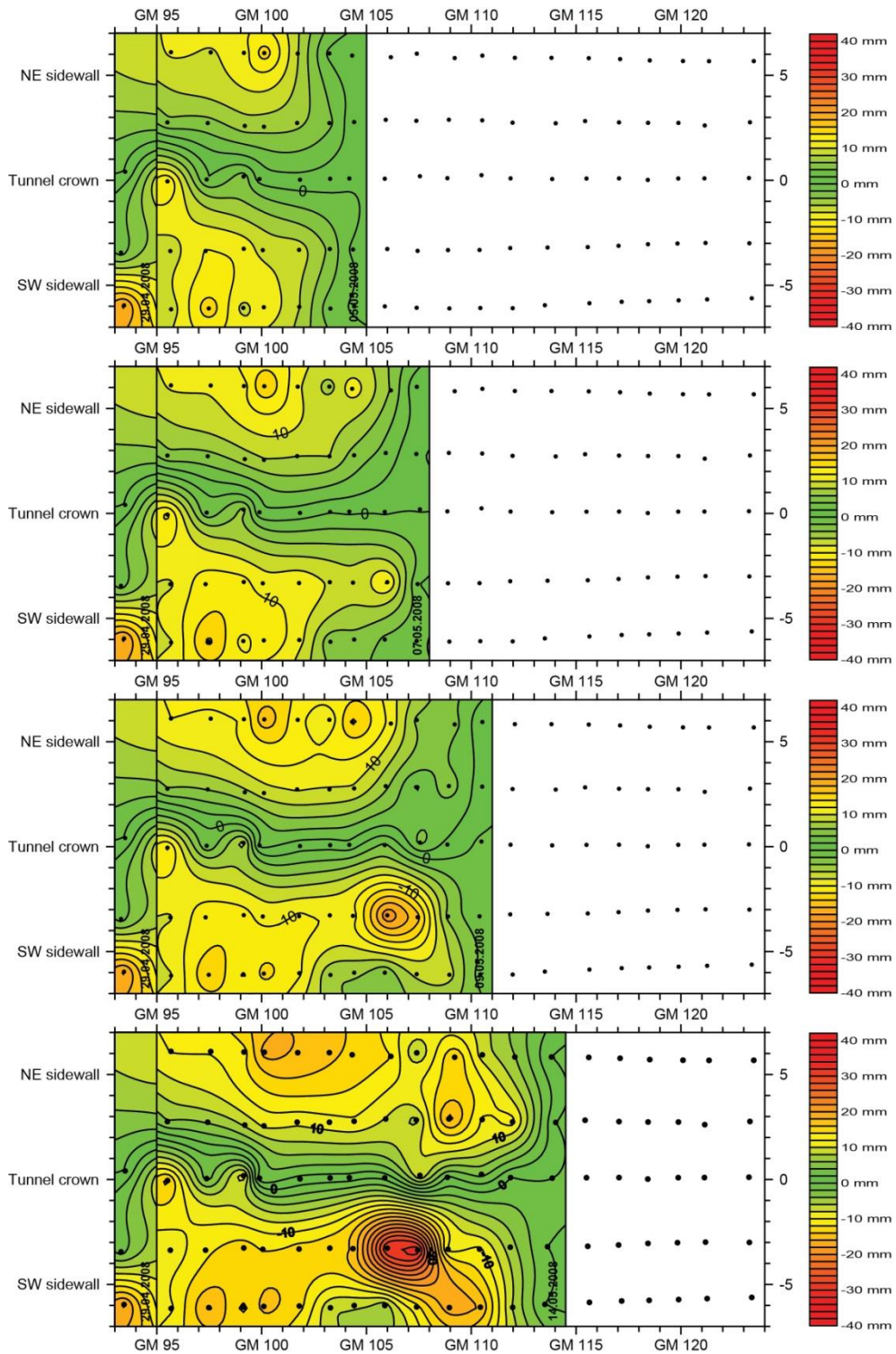


Figure 4-10: Cumulative horizontal displacement components derived from geodetic measurements showing the evolution of sidewall spalls on both sidewalls approximately half to one tunnel diameter behind the advancing tunnel face.

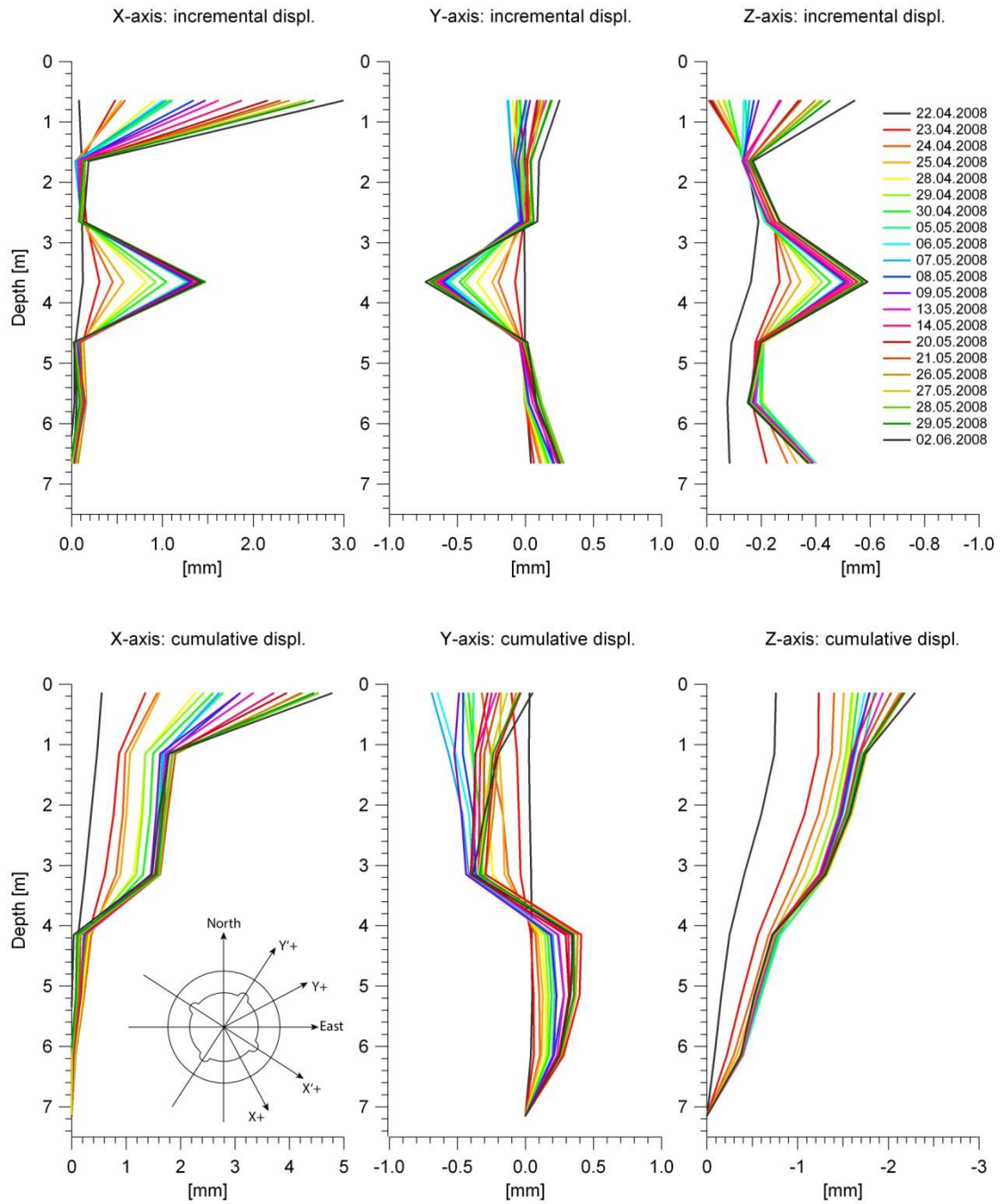


Figure 4-11: Incremental and cumulative displacements derived from the TRIVEC measurements in borehole BRC-1 throughout the excavation of the mine-by section.

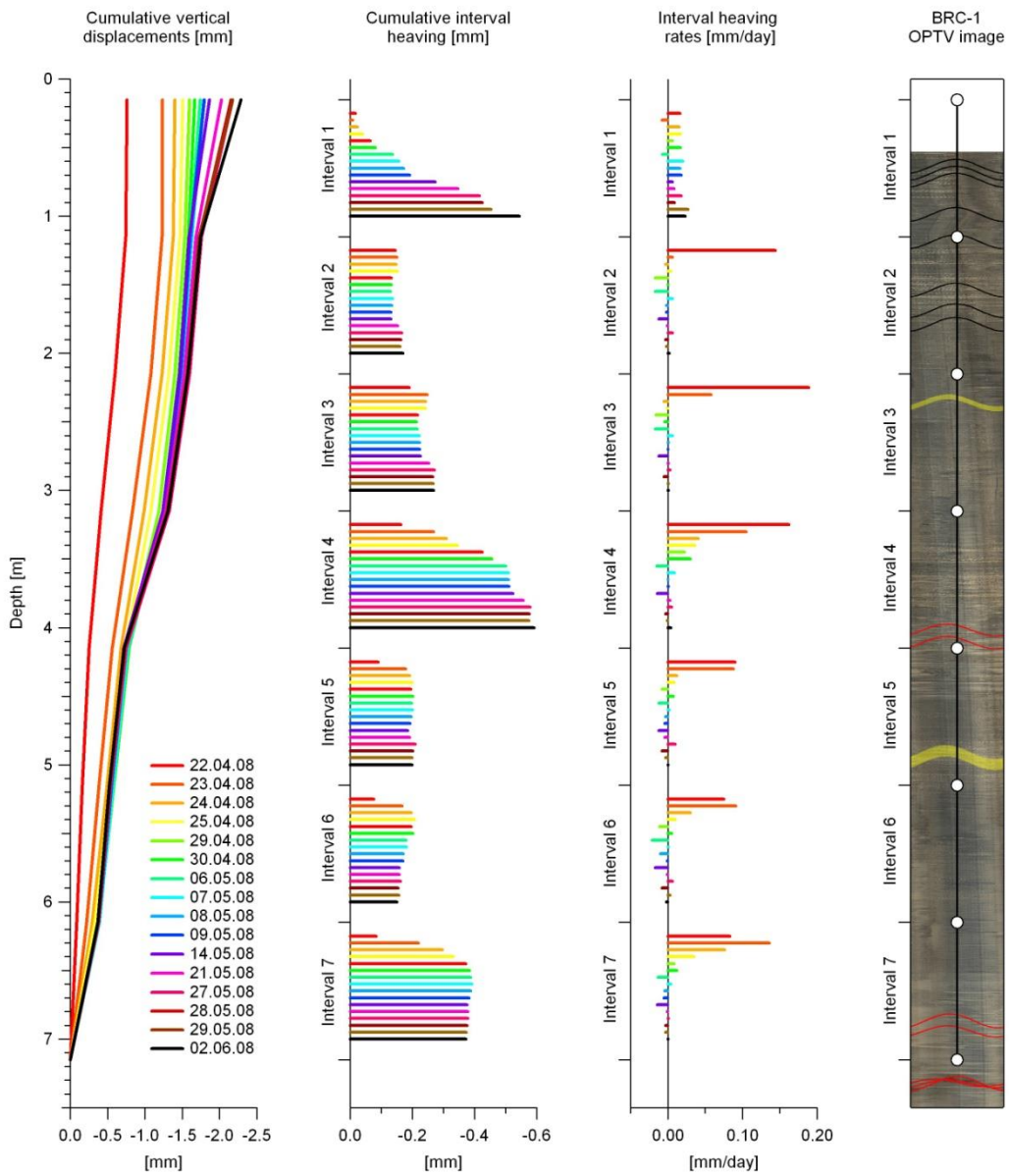


Figure 4-12: Temporal and spatial evolution of the invert heaving during the excavation of the mine-by experiment. Cumulative vertical displacements are presented together with the cumulative interval heaving and the corresponding interval heaving rates of each individual measuring interval. Geological structures such as tectonic faults (red), EDZ fractures (black) and sandy layers (yellow) are shown on the unwrapped OPTV image of the borehole wall.

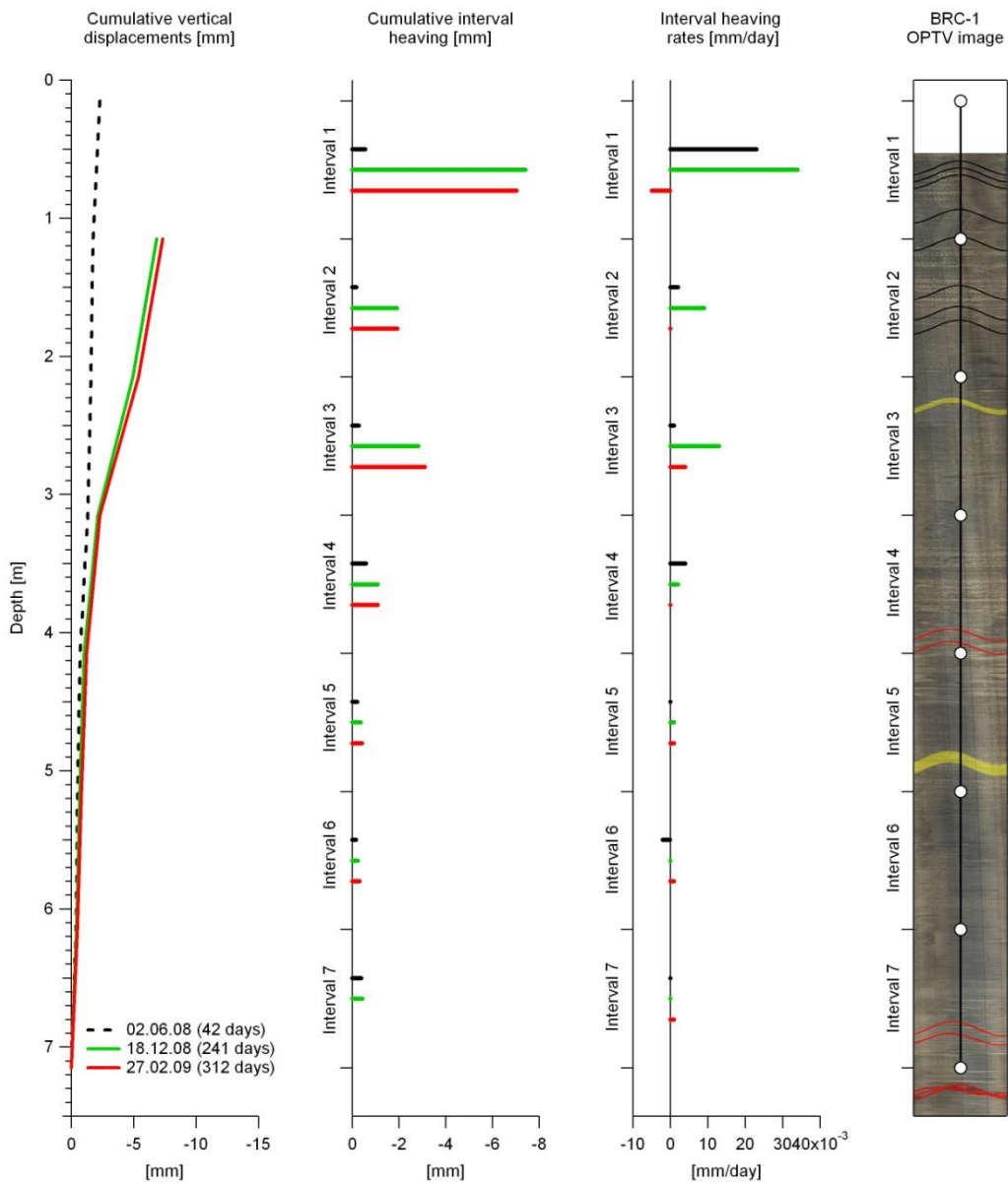


Figure 4-13: Temporal and spatial evolution of the invert heaving after the excavation of the mine-by experiment. Cumulative vertical displacements are presented together with the cumulative interval heaving and the corresponding interval heaving rates of each individual measuring interval. Geological structures such as tectonic faults (red), EDZ fractures (black) and sandy layers (yellow) are shown on the unwrapped OPTV image of the borehole wall.

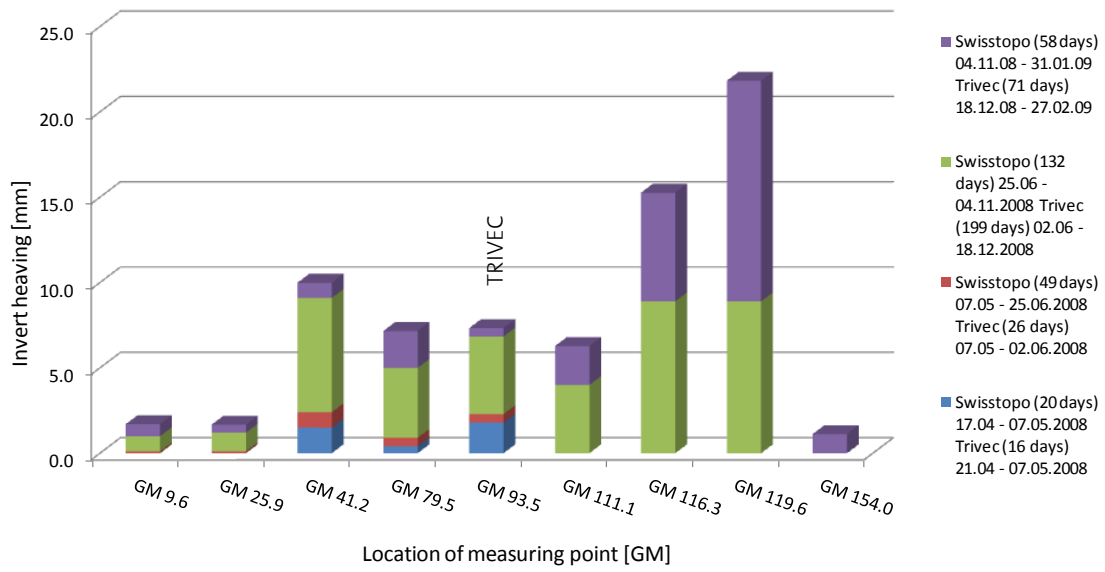


Figure 4-14: Measured invert heaving (i.e. vertical displacement component) along the Gallery 08 in comparison with the integrated vertical displacements derived from the TRIVEC measurement. Three measuring campaigns were conducted by Swisstopo between April and June 2008 and one was performed at the end of January 2009 (Kistler 2008, 2009).

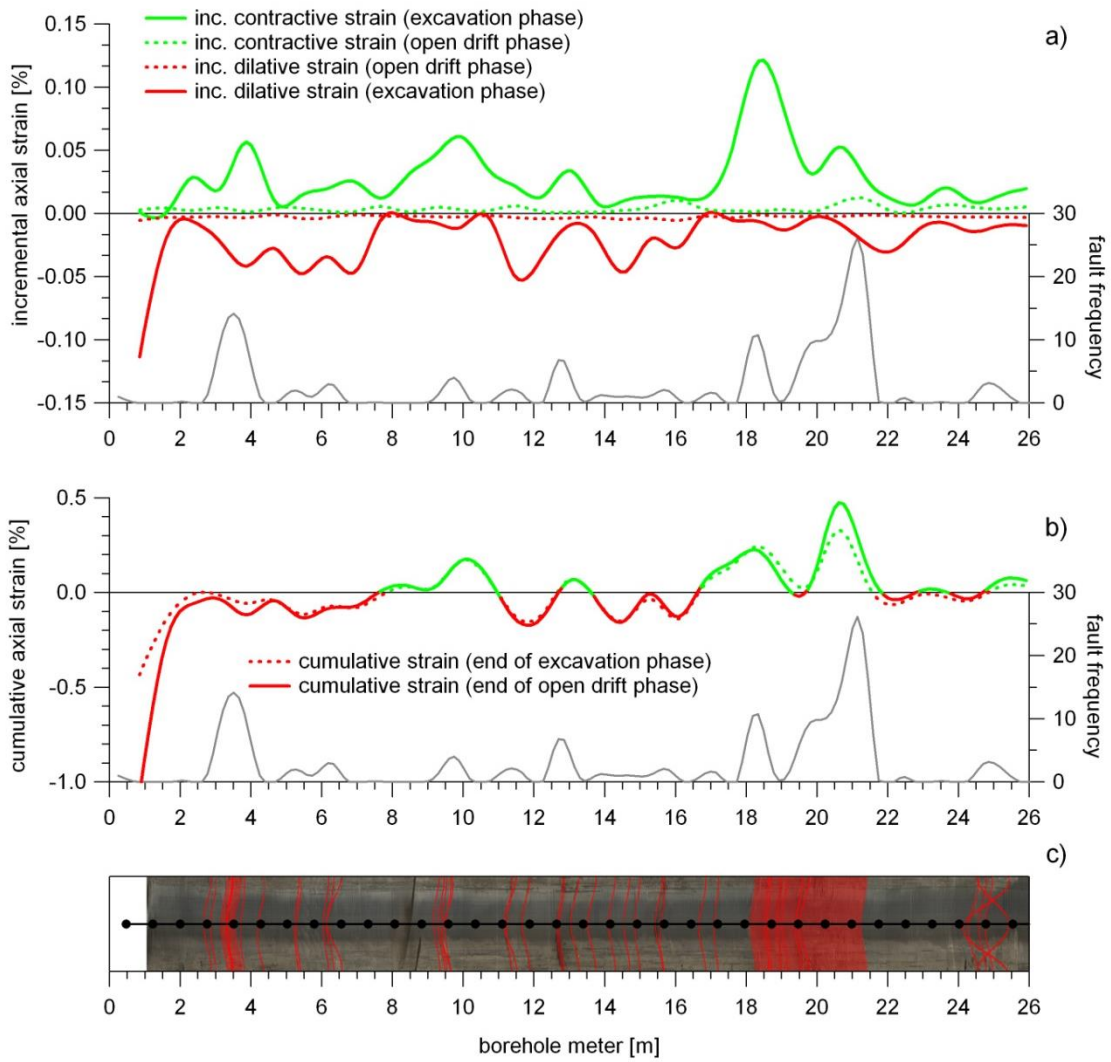


Figure 4-15: Longitudinal deformations along the borehole BRC-2 presented as a) incremental and b) cumulative axial strains derived from extensometer measurements. The fault frequency shown in c) was established by interval logging with an interval length of 0.5 m.

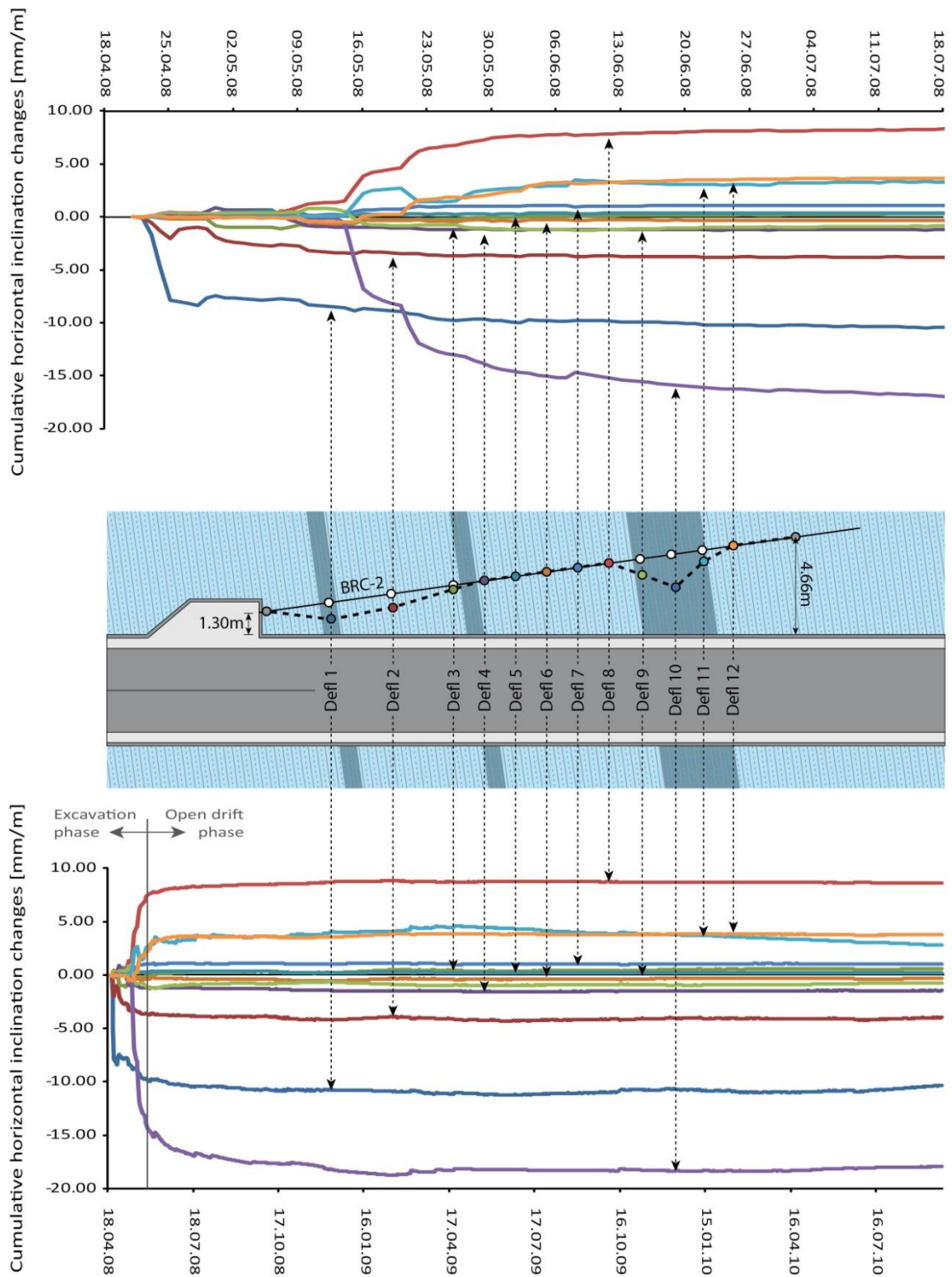


Figure 4-16: Horizontal deformations derived from deflectometer measurements in borehole BRC-2. Deformations presented as cumulative inclination changes are shown for the excavation phase at the top and for the entire measuring period from April 2008 to December 2010 at the bottom. A sketch of the deflectometer illustrates the initial configuration (solid line with white markers) and the configuration after the construction of the mine-by section (dashed line with color-coded markers).

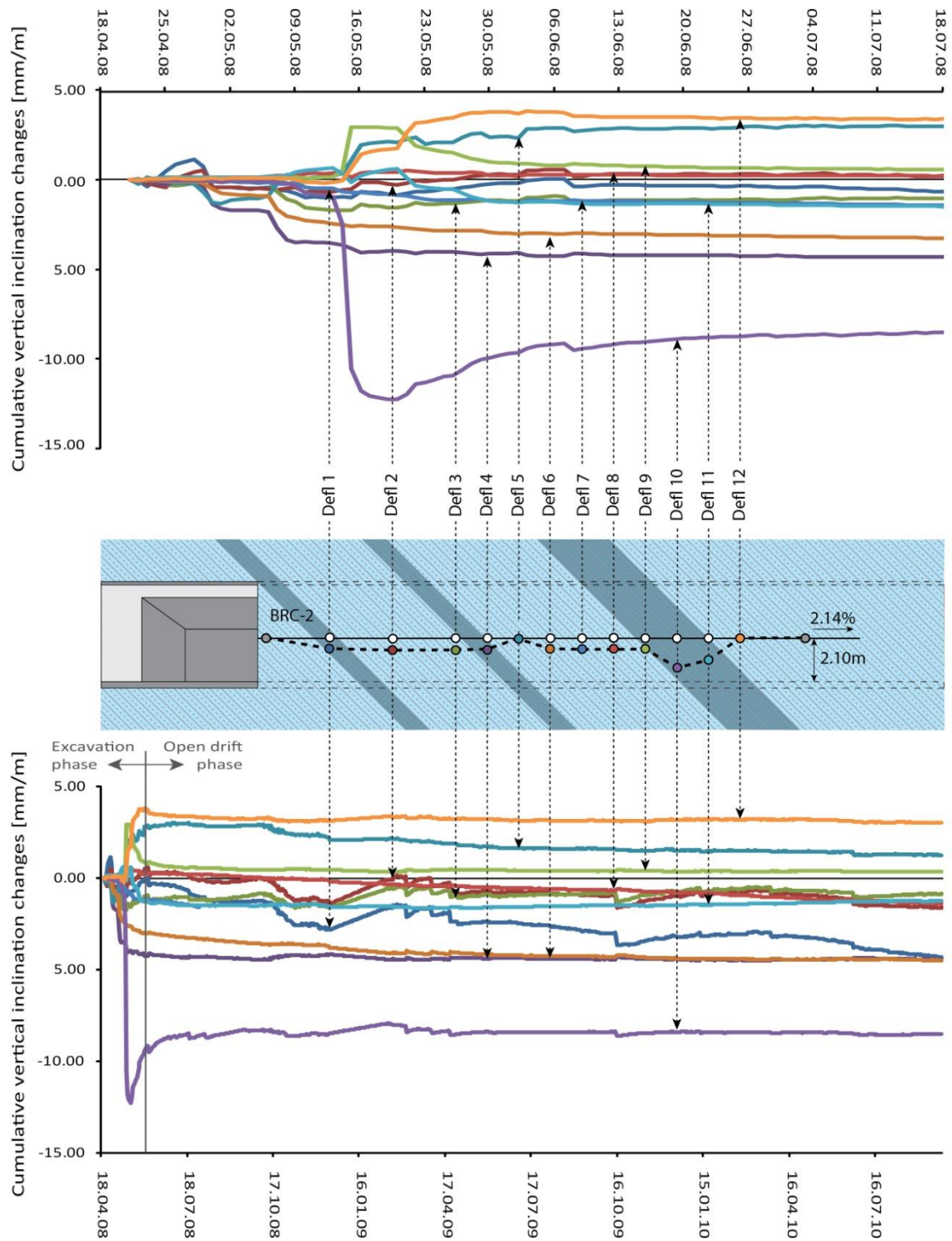


Figure 4-17: Vertical deformations derived from deflectometer measurements in borehole BRC-2. Deformations presented as cumulative inclination changes are shown for the excavation phase at the top and for the entire measuring period from April 2008 to December 2010 at the bottom. A sketch of the deflectometer illustrates the initial configuration (solid line with white markers) and the configuration after the construction of the mine-by section (dashed line with color-coded markers).

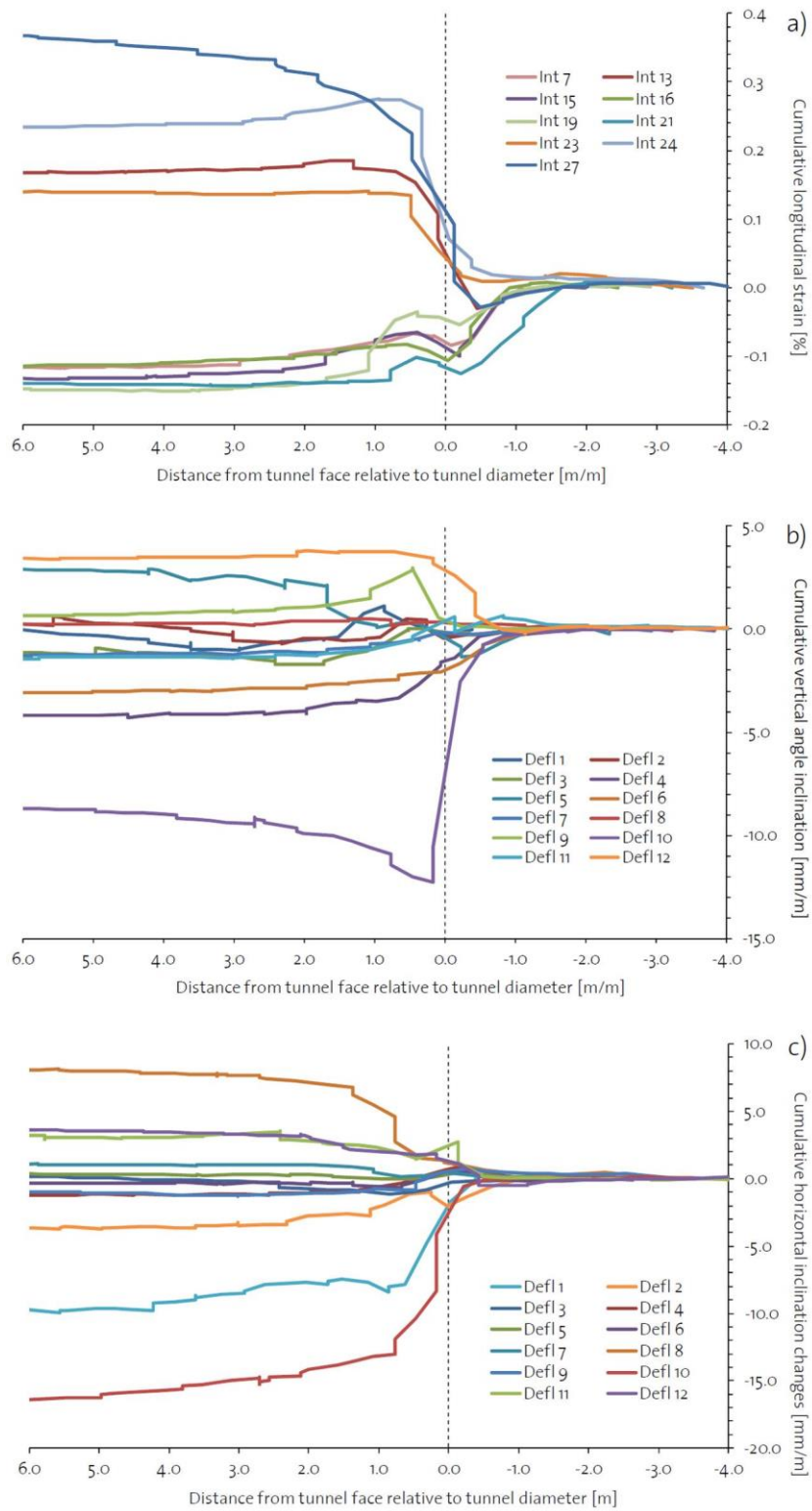


Figure 4-18: Rock mass deformations of the NE-sidwall with distance from the tunnel face normalized to the tunnel diameter for a) cumulative longitudinal strain derived from the extensometer, and cumulative b) vertical and c) horizontal inclination changes derived from the deflectometer.

5 EFFECTS OF DEFORMABILITY AND STRENGTH HETEROGENEITIES IN FAULTED OPALINUS CLAY ON THE EXCAVATION-INDUCED STRESS REDISTRIBUTION AND ASSOCIATED ROCK MASS BEHAVIOR

Abstract

A full-scale mine-by experiment was conducted at the Mont Terri Underground Rock Laboratory (URL) in Switzerland to investigate the influence of deformability and strength heterogeneities on the excavation-induced stress redistribution and associated rock mechanical processes in the near-field of an excavation in faulted Opalinus Clay. Excavation-induced stresses led to the formation of a heterogeneous excavation damage zone (EDZ) which resulted in unexpected large displacements. Structural and geological characterization of the initial EDZ revealed that the observed rock mass response is associated with extensile brittle failure processes combined with reactivation of tectonic faults and shearing along bedding planes.

Site-specific three-dimensional numerical modeling was used to examine the spatial and temporal evolution of the redistributed stress field around the mine-by section during its step-wise excavation. Initial elastic analyses revealed that heterogeneities in deformability, primary caused by multi-scale fault zones, resulted in substantial stress concentrations in the adjacent rock mass leading to an enhanced potential for induced fracturing. Elasto-plastic modeling requires considerations of both the deformability and strength heterogeneities to adequately reproduce spatial variations in EDZ depth and to reasonably capture associated displacements as observed in the field. Furthermore, elastic stress path analyses were able to adequately represent the mode of failure and the associated kinematic behavior for bedding and bedding-parallel fault planes as well as for intact rock failure. This study showed that the utilized numerical model was able to capture the short-term constitutive behavior of anisotropic and heterogeneous Opalinus Clay by using material parameters derived from conventional laboratory testing.

Key words: Numerical modeling, stress redistribution, stress path analysis, Opalinus Clay

5.1 Introduction

Clay rock formations are widely accepted as potential host rocks for deep geological disposal of nuclear waste as they inherently exhibit favorable isolation characteristics in their natural state. However, due to unfavorable rock mechanical characteristics such as a relatively low strength and a brittle failure behavior the rock mass around an excavation may exhibit substantial perturbations. Thus, construction of underground openings in clay rocks may lead to the formation of a distinct excavation damage zone (EDZ) when redistributed stresses exceed the rock mass strength in the near-field of the tunnel. Knowledge of excavation-induced stress redistribution around underground openings is crucial for understanding rock mechanical processes and associated failure mechanisms associated with tunnel excavations. Exploring the contributing factors that influence the redistributed stress field around an advancing tunnel are particularly relevant in the context of risk assessment of deep geological disposal facilities for nuclear waste in clay rock formations.

Numerous modeling studies have addressed the formation, the geometry, and the extent of the EDZ in the Opalinus Clay (OPA) around galleries, niches and boreholes using different numerical codes and constitutive models (e.g. Bluemling & Konietzky 2003; Martin et al. 2004; Corkum & Martin 2007; Te Kamp & Camusso 2009; Yong et al. 2010; Yong et al. 2013). Previous studies mainly focused on the characterization of deformations and induced failure processes around individual tunnel cross-sections. These models typically assume homogeneous and anisotropic conditions to account for the strength anisotropy due to the pronounced bedding exhibited by the Opalinus Clay. Relationships between rock mass heterogeneities and the spatial variations in induced fracturing in terms of intensity (i.e. EDZ fracture density) and changes in failure mechanisms along the tunnel axis has not been previously investigated. Thoeny (2014) conducted a large-scale mine-by experiment at the Mont Terri Underground Rock Laboratory (URL) focusing on identifying rock mechanical processes associated with deformability and strength heterogeneities associated with natural faults and fault zones and their effect on excavation-induced fracturing in faulted Opalinus Clay. His findings indicate substantial variations in the EDZ fracture density and fracture orientation, the type of induced failure mechanisms, and in the EDZ extent along the mine-by section. Further it was shown that the prevailing failure mechanism at the tunnel sidewalls is extensile brittle fracturing leading to large deformations (Thoeny 2014). At the tunnel crown, the tunnel invert and the tunnel face, reactivation of tectonic fault planes and shearing along bedding was dominant. At these locations shearing induced extensional failure perpendicular to bedding or fault planes was frequently observed and interpreted as secondary fracturing.

In this study, three-dimensional site-specific numerical modeling is combined with deformation monitoring data from the above mentioned mine-by experiment to gain insights into the role of rock mass characteristics on the EDZ development. The numerical analyses aim to explore effects of deformability and strength heterogeneities on the excavation-induced stress redistribution and associated induced fracturing in the near-field of the mine-by section. The constitutive material properties used for these numerical models were derived from conventional undrained laboratory tests. In contrast to previous studies only laboratory tests that were performed on specimens with a water content $> 6.5\%$ were used to establish elastic and plastic properties for the intact rock as well as for bedding and fault planes.

5.2 Mont Terri Underground Rock Laboratory

An instrumented in-situ experiment was conducted at the Mont Terri URL in northwestern Switzerland to investigate the rock mass response and associated rock mechanical processes to an excavation in faulted Opalinus Clay. The in-situ rock laboratory is located in the southeastern limb of the Mont Terri anticline within the Opalinus Clay formation that dips approximately 45° towards SSE at the level of the laboratory (Figure 5-1). The overburden varies between 250 to 320 m. At the Mont Terri URL, the formation can be characterized as an over-consolidated clay rock consisting of three facies: 1) the sandy facies, 2) the shaley facies and 3) the carbonate-rich facies (Thury & Bossart 1999). The mine-by experiment is located entirely within the shaley facies (Figure 5-2), which is composed of argillaceous and marly shales with intercalated cm-thick sandy layers and lenses (Nussbaum et al. 2011). The shaley facies is characterized by a porosity ranging between 12 to 18% and a natural water content between 7 and 8% (Wild 2010; Amann et al. 2011a; Wymann 2013). Within the mine-by section pronounced bedding is dipping towards SSE and dip angles are ranging between 35° and 50° (Thoeny 2014). Between GM 109 and GM 117 the mine-by section is intersected by a 2 - 3 m thick fault zone which can be traced through the entire rock laboratory (Figure 5-2). In addition to this major tectonic structure three fault sets were mapped in the mine-by section. The most frequently occurring fault set F1 is bedding-parallel dipping with 48° towards azimuth 150° . The second fault set F2 (mean dip / dip direction: $12^\circ/134^\circ$) is minor and composed of sub-horizontal faults branching from SSE dipping fault planes. Fault set F3 consists of slightly SW-dipping faults ($19^\circ/214^\circ$) and was only found in isolated regions of the mine-by section (Thoeny 2014).

Stress measurements conducted in the Mont Terri URL by Martin and Lanyon (2003) indicate a sub-vertical maximum principle stress σ_1 which is steeply inclined towards SSW and a sub-horizontal minimum principle stress σ_3 which is slightly inclined towards NE. The intermediate principle stress σ_2 is roughly aligned with the axis of the Gallery o8, trending with 10° towards NW (Figure 5-2).

5.3 Mine-by experiment

Excavation of the mine-by section was carried out concurrently with the construction of the Gallery o8, and lasted from April 22nd to June 4th 2008. The mine-by experiment is located in the straight tunnel section of Gallery o8 between GM 94.5 and GM 127 (Figure 5-2) where the gallery is intersected by a major fault zone. The mine-by section has a 5 m high horseshoe-shaped profile with a length of 32.5 m and was excavated full-face in 23 steps using a roadheader. The round length was 1.5 m on average and was carried out in a repetitive spatial and temporal sequence to ensure a consistent stress redistribution around the tunnel face. The tunnel advanced towards azimuth 152° at a down grade of approximately 2.14%, which is approximately perpendicular to the bedding strike and in the direction of bedding dip. Support measures throughout the experiment were installed immediately after each excavation round and consisted of wire mesh reinforcement (K 196) affixed on the tunnel ceiling and eight rock bolts installed approximately 0.7 m behind the advancing tunnel face. Shotcrete was not applied continuously thus allowing initial observations and monitoring of the short-term rock mass response to the excavation by geodetic and laser scanning surveys. Throughout and

after the excavation of the mine-by section additional data was gathered from pre-installed deformation monitoring devices (i.e. inclinometer, extensometer, and deflectometer) located in boreholes parallel and perpendicular to the gallery boundaries. A detailed description of the excavation procedure and the support measures, as well as the various field investigation methods applied throughout the mine-by experiment is presented in Chapter 2.

5.4 Numerical modeling of the mine-by experiment

Numerical modeling of the mine-by experiment was used to investigate the excavation-induced stress redistribution and the associated short-term rock mass response in the tunnel near-field. Particular emphasis was placed on the influence of large-scale deformability and strength heterogeneities (i.e. fault zones) on the stress redistribution and associated displacements. Tonon and Amedei (2002) found, that two-dimensional analyses of tunnel convergence behind the face are only applicable when the plane of isotropy strikes parallel to the tunnel axis. Since neither the principle stress directions nor the plane of isotropy are aligned with the tunnel axis, three-dimensional modeling is preferred. For the numerical analysis the commercial available three-dimensional continuum code FLAC3D (Fast Lagrangian Analysis of Continua in 3 Dimensions, Itasca 2009) was used which allows to simulate the elastic and plastic deformation behavior around the tunnel.

To the authors knowledge true drained properties obtained from consolidated drained tests on OPA specimens have not been determined yet. Thus, modeling of the mine-by experiment is based on a total stress approach, assuming that the short-term behavior is basically undrained during tunnel advancement (i.e. during the excavation phase). Therefore, the model does not allow for reproducing time-dependent displacements due to effective stress changes (e.g. consolidation) or physiochemical processes including mechanical swelling.

The numerical analyses were performed in two steps: 1) a purely elastic analysis using an isotropic and transversal isotropic model to investigate the influence of the rock anisotropy (due to bedding) and the rock mass heterogeneity (due to fault zones) on the stress and displacement field, and 2) an elasto-plastic analysis to quantify the effect of the redistributed stress field on the displacement magnitudes and the depth of failure (i.e. EDZ extent and geometry).

5.4.1 Model geometry

The FLAC3D model used for this study is shown in Figure 5-3. The model dimensions are 55 m in the Z-axis, 130 m in the Y-axis and 60 m in the X-axis. The vertical model axis corresponds to the Z-axis, while the horizontal Y- and X-axis are aligned parallel and perpendicular to the tunnel axis, respectively. The tunnel geometry consists of a horse-shoe shaped tunnel with a diameter of 5.3 m and a lateral niche at the beginning of the mine-by section (Figure 5-3). The distance from the tunnel contour to the lateral model boundaries is approximately 10 times the tunnel radius (2.65 m) which is sufficiently large for reducing the far-field boundary effects. The model consists of 548'528 zones with zone element sizes ranging from 0.3 m in the near-field of the mine-by experiment to approximately 2 m at the model boundaries.

The excavation sequence of the tunnel is subdivided into four sections (Figure 5-4). Section 1 with a length of 28 m was introduced to eliminate boundary effects close to the frontal model boundary. Section 2 and 4 are 16.5 m and 21.0 m in length and are representing the adjoining tunnel sections of Gallery 08 to the mine-by experiment. Section 3 represents the actual mine-by experiment and is 33.0 m in length. This section is intersected by four tabular-shaped zones dipping with 45 degrees towards the positive Y-axis. These zones represent fault zones that were encountered along the mine-by section. The surrounding material is further referred to as rock matrix which represents the tectonically undisturbed rock mass.

5.4.2 Excavation process and support measures

Section 1 was excavated in its entirety assuming that 50% of the deformation occurs ahead of the tunnel face (using the boundary reaction force method). After allowing 50% of deformation, shotcrete and rock bolts were applied simultaneously and model equilibrium was calculated after reducing the boundary reaction forces to zero. Rock bolts were evenly distributed along the excavated section with a spacing of 1.5 m and assumed to behave elastically to stress. The shotcrete lining with a nominal thickness of 0.15 m was modeled as a single layer using elastic shell elements. An initial Young's modulus of 10 GPa was used in this section. Before starting with the excavation procedure of Section 2 aging of the shotcrete was considered by applying a 28-days Young's modulus of 21.45 GPa.

For Section 2 and 4 a full-face excavation with a consistent round length of 1.5 m was utilized. For the start niche at the end of Section 2, the tunnel and niche were simultaneously excavated using round lengths of 2.0 m and 1.33 m, respectively (Figure 5-4). Subsequent to each excavation round, rock bolts were installed 0.75 m behind the tunnel face. Shotcrete consistently lags one round length behind. Aging of the shotcrete was simulated in the entire model by increasing its stiffness (i.e. Young's modulus) with time (Figure 5-5). Since the calculation involves no real time the actual excavation progress was used to define the shotcrete age after each simulated round. After completion of Section 2, a 0.3 m thick concrete slab represented by an elastic shell with a Young's modulus of 35 GPa, was applied at the tunnel invert.

In Section 3 the roadheader excavation was modeled as close as possible to reality using a consistent round length of 1.5 m. Each round was simulated in 9 steps to allow for a smooth rock mass response to the excavation advance. The utilized excavation scheme is illustrated in Figure 5-6. A comparison of round lengths used in reality and in the model is shown in Figure 5-7 and indicates a maximum difference of the face position of 0.7 m. Rock bolts were installed systematically, while shotcrete at the tunnel circumference (except the tunnel invert) was applied in three sequences. Shotcrete lining of the rounds 1 to 3 was applied after completion of round 4 and shotcrete lining of the rounds 4 to 12 was applied after completion of round 13. After completion of the mine-by experiment (prior to excavation of Section 4) shotcrete was applied for the remaining rounds 13 to 22 and the tunnel invert was lined with a 0.3 m thick concrete layer.

5.4.3 In-situ stress state and boundary conditions

The stress tensor assumed in this study is based on the suggestions given by Martin and Lanyon (2003) which accounts for the modification of the minimum principle stress magnitude by Corkum (2006). They analyzed a series of stress measurement campaigns and stress-induced borehole breakouts in the shaley facies. Their analyses suggest a sub-vertical maximum principle stress σ_1 (6 - 7 MPa) steeply inclined towards SSW, and sub-horizontal intermediate and minimum principle stresses sub-parallel and sub-perpendicular to the tunnel axis (Figure 5-2). The magnitude of σ_2 was estimated to range between 4 and 5 MPa, σ_3 ranges between 2 and 3 MPa. Principal stress orientations and magnitudes used for the numerical analysis are shown in Table 5-1. Based on the principle stress tensor, the Cartesian stress components were calculated and initialized throughout the model. At the model periphery stress boundary conditions were applied except for the bottom and front face of the model. At these two boundaries displacements were fixed.

5.4.4 Geodetic and stress path monitoring

Modeled displacements and stresses around and ahead of the tunnel boundary of Section 3 were captured using 22 monitoring arrays. Each array consists of 5 geodetic and 17 stress path monitoring points which are arranged in a vertical plane perpendicular to the tunnel axis as shown in Figure 5-8. Geodetic monitoring points are placed at the tunnel boundaries to capture the total x-, y- and z-component of the displacement vectors. For the displacement analyses it was distinguished between total accumulated displacements and measurable displacements. The latter allows a direct comparison to actually measured displacements by geodetic monitoring. Stress path monitoring points are located 0.35 and 1 m around the tunnel boundary as shown in Figure 5-8 to record the entire stress tensor. In addition, the shear and normal stress magnitudes as well as the direction of the shear components acting on a plane parallel to bedding were recorded. Monitoring arrays are located in the middle of each excavation round and thus have a consistent spacing of 1.5 m along the tunnel axis (Figure 5-8b). Stress measuring points ahead of the face are located along the centre line of the tunnel and thus are progressively excavated by the advancing tunnel.

5.5 Rock mechanical properties of Opalinus Clay

The stress-strain behavior and the strength properties of intact Opalinus Clay from the Mont Terri URL were investigated in numerous laboratory programs using standard laboratory tests (Rummel & Weber 2004, 2007; Schnier & Stuehrenberg 2007; Zhang et al. 2007; Lux et al. 2007; Popp & Salzer 2006, 2007; Graesle & Plischke 2007, 2010; Jahns 2010; Wild 2010; Amann et al. 2011a,b,c; Zimmer 2012; Wymann 2013). In several studies (Corkum 2006; Bock 2009; Graesle & Plischke 2010; Wild 2010; Amann et al. 2010) an increased peak strength with decreasing water content was observed. If it is assumed that the porosity (14 - 18%) of OPA is approximately constant, a decrease in water content is associated with a decrease in saturation and thus an increasing total suction (and vice versa). Recent laboratory tests showed that both, the tensile and compressive strength of Opalinus Clay increase substantially with increasing suction (Zimmer 2012; Wymann 2013). These studies also show that the mechanical properties are almost unaffected

when the water content exceeds 6.5%. Thus, only laboratory test results with a water content $> 6.5\%$ were considered to derive the constitutive material properties for this study.

5.5.1 Elastic material properties of Opalinus Clay

In the elastic domain the behavior of OPA is considered as transversal isotropic linear-elastic, and the constitutive properties were derived from specimens which were loaded either parallel (called P-specimens) or perpendicular (called S-specimens) to the bedding plane orientation. The linear-elastic properties used in this study were derived from recently performed uniaxial and triaxial compression tests (Amann 2011a,b; Wymann 2013) on intact P- and S-specimens (Table 5-2). The Young's modulus and Poisson ratio were determined in the linear part of the stress-strain curve at low axial loads. The elastic anisotropy ratio (E_{\max}/E_{\min}) was found to be 3. The Poisson ratio, however, was approximately 0.2 for both loading directions. For tectonically disturbed Opalinus Clay only two unconfined compressive strength tests on S-specimens are available. These tests suggest a Young's modulus of 1.2 GPa for a slightly disturbed specimen and 0.8 GPa for a moderately disturbed specimen. This corresponds to a reduction of the intact Young's modulus by a factor of 3/5 and 2/5, respectively. Poisson ratio for both specimens were in the order of 0.3, and thus slightly higher than for the undisturbed specimens. Elastic material properties derived from laboratory testing on tectonically undisturbed and disturbed OPA specimens are summarized in Table 5-2. Due to the limited number of laboratory test on tectonically disturbed specimens, derived Young's modulus and Poisson ratio may have a large uncertainty.

5.5.2 Plastic material properties of Opalinus Clay

Plastic properties used in this study were determined from published laboratory test data including uniaxial and triaxial compressive tests, indirect tensile strength tests, and direct shear tests on bedding and tectonic fault planes (Rummel & Weber 2004, 2007; Schnier & Stuehrenberg 2007; Zhang et al. 2007; Lux et al. 2007; Popp & Salzer 2006, 2007; Graesle & Plischke 2007, 2010; Haug 2009; Jahns 2010; Wild 2010; Amann et al. 2010, 2011a,b; Zimmer 2012; Wymann 2013).

Figure 5-9 and Figure 5-10 show the results of compressive and indirect tensile strength tests on P- and S-specimens with a water content $> 6.5\%$ represented by both a linear and bi-linear Mohr-Coulomb failure criterion. It can be seen that for both specimen geometries the failure envelope can be better represented by a bi-linear Mohr-Coulomb failure criterion as suggested by Amann et al. 2012. At low confining stresses (< 2 MPa) the peak and residual friction angle for P- and S-specimens was 43° and at higher confining stresses (> 2 MPa) both specimen geometries revealed a consistent peak and residual friction angle of 11° . The contrast in friction angle is interpreted as being related to dilatancy which may increase the frictional resistance at low confinement. The same friction angles were also obtained for Z-specimens (Table 5-4). These findings suggest that the strength of the different specimen geometries (i.e. P-, S- and Z-specimen) are only differing in their peak and residual cohesions. For both, the linear and bi-linear failure envelope the constitutive properties for P-, S- and Z-specimens are summarized in Table 5-3 and Table 5-4.

Tensile strengths for the rock matrix and the bedding planes were derived from indirect tensile strength tests (i.e. Brazilian tests) on P- and S-specimens (Jahns 2010; Graesle & Plischke 2010; Wild 2010; Zimmer 2012). Utilized specimen diameters ranged between 30 and 100 mm. For bedding-parallel loading of S-specimens (i.e. tensile stress is acting parallel to the bedding) a tensile strength of 1.8 MPa was obtained (Table 5-4). For P-specimens that were loaded perpendicular to bedding (i.e. tensile stress is acting parallel to the bedding) a tensile strength of 1.2 MPa was obtained (Table 5-4). Bedding-parallel loading of P-specimens (i.e. tensile stress is acting perpendicular to the bedding) resulted in a tensile strength of 0.6 MPa which reflects the tensile strength of the bedding planes (Table 5-6).

Constitutive strength properties representative for bedding planes were derived from direct shear tests (Popp & Salzer 2007; Amann et al. 2010). Z-specimens (i.e. load axis inclined to bedding) were not considered since small variations in the angle between the load axis and bedding plane orientation cause considerable variations in peak strength. The peak and residual strengths derived from laboratory results of the direct shear tests along bedding planes are shown in Figure 5-11 along with the obtained shear strengths of the tectonic faults. The bedding data show a considerable scatter especially when the normal stress is high (approximately beyond 2.0 MPa). Constitutive properties were derived through a linear least square regression analysis (Figure 5-11). Even though the scatter in the data points suggests using a linear fit, the strength of bedding planes determined from least square regression analyses would exceed the intact rock strength at high confinement (i.e. high normal stresses) due to a higher friction angle (21°). It is assumed that the friction angle along bedding planes at high confinement should not exceed the basic friction angle of 11° which was derived from both, triaxial tests on P- and S-specimens. Thus, a bi-linear failure criterion was established assuming a basic friction angle of 11° in the high confining range (i.e. > 2 MPa) and a friction angle of 30° derived from least square regression through data points at confining stress < 2 MPa (Figure 5-12). The latter is interpreted as friction plus dilation (i.e. $\phi+i$) as suggested by Patton (1966). The shear strength of tectonic fault planes was derived from 10 direct constant normal stress tests performed by Haug (2009) in a normal stress range between 0.4 and 4.1 MPa. As shown in Figure 5-11 and Figure 5-12, these tests showed no difference between peak and residual strength. Further, the peak and residual strength obtained from the fault planes is equal to the residual strength obtained from direct shear tests along bedding planes (Amann et al. 2010). For both, the linear and bi-linear failure envelope the constitutive properties for bedding and fault planes are summarized in Table 5-5 and Table 5-6.

5.6 Elastic analysis of the short-term rock mass response

For the elastic analyses two different constitutive models were examined to assess the effect of rock anisotropy (i.e. bedding) and rock mass heterogeneity (i.e. fault zones) on the stress redistribution and the associated failure mechanisms: 1) an isotropic linear-elastic (IE) model, and 2) a transversal isotropic linear-elastic model with the plane of the transverse isotropy dipping 45° towards the tunnel advance direction (i.e. positive Y-axis). The transversal isotropic linear-elastic model is further referred to as the anisotropic elastic (AE) model. In both models rock mass heterogeneities are represented by minor and major fault zones which are explicitly modeled (Figure 5-3) assuming an isotropic

elastic behavior. For the AE model rock matrix and fault zone properties were assigned as derived from compressive laboratory testing on intact and tectonically disturbed P- and S-specimens (Table 5-7). For the IE model, three different Young's moduli were considered for the rock matrix: 1) a Young's modulus of 6 GPa representing the stiffness of P-specimens, 2) a Young's modulus of 2 GPa representing the stiffness of S-specimens, and 3) an average Young's modulus of 4 GPa. The properties of the fault zones were derived from laboratory testing on tectonized specimens and were kept constant for all model runs. Properties were assigned to the model based on geophysical borehole measurements along the mine-by section reported by Thoeny 2014. These measurements indicate a dynamic Young's modulus (E_{dyn}) of 10 GPa for intact rock, a dynamic Young's modulus of 6 GPa for the two minor fault zones and the stratigraphic lower part of the major fault zone, and a dynamic Young's modulus < 5 GPa for the stratigraphic upper part of the major fault zone. Resulting deformability ratios are consistent with deformability ratios derived from static laboratory tests on slightly and moderately tectonically disturbed specimens. Thus, elastic Young's moduli derived from the laboratory tests were assigned to the fault zones as suggested by the geophysical measurements. The entire set of constitutive properties used for the elastic analysis is summarized in Table 5-7. Stiffness contrasts between fault zones and rock matrix are highest for the matrix properties derived from the P-specimens and lowest for the matrix properties derived from S-specimens. Additionally, two scenarios with a homogenous (i.e. not including fault zones) isotropic and anisotropic matrix were examined and used as reference models to assess the effect of rock mass heterogeneities on redistributed stresses and associated displacements.

5.6.1 Longitudinal stress variations in heterogeneous rock

Redistributed stresses of all scenarios are shown in Figure 5-13a-d and are presented in terms of differential stress profiles along the tunnel crown, the tunnel invert and both sidewalls. The radial distance of the stress monitoring points to the tunnel contour is approximately 0.35 m. Stress profiles of all four locations around the tunnel circumference resulted in increased differential stresses adjacent to fault zones and in reduced stress magnitudes within the fault zones. This behavior is consistent for all matrix property sets, but substantially different to the homogeneous reference model (grey dashed lines in Figure 5-13). Contrasts in deformability, in particular the contrast between the major fault zone and the surrounding rock mass, affect the differential stress to a considerable longitudinal extent (i.e. up to 2 tunnel diameters) which may have a substantial influence on depth, intensity and location of induced fracturing. Due to the inclination of the faults zones and the in-situ stress components in respect to the tunnel axis, the longitudinally affected zone with larger differential stresses is different for the NE and SW-sidewall. At the NE-sidewall increased differential stress are located in the foot wall of the fault zones, and at the SW-sidewall in the hanging wall. The same tendencies were found for the tunnel crown (similar to the NE-sidewall) and for the tunnel invert (similar to the SW-sidewall).

Laboratory test results suggest that a transversal isotropic elastic model represents the elastic behavior of OPA reasonably well. Results obtained from transversal isotropic models using constitutive properties derived from laboratory tests results are considered as representative for the situation encountered in this study. Deviations in the stress profiles obtained from a transversal anisotropic (AE) model are interpreted as being

related to non-representative stiffness contrasts between fault zones and rock matrix. This is reflected in the results obtained from the IE model assuming a matrix Young's modulus of 6 GPa. In this case the stiffness contrasts between fault zones and matrix are the highest and differential stress changes are often overemphasized (Figure 5-13). Note that the stiffness of the fault zones is considered constant for all model runs. For the IE model with a matrix Young's modulus of 2 GPa and thus with a comparatively low stiffness contrast, the stress changes are much smaller. As a result, the analyses showed that the IE model assuming an average Young's modulus gives a good approximation to the transversal isotropic (AE) model in terms of induced stress magnitudes and longitudinal stress variations (Figure 5-13). It must be mentioned that representing the deformability of an inherently anisotropic material as the OPA by using an averaged isotropic Young's modulus from P- and S-specimens is only applicable for the given stress tensor and the given orientation of the bedding planes and fault zones as encountered in this study.

5.6.2 Stress path analyses

Elastic stress paths analyses were performed in two different ways: 1) principal stress path analyses, and 2) shear and normal stress path analyses. Principal stress paths were interpreted using a bi-linear failure envelope for intact S- and Z-specimens to assess potential intact rock failure through the rock matrix and fault zones (Figure 5-14). Stress paths using the shear and normal stress acting on a plane parallel to bedding were interpreted with a linear shear strength envelope for bedding and fault planes to assess potential shear failure along these planes of weakness (Figure 5-15). Both stress path analyses were performed for the tunnel crown, the invert, both sidewalls and for the rock mass ahead of the tunnel face. The effect of rock mass heterogeneities on the redistributed stress field was examined by comparing stress paths derived from homogeneous and heterogeneous IE and AE models. For the heterogeneous model stress paths of the monitoring array 8 (Figure 5-16 and Figure 5-17) and monitoring array 12 (Figure 5-18 and Figure 5-19) are presented. Monitoring array 12 is located in close vicinity to the major fault zone, and is thus representing the stress redistribution in the near-field of the major fault zone (Figure 5-8). Monitoring array 8 is located at a longitudinal distance of approximately one tunnel diameter to the major fault zone and thus represents the stress redistribution which is less affected by the fault zone.

Figure 5-14 and Figure 5-16 show stress paths obtained for the monitoring array 8 from homogeneous and heterogeneous models assuming isotropic and transversal isotropic behavior. The comparison between these different cases suggests that at a longitudinal distance of one tunnel diameter to the fault zone the stiffness heterogeneities and assumptions for the elastic constitutive behavior are of minor relevance for both, the principal and shear stress paths. In all analyzed cases the stress path analyses suggest, that stress redistribution at the tunnel face is substantially different to the tunnel crown, invert and sidewalls. Stress paths in the principal stress diagram (Figure 5-14) suggest that failure through intact rock is unlikely or may only occur close to the tunnel face (< 0.75 m ahead of the face). However, induced shear stresses ahead of the tunnel face may exceed the strength of fault or bedding planes (Figure 5-15). Due to the lower shear strength of fault planes compared to bedding planes, fault plane reactivation is likely up to 3/4 tunnel diameter ahead of the advancing tunnel face. Shearing along bedding planes can be initiated starting from approximately 1/2 tunnel diameter ahead of the

face. The orientation of the shear stress components acting on fault or bedding planes ahead of the tunnel face revealed normal faulting. This is consistent with field observations during the construction of Gallery o8 (Nussbaum et al. 2011; Thoeny 2014). Stress paths at the crown and the tunnel invert are similar and show that failure of the intact rock is not likely to occur (Figure 5-14). However, induced shear stresses may exceed the strength of fault or bedding planes behind the advancing tunnel face (Figure 5-15). The orientation of shear stresses suggest thrust faulting at the tunnel crown and invert. The latter findings are consistent with field observation where thrust faulting along fault or bedding planes was observed (Thoeny 2014). However, most of the observed EDZ fractures oriented parallel to the bedding planes at the tunnel invert indicate no signs of shearing (i.e. shear fibres, slickensides), and were thus interpreted as unloading fractures (Nussbaum et al. 2011; Thoeny 2014). Stress paths analyses, however, suggest that shearing is the driving failure mechanism that lead to the formation of these bedding-parallel EDZ fractures. In addition to the bedding-parallel EDZ fractures, extensional fractures perpendicular to the bedding orientation were observed at the tunnel invert. This failure mechanism could be related to shearing-induced extensional failure (Thoeny 2014) which cannot be reproduced by the numerical models utilized in this study.

At the tunnel sidewalls the elastic stress path analyses suggest that reactivation of fault planes and bedding plane shear is unlikely due to substantially increased normal stresses (Figure 5-15). Instead, fracturing of the intact rock may occur behind the tunnel face. Stress paths of both sidewalls cross the failure envelope at low confinement (Figure 5-14), suggesting predominately extensional failure (Amann et al. 2012). Thoeny (2014) observed that with increasing distance to the advancing tunnel face major sidewall spalls developed on both sidewalls between the two minor and the major fault zones (Figure 5-26). He also found that the formation of these spalls is not associated with the rock or rock mass anisotropy. These observations are consistent with stress paths derived from the monitoring array 8, and the above mentioned extensional nature of the fracture process.

Stress paths in principal stress and shear-normal stress space shown in Figure 5-18 and Figure 5-19 are representative for monitoring points in vicinity of the major fault zone. The contrasting stiffness between matrix and fault zone causes substantially larger stress magnitudes compared to the homogeneous model as shown in Figure 5-14. Stress paths obtained from the heterogeneous model suggest that extensional fracturing at the NE-sidewall may occur ahead of the tunnel face, at the SW-sidewall behind the tunnel face (Figure 5-18). These different behaviors have a considerable effect on the orientation of induced extensional fractures. Principle stress trajectories behind the tunnel face are tangential to the tunnel sidewall, ahead of the tunnel they curve around the face. Thus, newly formed fractures ahead of the tunnel face will form oblique to the tunnel axis, while fractures which form behind the tunnel face form tangential to the tunnel circumference. This is in agreement with field observations where oblique extensional fractures were only observed in the footwall of the major fault zone at the NE-sidewall (Thoeny 2014).

5.6.3 Displacement pattern in anisotropic rock

Figure 5-20 presents the modeled elastic displacements for the homogeneous isotropic (IE) and anisotropic (AE) model after completion of the mine-by experiment in terms of

displacement magnitudes and displacement vector orientations. Both models show similar displacement magnitudes (indicated by similar colors and lengths of the displacement vectors in Figure 5-20), thus suggesting that the assumption of the constitutive elastic behavior is not relevant for the elastic displacement magnitudes. This is in contrast to the displacement vector orientation, where the constitutive model behavior plays a key role in controlling the direction of the displacement vectors along the tunnel axis. For the AE model where the plane of isotropy dips with 45° into the tunnel advance direction (i.e. positive Y-axis) displacement vectors are consistently oriented sub-perpendicular to the plane of isotropy (Figure 5-20a). At the tunnel invert displacement vectors are pointing into the direction of tunnel advance, while at the crown displacement vectors are pointing in the opposite direction against the tunnel advance direction (i.e. negative Y-axis). For the isotropic elastic model, however, displacement vectors are consistently oriented radial to the tunnel boundaries (Figure 5-20b). This general behavior is also consistent with the heterogeneous models, except for the fault zones where displacement magnitudes are substantially larger and the displacement vector orientations are progressively changing towards an orientation almost radial to the excavation circumference (Figure 5-21). The heterogeneous model also showed that 50% of the total elastic deformations occur ahead of the tunnel face, except for the deformations across the major fault zone. In this more compliant fault zone approximately 80 - 90% of the elastic deformation occur ahead of the tunnel face. These results demonstrate that for the given orientation of the tunnel in respect to the plane of isotropy, the assumption of an isotropic elastic model with averaged S- and P-specimen properties predict elastic deformation magnitudes in an anisotropic rock mass reasonably well, but do not reproduce the observed displacement pattern.

5.7 Elasto-plastic analysis of the short-term rock mass response

For the elasto-plastic analyses the commercially available ubiquitous joint model (FLAC_{3D}, Itasca 2009) was utilized. In the elastic domain (i.e. pre-failure region) this constitutive model assumes an isotropic linear-elastic stress-strain behavior. The elastic analyses in the previous section demonstrate that the assumption of a linear-elastic isotropic model, for the situation encountered in this study, gives similar results as the linear-elastic transversal isotropic model in terms of displacement and stress magnitudes when average elastic properties are assumed for the rock matrix. The elasto-plastic modeling thus allows the influence of the anisotropic failure criterion on the displacement pattern to be assessed.

Depending on the orientation of the maximum stress the ubiquitous joint model allows for failure through the intact rock and failure along ubiquitous joints, and can therefore be utilized to represent a material with a transversal isotropic strength. As previously shown in Section 5.6.1, the material strength for both, the intact rock and the bedding and fault planes is adequately represented by using a bi-linear Mohr-Coulomb failure envelope (Figure 5-10 and Figure 5-12). The constitutive strength properties (peak and residual strength) of the rock matrix were derived from compressive and indirect tensile strength tests on S-specimens. For the fault zones, the constitutive peak strength properties were represented by the residual strength of the Z-specimens, which is in good agreement with the uniaxial compressive strengths derived from two tectonically disturbed S-specimens. The residual strength properties of the fault zones were assumed to be equal to the residual strength properties of the bedding planes. The constitutive

strength properties of the ubiquitous joints are different for the rock matrix and the fault zones. Within the rock matrix the strength of the ubiquitous joints is represented by the strength properties (residual and peak strength) of the bedding planes, while within the fault zones the strength of the ubiquitous joints is governed by the strength properties of tectonic fault planes. For the peak strength properties of the intact rock matrix and the bedding planes a dilatancy was introduced for low confining stresses (< 2 MPa). This is in accordance with laboratory observations from triaxial compressive and direct shear testing on intact OPA specimens (Amann et al. 2010, 2011b). The complete set of material properties used for the elasto-plastic model is summarized in Table 5-8. Note, that the constitutive properties used for this model were solely derived from laboratory tests. For the elasto-plastic modeling a linear-elastic, brittle-plastic stress-strain behavior was utilized for both, the intact material (i.e. rock matrix and fault zones) and the ubiquitous joints (i.e. bedding and fault planes). In the post-failure region strain softening was taken into account.

In the elasto-plastic analysis, three scenarios were examined. The first scenario assumes homogeneous conditions (i.e. no faults included), the second scenario accounts for all major fault zones with a Young's modulus derived from laboratory testing and assigned as shown in the previous section, and a third scenario with a 50% reduction in Young's modulus in the fault zones. The latter scenario was introduced due to the uncertainties in Young's modulus for faults zones, and is considered to investigate the influence of increased stiffness contrasts between the rock matrix and the fault zones.

5.7.1 Three-dimensional EDZ extent along the mine-by section

Figure 5-22 shows the zone where plastic failure occurred (further referred to as the EDZ extent) for all three scenarios in a longitudinal horizontal cross-section through the centre line of the mine-by section. A comparison shows that the radial EDZ extent is substantially influenced by the occurrence of fault zones (i.e. heterogeneities in strength and stiffness). Scenario 1 indicates a constant EDZ depth of 0.5 m at the NE-sidewall, and an EDZ depth of 1 m at the SW-sidewall. This is in contrast to scenario 2 and 3 where both models show strong variations in EDZ depth which reaches up to 4 - 5 m depth within fault zones. The EDZ depth adjacent to fault zones extends up to 2 - 3 m depth and is considerably larger than the depths derived from the homogeneous model (i.e. scenario 1). Due to the given fault zone orientations and the inclined in-situ state of stress with respect to the tunnel axis, the rock mass adjacent to the fault zones reacts differently for the NE and SW-sidewall. In the NE-sidewall the longitudinal EDZ extent is more pronounced in the foot wall of the fault zones, and decreases in direction against the tunnel advance (i.e. negative Y-axis). For the SW-sidewall the EDZ extent is more pronounced in the hanging wall of the fault zones and decreases in the direction of tunnel advance (i.e. positive Y-axis). The same tendencies were found for the tunnel crown (similar to the NE-sidewall) and for the tunnel invert (similar to the SW-sidewall). These findings are consistent with the elastic analyses discussed previously which suggest asymmetric stress redistribution around fault zones. Enhanced EDZ depths adjacent to the major fault zone indicate a longitudinal range of influence of approximately $1 - 1\frac{1}{2}$ tunnel diameters. Scenario 3 which assumes a 50% reduced Young's modulus within the fault zones (i.e. increased stiffness contrast between fault zones and rock matrix) indicates a similar EDZ geometry as derived in scenario 2. However, EDZ depths within the fault zones are slightly reduced, while EDZ depths in the adjacent rock mass are

slightly increased. This suggests that an increase in stiffness contrast between rock matrix and fault zones lead to a more intensive fracturing in the rock mass adjacent to the fault zones due to stress concentration, and thus to a larger radial extent of the EDZ at these locations.

Figure 5-23 shows a 3-dimensional representation of the modeled EDZ derived from scenario 2 which is color-coded according to the material types. Purple zones indicate plastic failure within the rock matrix, reddish zones indicate plastic failure within the different fault zone types (i.e. fault zone I-III and fault zone IV). The oval-shaped EDZ with a slightly larger extent in the vertical direction than in the horizontal direction normal to the tunnel axis is in agreement with the conceptual EDZ geometry proposed by Thoeny (2014) and Martin & Lanyon (2004) for a similar tunnel orientation at the Mont Terri URL. Thoeny (2014) showed based on borehole deformation monitoring and seismic tomography that the EDZ along the sidewalls of the mine-by experiment has a lateral extension of > 4 m within fault zones, and up to 2 - 3 m in the adjacent rock mass. In slightly tectonized zones along the mine-by experiment the extent of the plastic zone below the tunnel was approximately up to 3 - 3.5 m. Both, the modeled EDZ depth and depth variations are in good agreement with field observations.

5.7.2 Three-dimensional displacement pattern along the mine-by section

Figure 5-24 shows the modeled crown settlements (i.e. measurable vertical displacements) within the mine-by section in comparison with the geodetic displacement measurements. The general displacement pattern is in agreement with the geodetic measurements, however, measured displacement magnitudes were not adequately reproduced in all tunnel sections. In particular between GM 96 - 98, GM 106 - 108, as well as at GM 110.5 and GM 118.5 measured displacements are considerably larger than the modeled displacements. This discrepancy can be explained by local crown instabilities. The largest vertical displacements measured between GM 96 - 98 and GM 106 - 108 were both associated with structural-driven slab formation which detached along pre-existing SW-dipping fault planes (Figure 5-26). Minor crown instabilities related to pre-existing structures and spalling phenomena were observed at GM 110.5 (Figure 5-26) and GM 118.5 (Figure 5-26), respectively. Even though the large displacement at GM 96 - 98 and GM 106 - 108 can be attributed to structural-controlled instabilities, the elastic analyses indicates substantial differential stress peaks in the same regions (Figure 5-24 c) which resulted from the stiffness contrast between rock matrix and fault zones. This suggests that the observed crown instabilities are a combination of stress-induced and structural-controlled failure. At locations where no crown instabilities occurred, modeled displacement magnitudes are consistent with the geodetic measurements and are in the order of 5 to 10 mm. Reducing the Young's modulus in the fault zones by 50% leads to an increase in differential stresses adjacent to the fault zones (Figure 5-24 c), in particular at GM 97. However, increased stresses resulted only in slightly enhanced vertical displacements ahead of the major fault zone.

In Figure 5-25 the modeled horizontal displacements (i.e. measurable horizontal displacements normal to the tunnel axis) along the NE-sidewall of the mine-by section are compared with the geodetic displacement measurements. Similar to the vertical displacements at the tunnel crown, the general displacement pattern is captured by the numerical model results. However, measured displacement magnitudes were not

adequately reproduced for all tunnel sections, in particular for the upper sidewall prisms (Figure 5-25 a). At these locations the measured displacements are in the order of 10 - 15 mm and thus significantly larger than the model displacements. This discrepancy can be attributed to the formation of a major sidewall spall between GM 103 - 109 and the reactivation of moderately SW-dipping fault planes which intersect the upper NE-sidewall between GM 98 - 103 (Figure 5-25 a). Figure 5-26d shows the open crack along which the spall is detached from the rock mass with the geodetic prisms located on top of the spall. Displacements obtained from prisms installed at the lower sidewall are, however, in general agreement with the modeled displacements. This slight difference between GM 94 - 98 and GM 117 - 122 is assumed to be related to dislocations along sub-horizontal tectonic faults, and the observed sidewall spalls between GM 106 and GM 110. The largest displacements were measured right ahead of the major fault zone for both, modeled and measured displacements. This is in good agreement with EDZ structures mapped in the footwall of the major fault zone at this location.

Figure 5-27 shows the distribution of the accumulated plastic shear strain magnitudes of the rock matrix and the fault zones along both sidewalls after completion of the mine-by experiment. The magnitude of the plastic shear strain is considered as a measure for the damage intensity (defined as inelastic deformation). On both sidewalls, the highest plastic shear strains are located within the fault zones where the matrix strength is the lowest. In between the fault zones, the maximum plastic shear strains are located in the lower NE-sidewall and the upper SW-sidewall. However, elastic stress path analyses suggest that the rock mass response at the sidewalls is different within the fault zones and the rock matrix. Within the fault zones shear failure through the matrix is the most likely failure mechanism, while in the rock matrix, particularly in between the fault zones, extensional fracturing is the dominant mode of failure. This different behavior is also supported by the distribution of the accumulated plastic shear strain along the ubiquitous joints (i.e. along bedding planes in the rock matrix and along fault planes within the fault zones) as shown in Figure 5-28. Plastic shear strain magnitudes are most pronounced within the fault zones, in particular at the fault zone boundaries, while shearing along bedding planes is most pronounced at the upper tunnel face and around the start niche. This is in agreement with the field observations gained during the mine-by experiment where extensional fracturing tangential to the tunnel sidewalls was dominant in tunnel sections with a low fault frequency and shear failure was dominant in tunnel sections with a fault frequency higher than 4 faults per meter (Thoeny 2014).

The distribution of accumulated plastic shear strain in the numerical results is consistent with the observed sidewall spalls in both the location and extent as shown in Figure 5-29. Figure 5-29 shows the horizontal displacement pattern between GM 93 and GM 124 derived from the geodetic measurements. Regions which show enhanced (> 10 mm) displacements are in general agreement with regions that show higher shear strain intensities. Similar to the modeled shear strain intensity, horizontal displacements are more pronounced in the lower NE-sidewall and the upper SW-sidewall. Thus, integrating the failure mechanisms derived from the elastic stress path analyses with the distribution of the plastic shear strain derived from the elasto-plastic analysis allows the rock mass behavior to be anticipated in terms of both the failure modes and locations.

5.8 Discussion of numerical modeling approach

It was demonstrated that the orientation of the far-field stresses in respect to the orientation of the tunnel and the large-scale rock mass heterogeneities have a substantial effect on stress localization and rotation around the tunnel circumference, and thus can significantly influence the failure mode and failure location. For the numerical analysis the in-situ stress tensor proposed by Martin and Lanyon (2003) was slightly modified. However, Martin and Lanyon (2003) showed that in-situ stress measurements in the Opalinus Clay at the Mont Terri URL are challenging and thus their proposed stress tensor is uncertain. Enachescu (2011) proposed an in-situ stress state with a horizontal σ_1 (8.6 MPa) oriented sub-perpendicular to the mine-by tunnel, a sub-vertical σ_2 (6.5 MPa) dipping towards ESE, and a sub-horizontal σ_3 (3.9 MPa) sub-parallel to the mine-by axis. Using the stress tensor proposed by Enachescu (2011) for the numerical models the modeled rock mass response (e.g. EDZ location and displacements) is not in good agreement with field measurements.

Numerical model results showed that both, the failure mode and displacement pattern can be reasonably well reproduced even though the model is based on a simplified representation of the encountered natural fracture network. In the utilized numerical model only fault zones intersecting the mine-by experiment were explicitly implemented, and bedding-parallel fault planes were implicitly modeled using an ubiquitous joint model. However, geological mapping of the mine-by section additionally revealed the occurrence of two additional fault sets (Thoeny 2014). It has been shown that these fault planes contribute to local instabilities such as slab formation at the tunnel roof or dislocations at the tunnel sidewalls. Further numerical investigations using a discontinuum code (e.g. 3DEC, Itasca 2009) are required to better resolve the measured displacement pattern, and to improve the understanding of the failure mechanisms associated with the interference of different fault sets. However, explicit discretization of individual fault planes in moderately to strongly faulted tunnel sections as encountered in the mine-by experiment is challenging and strongly limited by the quality of the geological map. Furthermore, detailed investigation of the natural fracture network around the mine-by section revealed that fault planes exhibit a large-scale waviness (local orientation to the induced stress field) which is may be relevant for their mechanical behavior on the tunnel-scale and thus cannot be simply represented by an infinite planar interface. It was also demonstrated that large displacements associated with the formation of major spalls cannot adequately be reproduced with the utilized constitutive models and continuum mechanical approach. This is mainly related to bulking effects associated with the progressive development of the spalls. However, the combination of elastic stress path and elasto-plastic analyses provide a very clear indication of the location and type of failure mechanisms which are to be anticipated.

5.9 Summary and conclusions

Numerical analyses performed in this study revealed new and important insights into the influence of rock mass heterogeneities such as faults and fault zones on excavation-induced fracturing around an advancing tunnel in faulted Opalinus Clay. Previous investigations were limited to induced failure processes around individual tunnel cross-sections and detailed information about spatial variations in induced fracturing in terms

of failure mechanisms and associated kinematic behavior of bedding and fault planes along the tunnel axis were previously not investigated. Through combined analysis of site-specific, three-dimensional numerical models and deformation monitoring data from a mine-by experiment at the Mont Terri URL in Switzerland, it is demonstrated that deformability and strength heterogeneities in the Opalinus Clay have a significant influence on the redistributed stresses and hence on induced fracturing and associated deformations in the tunnel near-field. Thus, numerical modeling requires considerations of both the rock anisotropy due to the bedding as well as the rock mass heterogeneity and anisotropy due to faults and fault zones to adequately reproduce the observed failure mechanisms and the associated displacement field. Numerical model results showed that the observed spatial variations in failure depth and in the displacement pattern are reasonably reproduced with the utilized linear elasto-plastic model by using constitutive material properties derived from conventional laboratory testing. Although not explicitly implemented in the model, information regarding the kinematic failure modes of bedding and fault planes was gained from elastic stress path analysis and determined to be highly informative for identifying potential failure modes. The conclusions from both the elastic and elasto-plastic modeling are primarily valid for the given orientation of the in-situ stress state in respect to the orientation of the tunnel and the plane of transversal isotropy as encountered in this study. However, the results may also help to understand the role of anisotropy and heterogeneity on local failure mechanisms associated with excavations in weak anisotropic rocks.

The key outcomes of the elastic analyses are:

- Large-scale heterogeneities in deformability, primary caused by spatial variations in fault plane density, lead to substantial stress concentrations in the rock mass adjacent to more compliant zones. Stress magnitudes and the affected extent in the adjacent rock mass are strongly dependent on the stiffness contrast between the fault zone and the rock matrix, whereby a high stiffness contrast results in the highest stress magnitudes and the largest extent along the tunnel axis.
- Longitudinal stress profiles from heterogeneous models revealed that variations in stress magnitudes in a transversal isotropic material, such as the Opalinus Clay, can be adequately represented with an isotropic model assuming an average Young's modulus (i.e. average between P- and S-specimens).
- Elastic analysis further revealed that total and measurable elastic displacements are similar in terms of displacement magnitudes and thus not substantially affected by the constitutive elastic model. However, elastic displacement vector orientations are significantly affected by the orientation of the plane of isotropy.
- Elastic stress path analyses obtained from linear-elastic isotropic and linear-elastic transversal isotropic models are qualitatively and quantitatively similar for homogeneous and heterogeneous models. Thus, the assumption of the constitutive elastic behavior is not relevant regarding the stress magnitudes when using an average Young's modulus for the isotropic model.
- Elastic stress path analyses were able to adequately identify the kinematic failure modes of discrete fault and bedding planes as observed in the field. Elastic modeling suggests that at the tunnel face shearing along fault and bedding planes is the most likely failure mechanism and primarily associated with normal faulting. Stress path analysis also indicate that reactivation of fault planes is initiated 2 - 3 m ahead of the face with shearing along bedding plane initiating

only 0.5 - 1 m ahead of the face. At the tunnel invert and the crown, shearing along fault and bedding planes is also the most likely failure mechanism, however, shearing is consistently initiated behind the tunnel face and primarily associated with reverse faulting. These findings are consistent with field observations. Elastic stress path analysis further suggests that extensional fracturing is the primary failure mechanism at the sidewalls. In the vicinity of fault zones substantially enhanced stresses ahead of the tunnel face may lead to the formation of extensional fractures sub-parallel to the tunnel face. At larger distance from the tunnel face (i.e. 0.5 - 1 tunnel diameter) extensional fractures may form on both sidewalls tangential to the tunnel circumference. Field observations showed that these extensional fractures had the potential to evolve into major sidewall spalls, in particular adjacent to major fault zones.

The key outcomes of the elasto-plastic analysis are summarized as follows:

- Elasto-plastic analyses showed that depth and depth variations of the excavation damage zone are substantially affected by strength and deformability heterogeneities along the tunnel. Model results suggest an EDZ depth of 4 to 5 m within fault zones, a depth of 2 - 3 m adjacent to fault zones and a depth of 0.5 to 1 m outside the range of influence of fault zones. The modeled EDZ depth and EDZ depth variations are in agreement with geological and geophysical field investigations along both sidewalls of the mine-by experiment.
- The elasto-plastic model also revealed displacement magnitudes similar to the measured magnitudes. The agreement with field measurements is, however, altered in zones where structural controlled instabilities or major faults and associated dilatant behavior was observed. Even though the displacement magnitudes in these zones are not well captured by the numerical model, these zones coincide in extent and location with the extent and location of the maximum modeled plastic shear strain.
- The analyses are based on newly established constitutive properties based solely on laboratory test results. Since both, the EDZ depth and displacements are reasonably well captured in the numerical model, it is concluded here that these properties are representative for the short-term undrained response of Opalinus Clay (shaley facies) at the Mont Terri URL.

5.10 References

Amann F, Button EA, Bluemel M, Thoeny R (2010) Insight into the mechanical behaviour of Opalinus Clay. Paper presented at European Rock Mechanics Symposium 2010, Lausanne, Switzerland, Rock Mechanics and Environmental Engineering, edited by Zhao, Labious, Dudt and Mathier, Taylor & Francis Group, London, ISBN 978-0-415-58654-2

Amann F, Button EA, Evans KF, Gischig VS, Bluemel M (2011a) Experimental study of the brittle behavior of clay shale in rapid unconfined compression. *Rock Mech Rock Eng* 44: 415-430

Amann F, Kaiser PK, Button EA (2011b) Experimental study of brittle behavior of clay shale in rapid triaxial compression. *Rock Mech Rock Eng* 45: 21-33

- Amann F, Thoeny R, Kaiser PK, Button EA (2011c) Insight into the brittle failure behavior of clay shales in unconfined and confined compression. Proceedings of the 45th US Rock Mechanics/Geomechanics Symposium 2011, San Francisco, CA, American Rock Mechanics Association, ARMA
- Amann F, Thoeny R, Martin CD (2012) Rock mechanical considerations associated with the construction of a nuclear waste repository in clay rock. Proceedings of the 46th US Rock Mechanics/Geomechanics Symposium 2012, Chicago, American Rock Mechanics Association, ARMA
- Bluemling P, Konietzky H (2003) Development of an excavation disturbed zone in Clay stone (Opalinus Clay). Geotechnical Measurements and Modelling, Natau, Fecker & Pimentel (eds), Swets & Zeitlinger, Lisse, ISBN 90-5809-603-3
- Bock H (2001) RA experiment: Rock mechanics analyses and synthesis: Data report on rock mechanics. Unpublished Mont Terri Technical Report 2000-02, Mont Terri Project, Switzerland
- Bock H (2009) RA experiment: Updated review of the rock mechanics properties of the Opalinus Clay of the Mont Terri URL based on laboratory and field testing. Unpublished Mont Terri Technical Report 2008-04, Mont Terri Project, Switzerland
- Corkum AG (2006) Non-linear behaviour of Opalinus Clay around underground excavations. PhD thesis, Department of Civil and Environmental Engineering, University of Alberta, Canada
- Corkum AG, Martin CD (2007) Modelling a mine-by test at the Mont Terri rock laboratory, Switzerland. International Journal of Rock Mechanics & Mining Sciences 44: 846-859
- Enachescu C (2011) DS experiment: Hydraulic fracturing tests in BDS-2 and BDS-4 at the Mt. Terri underground research facility. Unpublished Mont Terri Technical Report 2010-53, Mont Terri Project, Switzerland
- Freivogel M, Huggenberger P (2003) Modellierung bilanzierter Profile im Gebiet Mont Terri - La Croix (Kanton Jura). In: Heitzmann P, Tripet J-P, editors. Reports of the Federal Office for Water and Geology, Switzerland
- Graesle W, Plischke I (2007) LT experiment: Strength and deformation of Opalinus Clay. Unpublished Mont Terri Technical Report 2007-05, Mont Terri Project, Switzerland
- Graesle W, Plischke I (2010) Laboratory testing experiment: Mechanical behavior of Opalinus Clay. Unpublished Mont Terri Technical Report 2009-07, Mont Terri Project, Switzerland
- Haug C (2009) Mechanische Charakterisierung präexistenter tektonischer Trennflächen im Opalinuston. MSc thesis, Department of Earth Sciences, ETH Zurich, Switzerland
- Itasca Consulting Group Inc. (2009) Fast Lagrangian Analysis of Continua in 3 Dimensions, version 4.0. Minneapolis, USA
- Jahns E (2010) RA experiment: Opalinus Clay rock characterization. Unpublished Mont Terri Technical Note 2008-55, Mont Terri Project, Switzerland

- Lux KH, Duesterloh U, Czaikowski O (2007) Laboratory tests on indurated clay. Clausthal University of Technology. Final Report for EDZ long term evolution (WP 4.4). European Commission NF-PRO (Contract Number: FI6W-CT-2003-02389) (D 4.4.13)
- Martin CD, Lanyon GW (2003) Measurement of in-situ stress in weak rocks at Mont Terri Rock Lab. *International Journal of Rock Mechanics and Mining Sciences* 40: 1077-1088
- Martin CD, Lanyon GW (2004) Excavation disturbed zone (EDZ) in Clay Shale: Mont Terri. Unpublished Mont Terri Technical Report 2001-01, Mont Terri Project, Switzerland
- Nussbaum C, Bossart P, Amann F, Aubourg C (2011) Analysis of tectonic structures and excavation induced fractures in the Opalinus Clay, Mont Terri underground rock laboratory (Switzerland). *Swiss J Geosci* 104: 187-210
- Patton FD (1966) Multiple modes of shear failure in rock 1st Congress of International Society of Rock Mechanics 1: 509-513
- Popp T, Salzer K (2006) HE-D experiment: Influence of bedding planes. Unpublished Mont Terri Technical Report 2005-34, Mont Terri Project, Switzerland
- Popp T, Salzer K (2007) HE-D experiment: Influence of bedding planes. Unpublished Mont Terri Technical Report 2007-04, Mont Terri Project, Switzerland
- Rummel F, Weber U (2004) RA experiment: Rock mechanical testing and characterization on drillcores of boreholes BRA-1 and BRA-2. Unpublished Mont Terri Technical Note 2004-38, Mont Terri Project, Switzerland
- Rummel F, Weber U (2007) Rock mechanics analyses (RA) experiment: Results of uniaxial and triaxial tests on Opalinus Clay samples. Unpublished Mont Terri Technical Note 2005-57, Mont Terri Project, Switzerland
- Schnier H, Stuehrenberg D (2007) LT experiment: Strength tests on cylindrical specimens, documentation and evaluation. Unpublished Mont Terri Technical Report 2003-04, Mont Terri Project, Switzerland
- Te Kamp L, Camusso M (2009) MB (mine-by test) experiment: Numerical Modeling of the MB Experiment. Unpublished Mont Terri Technical Note 2009-24, Mont Terri Project, Switzerland
- Thoeny R (2014) Geomechanical analysis of excavation-induced rock mass behavior of faulted Opalinus Clay at the Mont Terri Underground Rock Laboratory (Switzerland). PhD thesis, Department of Earth Sciences, ETH Zurich, Switzerland
- Thury M, Bossart P (1999) Results of the hydrogeological, geochemical and geotechnical experiments performed in the Opalinus Clay (1996-1997). Geological report No. 23, Swiss Geological Survey, Switzerland
- Tonon F, Amadei B (2002) Effect of elastic anisotropy on tunnel wall displacements behind a tunnel face. *Rock Mechanics and Rock Engineering* 35 (3): 141-160
- Wild K (2010) Charakterisierung des Verhaltens von Opalinuston unter Zugbeanspruchung. BSc thesis, Department of Earth Sciences, ETH Zurich, Switzerland
- Wymann L (2013) The influence of saturation on the uniaxial compressive strength of Opalinus Clay. MSc thesis, Department of Earth Sciences, ETH Zurich, Switzerland

- Yong S (2008) A three-dimensional analysis of excavation-induced perturbations in the Opalinus Clay at the Mont Terri Rock Laboratory. PhD thesis, Engineering Geology, ETH Zurich, Switzerland
- Yong S, Kaiser PK, Loew S (2010) Influence of tectonic shears on tunnel-induced fracturing. *International Journal of Rock Mechanics & Mining Sciences* 47: 894-907
- Yong S, Kaiser PK, Loew S (2013) Rock mass response ahead of an advancing face in faulted shale. *International Journal of Rock Mechanics & Mining Sciences* 60: 301-311
- Zhang C-L, Rothfuchs T, Jockwer N, Wiczorek K, Dittrich J, Müller J, Hartwig L, Komischke M (2007) HE-D experiment: Thermal effects on the Opalinus Clay. Unpublished Mont Terri Technical Report 2007-02, Mont Terri Project, Switzerland
- Zimmer S (2012) Untersuchungen zur einaxialen Zugfestigkeit von Opalinuston in Abhängigkeit der Saugspannung. BSc thesis, Department of Earth Sciences, ETH Zurich, Switzerland

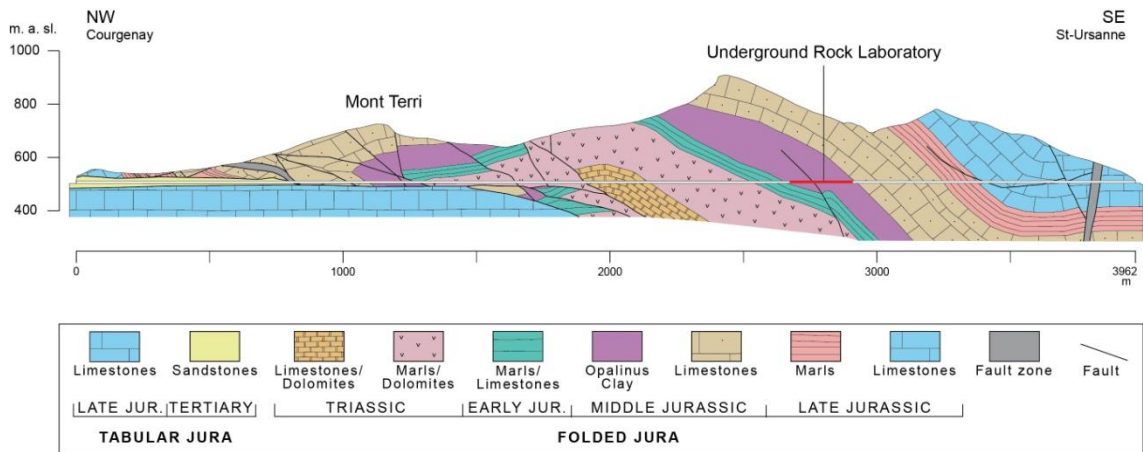


Figure 5-1: Geological cross-section along the Mont Terri motorway tunnel (from Freivogel & Huggenberger 2003). The rock laboratory is located in the southeastern limb of the Mont Terri anticline in the Opalinus Clay formation at a depth of 250 - 320 m.

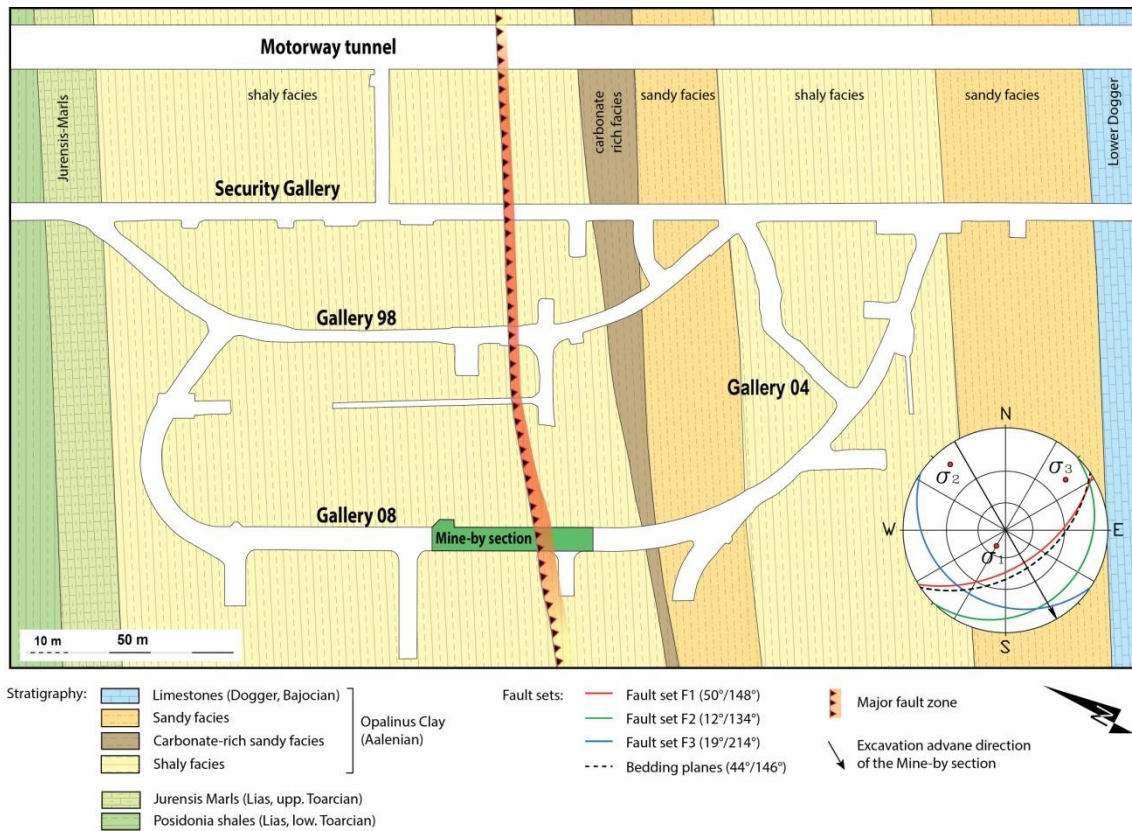


Figure 5-2: Horizontal cross-section through the Mont Terri URL showing the general layout of the rock laboratory and the stratigraphical units (modified from Nussbaum et al. 2011) with lower hemisphere projections of the in-situ stress field and the mean orientations of the most relevant geological structures encountered in the mine-by section. The mine-by section, highlighted in green, is entirely located within the shaly facies of the Opalinus Clay and is intersected by a major fault zone.

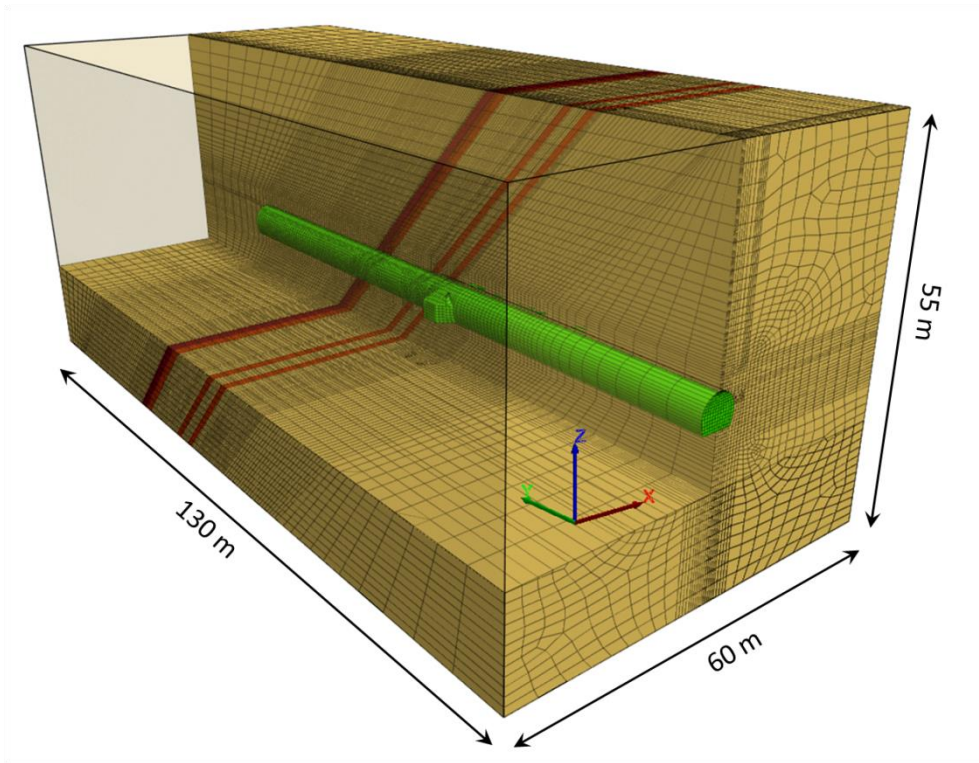


Figure 5-3: FLAC 3D model showing the model dimensions and the excavated tunnel geometry (green). Further shown are the geometry and orientation of the implemented mechanical rock mass heterogeneities (red and orange) encountered during the excavation of the mine-by section.

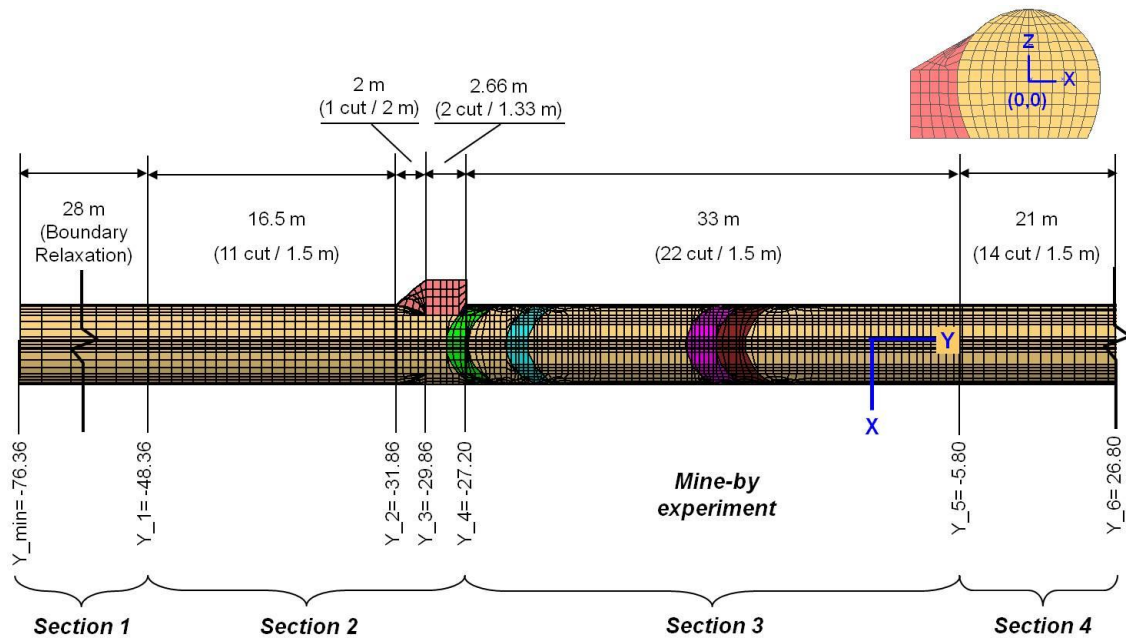


Figure 5-4: Modeled excavation sequence for the different tunnel sections indicated by their lengths and utilized round lengths.

Young's modulus of shotcrete [Pa]

- 2.1245e+10
- 2.12366e+10
- 2.12275e+10
- 2.12184e+10
- 2.12093e+10
- 2.12002e+10
- 2.11911e+10
- 2.1182e+10
- 2.11028e+10
- 2.09394e+10
- 2.0534e+10
- 1.89461e+10
- 1.6653e+10
- 1.17718e+10
- 1.28477e+09
- 3.5e+10

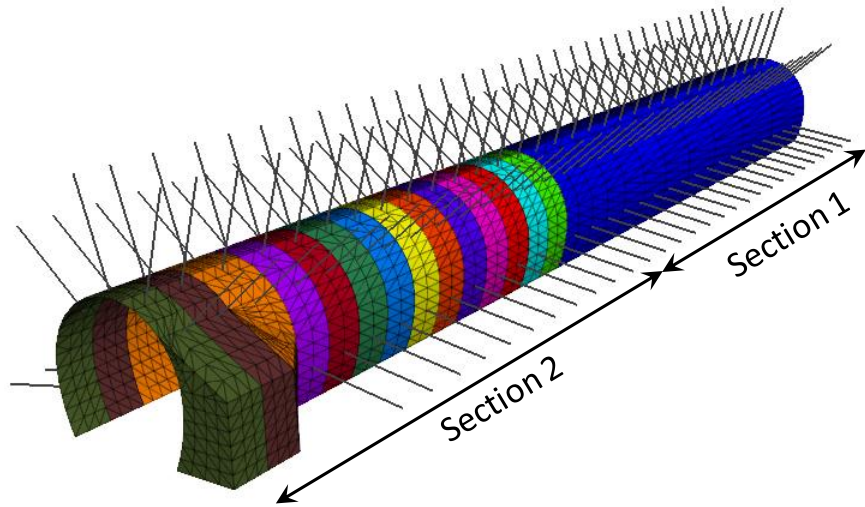


Figure 5-5: Support measures utilized in Section 1 and 2 after their completion. For both sections aging of the shotcrete was implemented and simulated in terms of an increasing stiffness with time.

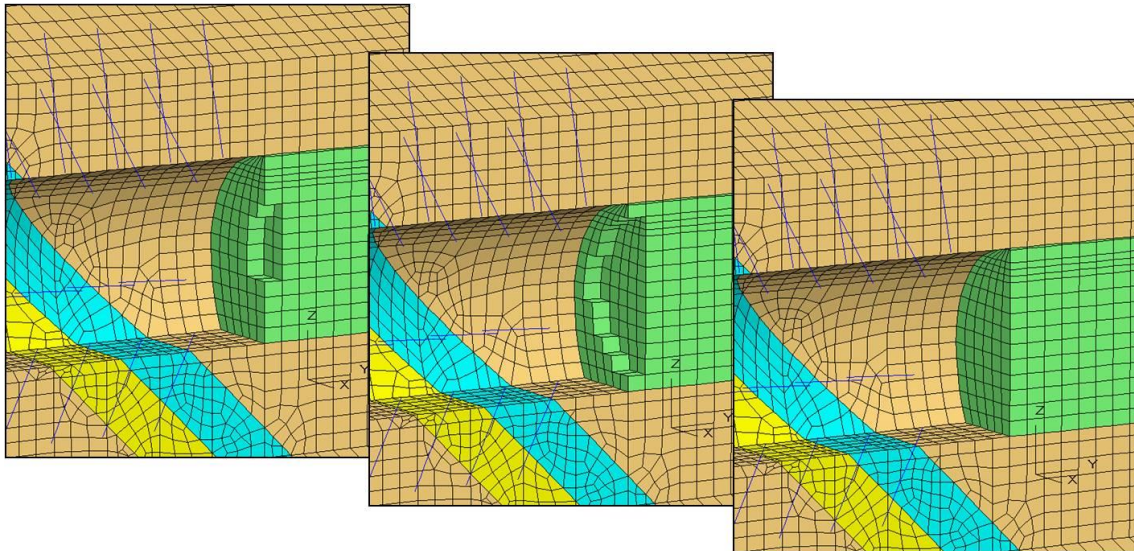


Figure 5-6: Adapted excavation scheme utilized in the mine-by section (Section 3). A round length of 1.5 m was excavated within 3 steps, whereby each of the 0.5 m steps was subdivided into three sub-steps as indicated in the series of figures.

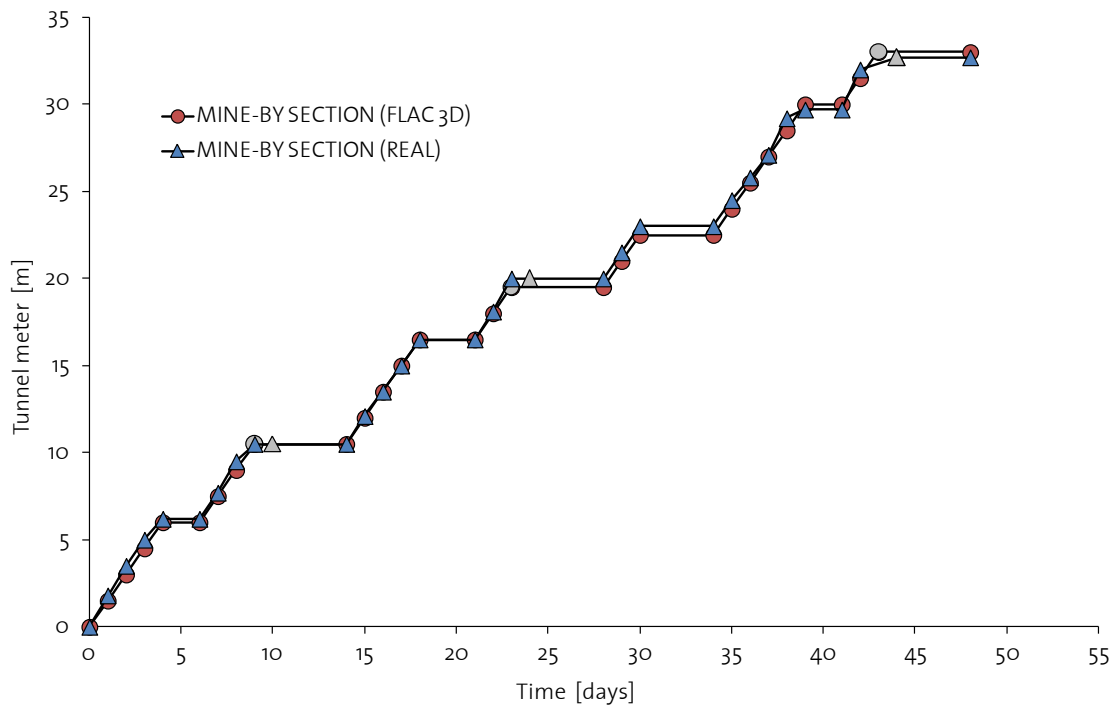


Figure 5-7: Comparison between real (blue infilling) and modeled (red infilling) excavation advancement and shotcrete emplacement (grey infilling) throughout the excavation of the mine-by section.

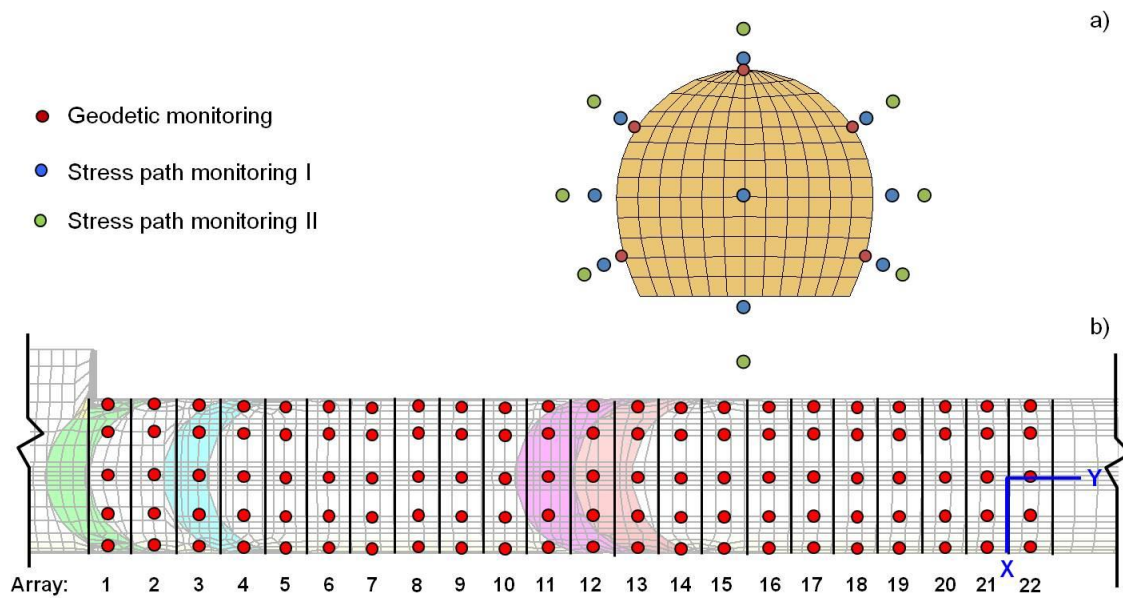


Figure 5-8: Layout of the stress and displacement monitoring setup along Section 3. a) Vertical cross-section showing the location of the monitoring points around the tunnel boundaries. b) Longitudinal horizontal cross-section showing the location of the monitoring arrays along the tunnel axis with respect to the implemented fault zones.

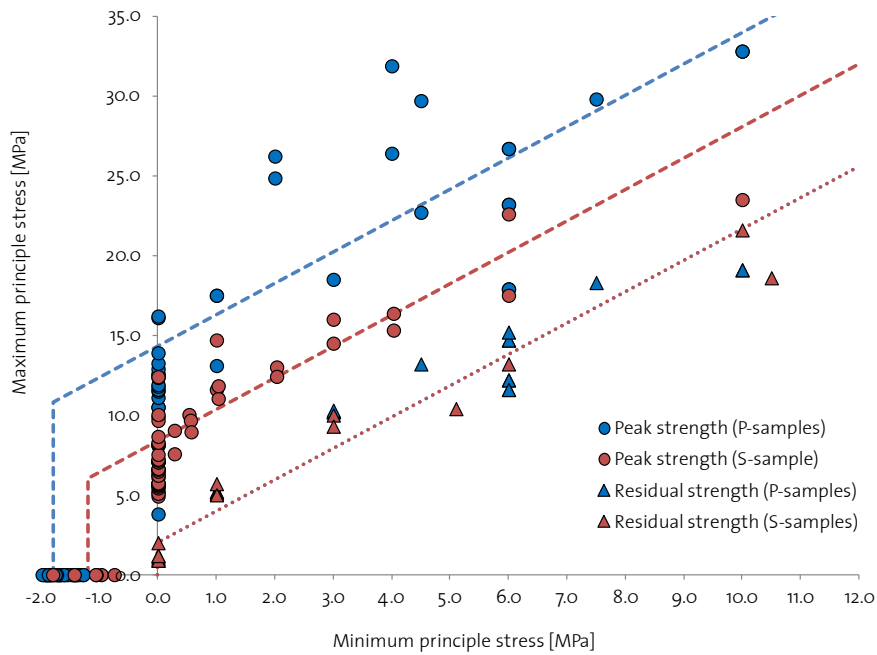


Figure 5-9: Linear Mohr-Coulomb shear failure criteria for peak and residual strengths of intact P- and S-specimens derived from compressive and indirect tensile strength tests. P-specimens were loaded parallel to the bedding plane orientation and S-specimens perpendicular to it.

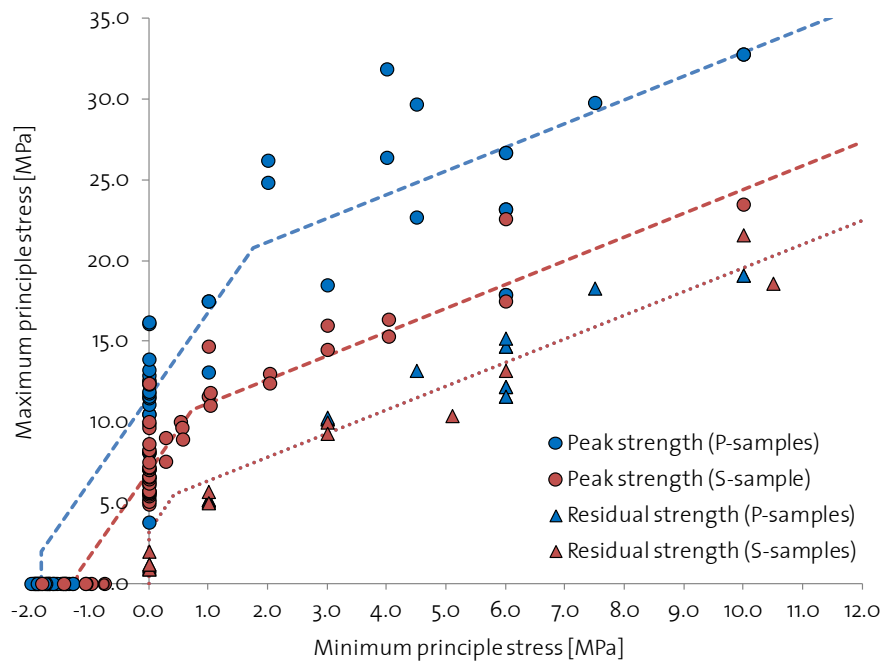


Figure 5-10: Bi-linear Mohr-Coulomb shear failure criteria for peak and residual strengths of intact P- and S-specimens derived from compressive and indirect tensile strength tests. P-specimens were loaded parallel to the bedding plane orientation and S-specimens perpendicular to it.

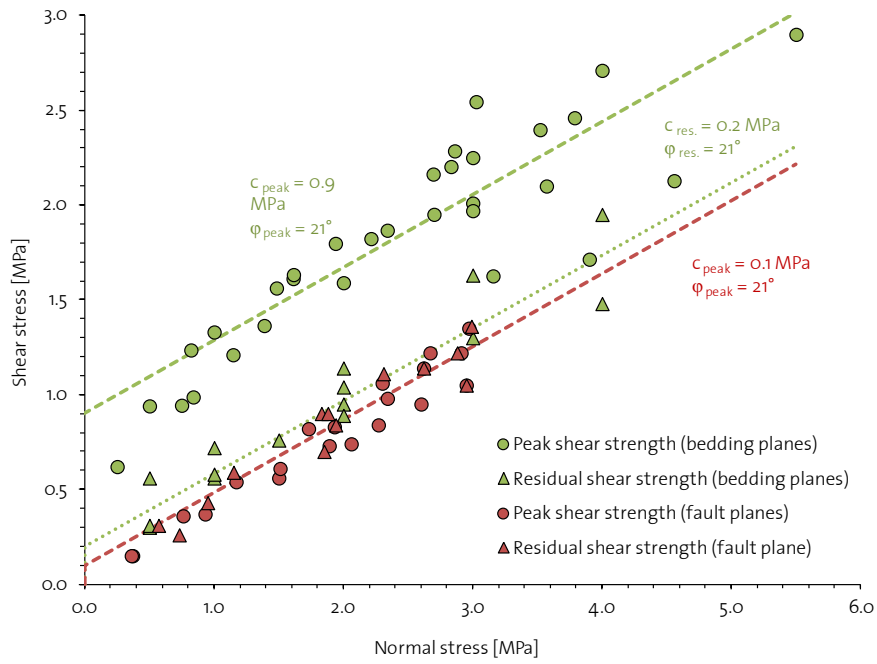


Figure 5-11: Linear Mohr-Coulomb shear failure criteria for peak and residual strengths of bedding and fault planes derived from direct shear testing (Popp & Salzer 2007; Haug 2009; Amann et al. 2010).

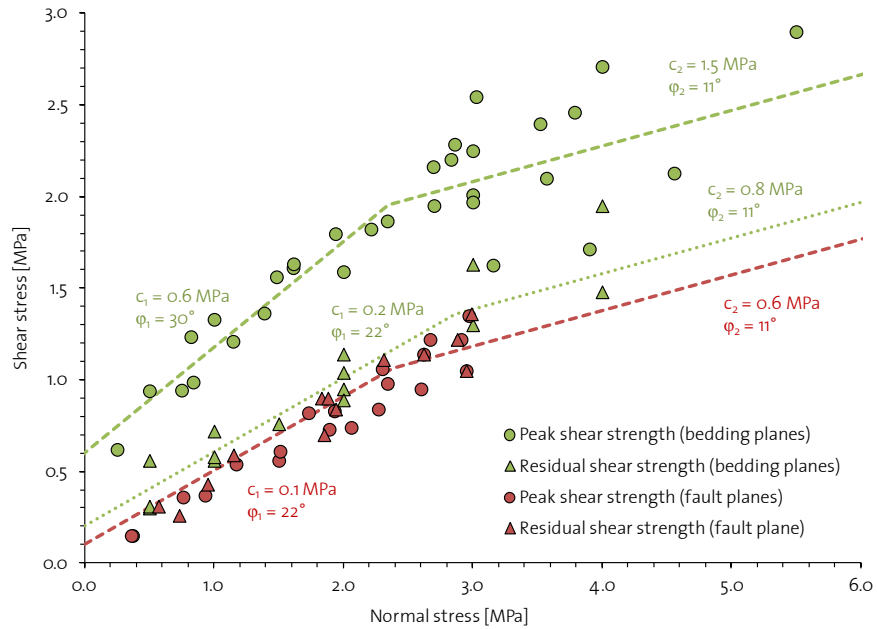


Figure 5-12: Bi-linear Mohr-Coulomb shear failure criteria for peak and residual strengths of bedding and fault planes derived from direct shear testing (Popp & Salzer 2007; Haug 2009; Amann et al. 2010).

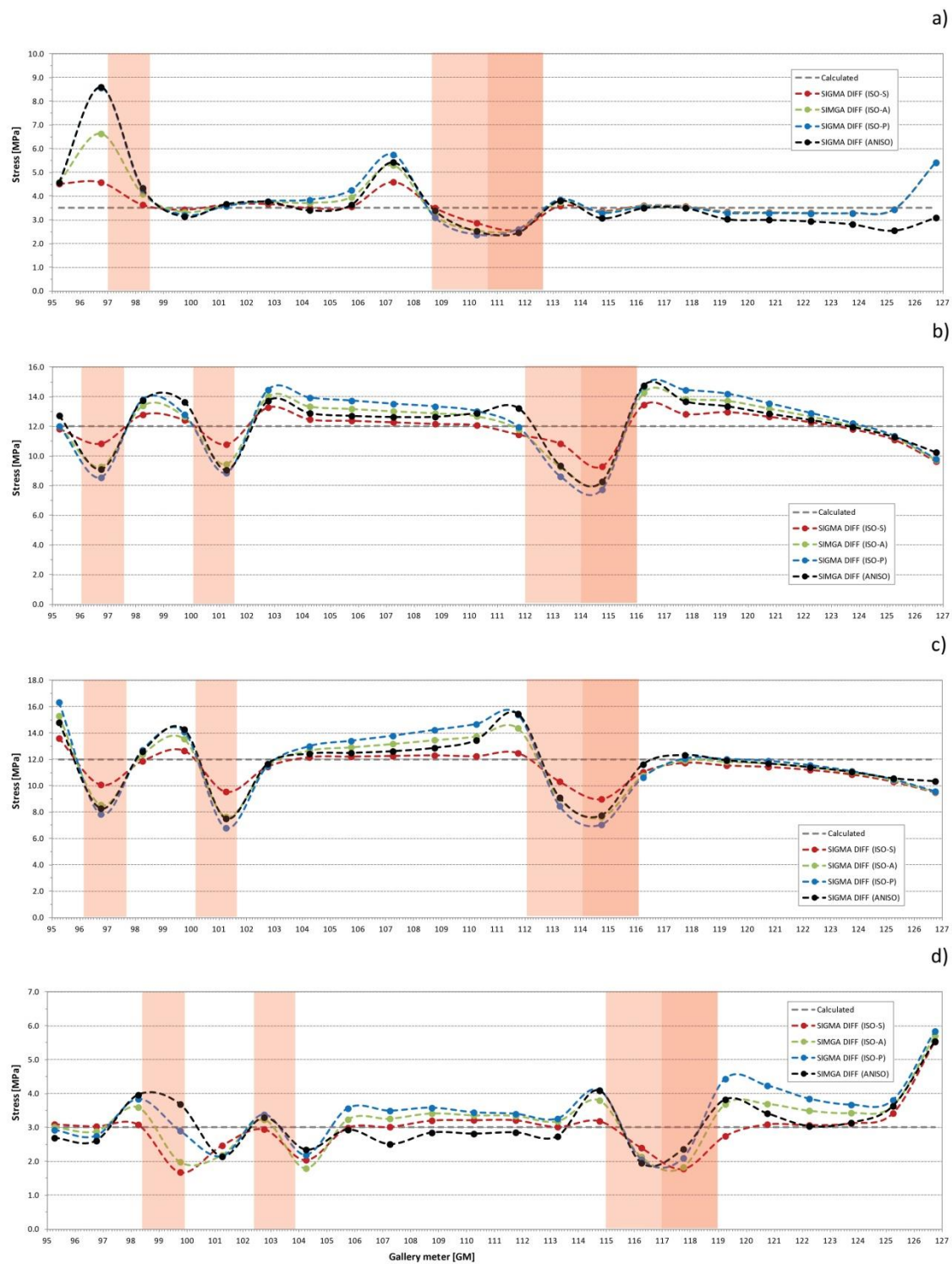


Figure 5-13: Longitudinal differential stress profiles around the tunnel circumference presented for a) the crown, b) the SW-sidewall, c) the NE-sidewall, and d) the tunnel invert. Locations of the fault zones I - III are indicated in light red and for the fault zone IV in dark red.

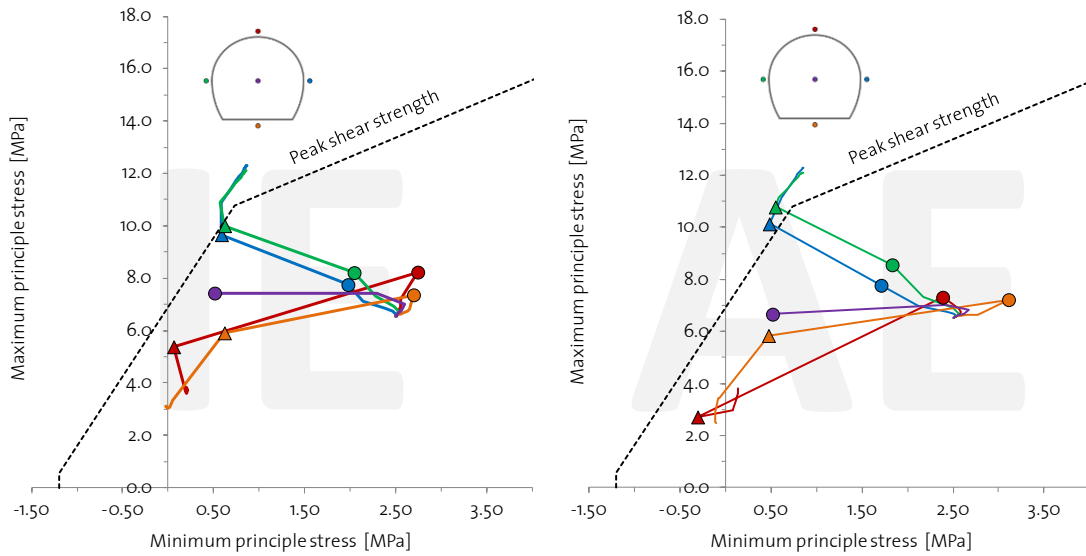


Figure 5-14: Stress path analysis for the intact rock representative for a homogenous model without fault zones. Results from the isotropic elastic (IE) model are shown on the left and results from the anisotropic elastic (AE) model are shown on the right. In both figures redistributed stresses are plotted against the bi-linear strength envelopes for intact S-specimens. The stress state at the beginning and at the end of the round length that passes the monitoring array is marked with a circle and a triangle.

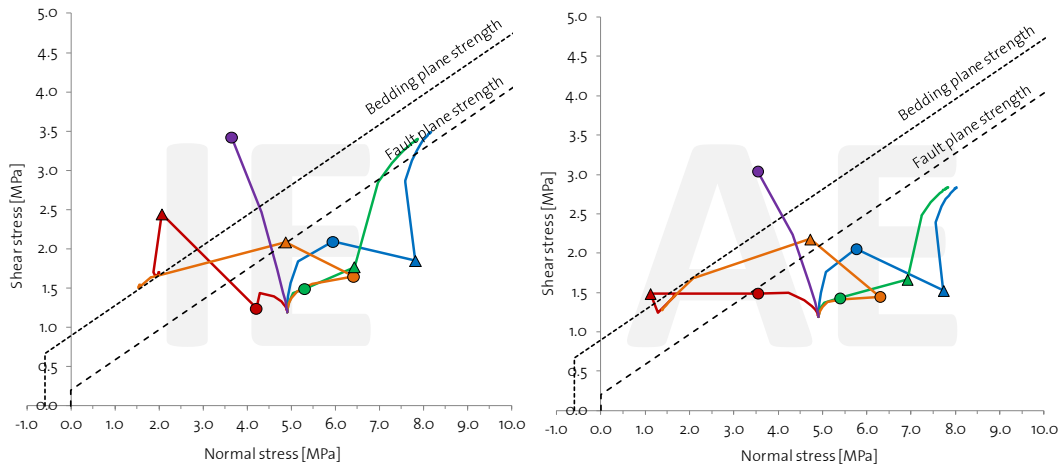


Figure 5-15: Stress path analysis for bedding and fault plane orientation representative for a homogenous model without fault zones. Results from the isotropic elastic (IE) model are shown on the left and results from the anisotropic elastic (AE) model are shown on the right. In both figures redistributed stresses are plotted against the linear strength envelopes for bedding and fault planes. The stress state at the beginning and at the end of the round length that passes the monitoring array is marked with a circle and a triangle.

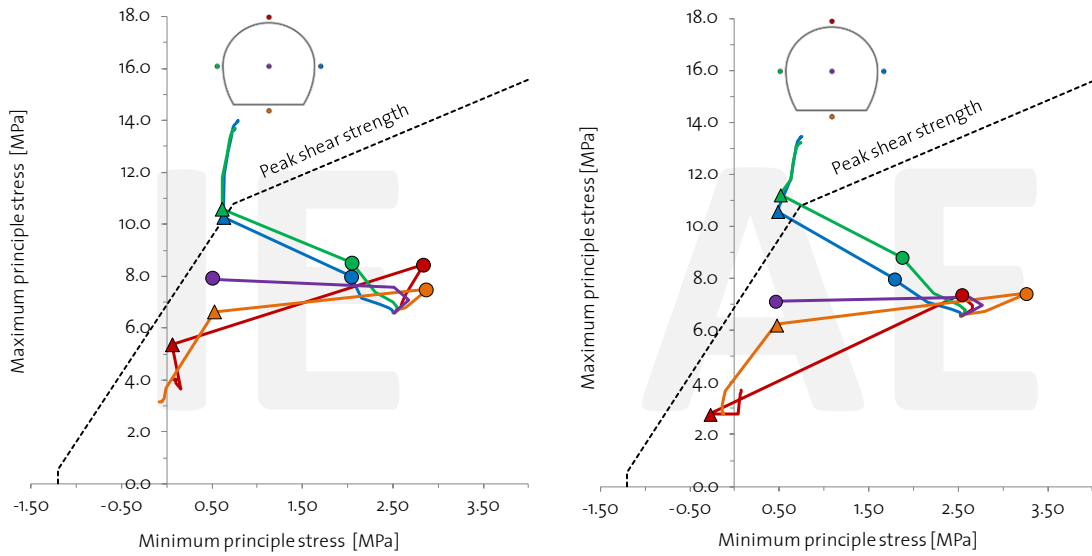


Figure 5-16: Stress path analysis for the intact rock presented for the monitoring array 8 located in the periphery of the fault zones. Refer to Figure 5-8 for monitoring array location. Results from the isotropic elastic (IE) model are shown on the left and results from the anisotropic elastic (AE) model are shown on the right. In both figures redistributed stresses are plotted against the bi-linear strength envelopes for intact S-specimens. The stress state at the beginning and at the end of the round length that passes the monitoring array is marked with a circle and a triangle.

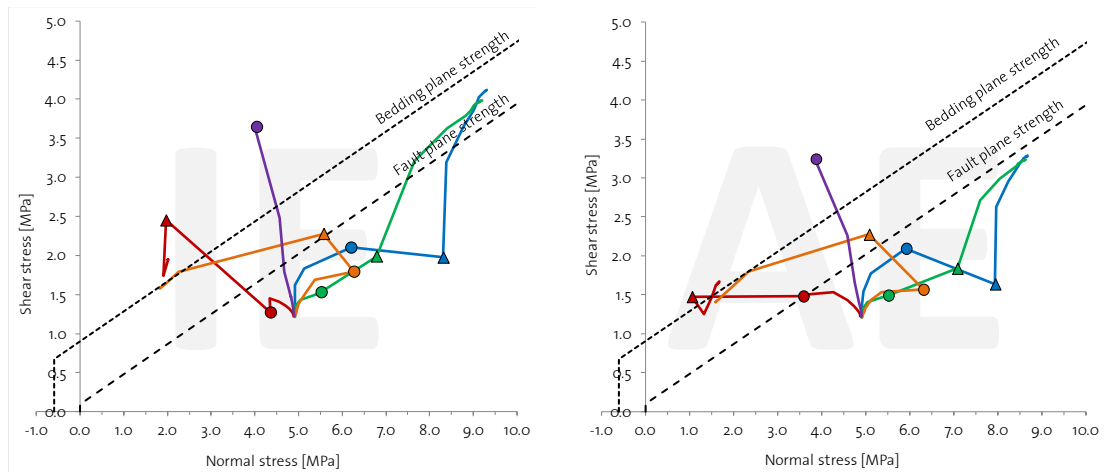


Figure 5-17: Stress path analysis for bedding and fault plane orientation presented for the monitoring array 8 located in the periphery of the fault zones. Refer to Figure 5-8 for monitoring array location. Results from the isotropic elastic (IE) model are shown on the left and results from the anisotropic elastic (AE) model are shown on the right. In both figures redistributed stresses are plotted against the linear strength envelopes for bedding and fault planes. The stress state at the beginning and at the end of the round length that passes the monitoring array is marked with a circle and a triangle.

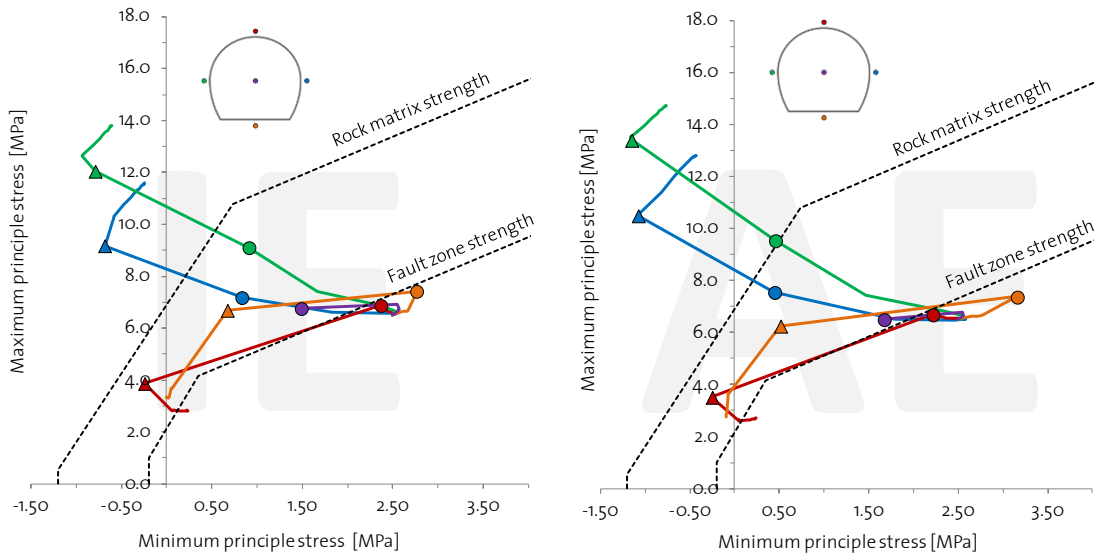


Figure 5-18: Stress path analysis for the intact rock presented for the monitoring array 12 located adjacent of the major fault zone. Refer to Figure 5-8 for monitoring array location. Results from the isotropic elastic (IE) model are shown on the left and results from the anisotropic elastic (AE) model are shown on the right. In both figures redistributed stresses are plotted against the bi-linear strength envelopes for intact S-specimens and the residual Z-specimens. The stress state at the beginning and at the end of the round length that passes the monitoring array is marked with a circle and a triangle.

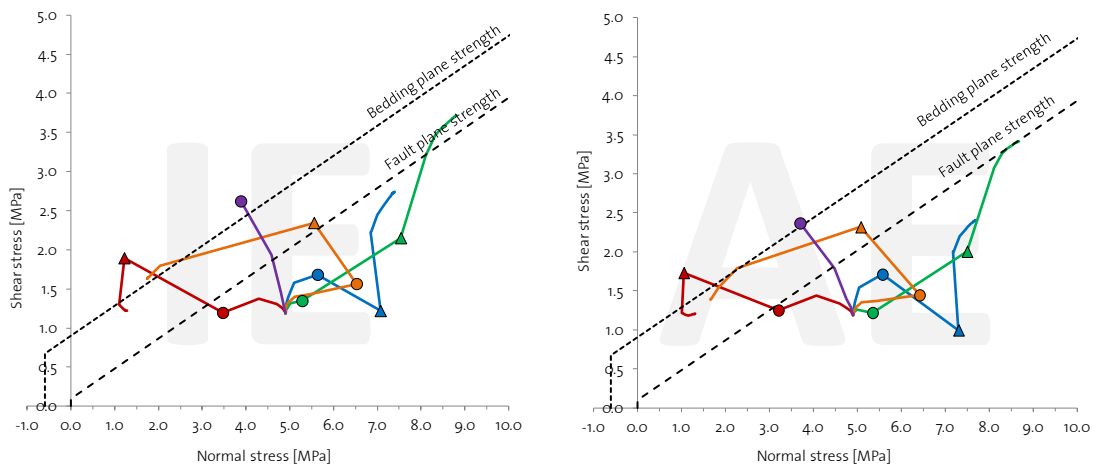


Figure 5-19: Stress path analysis for bedding and fault plane orientation presented for monitoring array 12 located in vicinity of the major fault zone. Refer to Figure 5-8 for monitoring array location. Results from the isotropic elastic (IE) model are shown on the left and results from the anisotropic elastic (AE) model are shown on the right. In both figures redistributed stresses are plotted against the linear strength envelopes for bedding and fault planes. The stress state at the beginning and at the end of the round length that passes the monitoring array is marked with a circle and a triangle.

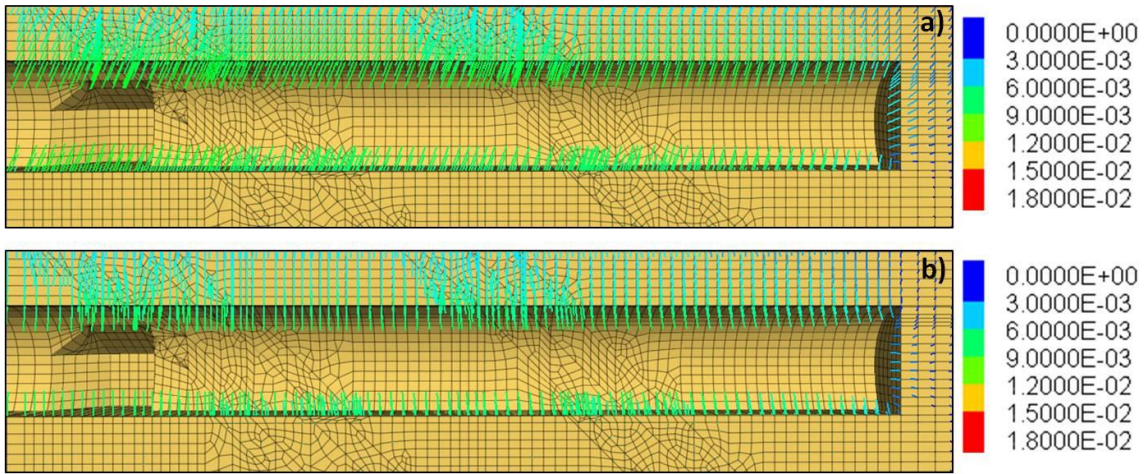


Figure 5-20: Total elastic displacement magnitudes (given in meter) and displacement vector orientations derived from a) the homogeneous anisotropic elastic model and b) the homogeneous isotropic elastic model.

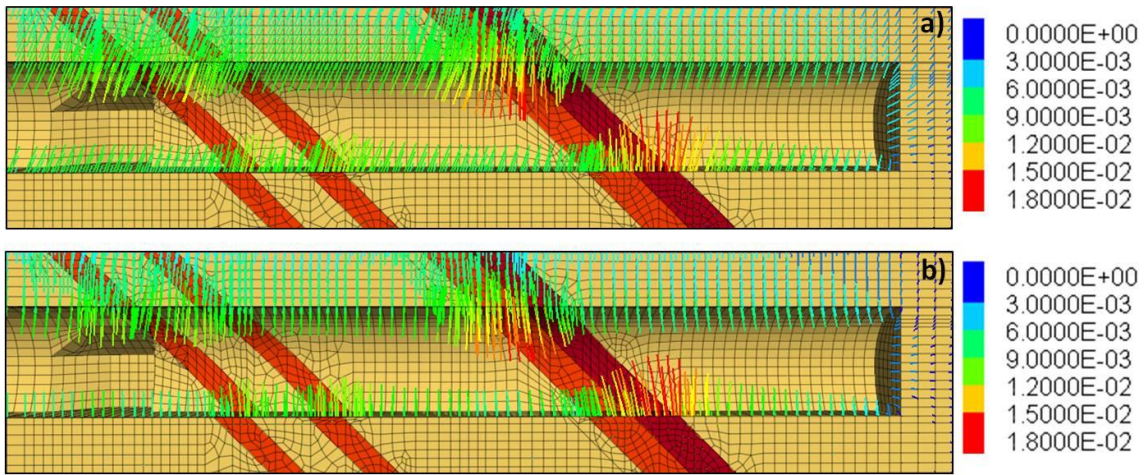


Figure 5-21: Total elastic displacement magnitudes (given in meter) and displacement vector orientations derived from a) the heterogeneous anisotropic elastic model and b) the heterogeneous isotropic elastic model.

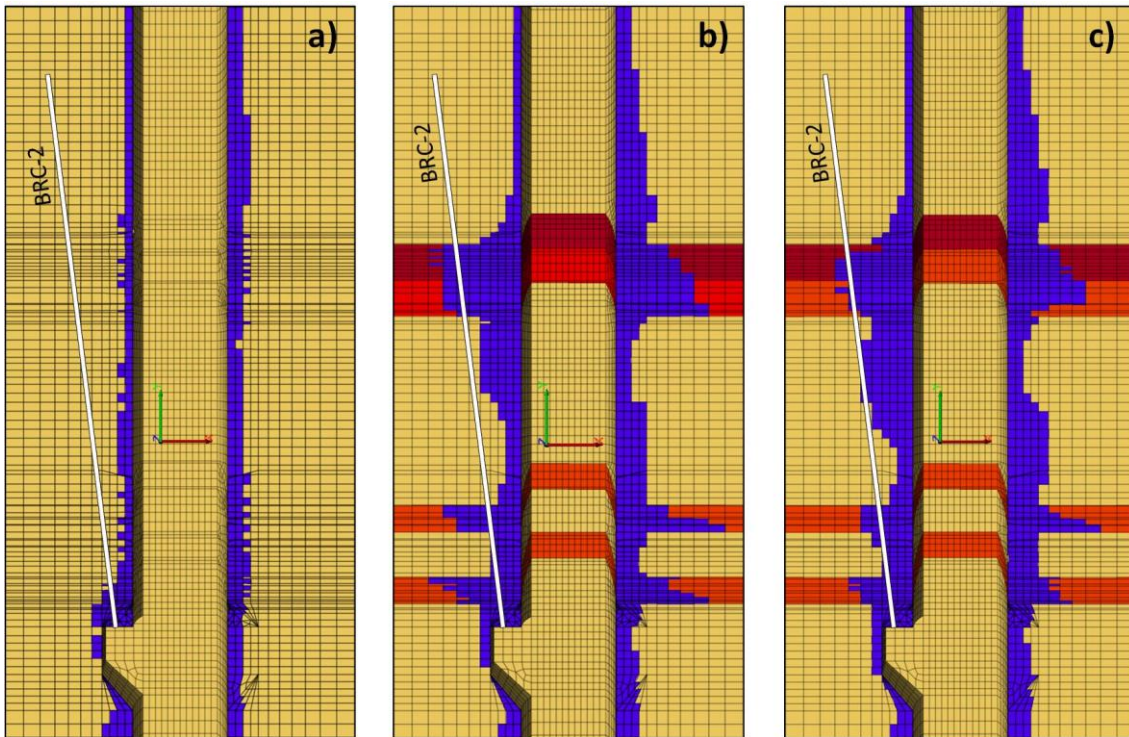


Figure 5-22: Horizontal cross-sections through the centerline of the tunnel showing the modeled radial extent of plastic failure (i.e. EDZ) for a) scenario 1 which does not include fault zones, b) scenario 2 with elastic fault zone properties as derived from laboratory testing, and c) scenario 3 assuming a 50% reduced Young's modulus in the fault zones.

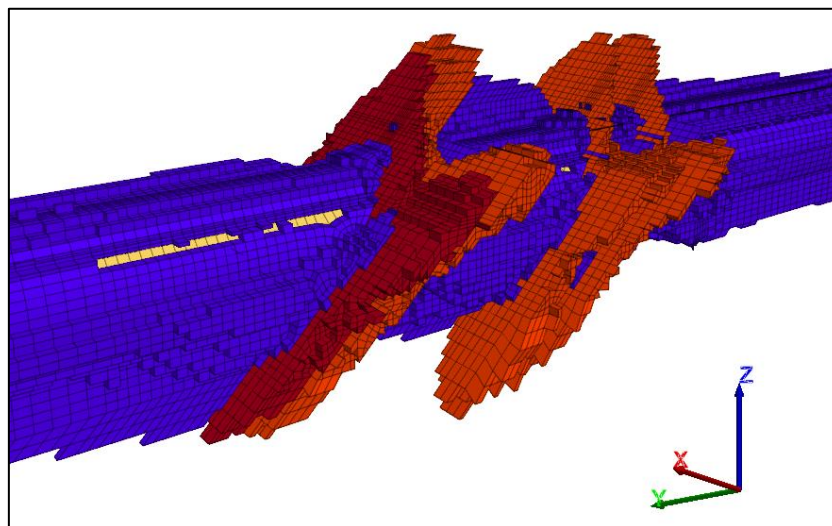


Figure 5-23: Three-dimensional representation of the modeled EDZ geometry around the mine-by experiment derived from scenario 2. Purple zones indicate plastic failure within the rock matrix and reddish zones indicate plastic failure within the different fault zone types. The oval-shaped EDZ with a larger extent in the vertical direction than in the radial direction normal to the tunnel axis is in general agreement with the conceptual EDZ geometry proposed by Thoeny 2014.

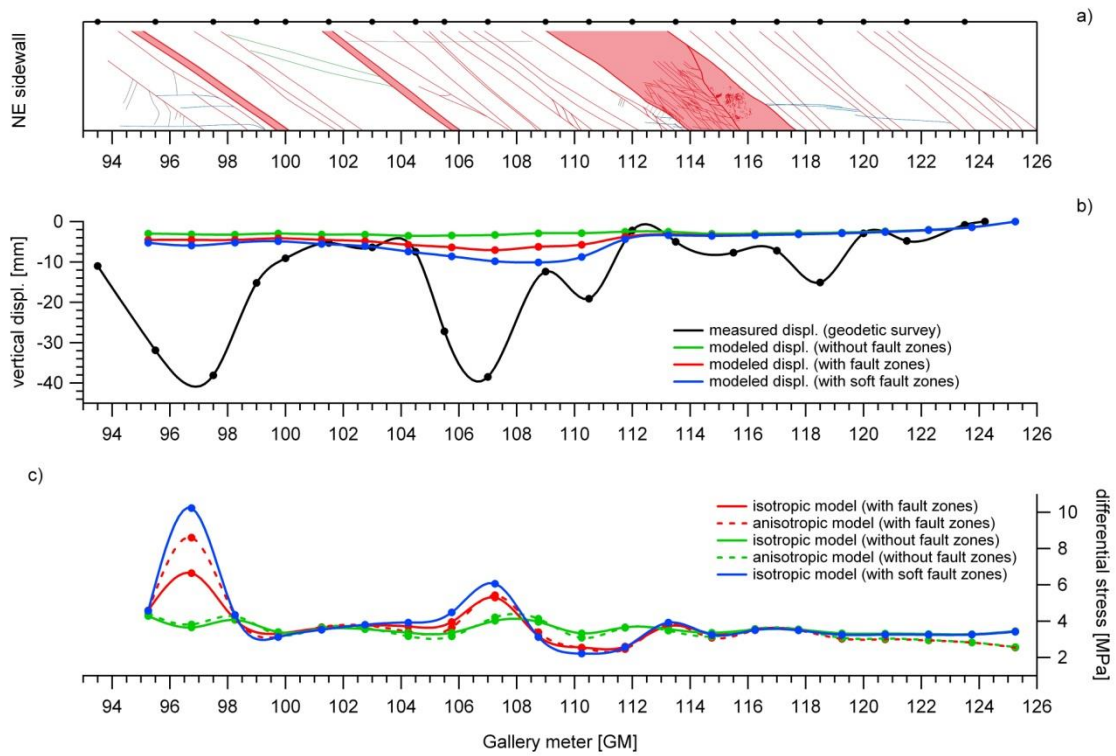


Figure 5-24: Vertical crown settlements derived from geodetic monitoring at the end of the excavation phase in comparison with elasto-plastic modeling results. a) Geological map of the NE-sidewall showing the location of the geodetic monitoring prisms in respect to the two minor and the major fault zone. b) Vertical crown displacements derived from geodetic monitoring and isotropic elasto-plastic (IEP) modeling. Note that for the modeled displacements, deformability of the fault zones were systematically decreased which results in enhanced displacements ahead of them. c) Differential stresses along the mine-by section derived from isotropic elastic (IE) and anisotropic elastic (AE) modeling.

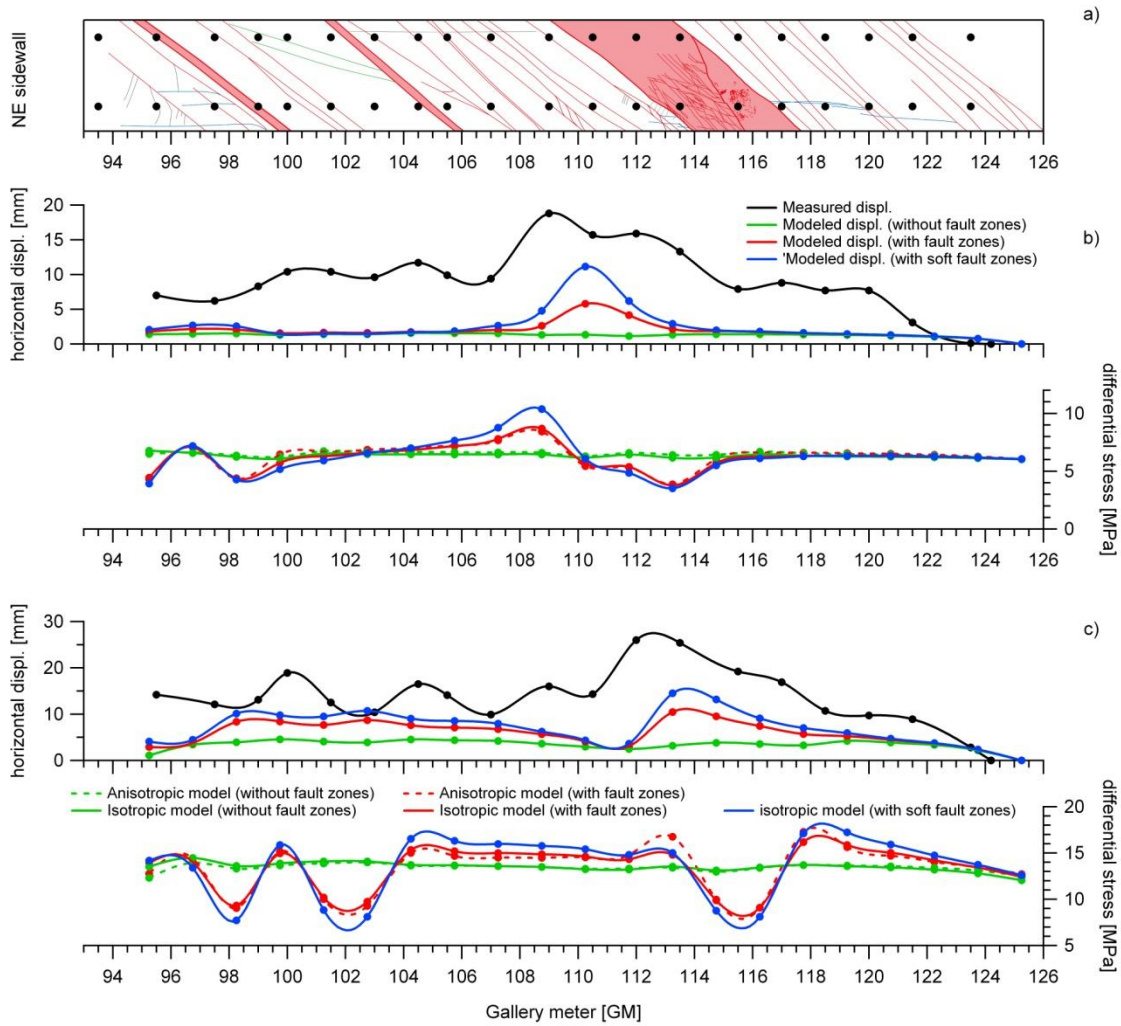


Figure 5-25: Horizontal displacements derived from geodetic monitoring at the end of the excavation phase in comparison with elasto-plastic modeling results. a) Geological map of the NE-sidewall showing the location of the geodetic monitoring prisms (upper and lower sidewall prisms) in respect to the two minor and the major fault zone. b) Horizontal displacements of the upper sidewall prisms derived from geodetic monitoring and isotropic elasto-plastic (IEP) modeling at the top, and corresponding differential stresses derived from isotropic elastic (IE) and anisotropic elastic (AE) modeling at the bottom. c) Horizontal displacements of the upper sidewall prisms derived from geodetic monitoring and isotropic elasto-plastic (IEP) modeling at the top, and corresponding differential stresses derived from isotropic elastic (IE) and anisotropic elastic (AE) modeling at the bottom.

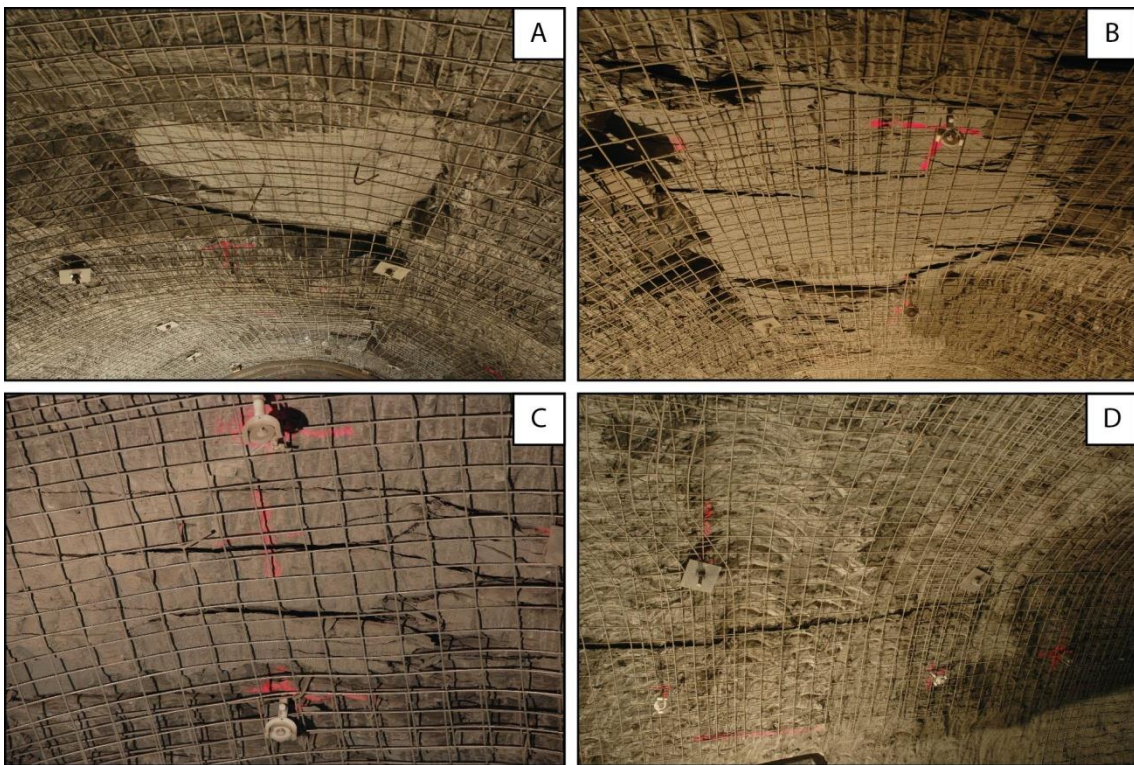


Figure 5-26: Observed failure mechanisms of the rock mass throughout the excavation of the mine-by section leading to minor and major tunnel instabilities. (A) Slab at the crown (GM 106 - GM 108) that progressively detached along a SW-dipping fault plane leading to settlements up to 45 mm. (B) Structural-controlled crown instability between GM 109 and GM 112. (C) Locally disintegrated rock mass at GM 118.5. (D) Upper discrete boundary of the sidewall spall on the NE-sidewall between GM 102 and GM 109. The upper sidewall prisms located on the spall indicating horizontal displacements up to 15 mm.

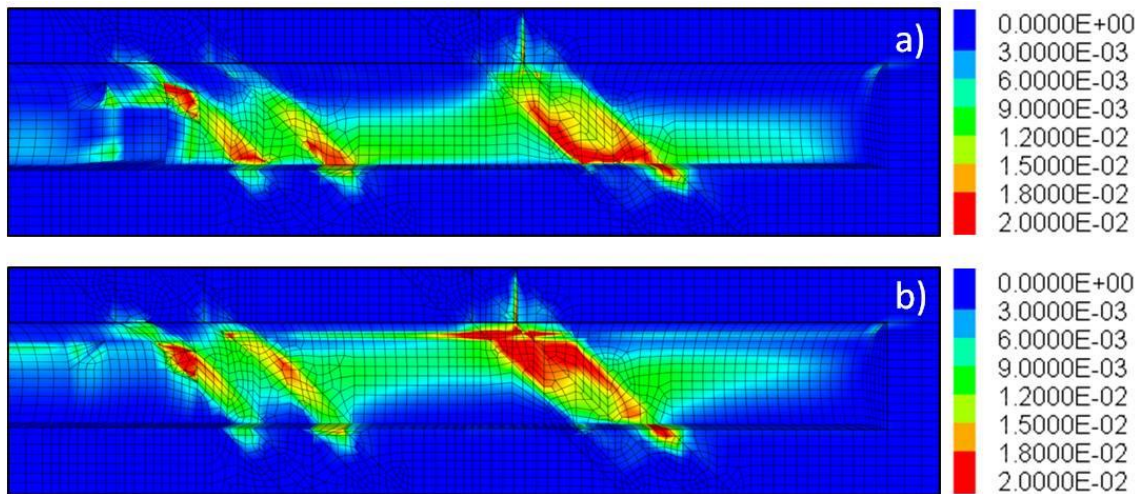


Figure 5-27: Distribution of accumulated plastic shear strain magnitudes of the rock matrix and the fault zones along a) the NE-sidewall and b) the SW-sidewall of the mine-by section. Plastic shear strain magnitudes are highest (yellow to red) within the fault zones and substantially enhanced (green) in the rock matrix in between the fault zones.

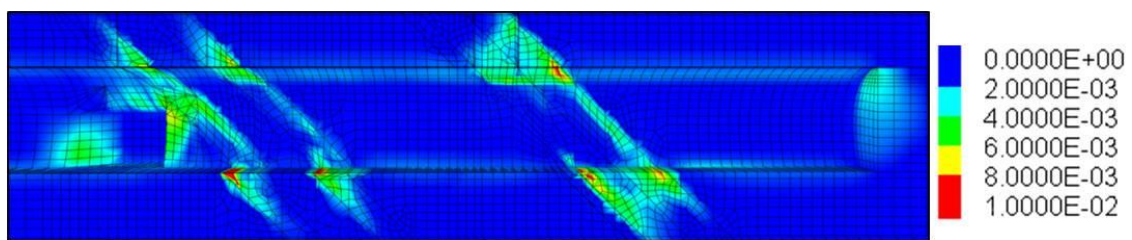


Figure 5-28: Distribution of accumulated plastic shear strain magnitudes of the ubiquitous joints along the NE-sidewall of the mine-by section. Plastic shear strain magnitudes are most prominent within the fault zones, in particular at the fault zone boundaries, while shearing along bedding planes is most pronounced at the upper tunnel face and around the start niche.

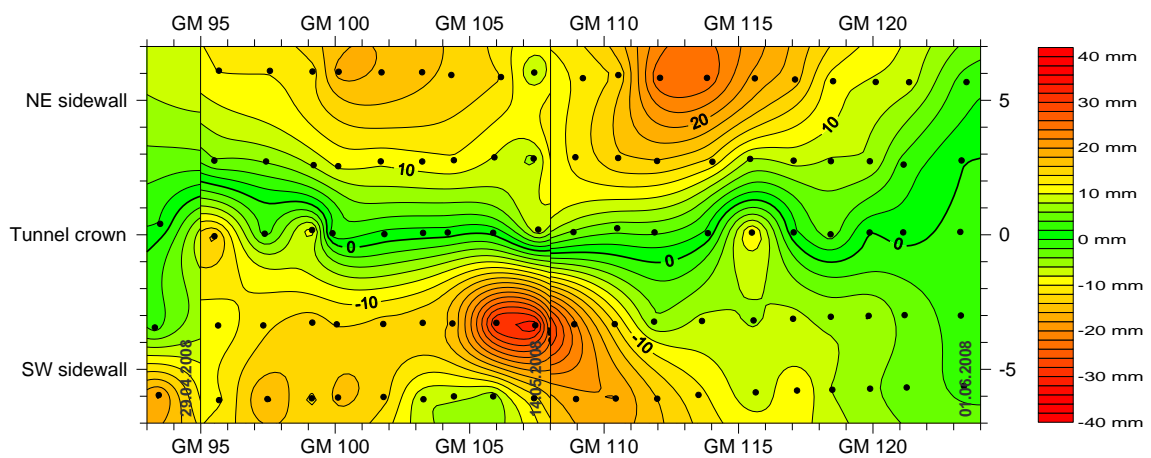


Figure 5-29: Horizontal displacement magnitudes derived from geodetic measurements at the end of the mine-by experiment presented as unwrapped contour map.

Table 5-1: Magnitudes and orientations of the in-situ principle stresses modified from Martin and Lanyon (2003) and Corkum (2006)

Principal stress	Stress tensor used in this study		Corkum (2006)	
	Magnitude	Trend / Plunge	Magnitude	Trend / Plunge
σ_1	6.5 MPa	210° / 70°	6 - 7 MPa	210° / 70°
σ_2	4.5 MPa	320° / 10°	4 - 5 MPa	320° / 07°
σ_3	2.5 MPa	050° / 15°	2 - 3 MPa	052° / 18°

Table 5-2: Elastic material properties derived from laboratory testing on intact (P- and S-specimen) and tectonically disturbed (S-specimen) OPA specimens (Amann et al. 2011a, b; Wymann 2013)

Elastic properties	P-specimen		S-specimen	
	intact	intact	slightly faulted	moderately faulted
Young's modulus (E)	6.0 GPa	2.0 GPa	1.2 GPa	0.8 GPa
Poisson's ratio (ν)	0.2	0.2	0.3	0.3

Table 5-3: Linear strength properties for peak and residual strength of P-, S- and Z-specimens derived from laboratory testing of intact OPA specimens with a water content > 6.5%

Plastic properties	P-specimen	S-specimen	Z-specimen
Peak cohesion (c_{peak})	5.0 MPa	3.0 MPa	2.0 MPa
Peak friction angel (ϕ_{peak})	19°	19°	19°
Tensile strength ($\sigma_{t peak}$)	1.8 MPa	1.2 MPa	1.5 MPa
Residual cohesion ($c_{residual}$)	0.5 MPa	0.5 MPa	0.3 MPa
Residual friction ($\phi_{residual}$)	19°	19°	19°

Table 5-4: Bi-linear strength properties for peak and residual strength of P-, S- and Z-specimens derived from laboratory testing of intact OPA specimens with a water content > 6.5%

Plastic properties	P-specimen	S-specimen	Z-specimen
Peak cohesion (c_1)	2.5 MPa	1.5 MPa	1.0 MPa
Peak friction angel (φ_1)	43°	43°	43°
Dilation angle (i_1)	32°	32°	32°
Peak cohesion (c_2)	7.5 MPa	4.0 MPa	3.0 MPa
Peak friction (φ_2)	11°	11°	11°
Tensile strength (σ_t)	1.8 MPa	1.2 MPa	1.5 MPa
Residual cohesion (c_1)	0.7 MPa	0.7 MPa	0.5 MPa
Residual friction (φ_1)	43°	43°	43°
Residual cohesion (c_2)	2.0 MPa	2.0 MPa	1.5 MPa
Residual friction (φ_2)	11°	11°	11°

Table 5-5: Linear strength properties for peak and residual strength of bedding and fault planes derived from direct shear testing (Popp & Salzer 2007; Haug 2009; Amann et al. 2010)

Plastic properties	Bedding planes	Tectonic fault planes
Peak cohesion (c_{peak})	0.9 MPa	0.1 MPa
Peak friction angel (φ_{peak})	21°	21°
Tensile strength ($\sigma_{t peak}$)	0.6 MPa	0.6 MPa *
Residual cohesion ($c_{residual}$)	0.2 MPa	0.1 MPa
Residual friction ($\varphi_{residual}$)	21°	21°

* assumed from tensile strength of bedding planes

Table 5-6: Bi-linear strength properties for peak and residual strength of bedding and fault planes derived from direct shear testing (Popp & Salzer 2007; Haug 2009; Amann et al. 2010)

Plastic properties	Bedding planes	Tectonic fault planes
Peak cohesion (c_1)	0.6 MPa	0.1 MPa
Peak friction angel (φ_1)	30 °	22 °
Dilation angle (i_1)	19 °	11 °
Peak cohesion (c_2)	1.5 MPa	0.6 MPa
Peak friction (φ_2)	11 °	11 °
Tensile strength (σ_t)	0.6 MPa	0.6 MPa *
Residual cohesion (c_1)	0.2 MPa	0.1 MPa
Residual friction (φ_1)	22 °	22 °
Residual cohesion (c_2)	0.8 MPa	0.6 MPa
Residual friction (φ_2)	11 °	11 °

* assumed from tensile strength of bedding planes

Table 5-7: Material properties used for the isotropic and anisotropic elastic model

Elastic properties	Isotropic model	Anisotropic model
Rock density	2450 kg/m ³	2450 kg/m ³
Rock matrix		
Young's modulus parallel to bedding ($E_1 = E_2$)	2.0 / 4.0 / 6.0 GPa	6.0 GPa
Young's modulus perp. to bedding (E_3)		2.0 GPa
Shear modulus perp. to bedding ($G_{13} = G_{23}$)		1.15 GPa
Poisson's ratio parallel to bedding (ν_{12})	0.2	0.2
Poisson's ratio perp. to bedding ($\nu_{13} = \nu_{23}$)		0.2
Fault zones I - III		
Young's modulus (E)		1.2 GPa
Poisson's ratio (ν)		0.3
Fault zone IV		
Young's modulus (E)		0.8 GPa
Poisson's ratio (ν)		0.3

Table 5-8: Material properties used for the elasto-plastic ubiquitous joint model

Elastic properties	Intact rock	Fault zone I-III	Fault zone IV
Rock matrix			
Rock density (ρ)	2450 kg/m ³	2450 kg/m ³	2450 kg/m ³
Young's modulus (E)	4.0 GPa	1.2 / 0.6 GPa	0.8 / 0.4 GPa
Poisson's ratio (ν)	0.2	0.3	0.3
Plastic properties			
Rock matrix	(S-specimen prop.)	(residual strength of Z-specimen)	
Peak cohesion (c_1)	1.5 MPa	0.5 MPa	
Peak friction angle (ϕ_1)	43°	43°	
Dilation angle (i_1)	32°	0°	
Peak cohesion (c_2)	4.0 MPa	1.5 MPa	
Peak friction (ϕ_2)	11°	11°	
Tensile strength (σ_t)	1.2 MPa	0.6 MPa	
Residual cohesion (c_1)	0.7 MPa	0.2 MPa	
Residual friction (ϕ_1)	43°	43°	
Residual cohesion (c_2)	2.0 MPa	0.8 MPa	
Residual friction (ϕ_2)	11°	11°	
Ubiquitous joints	(bedding prop.)	(fault prop.)	
Peak cohesion (c_1)	0.6 MPa	0.2 MPa	
Peak friction angle (ϕ_1)	30°	22°	
Dilation angle (i_1)	19°	0°	
Peak cohesion (c_2)	1.5 MPa	0.6 MPa	
Peak friction (ϕ_2)	11°	11°	
Tensile strength (σ_t)	0.6 MPa	0.6 MPa	
Residual cohesion (c_1)	0.2 MPa	0.2 MPa	
Residual friction (ϕ_1)	22°	22°	
Residual cohesion (c_2)	0.8 MPa	0.6 MPa	
Residual friction (ϕ_2)	11°	11°	

6 SUMMARY AND RECOMMENDATIONS

6.1 Summary

This thesis utilized detailed field data from a mine-by experiment at the Mont Terri Underground Rock Laboratory in Switzerland and subsequent site-specific numerical modeling to contribute to the advancing knowledge of rock mechanical processes in the near-field of a future emplacement drift in heterogeneous and anisotropic Opalinus Clay. The thesis illustrates that spatial variations in rock mass properties, primarily caused by tectonic faults and fault zones, have a significant influence on redistributed stresses and hence on induced fracturing and associated deformations in the near-field of a tunnel in faulted Opalinus Clay. Open questions regarding the geomechanical influence of multi-scale tectonic faults on the short- and long-term rock mass response were successfully addressed and delivered new insights into their mechanical and kinematic behavior in response to the tunnel excavation and development of the EDZ. The major findings and results of this study are summarized in the following:

6.1.1 Structural and kinematic relationship between natural and excavation-induced fractures

- Complementary geological and geophysical characterization techniques on the tunnel and borehole-scale were used for a qualitative and quantitative analysis of the structural and kinematic relationship between natural and excavation-induced fractures around the mine-by experiment. The fracture network prior to and after excavation was characterized by integrating structural data from geological mapping of excavation surfaces and from four pre- and post-excavation boreholes, comprising geological drillcore logging and optical televiewer imaging. Geophysical investigations including single-hole interval velocity measurements and seismic refraction tomography were used to quantify spatial variations in the seismic velocities and thus in the rock mass properties and the extent of the excavation-induced damage zone.
- Integration of geological mapping, borehole logging and seismic velocity measurements revealed that spatial variations in fault frequency along the tunnel axis alter the homogeneity of the rock mass in strength and deformability which has a substantial effect on the location and the radial extent of induced damage on both, the borehole and the tunnel-scale. Induced fracturing was consistently enhanced in the stiffer rock mass adjacent to the more compliant fault zones.
- Detailed structural and kinematic analyses revealed that failure mechanisms, orientations and frequencies of excavation-induced fractures are significantly influenced by the occurrence and characteristics of pre-existing tectonic faults. At the sidewalls where fault plane reactivation or bedding shear was kinematically constrained, extensional fracturing tangential to the tunnel circumference was the dominating failure mode. At the tunnel face and the tunnel invert, where fault and bedding planes were kinematically free, extensional brittle failure and shearing along bedding planes was dominant in sparsely faulted ($0 - 1$ fault/m²) tunnel sections, while a combination of shearing along fault planes associated

with extensile failure prevailed in tunnel sections that are intersected by 1 - 3 faults/m². With increasing fault density (> 4 faults/m²), reactivation of densely spaced fault planes became more evident indicating a transition from extensional macroscopic failure to shearing. Furthermore it was observed that bedding shear and reactivation of tectonic fault planes occurred in normal faulting mode at the tunnel face, and in thrust faulting mode at the tunnel invert. Thus, consideration of pre-existing faults and fault zones and their mechanical characteristics was necessary to understand both the failure mechanisms and the spatial distribution of macroscopic EDZ fractures along the mine-by experiment.

- Integration of geological mapping and borehole logging data revealed that the excavation-induced damage zone around the mine-by experiment is composed of reactivated fault planes and seven different types of induced fractures (IF):
 - (IF1) extensional fractures parallel to the sidewalls,
 - (IF2) extensional fractures oblique to the tunnel axis at the sidewalls,
 - (IF3) sub-horizontal extensional fractures parallel to the tunnel invert,
 - (IF4) extensional and/or shear fractures along bedding planes at the tunnel invert,
 - (IF5) extensional fractures perpendicular to sheared bedding or reactivated fault planes at the tunnel invert,
 - (IF6) shear fractures along bedding planes at the tunnel face,
 - (IF7) extensional fractures sub-perpendicular to sheared bedding planes or reactivated tectonic faults at the tunnel face.
- Based on geological and geophysical data a new conceptual model of the EDZ geometry around the mine-by section was established. The model suggests a strongly damaged inner zone with a consistent radial extent of 0.5 - 1.5 m and less damaged outer zones with a radial extent of 4 m within fault zones and 2 - 3 m in between the fault zones. The depth of the inner zone seems to be unaffected by variations in fault plane density, while the radial extent of the outer zone is substantially influenced by fault zones.

6.1.2 Spatial and temporal evolution of the excavation-induced displacement field

- A multi-component monitoring system, including a Chain-Deflectometer, an inclinometer and two multi-point Magnet-Extensometers located in boreholes parallel and perpendicular to the gallery boundaries was used to continuously capture the rock mass response throughout and after the excavation of the mine-by section. Complementary, high resolution geodetic and laser scanning surveying was performed throughout the excavation phase. These data provided a sound basis to analyze the spatial and temporal evolution of excavation-induced deformations in the near-field of the mine-by section.
- Geodetic displacement monitoring data revealed that the overall rock mass response of faulted Opalinus Clay is mainly controlled by the intact rock anisotropy due to the pronounced bedding. Displacement vectors consistently showed a preferred orientation sub-perpendicular to bedding planes thereby indicating heaving at the lower sidewalls and below the tunnel invert and settlements at the crown and the upper sidewalls. Pre-existing tectonic faults and

their spatial variations along the tunnel axis significantly modify the general surface displacement field in magnitude, but also in direction depending on their orientation relative to the tunnel orientation.

- Integration of geodetic and laser scanner measurement data revealed that the short-term rock mass response of faulted Opalinus Clay is substantially governed by both the rock anisotropy and the failure behavior of individual fault planes, while the overall rock mass behavior correlates more with variations in larger-scale deformability and strength heterogeneities. Integration of surface displacements and borehole deformations considering both the fracture and the tunnel-scale revealed that individual fault planes were most influential on the rock mass response at the tunnel face, crown and the invert, but were less influential at the sidewalls and at larger depths in the rock mass. At the sidewalls, where fault plane reactivation was of minor relevance due to their unfavorable orientation, the rock mass response was dominated by extensional fracturing through the intact rock matrix resulting in large displacements adjacent to large-scale rock mass heterogeneities. This failure behavior was associated with the formation of slab-like structures approximately half a tunnel diameter behind the advancing tunnel face which decisively affected the tunnel stability.
- Borehole-based deformation monitoring data during the excavation phase revealed that excavation-induced deformations at depth were primarily accommodated along minor and major fault zones at the tunnel sidewall and along discrete fault planes at the tunnel invert. However, long-term deformations below the tunnel invert exceeded the deformations that were measured during the excavation phase by far, in particular in the vertical direction (i.e. oblique to the rock mass anisotropy). This is in contrast to the long-term deformation behavior observed at the sidewall which suggests that differential displacements are irrelevant at the given stress level in the long-term, even though the rock mass is considerably heterogeneous.

6.1.3 Stress redistribution around an excavation in anisotropic and heterogeneous clay rock

- A numerical study exploring the effect of the rock anisotropy (due to bedding) and large-scale rock mass heterogeneities (due to fault zones) on excavation-induced stress redistribution and associated displacements was performed with the three-dimensional continuum code FLAC_{3D} which allows to simulate the elastic and plastic deformation behavior around the tunnel. Both, elastic and plastic material properties used in this numerical study were solely derived from conventional laboratory testing on Opalinus Clay specimens with a water content higher than 6.5%. Through combined analysis of the site-specific, three-dimensional numerical models and deformation monitoring data from the mine-by experiment, it was demonstrated that deformability and strength heterogeneities in faulted Opalinus Clay have a significant influence on the redistributed stresses and hence on induced fracturing and associated deformations in the tunnel near-field.
- Elastic analyses revealed that large-scale heterogeneities in deformability lead to substantial stress concentrations in the rock mass adjacent to more compliant zones. Stress magnitudes and the affected extent in the adjacent rock mass are

strongly dependent on the stiffness contrast between the fault zone and the rock matrix, whereby a high stiffness contrast results in the highest stress magnitudes and the largest extent along the tunnel axis.

- Although not explicitly implemented in the numerical model, information regarding the kinematic failure modes of bedding and bedding-parallel fault planes was gained from elastic stress path analyses. Elastic modeling suggested that at the tunnel face shearing along fault and bedding planes is the most likely failure mechanism and primarily associated with normal faulting. Stress path analysis also indicated that reactivation of fault planes is initiated 2 - 3 m ahead of the face, while shearing along bedding planes initiating only 0.5 - 1 m ahead of the face. At the tunnel invert and the crown, shearing along fault and bedding planes is also the most likely failure mechanism, however, shearing is consistently initiated behind the tunnel face and primarily associated with reverse faulting. Elastic stress path analysis further suggested that extensional fracturing is the primary failure mechanism at the sidewalls. In the vicinity of fault zones substantially enhanced stresses ahead of the tunnel face may lead to the formation of extensional fractures sub-parallel to the tunnel face. At larger distance from the tunnel face (i.e. 0.5 - 1 tunnel diameter) extensional fractures may form on both sidewalls tangential to the tunnel circumference. Elastic stress path analyses were able to adequately predict both, the failure locations around the tunnel and the kinematic failure modes of discrete fault and bedding planes as observed in the field.
- Elasto-plastic analyses showed that depth and depth variations of the EDZ are substantially affected by strength and deformability heterogeneities along the tunnel axis. Model results suggest an EDZ depth of 4 - 5 m within fault zones, a depth of 2 - 3 m adjacent to fault zones and a depth of 0.5 - 1 m outside the range of influence of fault zones. The modeled EDZ depth and EDZ depth variations are in agreement with geophysical field investigations along both sidewalls of the mine-by experiment.
- The elasto-plastic modeling revealed displacement magnitudes similar to the measured magnitudes. The agreement with field measurements is, however, altered in zones where structural controlled instabilities or major faults and associated dilatant behavior was observed. Even though the displacement magnitudes in these zones are not well captured by the numerical model, these zones coincide in extent and location with the extent and location of the maximum modeled plastic shear strain.
- Since elasto-plastic models were able to reasonably reproduce observed displacement magnitudes and depth variations in the EDZ by using a site-specific geometry and strength properties derived from laboratory testing, it is suggested that these properties are representative for the short-term undrained response of Opalinus Clay (shaley facies) at the Mont Terri URL.

6.2 Recommendations

This thesis illustrates the mechanical relevance of pre-existing faults on the excavation-induced rock mass behavior of faulted Opalinus Clay during and after tunnel construction. It was shown that the kinematics associated with pre-existing faults and

fault zones play a key role in the type of excavation-induced damage and the resulting formation of the EDZ as well as its spatial development. Furthermore, it was demonstrated that spatial variations in rock mass properties, primarily caused by tectonic faults and fault zones, have a significant influence on redistributed stresses and hence on induced fracturing and associated deformations in the tunnel near-field. Thus, identification and characterization of the pre-existing tectonic faults is a major issue in the prediction of the EDZ geometry around a tunnel and the assessment of tunnel performance, in particular in faulted rock masses. However, the identification of natural faults in anisotropic clay rocks, especially bedding-parallel fault planes, is challenging. Application of only one investigation method might be misleading or incomplete as shown for the identification of the major fault zone with the pre-excavation borehole BRC-2. Core logging and OPTV logging were not sufficient to accurately identify the three meter thick fault zone. Only when seismic methods (i.e. USIVM surveying) were applied its exact location and extent could be confirmed. It was shown that combining complementary investigation methods vastly improves the reliability of the characterization of the natural fracture network. Seismic methods, however, further allow variations in rock mass properties to be quantified and thus the identification of large-scale rock mass heterogeneities which alter the rock mass strength and deformability to be more precisely characterized. Knowledge of fault locations and orientations along instrumented boreholes is of major relevance for a reliable analysis and interpretation of the measured displacements and deformations.

Assessment of rock mechanical processes in the near-field of the tunnel requires reliable knowledge about the in-situ rock mass properties. Based on newly performed and existing laboratory test results, bi-linear strength criteria were established which account for the failure behavior in the low confining stress range as encountered in the near-field of an underground excavation. For the analysis only specimens with a natural water content higher than 6.5% were used. These test results are considered more representative of the short-term in-situ conditions. Results from specimens with lower water content are highly influenced by matrix suction and thus should not be utilized for the modeling of the short-term response as investigated herein.

6.3 Outlook

Rock mechanical processes relevant for the long-term response of Opalinus Clay in the near-field of the tunnel were evident in the displacement monitoring data of the TRIVEC, the extensometer and the deflectometer, but were not considered in this study. It is suggested that these long-term deformations can be attributed to hydro-mechanical processes. However, as shown in the laboratory tests, water content and thus saturation have a significant influence on the deformation and strength behavior of Opalinus Clay. De- and re-saturation of the rock mass in the near-field of the tunnel surface as consequence of variations in relative humidity thus have a significant effect on the long-term strength and deformation behavior of the surrounding rock, and thus must be understood to implement them into numerical models. The long-term evolution of the EDZ and displacements which might be, to a certain extent, associated with dissipation of excess pore pressure cannot be modeled with the currently available rock mechanical properties (i.e. undrained properties). However, detailed studies are on the way for determining both, the poroelastic properties and the drained strength properties.

Limitations due to available constitutive laws of the code FLAC_{3D} did not allow for elasto-plastic modeling with an anisotropic model. The measured rock mass response, however, is anisotropic and thus an anisotropic elasto-plastic model should be used to adequately model the stress redistribution around the tunnel and reproduce the displacement vector directions. Due to the complex geological conditions that were encountered within the mine-by section, modeling of discrete fault planes with a discontinuum code was not possible. However, modeling of discrete fault planes which allow for slip and opening along them may reveal additional information about the kinematic behavior of pre-existing structures and associated local stress changes. However, numerical modeling of discrete fault planes should first be applied for tunnel sections in less faulted Opalinus Clay to understand the fundamental behavior without the influence of interfering faults and fault zones. Fracture mechanics codes in which a limited number of pre-existing structures can be implemented would also provide relevant information related to the local influence of shearing and induced brittle failure in clay rocks.

APPENDIX A

A1 Borehole data: Drillcore maps

A total of four boreholes were drilled throughout the mine-by experiment (Figure B 1). Borehole BRC-1 is located at GM 93.5 and was drilled from the tunnel invert vertically down to a depth of 8.1 meter, crossing the bedding at approximately 45 degrees. Borehole BRC-2 is located within the NE-sidewall of the mine-by section and was drilled from the start niche sub-parallel to the tunnel alignment (azimuth 152°) at the level of the springline. The borehole axis dips with 2 degrees towards azimuth 144° , thus crossing the bedding at an angle of approximately 45 degrees. Boreholes BRC-3 and BRC-4 were both drilled from the tunnel invert with an inclination of 60 degrees towards azimuth 335° and 331° , respectively. Thus both cross the bedding sub-perpendicularly. Borehole BRC-3 was drilled from GM 110 to a length of 24.5 m, and borehole BRC-4 was drilled from GM 107 to a length of 19.6 m. All boreholes were drilled with double (BRC-1 and 2) or triple (BRC-3 and 4) tube core barrels to minimize drilling-induced fracturing and to acquire high quality core samples for rock mechanical laboratory testing. Drillcores were mapped and photographed immediately after extraction from the drill stem. The digitized maps are presented in the following for each borehole separately.

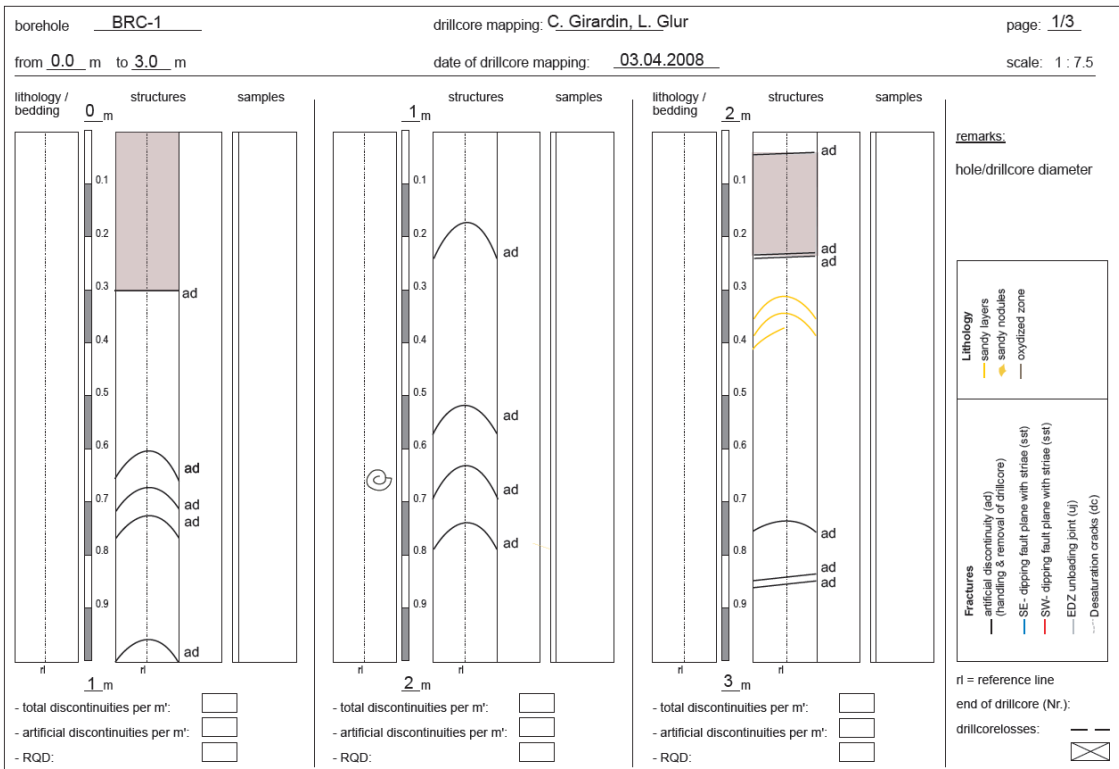


Figure A 2: Drillcore map of BRC-1 (Girardin et al. 2008).

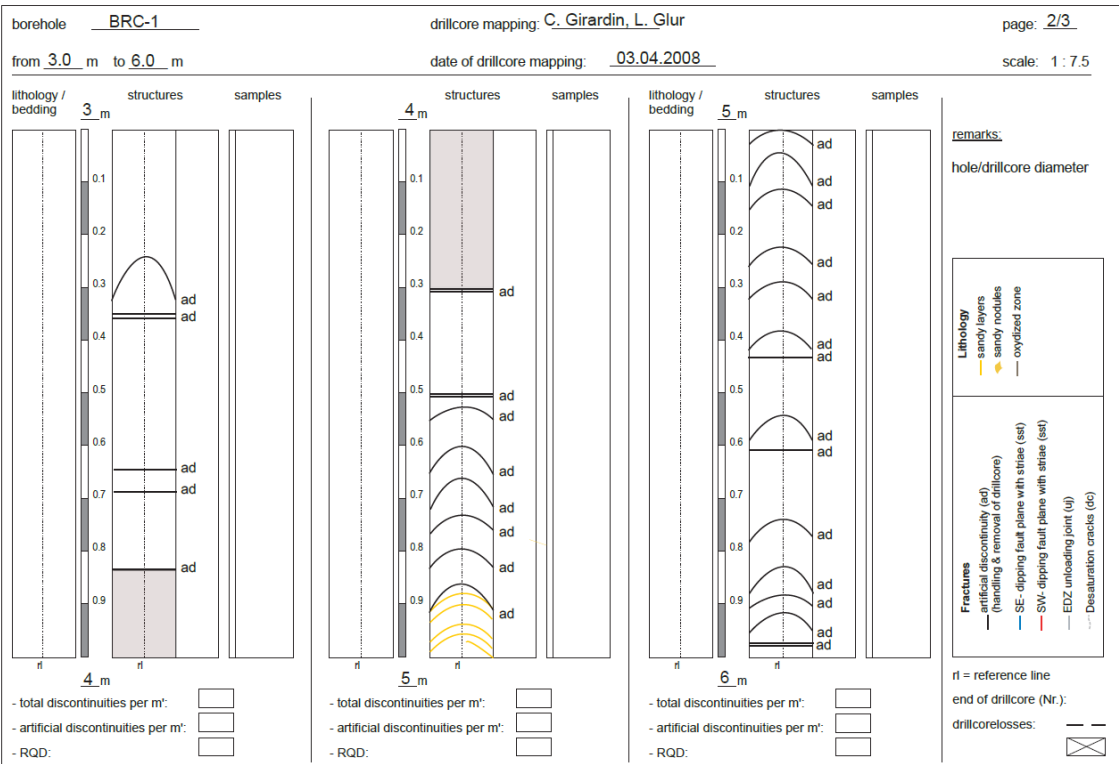


Figure A 3: Drillcore map of BRC-1 (Girardin et al. 2008).

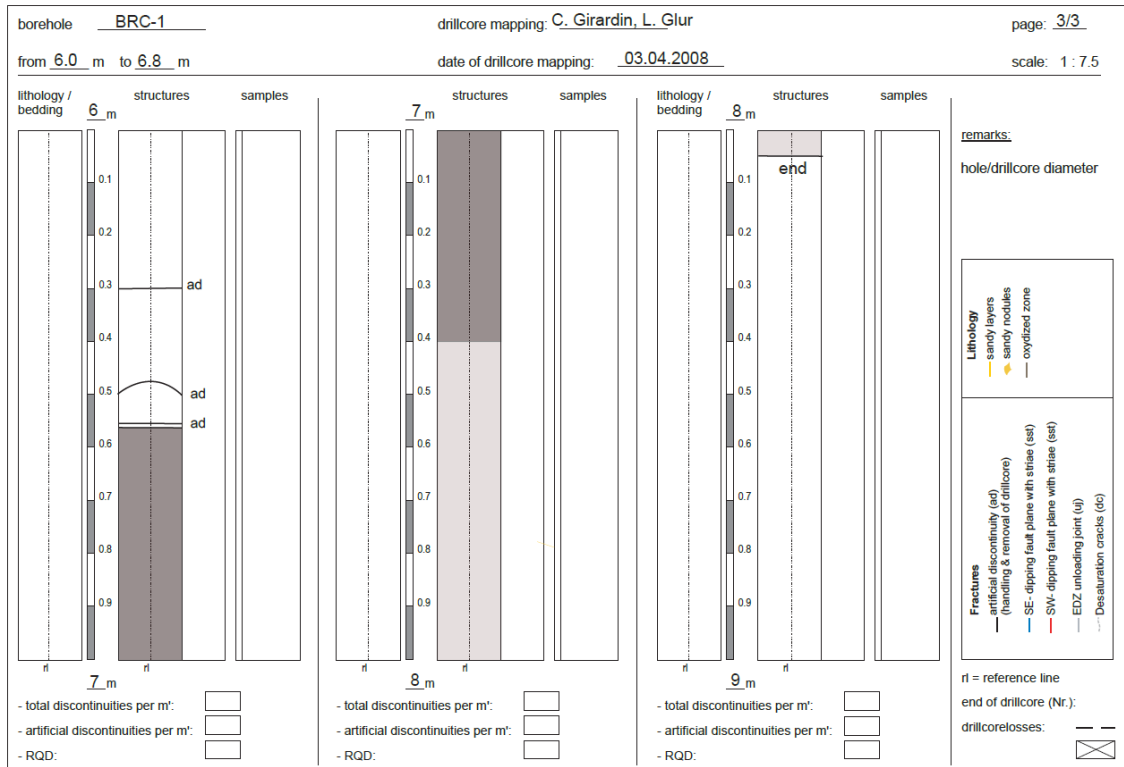


Figure A 4: Drillcore map of BRC-1 (Girardin et al. 2008).

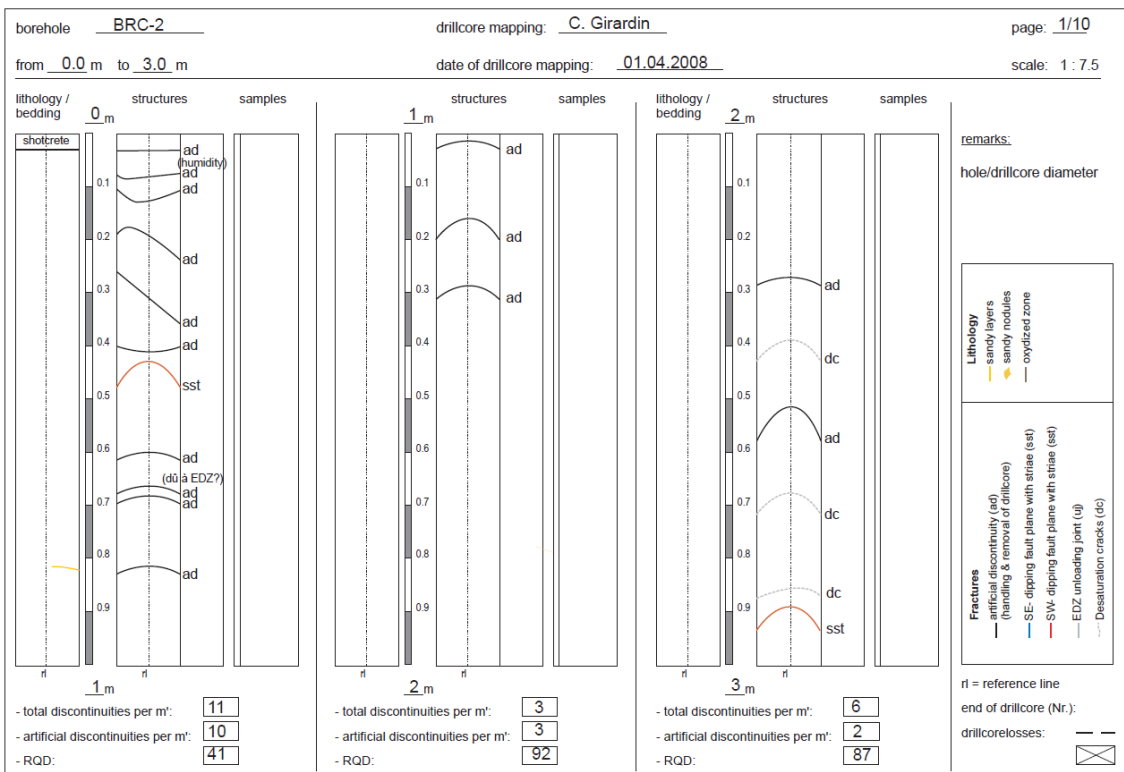


Figure A 5: Drillcore map of BRC-2 (Girardin et al. 2008).

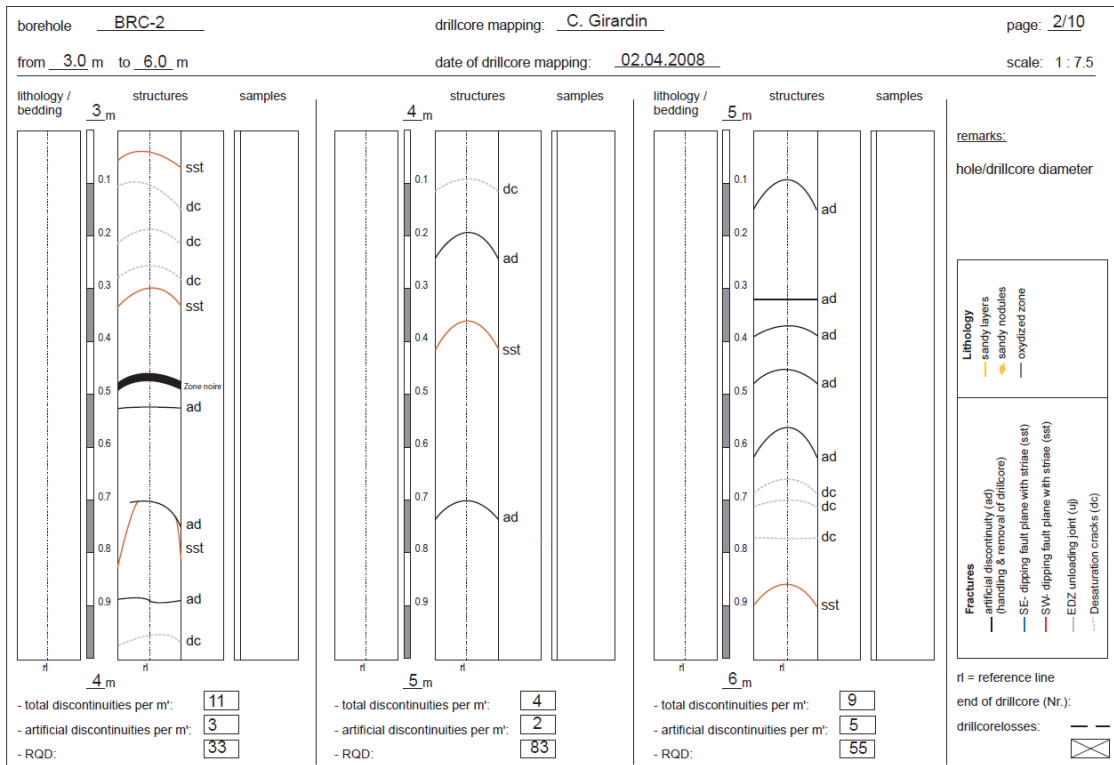


Figure A 6: Drillcore map of BRC-2 (Girardin et al. 2008).

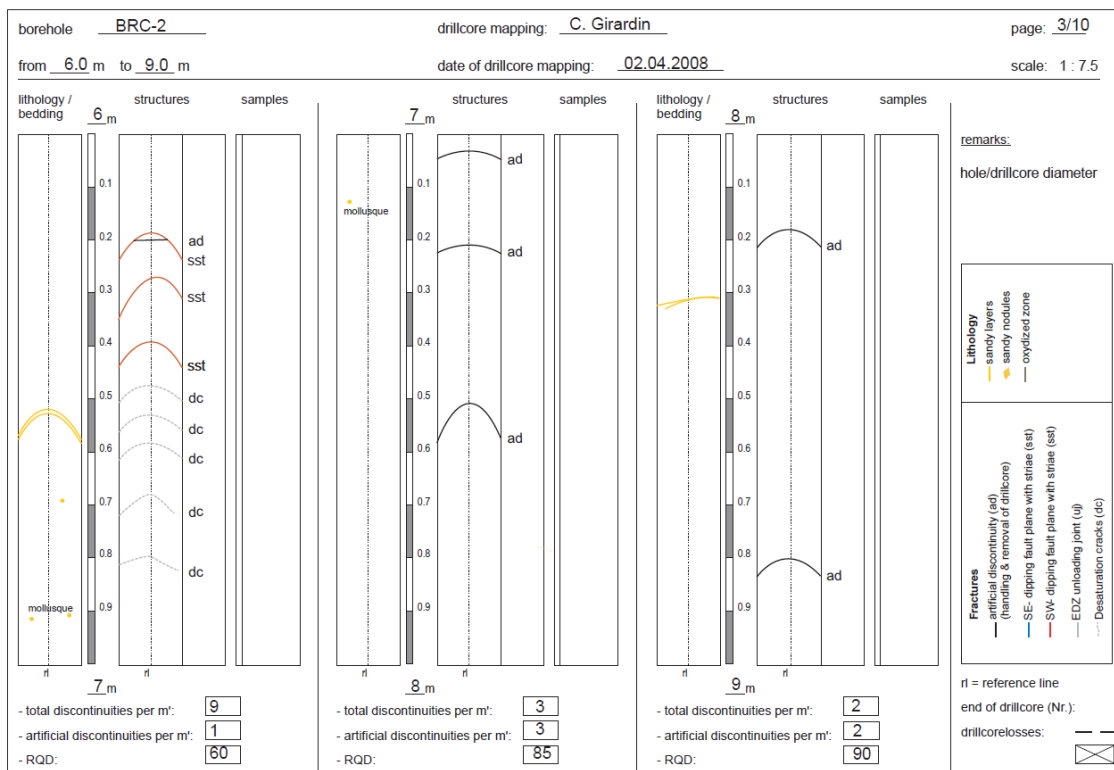


Figure A 7: Drillcore map of BRC-2 (Girardin et al. 2008).

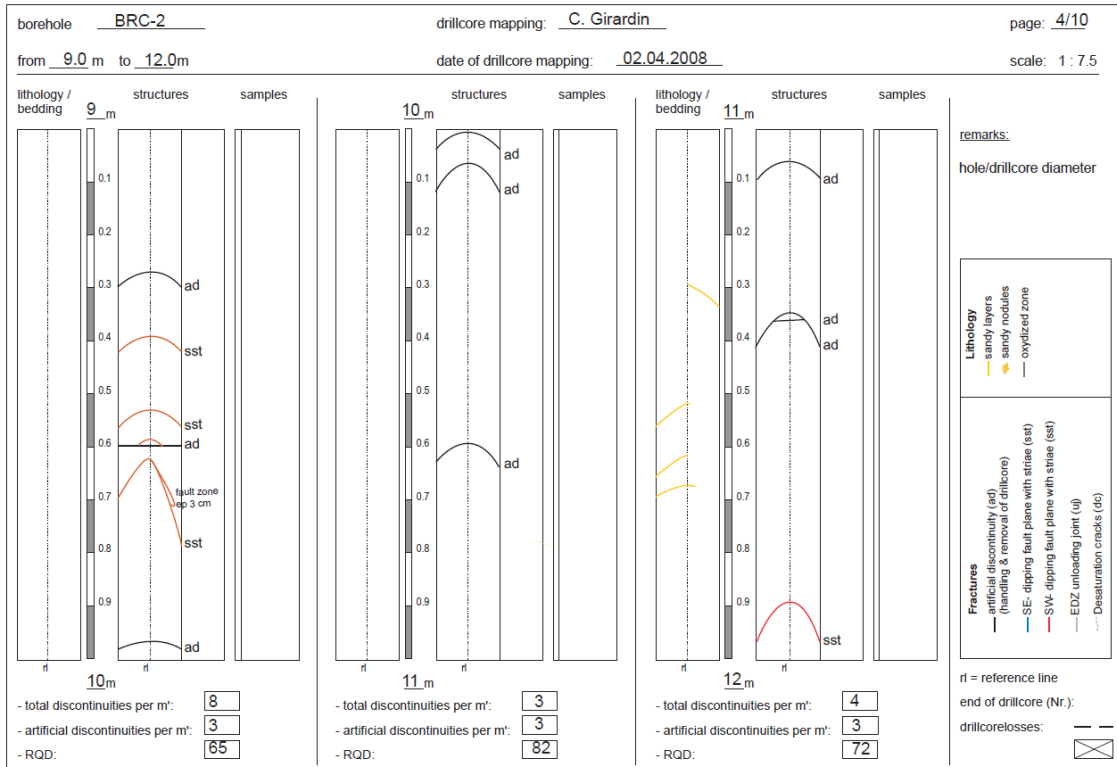


Figure A 8: Drillcore map of BRC-2 (Girardin et al. 2008).

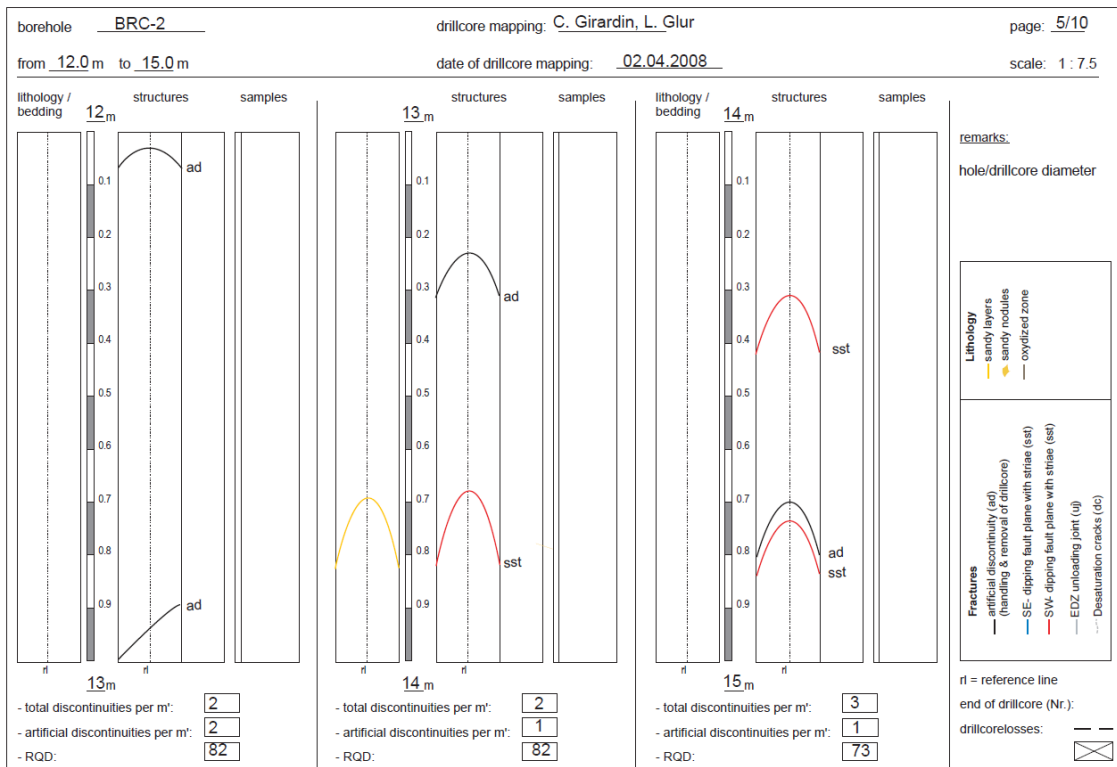


Figure A 9: Drillcore map of BRC-2 (Girardin et al. 2008).

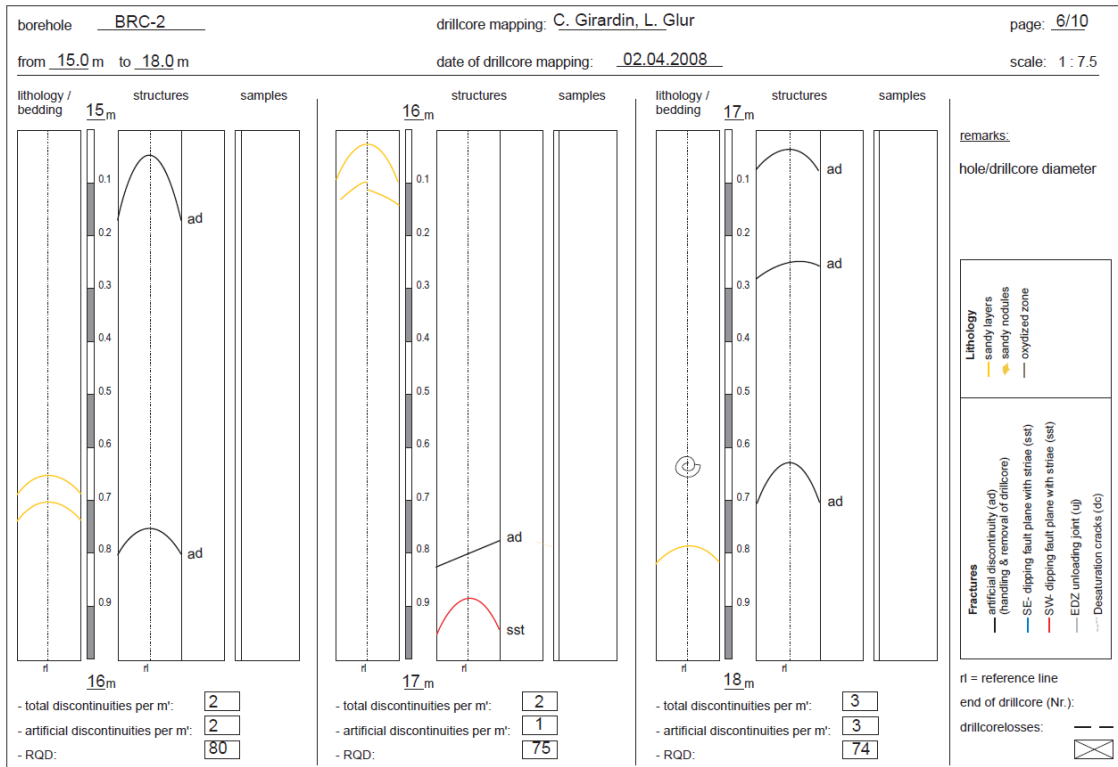


Figure A 10: Drillcore map of BRC-2 (Girardin et al. 2008).

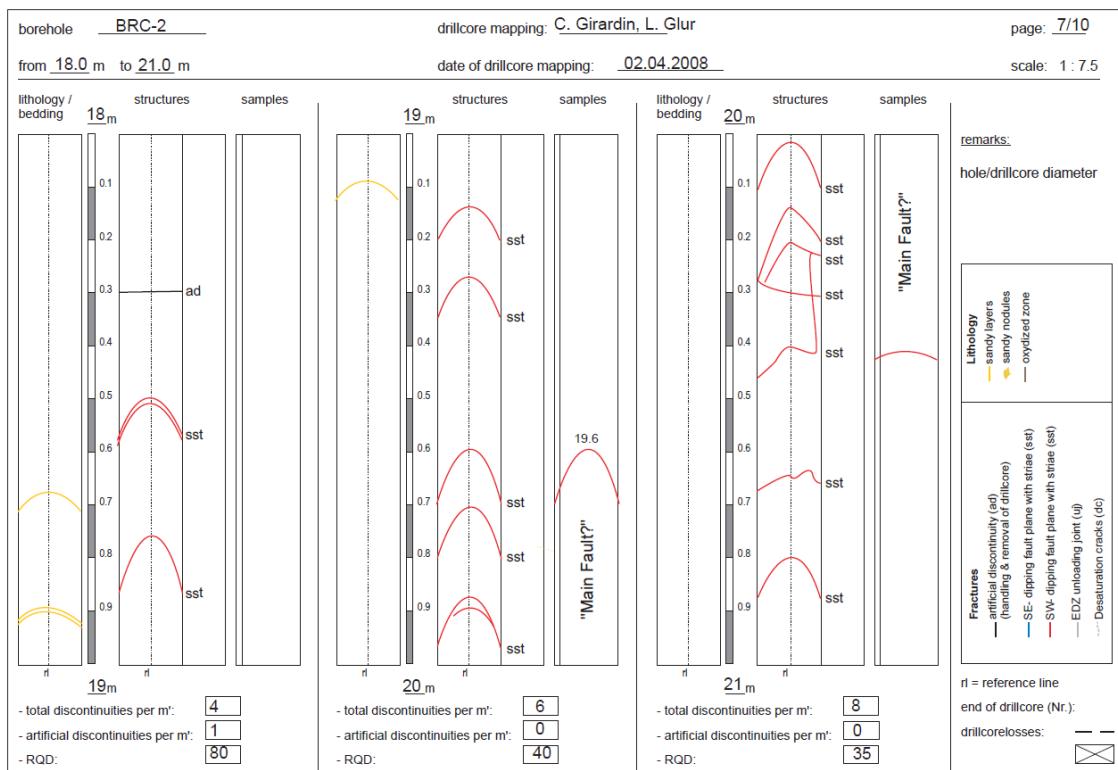


Figure A 11: Drillcore map of BRC-2 (Girardin et al. 2008).

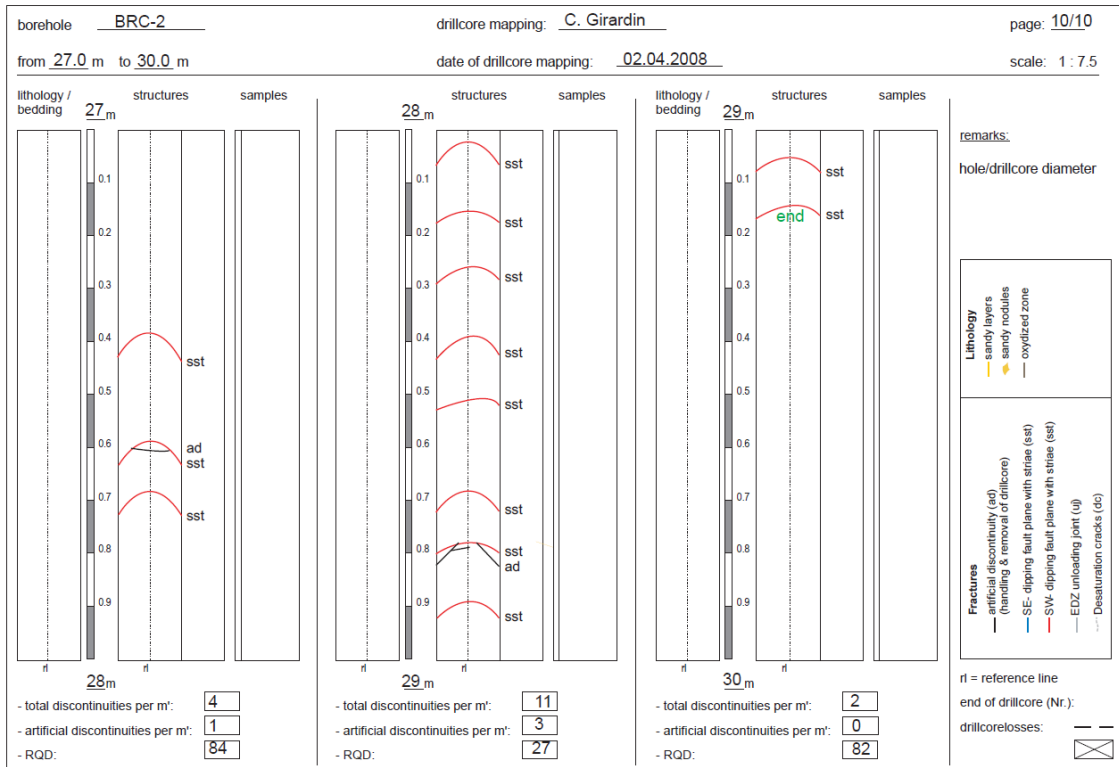


Figure A 14: Drillcore map of BRC-2 (Girardin et al. 2008).

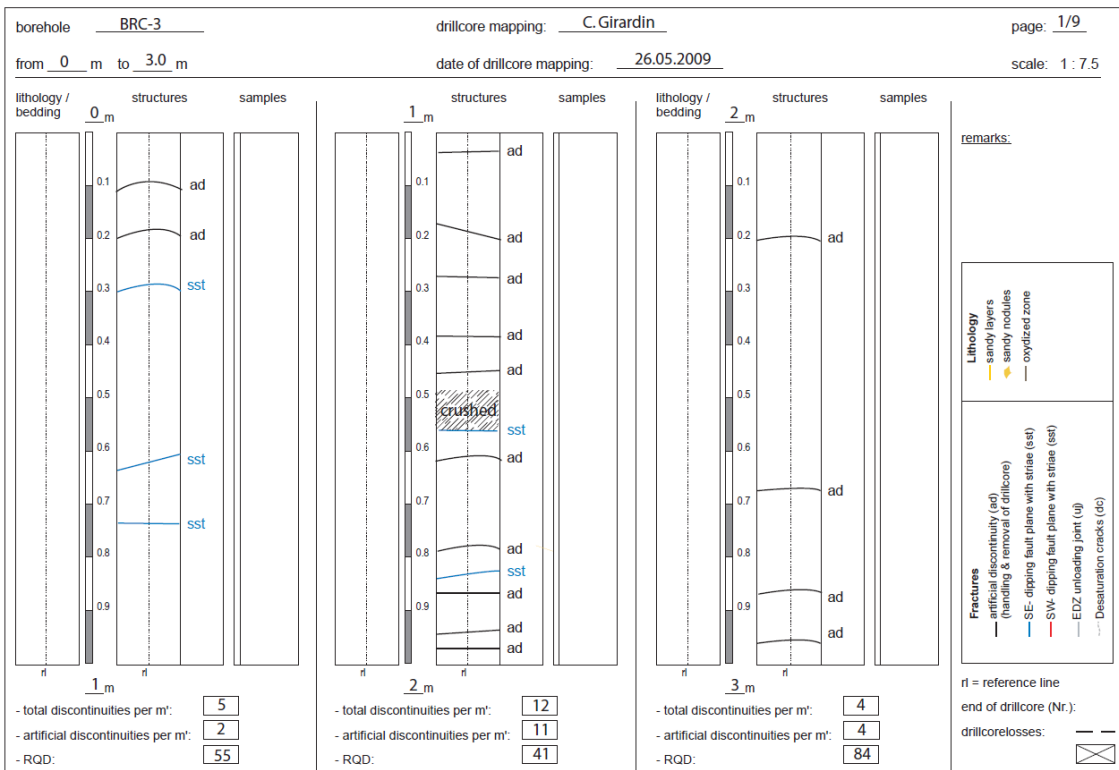


Figure A 15: Drillcore map of BRC-3 (Girardin et al. 2009).

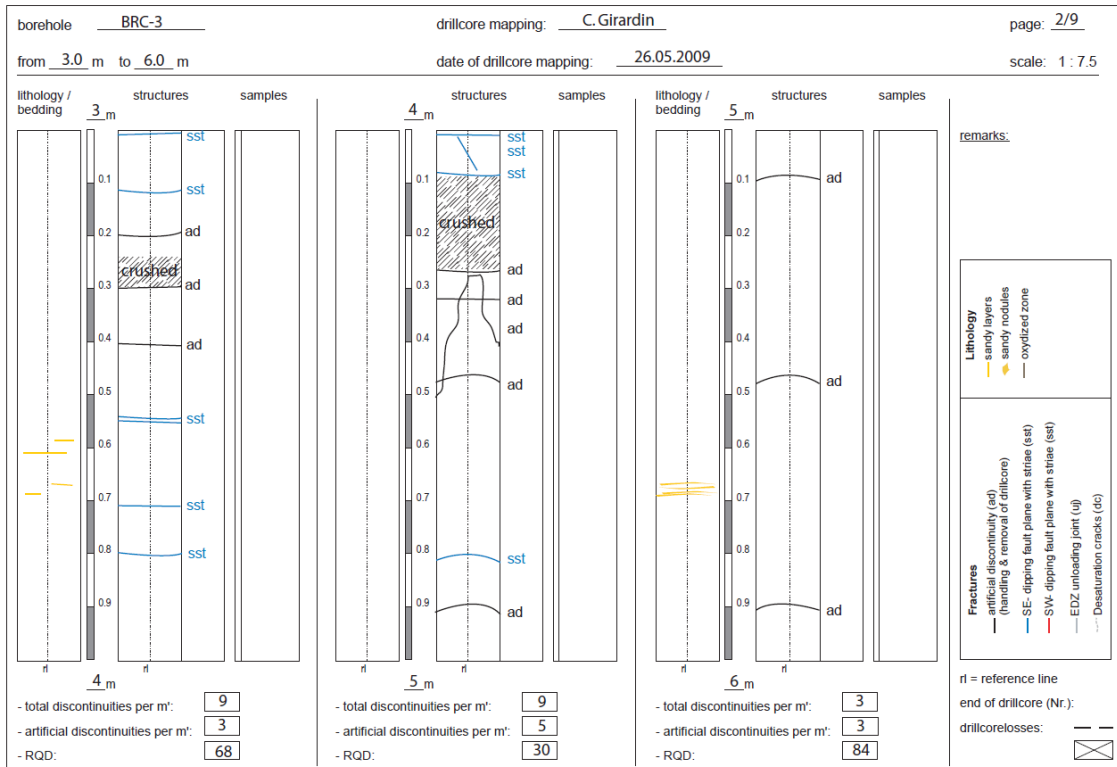


Figure A 16: Drillcore map of BRC-3 (Girardin et al. 2009).

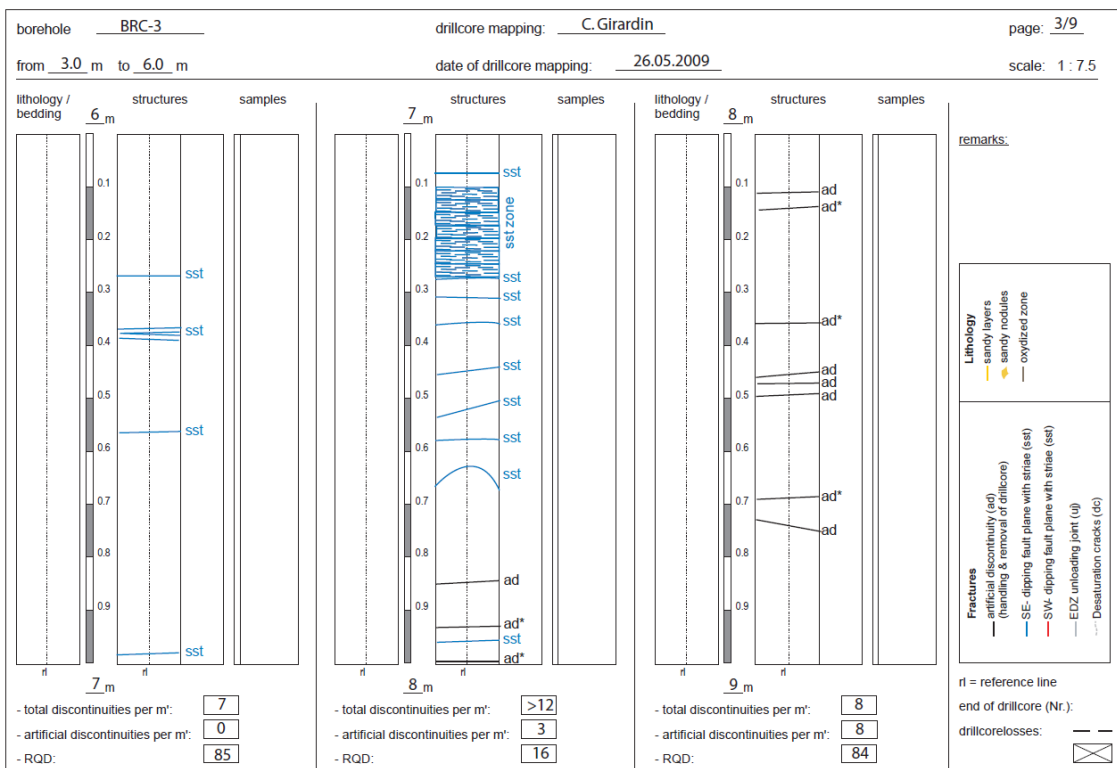


Figure A 17: Drillcore map of BRC-3 (Girardin et al. 2009).

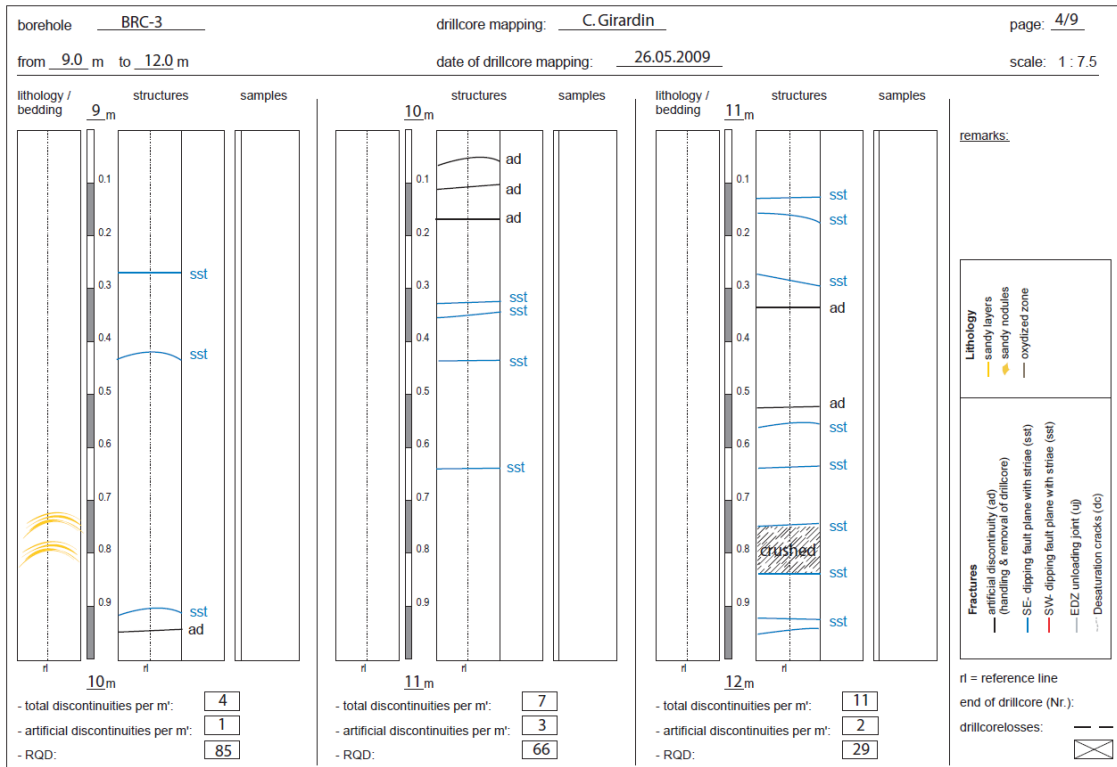


Figure A 18: Drillcore map of BRC-3 (Girardin et al. 2009).

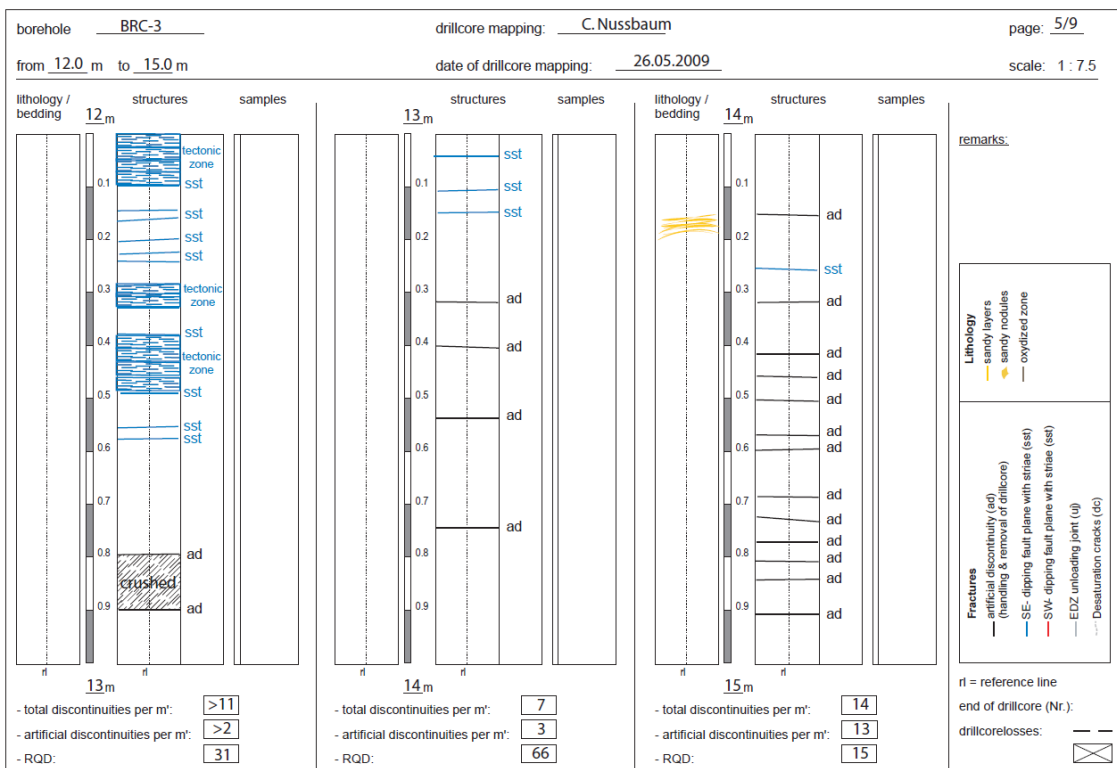


Figure A 19: Drillcore map of BRC-3 (Girardin et al. 2009).

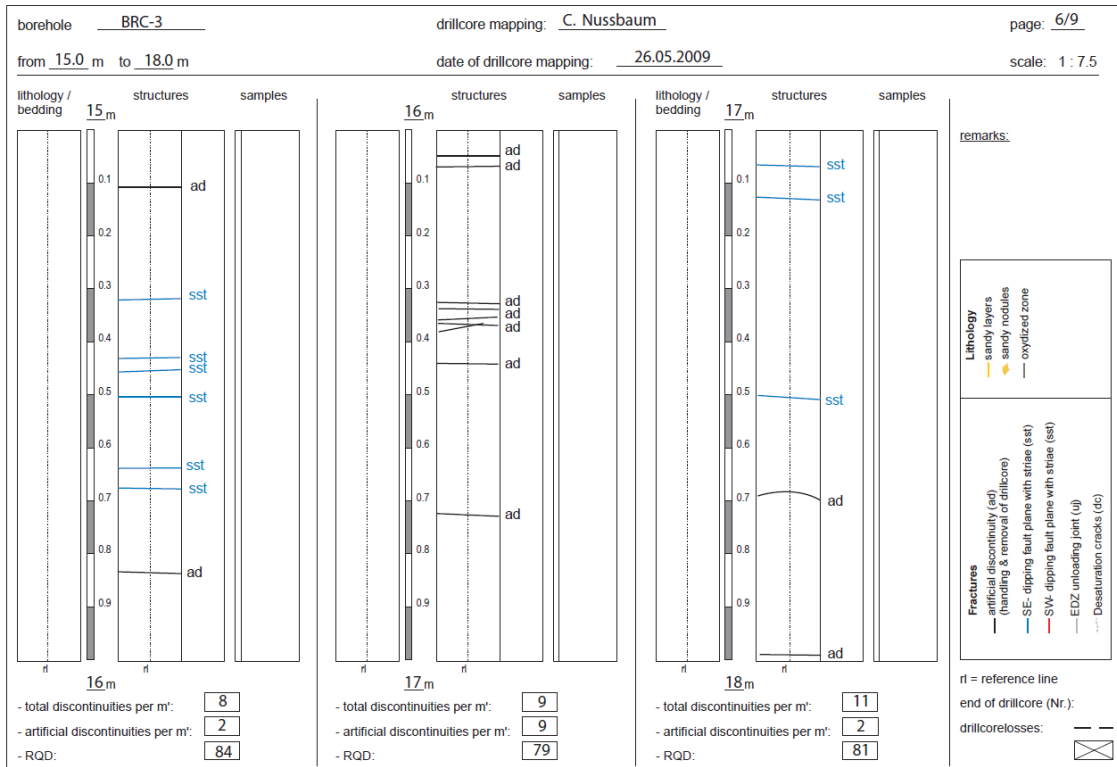


Figure A 20: Drillcore map of BRC-3 (Girardin et al. 2009).

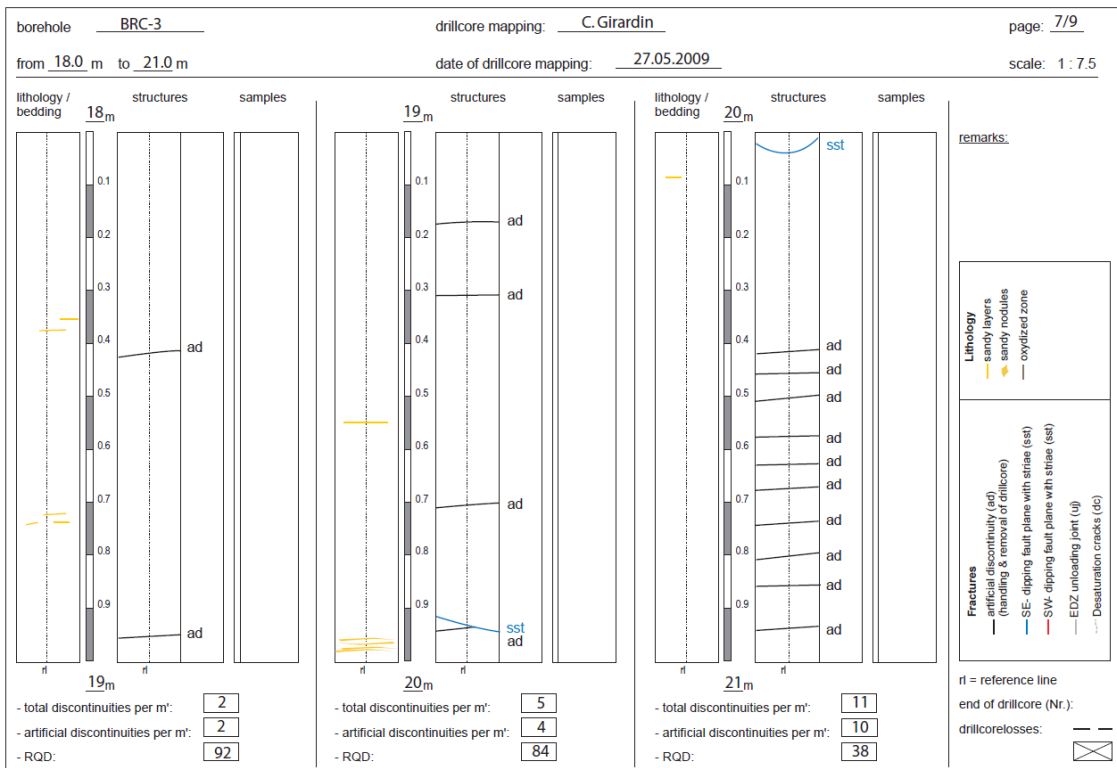


Figure A 21: Drillcore map of BRC-3 (Girardin et al. 2009).

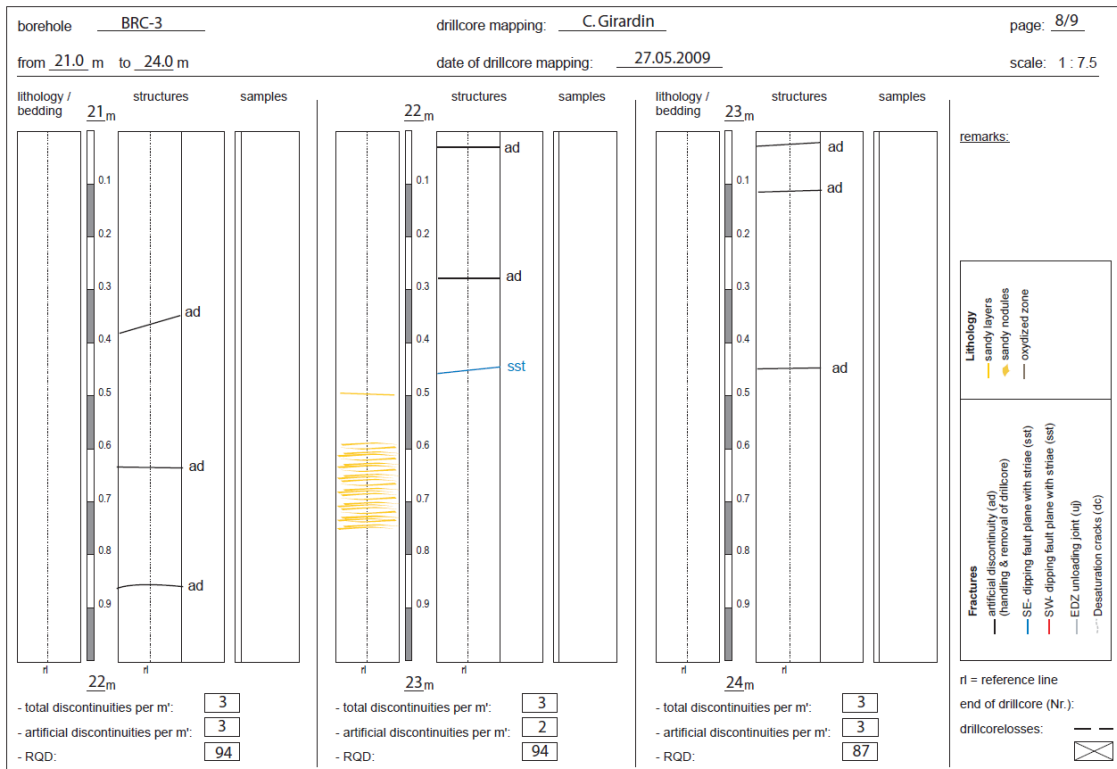


Figure A 22: Drillcore map of BRC-3 (Girardin et al. 2009).

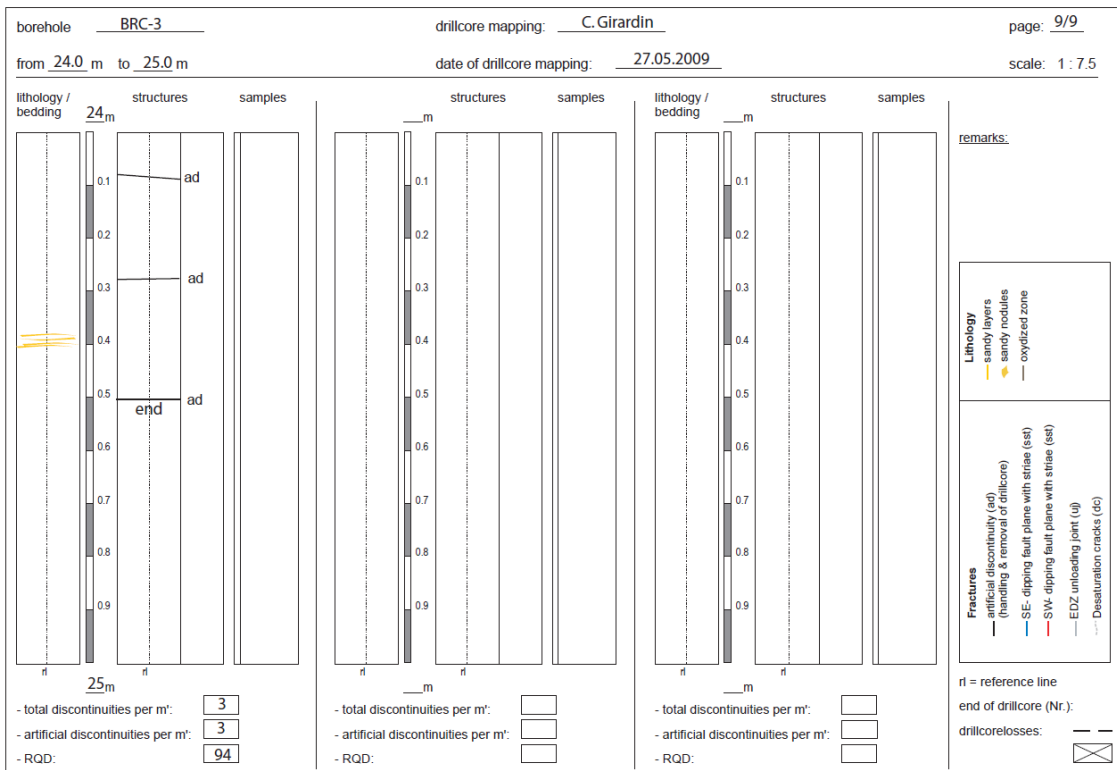


Figure A 23: Drillcore map of BRC-3 (Girardin et al. 2009).

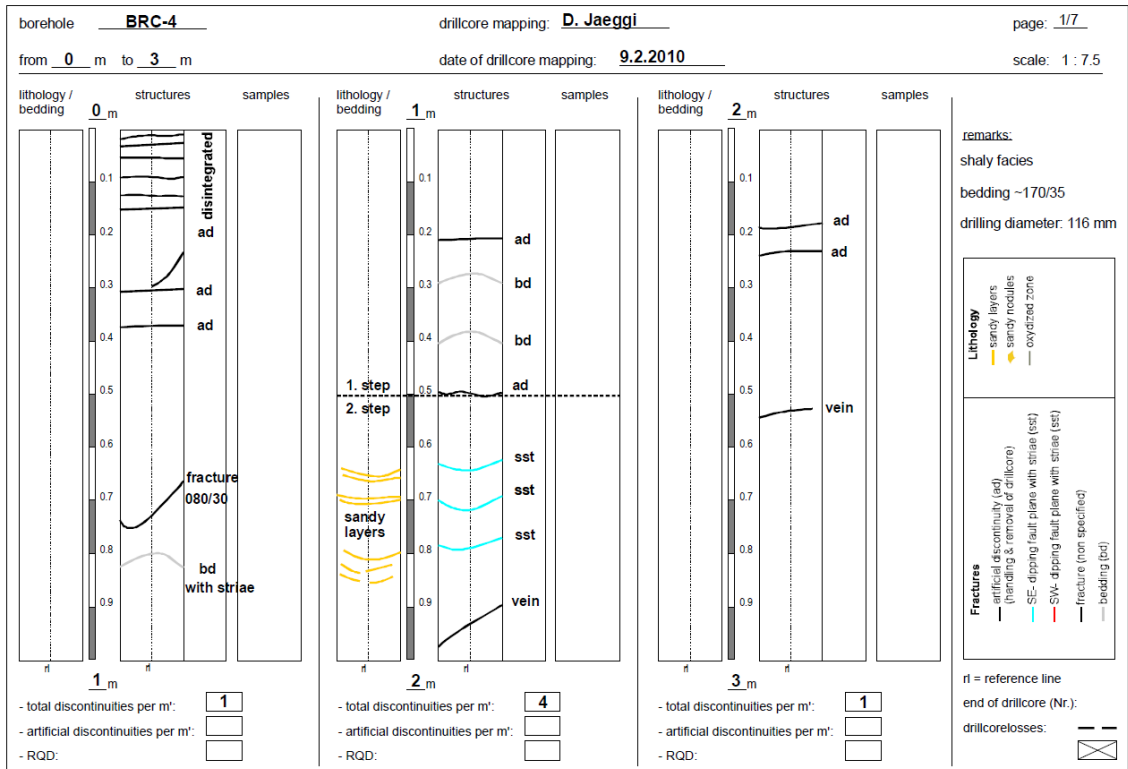


Figure A 24: Drillcore map of BRC-4 (Pfister et al. 2011).

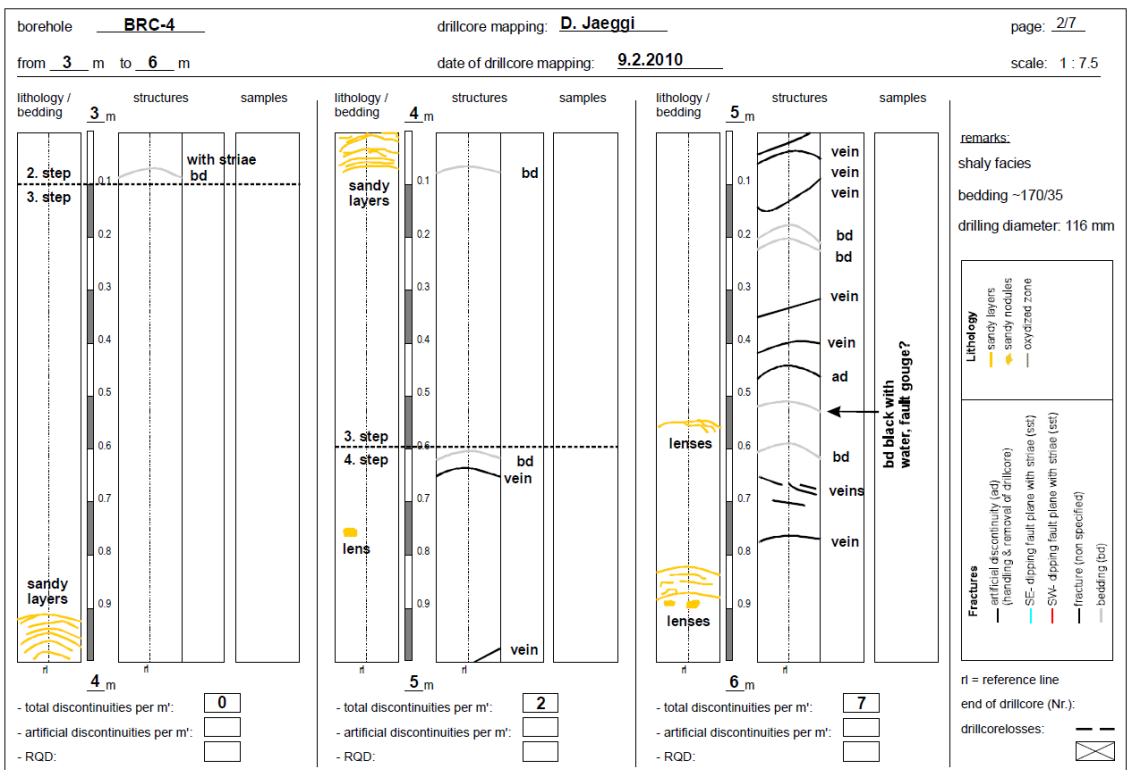


Figure A 25: Drillcore map of BRC-4 (Pfister et al. 2011).

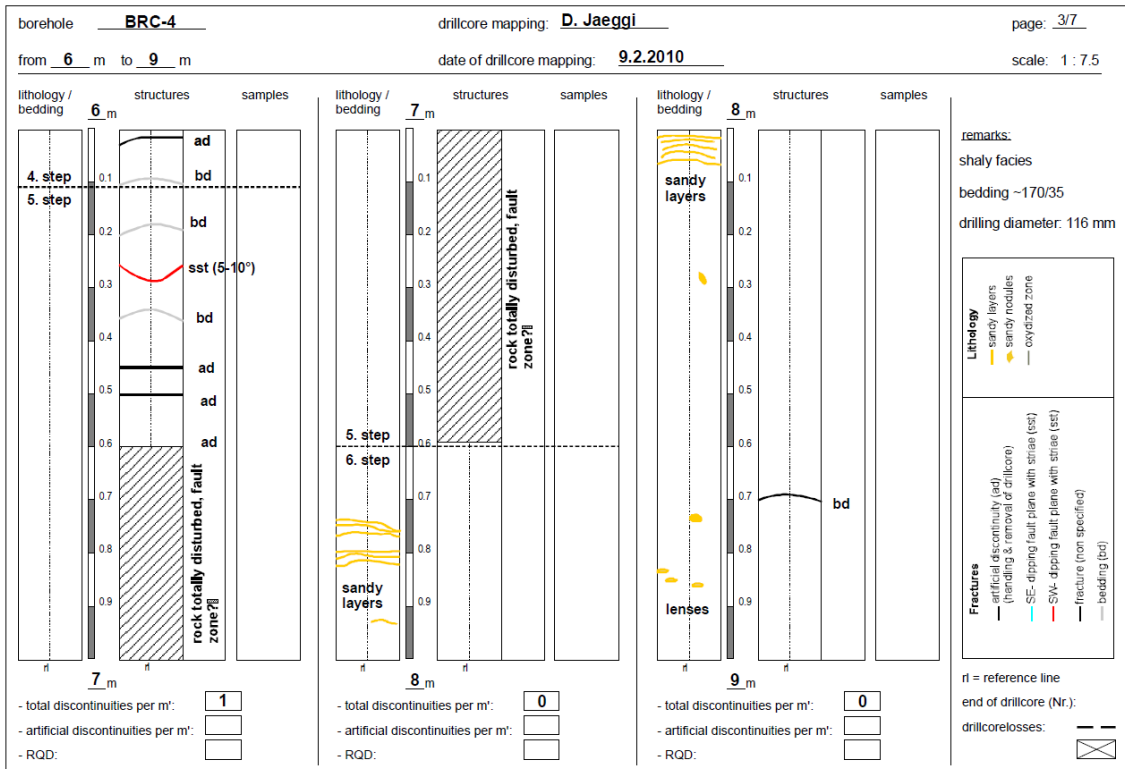


Figure A 26: Drillcore map of BRC-4 (Pfister et al. 2011).

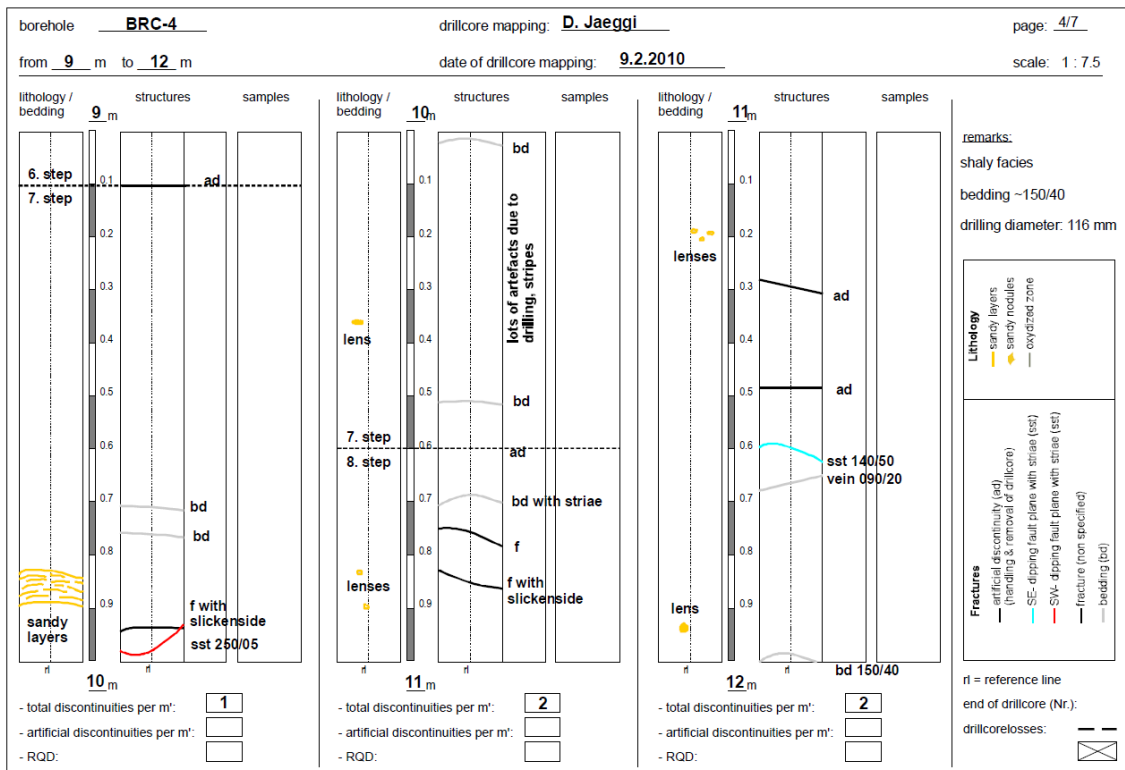


Figure A 27: Drillcore map of BRC-4 (Pfister et al. 2011).

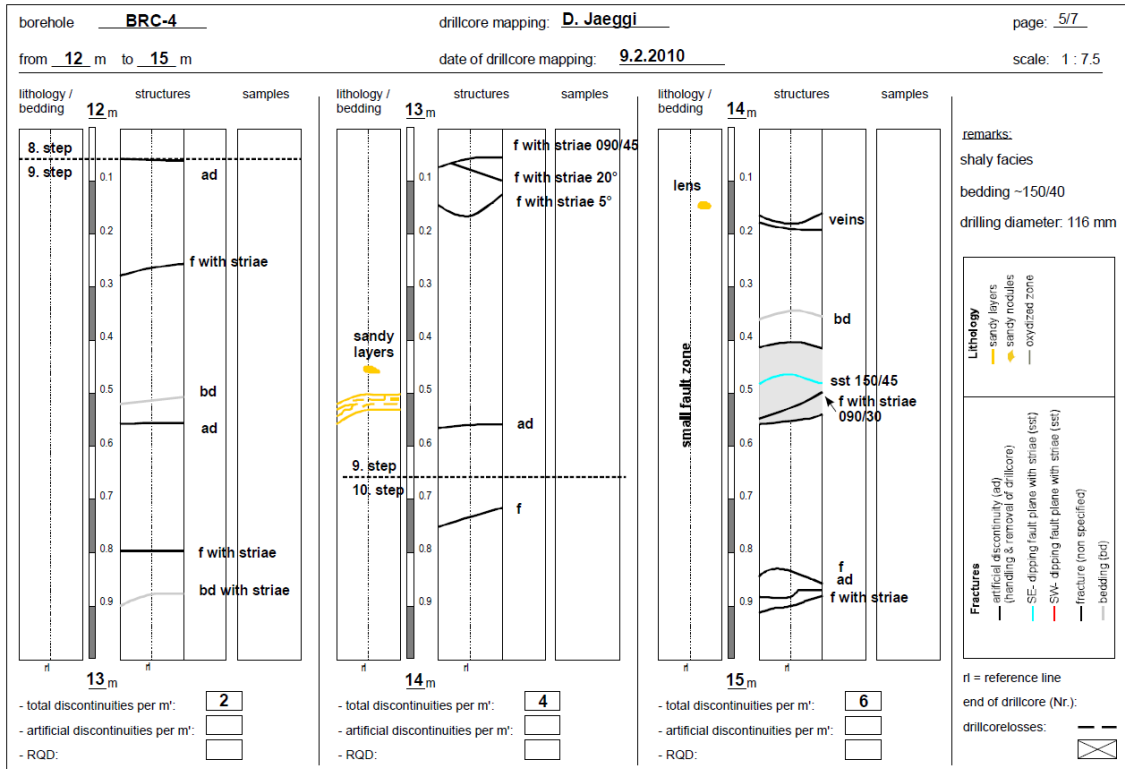


Figure A 28: Drillcore map of BRC-4 (Pfister et al. 2011).

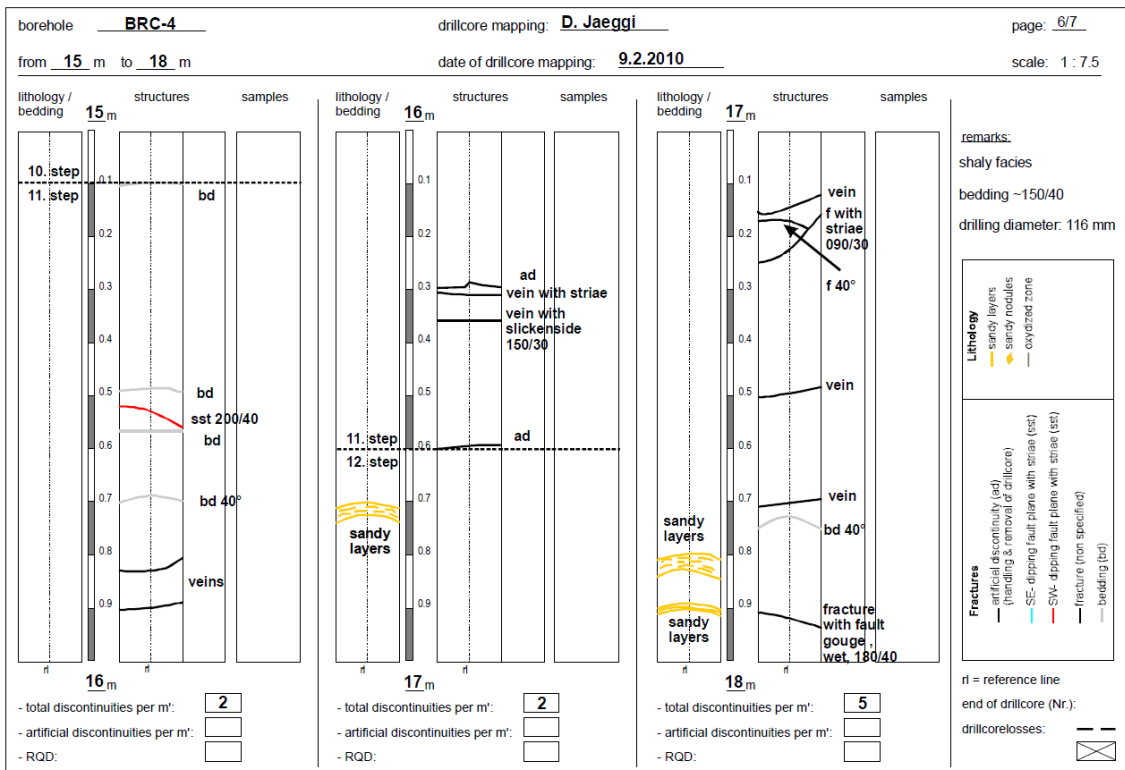


Figure A 29: Drillcore map of BRC-4 (Pfister et al. 2011).

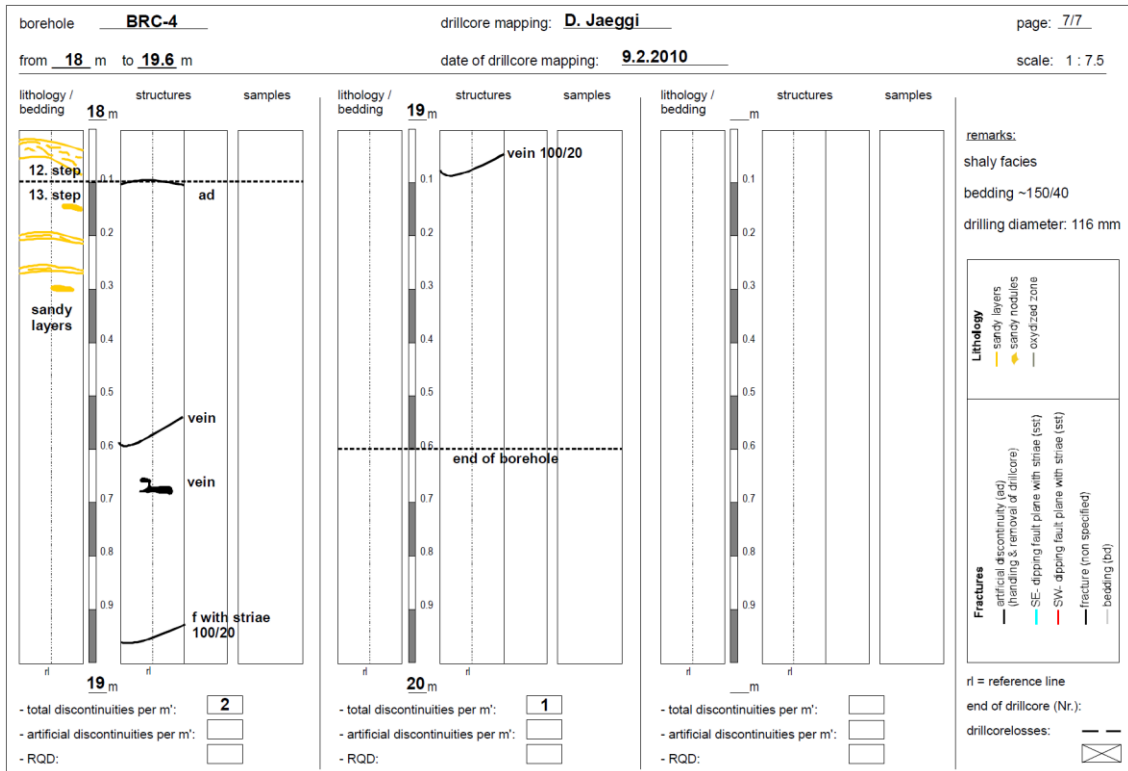


Figure A 30: Drillcore map of BRC-4 (Pfister et al. 2011).


APPENDIX B

B1 Tunnel data: Geological maps

Systematic geological tunnel face and sidewall mapping took place immediately after each excavation round between GM 40 and GM 127. Emphasis was placed on the identification and characterization of pre-existing tectonic and excavation-induced discontinuities and their spatial relationships to identify possible interactions. Geological maps of the tunnel invert, the sidewalls and the tunnel faces were provided by the site geologists and are compiled in the following.

Legend:

Tectonic Structures (pre-existing)


 SE-dipping fault planes and subhorizontal planes

 strongly tectonised zone


Lithologies


 bedding trace


 extension vein

 ammonite

EDZ Structures (related to excavation)

 striated fractures with shear sense (mode II)

 extension fractures (mode I) without plumose

 extension fractures (mode I) plumose with impact point

145/53 orientation measurement of plane (dip-direction/dip)

L126/23 lineation measurement

(after Nussbaum et al. 2008)

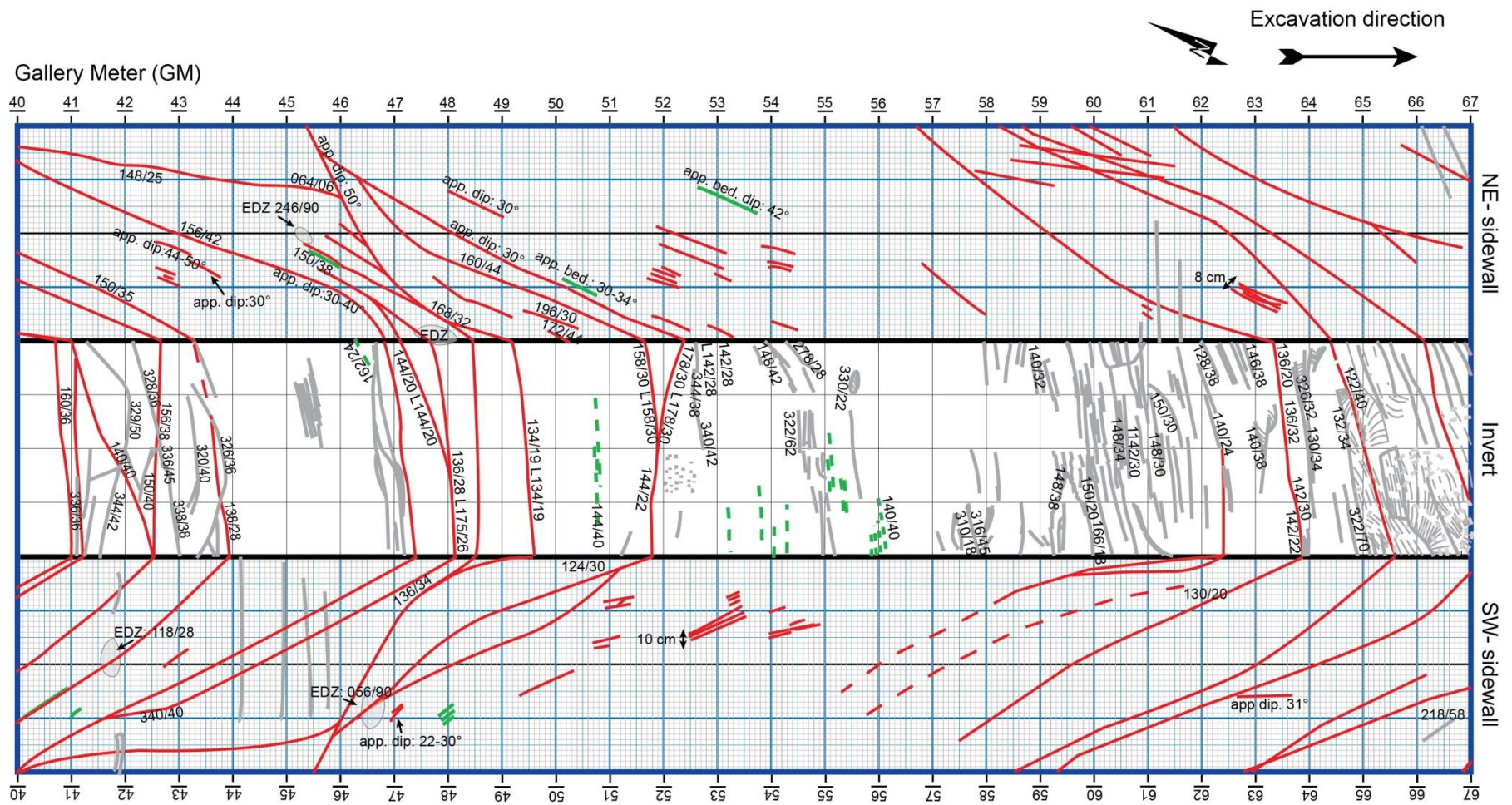


Figure B 1: Geological map of the tunnel invert and the tunnel sidewalls between GM 40.0 and GM 67.0 (after Nussbaum et al. 2008).

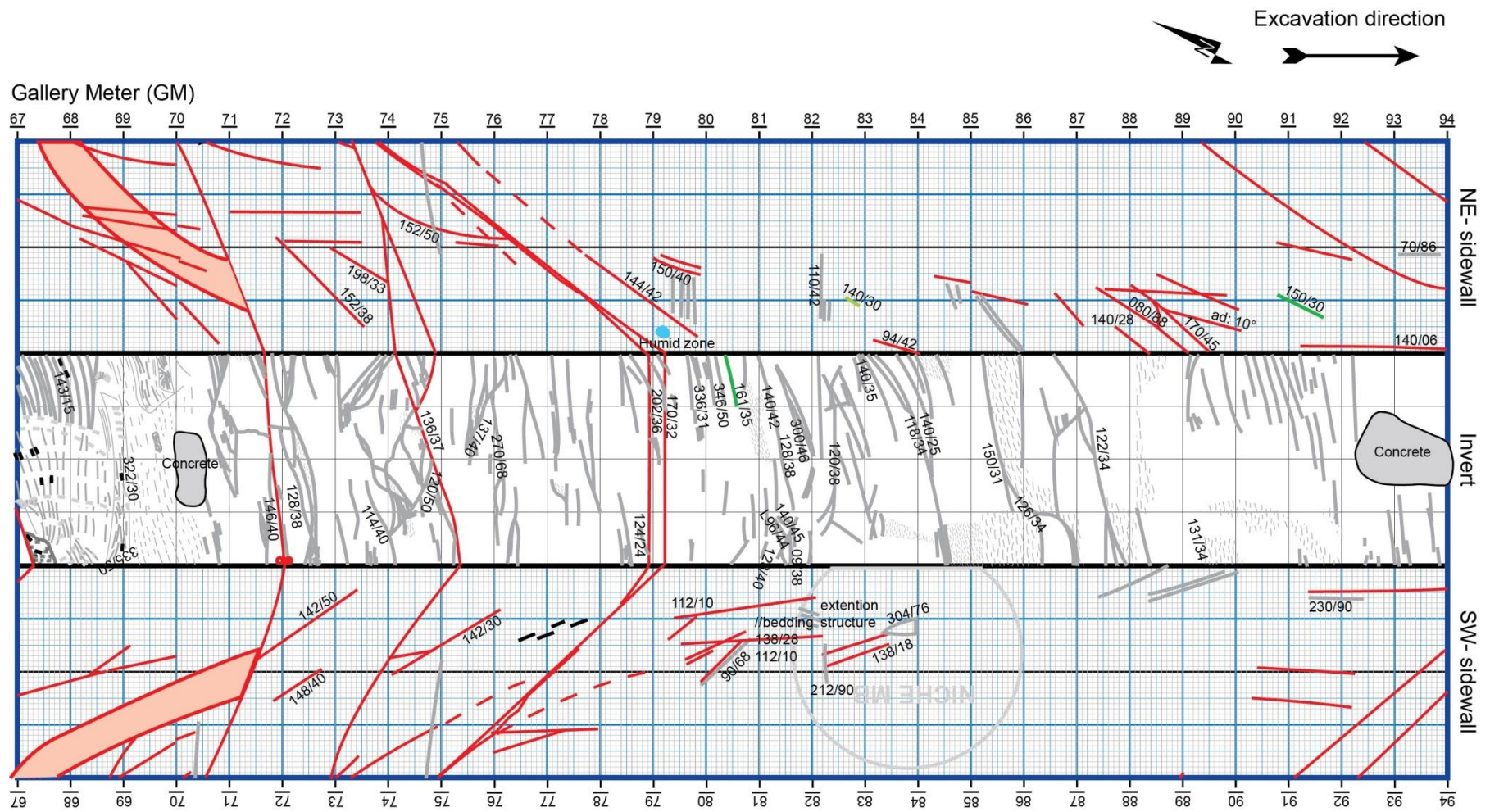


Figure B 2: Geological map of the tunnel invert and the tunnel sidewalls between GM 67.0 and GM 94.0 (after Nussbaum et al. 2008).

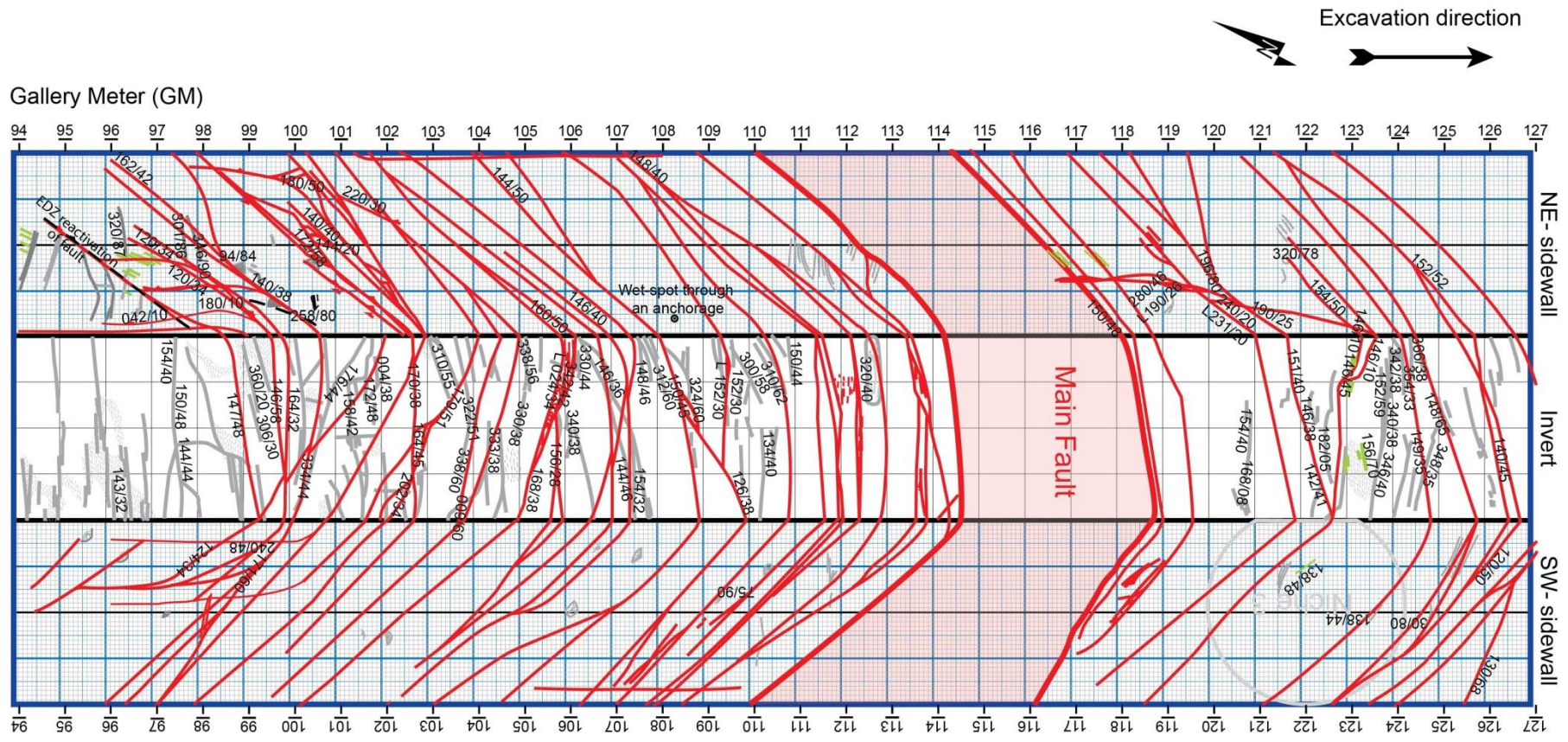


Figure B 3: Geological map of the tunnel invert and the tunnel sidewalls between GM 94.0 and GM 127.0 (after Nussbaum et al. 2008).

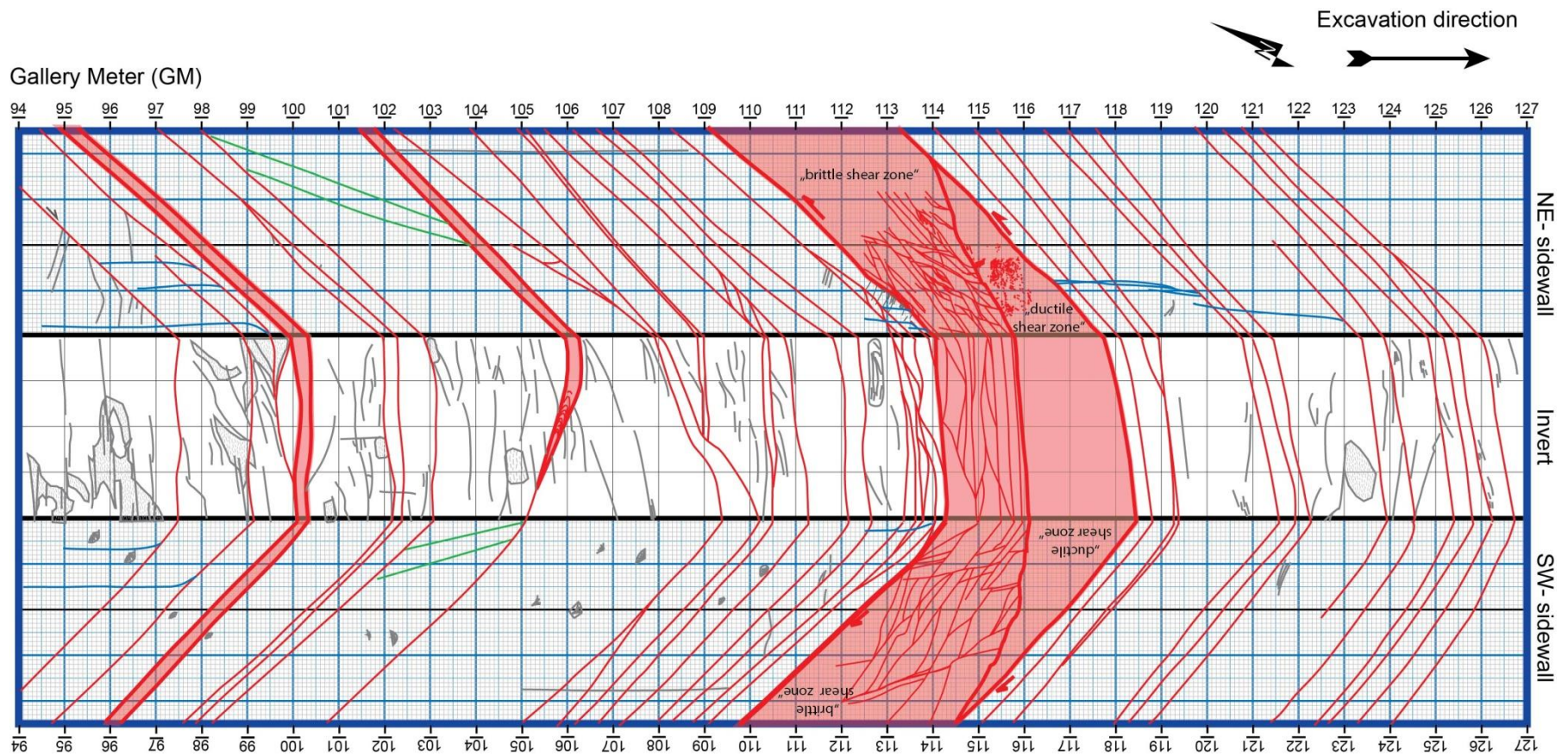


Figure B 4: Geological map of the tunnel invert and the tunnel sidewalls between GM 94.0 and GM 127.0 (after Nussbaum et al. 2013).

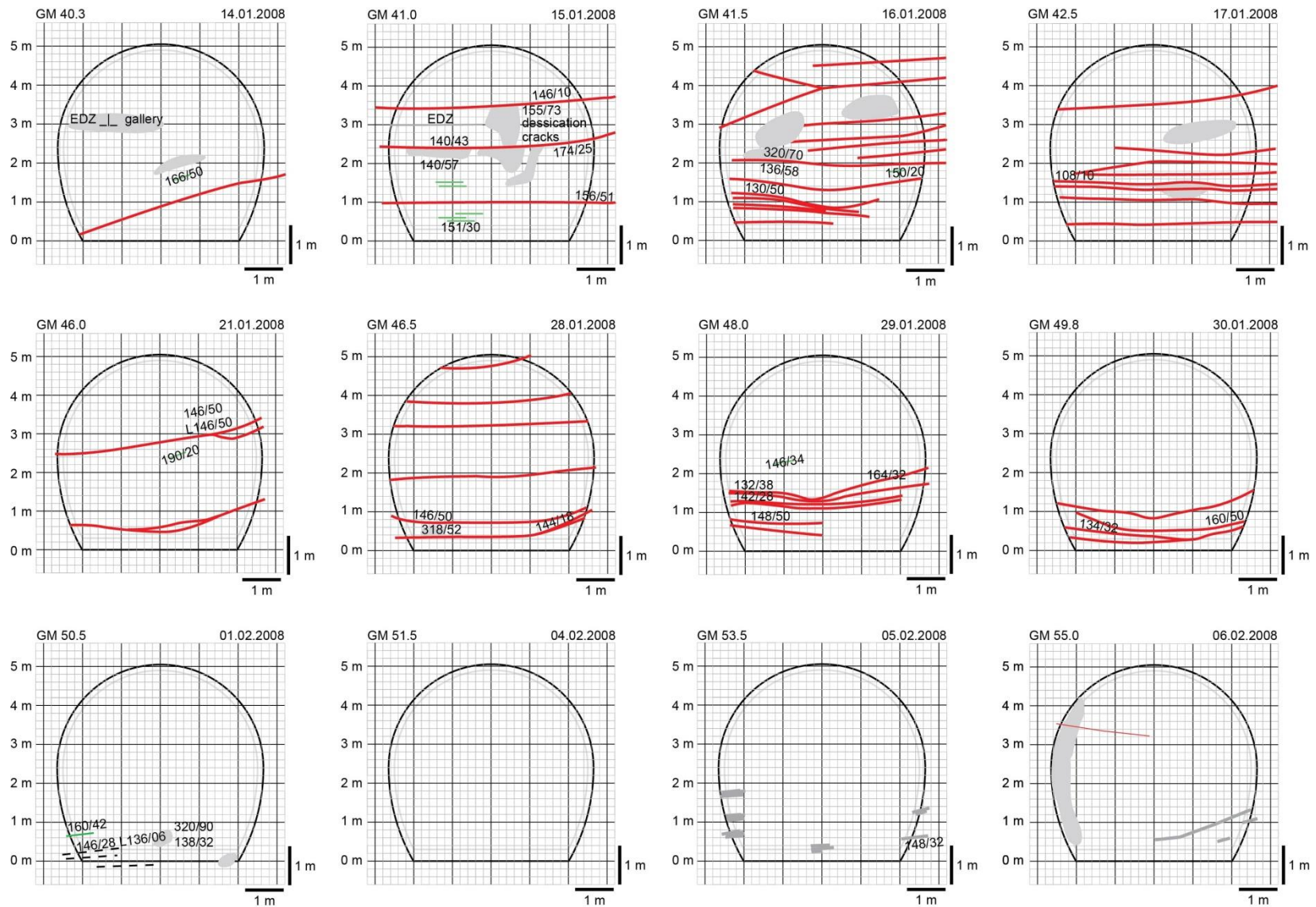


Figure B 5: Geological maps of the tunnel faces from GM 40.3 to GM 55.0 (after Nussbaum et al. 2008).

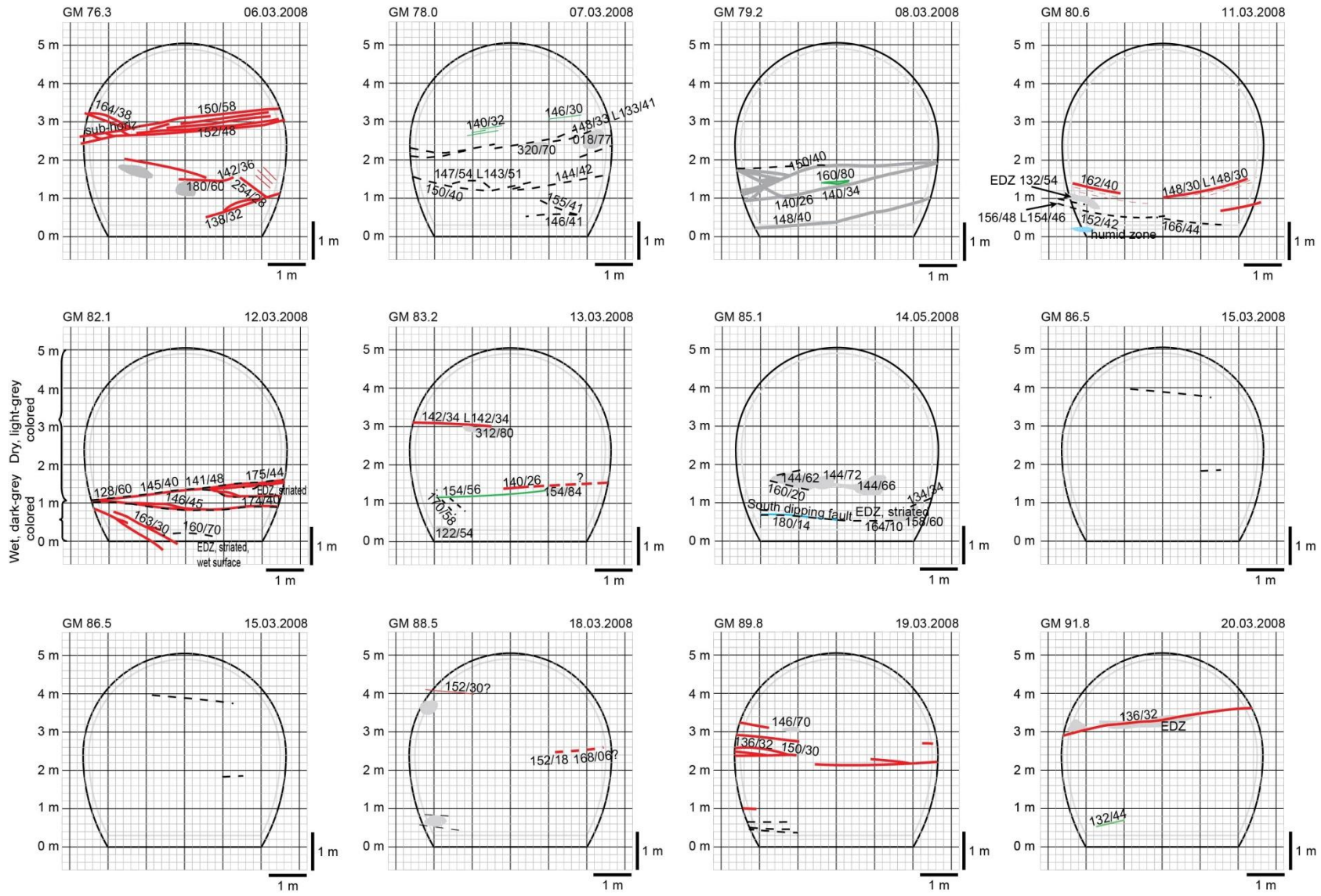


Figure B 7: Geological maps of the tunnel faces from GM 76.3 to GM 91.8 (after Nussbaum et al. 2008).

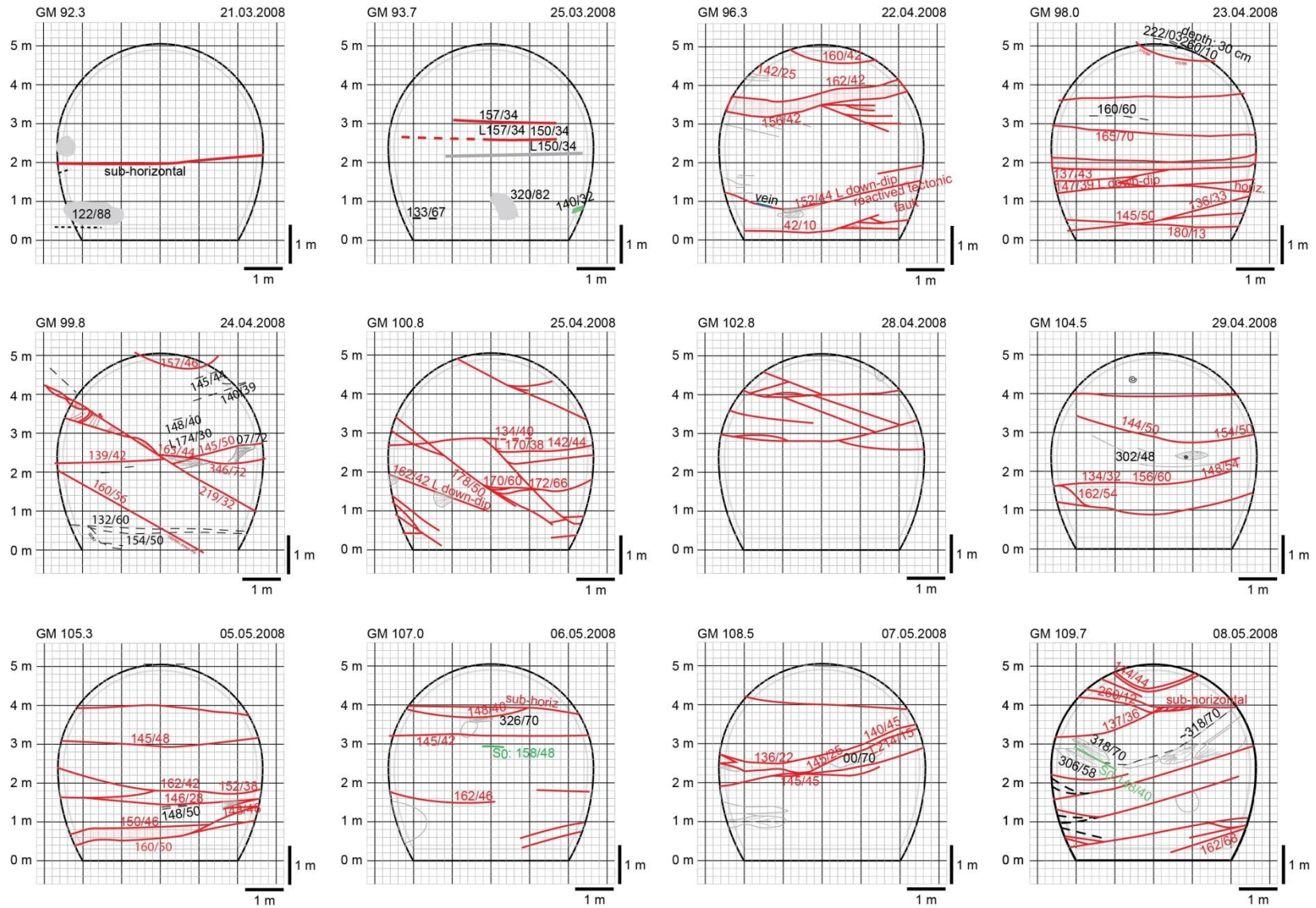


Figure B 8: Geological maps of the tunnel faces from GM 92.3 to GM 109.7 (after Nussbaum et al. 2008).

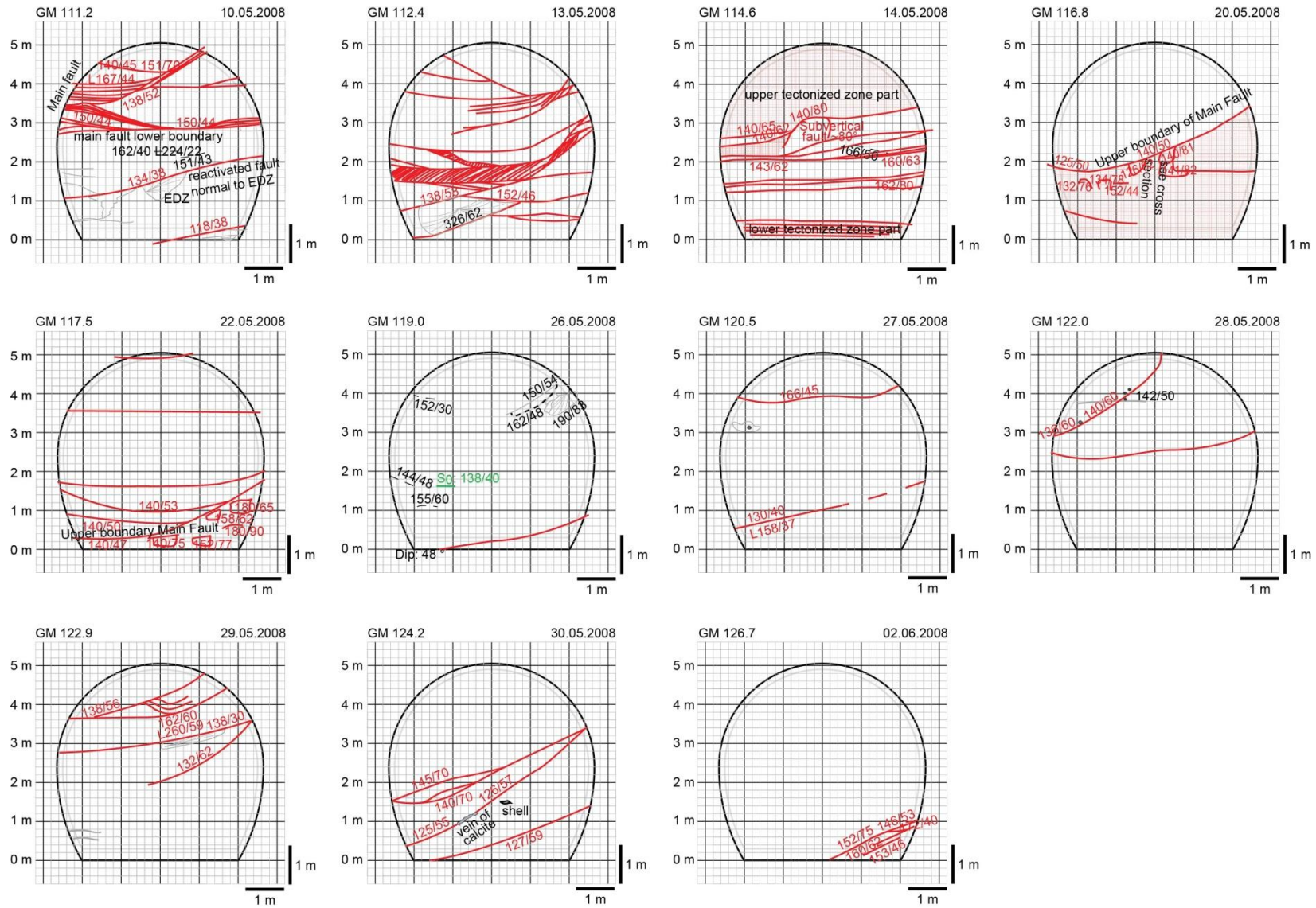


Figure B 9: Geological maps of the tunnel faces from GM 111.2 to GM 126.7 (after Nussbaum et al. 2008).

Curriculum Vitae

Personal

Name: Reto Thöny
Date of birth: 22. December 1981
Place of birth: Chur (GR), Switzerland
Nationality: Switzerland

Education

11/2008 - 06/2013: PhD in Engineering Geology, Department of Earth Sciences, ETH Zurich
10/2006 - 10/2008: Master of Science in Earth Sciences, Department of Earth Sciences, ETH Zurich. Major in Engineering Geology
10/2003 - 09/2006: Bachelor of Science in Earth Sciences, Department of Earth Sciences, ETH Zurich
08/1997 - 07/2002: Matura diploma, Bündner Kantonsschule Chur (GR), Switzerland

Work experience

02/2008 - 11/2012: Teaching and research assistantship: ETH Zurich, Switzerland
Teaching assistant in the Engineering Geology Master program: Landslide Analysis Course, Rock Mechanics and Rock Engineering Course, Soil Mechanics and Foundation Engineering Course, Geotechnical Laboratory Course for Rocks and Soils, Borehole Geophysics Course
Co-supervising of Bachelor and Master theses in Engineering Geology

Publications

Thoeny R, Amann F, Loew S (2013): RC experiment - Rock mass characterization, *Research and Experience Report 2012*, Swiss Federal Nuclear Safety Inspectorate, ISSN 1664-3151
Amann F, Thoeny R, Martin CD (2012): Rock mechanical considerations associated with the construction of a nuclear waste repository in clay rock, *Proceedings of the 46th US Rock Mechanics/Geomechanics Symposium 2012*, Chicago, American Rock Mechanics Association, ARMA
Thoeny R, Amann F, Button EA, Loew S (2012): RC experiment - Rock mass characterization, *Research and Experience Report 2011*, Swiss Federal Nuclear Safety Inspectorate, ISSN 1664-3151
Amann F, Thoeny R, Kaiser PK, Button EA (2011): Insight into the brittle failure behavior of clay shales in unconfined and confined compression, *Proceedings of the 45th US Rock Mechanics/Geomechanics Symposium 2011*, San Francisco, CA, American Rock Mechanics Association, ARMA 11-536

- Amann F, Thoeny R, Button EA, Loew S (2011): RC experiment - Rock mass characterization, *Research and Experience Report 2010*, Swiss Federal Nuclear Safety Inspectorate, ISSN 1664-3178
- Thoeny R, Amann F, Button EA (2010): Ground conditions and the relationship to ground behavior - a new mine-by project in Opalinus clay at Mont Terri Rock Laboratory, *Proceedings of the European Rock Mechanics Symposium 2010*, Lausanne, Switzerland, *Rock Mechanics and Environmental Engineering*, edited by Zhao, Labious, Dudt and Mathier, Taylor & Francis Group, London, ISBN 978-0-415-58654-2
- Amann F, Button EA, Thoeny R, Loew S (2010): RC experiment - Rock mass characterization, *Research and Experience Report 2009*, Swiss Federal Nuclear Safety Inspectorate, ISSN 1661-2884
- Amann F, Button EA, Bluemel M, Thoeny R (2010): Insight into the mechanical behaviour of Opalinus Clay, *Proceedings of the European Rock Mechanics Symposium 2010*, Lausanne, Switzerland, *Rock Mechanics and Environmental Engineering*, edited by Zhao, Labious, Dudt and Mathier, Taylor & Francis Group, London, ISBN 978-0-415-58654-2
- Amann F, Loew S, Button EA, Thoeny R (2009): RC experiment - Rock mass characterization, *Research and Experience Report 2008*, Swiss Federal Nuclear Safety Inspectorate, ISSN 1661-2892
- Thoeny R (2008): Dynamic fluid electric conductivity logging for identification and characterization of preferential groundwater flow in the Aknes rockslide (Norway), *MSc Thesis*, Geological Institute, ETH Zurich
- Thoeny R (2006): Massenbewegung und Gefahrenanalyse - Felssturz von Felsberg (Switzerland), *Bachelor Thesis*, Geological Institute, ETH Zurich